gazi
MÜHENDİSLİK BİLİMLERİ DERGİSİ

Gazi AKADEMİK YAYINCILIK

p-ISSN: 2149-4916 • e-ISSN: 2149-9373

Cilt 10 • Sayı 1 • Nisan 2024

Volume 10 • Issue 1 • April 2024

GAZI JOURNAL OF ENGINEERING SCIENCES

Gazi AKADEMİK YAYINCILIK

GAZİ
JOURNAL OF ENGINEERING SCIENCES

EDİTÖR / EDITOR - IN – CHIEF

İsmail ŞAHİN
Gazi University, Ankara, Turkey
e-mail: editorgjes@gmail.com

YARDIMCI EDİTÖRLER / ASSOCIATE EDITORS

Harun GÖKÇE
Gazi University
e-mail: harungokce@gazi.edu.tr

Murat DÖRTERLER
Gazi University
e-mail: dorterler@gazi.edu.tr

ALAN EDİTÖRLERİ / SECTION EDITORS

Abdullah AKDOĞAN
Pamukkale University

Adem TEKEREK
Gazi University

Alper BÜYÜKKARAGÖZ
Gazi University

Amin MIRZAPOUR
Zanjan Islami Azad University

Ayhan AYTAÇ
National Defense University

Bülent ÖZKAN
Gazi University

Erdem CÜCE
Recep Tayyip Erdoğan University

Fecir DURAN
Gazi University

Fatih ŞAHİN
Gazi University

G. Serdar TOMBUL
ASELSAN

Halil KARAKOÇ
Hacettepe University

Hüseyin GÖKÇE
Çankırı Karatekin University

M. Hanefi CALP
Karadeniz Technical University

Mustafa BOZ
Karabuk University

Mustafa GÜNAY
Karabük University

Neslihan TOP
Gazi University

Serhat KARAP
TUBİTAK-SAGE

Tayfun MENLİK
Gazi University

Umit ATİLA
Gazi University

YAYIN DANIŞMA KURULU / ADVISORY BOARD

Adnan SÖZEN
Gazi University, Turkey

Andrew PINKERTON
Lancaster University, England

Bekir Sami YILBAŞ
King Fahd University, Sudia Arabia

Farzollah MIRZAPOUR
University of Zanjan, Iran

Majid MEGHDADI
University of Zanjan, Iran

Mustafa KURT
Gazi University, Turkey

Nowruz ALLAHVERDİ
Karatay University, Turkey

Reza Negarastani
RIETEX, England

PRINT ISSN: 2149-4916 E-ISSN: 2149-9373 © 2022 Gazi Akademik Yayıncılık

Gazi AKADEMİK YAYINCILIK

GAZİ
JOURNAL OF ENGINEERING SCIENCES

Herbert M. REYNOLDS
Michigan State University, USA

Jamal KHATIB
University of Wolverhampton, England

John KINUTHIA
University of South Wales, England

Jonathan C. BORG
University of Malta, Malta

Hossam KISHAWY
University of Ontario Technology, Canada

Kürşad SEZER
Gazi University, Turkey

Salman NISAR
National University of Sci. and Tech., Pakistan

Shahin JALILI
Tebriz University, Iran

Şakir TAŞDEMİR
Selçuk University, Turkey

Tahsin Tecelli ÖPÖZ
John Moores University, England

Yasir JOYA
GIK Institute, Pakistan

DİL EDİTORLERİ / LANGUAGE EDITORS

Türkçe/Turkish: V. Savaş YELOK (Hacı Bayram Veli University)

İngilizce/English: H. Kürşad SEZER (Gazi University)

TEKNİK EDİTÖR / TECHNICAL EDITOR

Neslihan TOP
Gazi University

Nurullah YÜKSEL
Gazi University
e-mail: editorgjes@gmail.com

MİZANPAJ EDİTÖRÜ / LAYOUT EDITOR

M. Efe CEYLAN
Gazi University
e-mail: editorgjes@gmail.com

BU SAYININ HAKEMLERİ / REVIEWER OF THIS ISSUE

Ahmet İyigör
Ahmet Serdar Güldibi
Ayhan Onat
Barış Özlü
Caner Kara
Emre Delibaş
Emre Alvur
Erhan Polat
Erinç Karataş
Fikriye Ataman
Gültekin Uzun
Hilal Kaya
Hülya Öztürk Doğan
Kerem Taştan
Kerim Martin
Mehmet Şimşek
Muhammed Elitaş
Murat Uçar
Mustafa Günay
Mustafa Akkaya
Orhan Çakar
Osman Yıldız
Serkan Savaş
Taha Etem
Tuncay Karaçay
Çağrı Vakkas Yıldırım
İ. Ethem Karadirek
İbrahim Arda Cankaya
İpek Aytaç
İsmail Altın

GAZİ
JOURNAL OF ENGINEERING SCIENCES

Gazi Journal of Engineering Sciences has been published three issues per year

CORRESPONDENCE ADDRESS :

Gazi Akademik Yayıncılık
Mustafa Kemal Mah. 2118 Cad. No:4C/140 Çankaya/Ankara
Tel: +90-312-9113311 Fax: +90-312-9113312
e-mail: editorgjes@gmail.com

GAZİ
JOURNAL OF ENGINEERING SCIENCES

İÇİNDEKİLER / CONTENTS

Kümelenme Analizi için Meta-Sezgisel Algoritmaların K-Means ile Hibritlenmesi: Tıbbi Veri Kümeleri Üzerine Bir İnceleme

Hybridization of Meta-heuristic Algorithms with K-Means for Clustering Analysis: Case of Medical Datasets

Safa DÖRTERLER, Hatem DUMLU, Durmuş ÖZDEMIR, Hasan TEMURTAŞ.....1-11

3D-FDM'de Charpy Darbe Testinin Yapay Zekâ ile Optimizasyonu

Charpy Impact Test in 3D-FDM and Optimization with Artificial Intelligence

Mehmet ALTUĞ.....12-26

Fiyat Karşılaştırma Sistemi Girişimi

An Attempt for Price Comparison System

Emre ÖZAKYILDIZ, Oğuzhan MENEMENCİOĞLU, Adib HABBAL.....27-37

Endüstriyel Soğutucularda Enerji Verimliliğini Arttırmaya Yönelik Çeşitli Yöntemler

Various Methods to Improve Enegy Efficiency in Industrial Refrigerators

Buğra ŞENSOY, Mustafa AKTAŞ.....38-59

Eklemeli İmalat ile Üretilen PLA Parçaların Yorulma Ömründe Test Frekansının Etkileri Üzerine Bir Çalışma

A Study on the Effects of Test Frequency on the Fatigue Life of PLA Parts Manufactured by Additive Manufacturing

Yusuf AYAN.....60-71

Derinme Öğrenme Kullanarak Görüntü Tabanlı Web Sayfası Sınıflandırma

Image Based Web Page Classification by Using Deep Learning

Muhammed Mutlu YAPICI.....72-83

Kesikköprü Baraj Gölü Havzasındaki Noktasal Kirlilik Kaynaklarının Etkilerinin Belirlenmesi

Determination of Effects of Point Pollution Sources in Kesikköprü Dam Lake Basin

Olcay GÜLÇİÇEK Uysal, Kağan CEBE.....84-101

Nanopartikül Takviyeli Minimum Miktarda Yağlama (MMY) Yönteminin Kesme Performasına Etkisinin Deneysel ve İstatistiki Araştırılması

Experimental and Statistical Investigation of the Effect of Nanoparticle Minimum Quantity Lubrication (nano-MQL) Method on Cutting Performance

Fuat KARA.....102-113

Büyüklüğe Bağlı ZrO_2 Nanoyapılarının Yapısal Parametreleri ve Optiksel Sabitlerinini Hesaplanması

Calculation of structural parameters and optical constants of size dependent ZrO2 nanostructures

Gülsen ŞAHİN, Sultan GÖKTAŞ.....114-124

Batman İli Şartlarında Güneş Enerjisi Destekli Kurutma Sisteminde Kurutma Parametrelerinin İncelenmesi

PRINT ISSN: 2149-4916 E-ISSN: 2149-9373 © 2022 Gazi Akademik Yayıncılık

GAZİ
JOURNAL OF ENGINEERING SCIENCES

Investigation of Drying Parameters in Solar Energy Supported Drying System in Batman Provincial Conditions

Neşe Budak ZİYADANOĞULLARI.....125 -140

Makine Öğrenmesi Yöntemleri Kullanılarak Melanom Cilt Kanserinin Tahmin Edilmesi

Predicting of Melanoma Skin Cancer Using Machine Learning Merhods

Resul BÜTÜNER, Muhammed Hanefi CALP.....141-154

Direngenliğin Maksimize Edildiği Topolojilere Sahip Esnek Atalet Artırımı Mekanizmaları ile Düşük Ağırlıklı Periyodik Titreşim Yalıtıcısı Tasarımı

Lightweight Periodic Vibration Isolator Design via Compliant Inertial Amplification Mechanisms with Stiffness Maximized Topologies

Osman YUKSEL, Erol TÜRKEŞ.....155-171

Temizlik Kâğıdı Gofraj Sistemindeki Lastik Silindirin Soğutulması

Cooling of the Rubber Embossing Cylinder for Tissue Paper

Uğur Cem SARI, Bayram Kesmen, Ali KİBAR.....172-182

Üretici Ağlar ile Ontoloji Tabanlı Genelleştirilmiş Sıfır-Atışlı Öğrenme

Ontoloji-Based Generalized Zero-Shot Learning with Generative Networks

Pınar CİHAN, Husayin Kurtulus OZCAN, Atakan ONGEN.....557-573

This is an open access article under the CC-BY license

GAZİ
JOURNAL OF ENGINEERING SCIENCES

Hybridization of Meta-heuristic Algorithms with K-Means for Clustering Analysis: Case of Medical Datasets

Safa Dörterler*[a], Hatem Dumlu [b], Durmuş Ozdemir[c], Hasan Temurtas [d]

Submitted: 16.07.2023 Revised: 21.01.2024 Accepted: 09.03.2024 doi:10.30855/gmbd.0705N01

ABSTRACT

K-Means clustering is commonly used for data clustering, but it suffers from limitations such as being prone to local optima and slow convergence, particularly when handling large medical files. The literature recommends employing metaheuristic algorithms in clustering studies to address these issues. This study aims to accurately diagnose diseases in four medical datasets (Dermatology, Diabetes, Parkinson's, and Thyroid) and increase the rate of correct diagnosis of diseases. We utilized optimization algorithms to assign weights to input parameters determining diseases in these datasets, thereby improving clustering performance. Our proposed model incorporates the Crow Search Algorithm, Tree Seed Algorithm, and Harris Hawks Optimization algorithms in a hybrid structure with K-Means. We conducted statistical evaluations using performance metrics. The study demonstrated that the hybrid Harris Hawks Optimization algorithm achieved the highest accuracy rate (97.19%) among the tested algorithms on the Dermatology dataset. The hybrid Crow Search Algorithm obtained a 96.29% accuracy rate on the Thyroid dataset, while the hybrid Tree Seed Algorithm achieved a 95.32% accuracy rate on the Dermatology dataset. This study offers significant benefits, including reduced staff workload, lower test costs, improved accuracy rates, and faster test results for detecting various diseases in medical datasets.

Keywords: K-Means clustering, Metaheuristic algorithms, Disease diagnosis, Optimization, Decision support systems

[a,*] Kutahya Dumlupinar University, Engineering Faculty, Computer Engineering 43100 - Kutahya, Türkiye
Orcid: 0000-0001-8778-081X
e mail:safa.dorterler@dpu.edu.tr

[b] Kutahya Dumlupinar University, Engineering Faculty, Computer Engineering 43100 - Kutahya, Türkiye
Orcid: 0000-0002-9056-4437

[c] Kutahya Dumlupinar University, Engineering Faculty, Computer Engineering 43100 - Kutahya, Türkiye
Orcid: 0000-0002-9543-4076

[d] Kutahya Dumlupinar University, Engineering Faculty, Computer Engineering 43100 - Kutahya, Türkiye
Orcid: 0000-0001-6738-3024

*Corresponding author:
safa.dorterler@dpu.edu.tr

Kümeleme Analizi için Meta-sezgisel Algoritmaların K-Means ile Hibritlenmesi: Tıbbi Veri Kümeleri Üzerine Bir İnceleme

ÖZ

K-Means kümeleme, veri kümeleme için yaygın olarak kullanılan bir yöntemdir. Ancak özellikle büyük tıbbi verilerle çalışırken yerel optimuma takılmak ve yavaş yakınsama gibi sorunlarla karşılaşılabilir. Literatürde bu tür sorunları ele almak için kümeleme çalışmalarında metasezgisel algoritmaların kullanılmasının önerildiği görülmektedir. Bu çalışma, dört farklı tıbbi veri kümesi üzerinde (Dermatoloji, Diyabet, Parkinson ve Tiroid) hastalıkların doğru teşhisini koymayı ve hastalıkların doğru teşhis oranını artırmayı amaçlamaktadır. Bu veri kümelerindeki hastalıkları belirleyen girdi parametrelerine ağırlık atamak için optimizasyon algoritmalarını kullandık ve sonuç olarak kümeleme performansını artırdık. Önerilen modelimiz, Karga Arama Algoritması, Ağaç Tohum Algoritması ve Harris Hawks Optimizasyon algoritmalarını K-Means ile hibrit bir yapıda birleştirmektedir. Performans metrikleri kullanarak istatistiksel değerlendirmeler yaptık. Sonuçlar hibrit Harris Hawks Optimizasyon algoritmasının Dermatoloji veri kümesinde test edilen algoritmalar arasında en yüksek doğruluk oranına (%97,19) ulaştığını göstermektedir. Ayrıca hibrit Karga Arama Algoritması, Tiroid veri kümesinde %96,29 doğruluk oranı elde ederken, hibrit Ağaç Tohumu Algoritması Dermatoloji veri kümesinde %95,32 doğruluk oranı elde etmiştir. Bu çalışma, tıbbi veri kümelerinde çeşitli hastalıkları tespit etmek için daha az personel iş yükü, daha düşük test maliyetleri, gelişmiş doğruluk oranları ve daha hızlı test sonuçları gibi önemli faydalar sunmaktadır.

Anahtar Kelimeler: K-Means kümeleme, Metasezgisel algoritmalar, Hastalık teşhisi, optimizasyon, Karar destek sistemleri

To cite this article: S. Dorterler, H. Dumlu, D. Ozdemir and H. Temurtas "Hybridization of Meta-heuristic Algorithms with K-Means for Clustering Analysis: Case of Medical Datasets," *Gazi Journal of Engineering Sciences*, vol. 10, no.1, pp.1-11, 2024. doi:10.30855/gmbd.0705N01

1. Introduction

The grouping of data with similar characteristics in a dataset is called clustering [1]. Clustering operations are used in statistical data analysis, data mining, vector quantization, and data compression [2,3]. The clustering process brings problems along with its advantages [4]. The multidimensionality and large size of the data can cause time costs. In addition, when using distance-based clustering, it is difficult to determine the linked cluster in multidimensional space when it is impossible to measure the distance between clusters. Results from clustering processes can be interpreted differently due to the differences in the structure of clustering methods. [5]. Two categories, supervised and unsupervised, are typically used to categorize the classification process. The main task of supervised classification is to put unclassified data in the most appropriate class. Unsupervised classification aims to create meaningful subsets from the unclassified data in a cluster [6]. The unsupervised classification approach is used to assess the clustering process. Fraley and Raftery [7] classified clustering into two categories: hierarchical and partitional. Without notice, the top-down or bottom-up division of the number of clusters in a tree structure creates hierarchical clustering. In contrast, partitional clustering splits data into groups without regard to hierarchy and with a predetermined number of clusters. The Euclidean distance is the basis of the partitional clustering. Calculating the distance between each cluster and each point, then including that point in the cluster that minimizes this distance, is how the Euclidean distance is stated. There are many different clustering methods available. K-Means, Hierarchical clustering, and Gaussian mixture models (GMMs) for clustering are the most well-known ones [8].

Clustering analysis is used in fields such as field of medicine [9–14], machine learning [15], identification of images [16], data mining [17,18], market and consumer segmentation [19–21], biology [22], statistics [23], and pattern recognition [24]. K-Means is a popular center-based, straightforward, and quick clustering algorithm [25]. The K-Means algorithm is used in marketing [26,27], chemistry [28], geographic systems [29], meteorological phenomena [30], and social sciences [31], and it has been extensively utilized in scientific and industrial fields, particularly in the field of medicine. Liu et al. [26] performed customer classification and market analysis using the K-Means algorithm with retail company data. Heil et al. [32] classified the agricultural lands in West Africa using data based on geological and climatic parameters and the K-Means algorithm. Additionally, they demonstrated how the fuzzy K-Means algorithm is superior to the standard K-Means algorithm. Similarly, Tang et al. [28] used the K-Means algorithm to classify industrial polymers. Xiaoying et al. [33] analyzed the chemical molecules in rice and classified rice according to geographical origin. Anderson [34] used the K-Means algorithm and kernel density calculation to determine the points where traffic accidents are most intense. Bacao et al. [35] studied K-Means for self-organizing maps. Kanthan and Sujantha [30] clustered raindrops with the K-Means algorithm. Chakraborty et al. [36] suggested a methodology for weather forecasting with K-Means. Kurniawan and Fatulloh [37] used the K-Means algorithm and geographic information system data to classify the social life conditions of a city in Indonesia. Zhou et al. [38] clustered crime points using real case data. Evans et al. [39] examined the risks and negative consequences of medicines used in medicine on people. They utilized the K-Means method in order to classify medicines. They concluded that high-risk characteristics included the patient's age, weight, gender, and medicine dosage. A study conducted in the field of dentistry investigated whether psychological and social changes have an effect on the case of acute pain after surgery. The K-Means algorithm was used to cluster the patients into groups based on their psychological characteristics and symptoms. In conclusion, it was observed that patients who were female, depressed, and anxious experienced more pain after surgery [40]. In a different research project in the psychiatric field [41], various personality inventories were used for cluster analysis. By analyzing the clusters, the differences between the two groups were revealed. Thus, unknown aspects of psychopathy were tried to be discovered. Likewise, Kim et al. [42] used K-Means to divide the 888 instances submitted to the Korean emergency service into two categories. It was found that 85% of suicide attempts were impulsive, and 15% were planned based on a variety of demographic and clinical factors. Studies in the field of genetics have also used the K-Means algorithm. Shai et al. [43] revealed molecular subtypes of unknown pathological kinds and classes using the K-Means algorithm. Bertucci et al. [44] used hierarchical clustering to describe five breast cancer subtypes. According to research and observations of Ushizawa et al. [45], animal embryo gene profiles were examined using cDNA microarray, and the K-Means method was utilized to cluster genes. Doctors in the medical field diagnose patients by using a variety of tests, observations, and information about the patient's past. In the health sector, decision support systems are developed with various techniques to help doctors [46–51]. The K-Means algorithm has

the drawback of being stuck to local optima despite performing fast and effective clustering [52]. Results from the K-Means technique are based on the initial clustering reference points. In other words, the search always converges to the closest local optimum from the initial point. Researchers solve the optimum local problem using hierarchical, artificial intelligence-based, partition-based, and density-based clustering techniques. The dataset is divided into a fixed number of partitions in partition-based clustering [53]. Each point shifts its center until it is closest to its cluster center. This method is most advantageous when the dataset is homogeneous [54]. In density-based clustering, clusters are formed from areas with high data density [55]. This approach clusters data points based on their density. It is advantageous when dealing with heterogeneous datasets [54]. The partition-based clustering method focuses on specific parts, while the density-based clustering method determines clusters based on their density. Examples of the techniques used are as follows: Graph Theory [56], Artificial Neural Networks [57], Statistical methods [58], and heuristic algorithms [19, 59–64]. These techniques were used to avoid being stuck with the local optimum and to increase the clustering success rate.

In this study, the meta-heuristic algorithms Crow Search Algorithm (CSA), Harris Hawks Optimization (HHO), and Tree Seed Algorithm (TSA) are used together with the K-Means algorithm to improve clustering performance. Three new algorithms, Hybrid CSA (H-CSA), Hybrid HHO (H-HHO), and Hybrid TSA (H-TSA), were developed from the hybrid use of the algorithms. By identifying the significance of parameter values used in diagnosing diabetes, dermatology, Parkinson's, and thyroid diseases, heuristic algorithms have improved clustering success. In summary, if any parameter in a disease is more important, the importance coefficient of that parameter is increased. Thus, a more accurate diagnosis is provided. Likewise, if any parameter is less critical in a disease, the importance of this parameter is lowered. Thus, we planned to prevent misdiagnoses. Thus, the K-Means algorithm being stuck to the local optimum has been resolved. In addition, the relevant coefficients have been correctly optimized to increase the clustering success.

2. Materials and Methods

In this study, the K-Means algorithm was combined with CSA, TSA, and HHO algorithms to obtain H-CSA, H-HHO, and H-TSA algorithms that demonstrate superior clustering integrity performance. The developed model utilized four distinct medical datasets, Dermatology, Diabetes, Parkinson's, and Thyroid, as input parameters. The datasets were obtained from the UCI Machine Learning Repository and additional sources [65–69]. Figure 1 shows a summary of our methodology in the study.

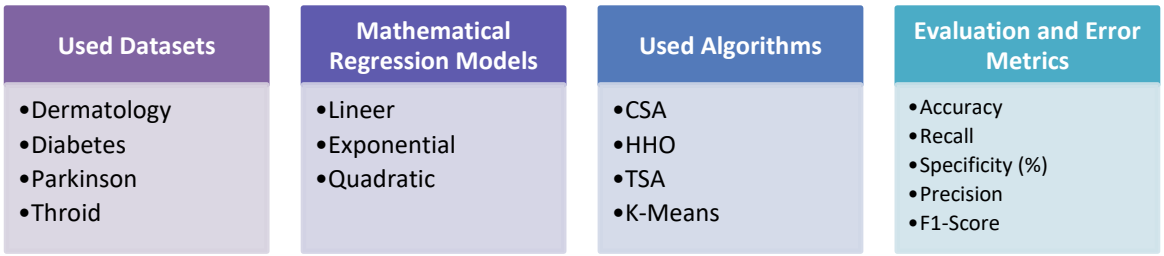

Figure 1. A brief summary of methodology

2.1. K-Means Algorithm

The K-Means algorithm, initially proposed in 1967 by James MacQueen, is a widely used and efficient clustering technique in machine learning, data exploration, and data mining [70]. The algorithm aims to group data in a dataset based on similarities and divides them into distinct clusters. The clusters are formed around the k initial cluster centers that the algorithm selects, and data are assigned to the clusters closest to these centers. Then, the centers of the clusters are recalculated, and the data is reassigned to the corresponding clusters. This step is repeated until the data distribution is corrected. This process aims to sort the data into clusters that best reflect their similarity. Equation 1 defines the objective function.

$$j = \sum_{j=1}^{k} \sum_{i=1}^{n} \left\| x_i^{(j)} - c_j \right\|^2 \quad (1)$$

Where $\left\|x_i^{(j)} - c_j\right\|^2$ is the distance between $x_i^{(j)}$ and the c_j (center of cluster). The goal is to find the lowest J [8]. Thus, $x_i^{(j)}$ belongs to the c_j centered cluster for minimum J value.

A method has yet to be presented to determine the number of clusters (K) in the K-Means algorithm. This is a disadvantage besides the simplicity and popularity of the K-Means algorithm. K-Means cannot guarantee convergence to a global optimum using its iteratively optimal procedure. Additionally, the K-Means technique is susceptible to outliers and noisy data. The deformation of cluster geometries is an additional problem because it attempts to include an object in a cluster even if it is far from one [70].

2.2. Harris Hawks Algorithm

The Harris Hawk Algorithm emulates the rabbit hunting approach of the intelligent Harris hawk. Before hunting, the leader and other flock members conduct reconnaissance flights. Following prey detection, the hunting process commences. Heidari presented a mathematical model outlining these characteristics of the Harris hawk in 2019 [71].

Exploration phase: When Harris hawks roam randomly, they use two exploration strategies. These strategies are as in Equation 2. The probability value q here indicates which tactic will be in use.

$$x(t+1) = \begin{cases} x_{rand}(t) - r1\,|x_{rand}(t) - 2r_2 x(t)|, & q \geq 0.5 \\ \left(x_{rabbit}(t) - x_m(t)\right) - r_3\left(LB + r_4\,(UB - LB)\right), & q < 0.5 \end{cases} \quad (2)$$

Here x(t + 1) is the position vector of Harris in each iteration. The position vector of the prey is xrabbit(t). The current position of the hawk is x(t). r_1, r_2, r_3, r_4, and q are random numbers (0,1). The lower value and the upper value, respectively, are denoted by LB and UB. $x_{rand}(t)$ shows a hawk randomly chosen from the current population. $x_m(t)$ is the average position of the current hawk population. The average position is found using Equation [71].

$$x_m(t) = \frac{1}{N}\sum_{i=1}^{N} x_i(t) \quad (3)$$

Here, t denotes the number of iterations, and N denotes the number of hawks. After completing the exploration process, the exploitation phase is presented in Equation 4.

$$E = 2E_0\left(1 - \frac{t}{T}\right) \quad (4)$$

Here E is the total energy of the escaped prey, the prey's initial energy is E_0 is the maximum iterations number.

Exploitation phase: Four different strategies are used to simulate the exploitation phase. Soft besiege, hard besiege, soft besiege with progressive rapid dives and hard besiege with progressive rapid dives.

At the soft besiege stage, the Harris hawk makes misleading jumps so that reduce energy of prey ($r \geq 0.5, E \geq 0.5$). This soft encirclement strategy is mathematically given in Equations 5 and 6. Here, r is the chance of catching the escaped prey. E is the energy of the rabbit. $\Delta x(t)$ is the difference between the current position in the t.th iteration and the current position of the prey (rabbit). For the purpose of simulating natural rabbit movement, J is a value that changes with each iteration.

$$x(t+1) = \Delta x(t) - E|Jx_{rabbit}(t) - x(t)| \quad (5)$$

$$\Delta x(t) = x_{rabbit}(t) - x(t) \quad (6)$$

In the *Hard Besiege* strategy, the energy of the prey is considerably reduced ($r \geq 0.5$, $|E| \leq 0.5$). This situation is mathematically modeled as in Equation 7.

$$x(t+1) = x_{rabbit}(t) - E|\Delta x(t)| \quad (7)$$

Soft besiege with progressive rapid dives stage, it is thought that the Hawks decided their next move

according to Equation 8 before starting the soft besiege.

$$Y = x_{rabbit}(t) - E|Jx_{rabbit}(t) - x(t)| \quad (8)$$

Harris Hawks dive fast and compare to their previous dives. If the new dive situation is not suitable, the hawks continue to fast dive into their prey. A Levy Flight based motion structure is used while deciding this. Equation 9 describes this condition.

$$Z = Y + SxLF(D) \quad (9)$$

Here D is the problem size. S is a random vector of size 1xD. Y determines the position of the prey relative to its decreasing energy. Z is the variable that decides whether the hawks will attack its prey. Equation 10 gives the levy function, abbreviated LF.

$$LF(x) = 0.01x\left(\frac{\mu x \sigma}{|\mu|^{\frac{1}{\beta}}}\right), \sigma = \left[\frac{\Gamma(1+\beta)xsin\left(\frac{\pi\beta}{2}\right)}{\Gamma\left(\frac{1+\beta}{2}\right)x\beta x2^{\left(\frac{\beta-1}{2}\right)}}\right] \quad (10)$$

Where u is the random number between v (0,1) and β is 1.5. The hawks' current locations are updated during the soft besiege phase using Equation 11.

$$x(t+1) = \begin{cases} Y\ if\ F(Y) < f(x(t)) \\ Z\ if\ F(Z) < F(x(t)) \end{cases} \quad (11)$$

Y and Z are found using Equations 8 and 9.

Hard besiege with progressive rapid dives stage, the prey lacks the energy to escape. The Harris hawk makes a hard besiege before a surprise attack to catch its prey. The hard besiege condition is found using Equation 12.

$$x'(t+1) = \begin{cases} Y'\ if\ F(Y') < f(x(t)) \\ Z'\ if\ F(Z') < F(x(t)) \end{cases} \quad (12)$$

Where Y' and Z' are found by Equations 13 and 14.

$$Y' = x_{rabbit}(t) - E|Jx_{rabbit}(t) - x_m(t)| \quad (13)$$

$$Z' = Y' + SxLF(D) \quad (14)$$

2.3. Tree Seed Algorithm

Kiran [72] introduced the Tree Seed Algorithm (TSA) in 2015, a new metaheuristic optimization algorithm that addresses continuous optimization problems. The TSA is based on the inherent relationship between trees and seeds in nature. Tree seeds are spread in the soil and grow into trees over time [73]. The position of trees and seeds indicates potential solutions for persistent issues when tree soils are considered in the research field [74]. As a result, the significance of seed sites in the formation of trees has grown. The search space is described by two equations. The first is the procedure for producing seeds for the best tree population placement. This strengthens the algorithm's ability to perform local searches. For the purpose of creating a new seed, the other equation uses two alternative tree places [72].

$$S_{i,j} = T_{i,j} + (a_{i,j})x(B_j - T_{r,j}) \quad (15)$$

$$S_{i,j} = T_{i,j} + (a_{i,j})x(T_{i,j} - T_{r,j}) \quad (16)$$

where, $S_{i,j}$ is jth dimension of ith seed that will be produced ith tree,$T_{i,j}$ is the jth dimension of ith tree, B_j is the jth dimension of best tree location obtained so far, $T_{r,j}$ is the jth dimension of rth tree randomly selected from the population, the scaling factor is α which is randomly produced in range of [−1, 1] and i and r are seperate indices.

Equation 17 is used to generate the initial tree locations, which are potential solutions to the optimization problem, at the beginning of the TSA search.

$$T_{i,j} = L_{j,min} + r_{i,j}\,(H_{j,max} - L_{j,min}) \tag{17}$$

where, $L_{j,min}$ is the lower bound of the search space, $H_{j,max}$ is the higher bound of the search space and $r_{i,j}$ is a random number produced for each dimension and location, in range of [0, 1].

Equation 18 is used to choose the best solution from the population for minimization.

$$B = min\{f(\vec{T}_i)\} i = 1,2,\dots,N \tag{18}$$

N is the total population of trees.

The maximum number of function evaluations (Max_FEs) is chosen as the termination condition, and it is set using the function's dimensionality given in Equation 19.

$$Max_{FEs} = Dx10.000 \tag{19}$$

2.4. Crow Search Algorithm

Crows live in flocks and have a powerful memory [75]. They store the food they find and return to their hiding place when needed. Crows can also follow each other to learn the location of food stores and steal each other's food. Crows can take precautions against this by flying to different places to confuse other crows. Inspired by this intelligent behavior of crows, Askarzadeh developed the Crow Search Algorithm to solve the optimization problem [75]. The algorithm consists of 4 steps.

Step 1: Initial values are given to algorithm parameters. Then, N crows are randomly placed in the d-dimensional search space. In the initialization phase, all crows store their food in the positions in which they are randomly placed. The fitness values of all positions are calculated, and their memory holding their best position is initialized.

Step 2: Each crow randomly chooses a crow and follows it to find the crow's food. New positions are created depending on whether the jth crow knows or does not know that it is being followed by the ith crow Equation 20.

$$x^{i,itr+1} = \begin{cases} x^{i,itr} + r_i \times fl^{i,itr} \times (m^{j,itr} - x^{i,itr}), & r_i \geq AP^{j,itr} \\ a, & otherwise \end{cases} \tag{20}$$

Here $x^{i,itr}$ denotes the position of the ith crow in itrth iteration. r_i is a randomly distributed random number between 0-1, m (memory) is the variable that holds the best position of the crow, and a is the random position. fl (flight length), the algorithm's adjustment parameters are called AP (awareness probabilities). fl is the range at which the crow can fly, and AP represents the probability of the crow noticing that it is being followed.

Step 3: The feasibility of the new locations found is checked. The crows' positions may be changed as necessary to create new ones. Otherwise, the crow position will not be changed.

Step 4: All positions' fitness values are calculated, and the memories of the crows are updated according to Equation 21.

$$m^{i,itr+1} = \begin{cases} x^{i,itr+1} & f(x^{i,itr+1}) is\ better\ than\ f(m^{i,itr}) \\ m^{i,itr} & otherwise \end{cases} \tag{21}$$

Here $f(x^{i,itr+1})$ shows the fitness value of the ith crow. If the fitness value of the new position is better than the fitness value of the location that was previously memorized, the update takes place according to the new position. If the stopping requirement is not met, iteration continues. The position of the crow with the best fitness value is selected, and the algorithm is terminated.

2.4. Proposed model

The K-Means algorithm works effectively when the distribution of objects in the dataset is normally distributed. However, if the distribution of objects in the dataset is non-normally distributed, the algorithm may become ineffective. Similarly, suppose there are significant or minimal differences between the properties of the objects in the data set. In that case, the K-Means algorithm will not work effectively and may not give what is expected [76,77]. K-Means approach and heuristic algorithms (CSA, HHO, and TSA) were combined in this study to improve clustering performance. Meta-heuristic algorithms were utilized for weighting various health data used in diagnosing Dermatology, Diabetes, Parkinson's, and Thyroid ailments. In summary, high or low-impact data in determining the disease were found with meta-heuristic algorithms, increasing diagnostic success and making more accurate diagnoses. Thus, the classical K-Means algorithm was prevented from being stuck at local optimum points. Clustering success was increased by optimizing the disease coefficients according to the degree of importance, thus preventing misdiagnoses. First, a W pool is created to rate all dimensions of health data.

$$W = [w_1, w_2, \dots, w_m] \tag{22}$$

W are the weight values that the optimization algorithm will optimize. Each w value is weighted by the optimization algorithm according to its importance in the diagnosis of the disease. All dimensions (X_n) are multiplied by a weight parameter (W_m). Thus, the coefficient of the importance of the relevant data (dimension) in determining the disease is found.

$$X_{n,m} = W_m * X_{n,m}, \quad n = 1, \dots, N, \quad m = 1, \dots, M, \quad n \leq N, \quad m \leq M, \quad M < N \tag{23}$$

where N represents the total amount of data and M represents the total number of data attributes. To generate a new $X_{n,m}$ pool, each characteristic is multiplied by W_m. After that, Equation 24 is used to determine the centers of all the data in this pool.

$$C_k = \frac{\sum_{n=1}^{N} a_{n,k} * X_n}{\sum_{n=1}^{N} a_{n,k}}, a_{n,k} = \begin{cases} 1 & y_n = k \\ 0 & y_n \neq k' \end{cases} \qquad k = 1, 2, \dots, K \tag{24}$$

Here K represents the number of clusters, y_n represents the data set, and a represents a variable consisting of 1 or 0. The actual value of the data is compared with the first set *(k.)*. If a match is achieved as a result of the comparison, a takes the value of 1, and the *(k.)* elements of the relevant set are added. This way, the cluster's center point in the k row is found. The center points of all clusters are found in this way. Then, using Equation 25, the class of the data is found according to the center points.

$$f_n = k, \ if \ \min(|x_n - c_1|, |x_n - c_2|, \dots, |x_n - c_K|,) \tag{25}$$

f_n is found values that represent data sets. The data is assigned to the f_n variable to belong to whichever center point is closer. Then, the weight values that give the optimum result are found with the proposed meta-heuristics by processing the available data. The objective function used is shown in Equation 26.

$$\max f(v) = {}^{100}/_{N} * \sum_{n=1}^{N} b_n, \qquad b_n = \begin{cases} 1 & y_n = f_n \\ 0 & y_n \neq f_n \end{cases} \tag{26}$$

Here, N is the number of data, and b is the variable that takes the value 0 or 1. If the found value and the actual value are equal, b is given the value 1; otherwise, it is given the value 0. These steps continue until the number of iterations is completed. Then, the weight values that give the optimum fitness value are found. An illustration of these procedures is shown in a flow chart in Figure 2.

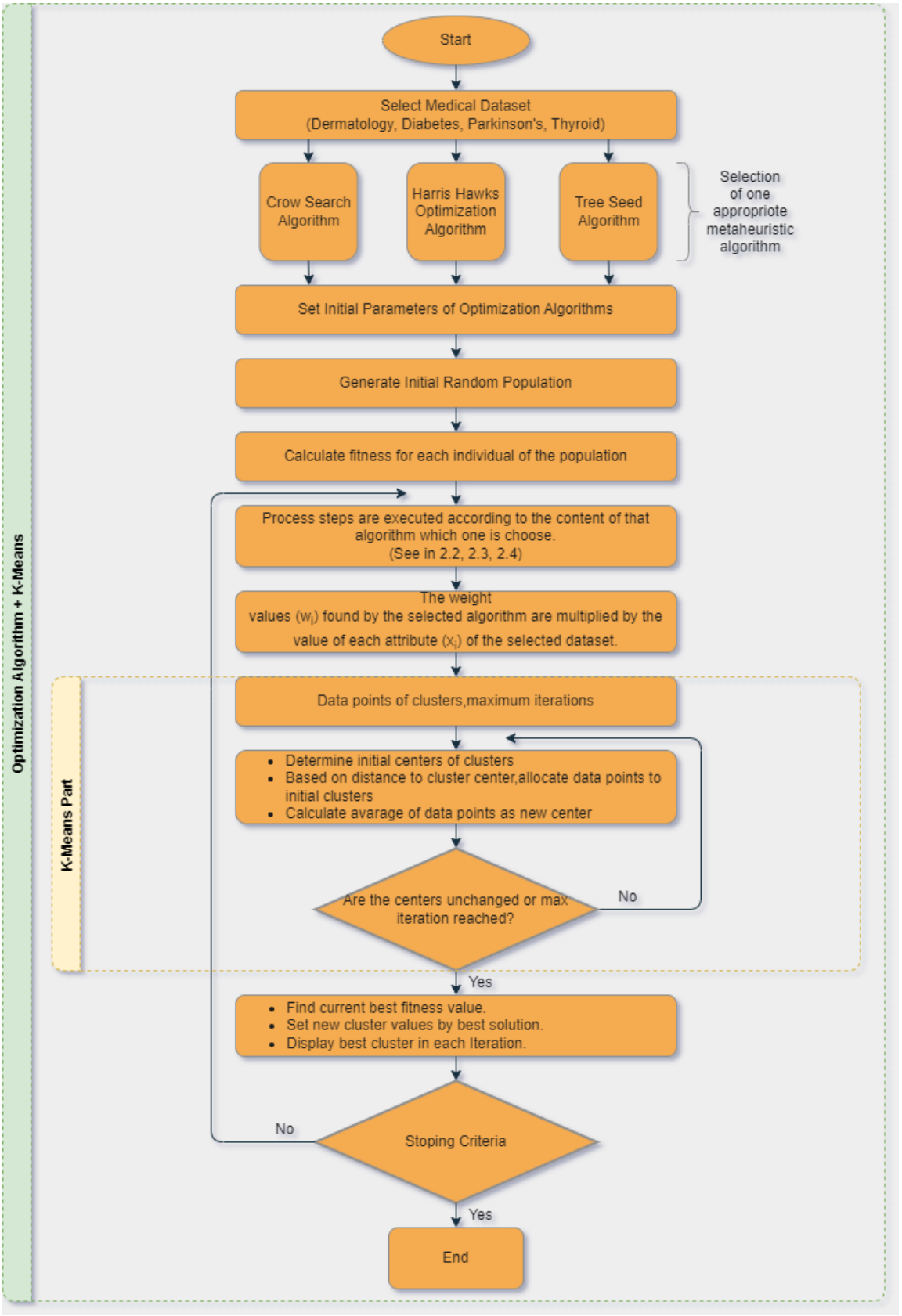

Figure 2. Flow chart of conceptual approach

2.6. Dataset

Four distinct medical datasets were employed in this research: Dermatology, Diabetes, Parkinson's, and Thyroid. The datasets were obtained from several sources, including the UCI Machine Learning Repository, and 70% of the data was allocated for training purposes, while the remaining 30% was reserved for testing [65–69].

2.6.1 Dermatology dataset

The dermatology dataset was obtained from UCI Machine Learning Repository [65,69]. There are 34 attributes in the dataset. There are 358 sample data and six different classes (Pityriasis Rubra Pilaris, Psoriasis, Seborrheic Dermatitis, Pityriasis Rosea, Lichen Planus, Chronic Dermatitis).

2.6.2. Diabetes dataset

The diabetes dataset was obtained from the National Institute of Diabetes and Digestive and Kidney Diseases [66]. The dataset has eight attributes. These are age, blood pressure, pregnancy, skin thickness, glucose, insulin, BMI and diabetes pedigree function. This dataset contains 768 records. It is divided into two results: diabetic or not.

2.6.3. Parkinson dataset

This dataset is taken from the UCI Machine Learning Repository [65,67]. It consists of different biomedical sound measures obtained from 195 Parkinson's disease patients. This dataset contains 22 attributes, and there are two groups of outcomes: "1" if Parkinson's disease is present and "0" if not.

2.6.4. Thyroid function dataset

The thyroid dataset was taken from the UCI Machine Learning Repository [65,68]. This dataset has 7200 records and 20 attributes, including sex, age, query_on_thyroxine, on_thyroxine, on_antithyroid_medication, pregnant, sick, thyroid_surgery, I131_treatment, query_hyperthyroid, query_hypothyroid, tumor, lithium, psych, goiter, hypopituitary, T3, TSH, T4U, TT4. There are three classes in the result set. These are not-hypothyroid (normal), subnormal function and hyperfunction.

Table 1. Datasets of study

Type of Feature	Datasets	Inputs	Classes	Instances
Numeric	Dermatology Dataset	34	6	358
Numeric	Diabetes Dataset	8	2	768
Numeric	Parkinson Dataset	22	2	195
Numeric	Thyroid Function Dataset	20	3	7200

2.7. Statistical performance metrics

The models used in the current study were evaluated with performance measurement metrics. Formulas of performance metrics are given in Equations 27, 28, 29, 30, and 31 [78–80].

$$Accuracy = \frac{TP+TN}{TP+FN+TN+FP} \quad (27)$$

$$Recall = \frac{TP}{TP+FN} \quad (28)$$

$$Specificity = \frac{TN}{TN+FP} \quad (29)$$

$$Precision = \frac{TP}{TP+FP} \quad (30)$$

$$F1\ Score = 2 \times \frac{Presicion \times Recall}{Precision + Recall} \quad (31)$$

Some abbreviations are used in the equations. True Positive (TP) represents a sick person as sick, False Positive (FP) represents a healthy as sick (which is incorrect), True Negative (TN) represents a healthy person as not sick, False Negative (FN) represents healthy to the person who is sick.

3. Experimantal Results

In this study, CSA, HHO, TSA, and K-Means algorithms were hybridized to create H-CSA, H-HHO, and H-TSA algorithms and were used to diagnose four different diseases. The algorithm was run on a computer with an Intel Core i7, 2.4 GHz CPU, and 8 GB RAM with Windows® 11 operating system, using MATLAB 2022b programming language. The parameter settings used in the algorithms are given in Table 2.

Table 2. Parameter settings

Algorithm	Parameter Settings	Iteration Number	Population Number
CSA	*AP=0.1; *FL=2	100	40
HHO	*ß=1.5	100	40
TSA	*ST=0.1	100	40

* AP (Awareness Probability), FL (Flight Length), ß (Beta), ST (Search Tendency)

The termination criterion of the proposed hybrid model is the number of iterations. The proposed model runs for 100 iterations and then terminates and finds the weight values that give the best result. In this way, the algorithms are run 20 times, and the weight values that give the best fitness value are found. The weight values obtained for the dermatology, diabetes, Parkinson's, and thyroid datasets are presented in Table 3. Furthermore, Table 4 presents the statistical results of mean runtime, Standard Deviation, Average Fitness, Worst Fitness, and Best Fitness values. Each dataset has been evaluated separately, and better results produced are shown in bold.

The hybrid models proposed for each dataset are separately evaluated in Table 4, and the values that yield superior results are shown in bold. The H-HHO algorithm found more successful fitness values in the Dermatology dataset than other algorithms regarding the worst and best fitness values. On the other hand, the H-CSA algorithm produced better values than other algorithms in terms of average fitness, worst fitness, and mean runtime values. In terms of standard deviation, H-TSA produced better results. H-CSA and H-HHO Diabetes found the best fitness values in the dataset. The best values in average fitness and standard deviation were obtained from the H-TSA algorithm. In the Parkinson's dataset, the H-TSA algorithm found the best fitness with 81.03%. Similarly, the most successful algorithm regarding the average fitness value is H-TSA. For the Thyroid dataset, the H-HHO algorithm gave the best values in Standard Deviation, Average Fitness, Best Fitness, and Worst Fitness. The H-CSA algorithm was found to have the lowest average runtime when evaluating the statistical results in terms of mean time. Table 5 shows the fitness values and runtime results of the K-Means Algorithm for each data set separately.

Analyzing the results in Tables 4 and 5, it is evident that the H-CSA, H-HHO, and H-TSA models outperform K-Means in terms of best fitness values. However, hybrid algorithms use two algorithms, so the proposed models run slower than the K-Means algorithm. However, the high achievements show that hybrid algorithms can make this speed difference tolerable and advantageous, especially when problem complexity and dataset characteristics are considered. In addition, the complexity matrices of the algorithms using the test dataset are presented and statistical performance results are given. Table 6 shows the values of the results for the Dermatology test dataset.

Table 3. Coefficient of Dermatology, Diabetes, Pakinson's, and Thyroid dataset

	Dermatology			**Diabetes**			**Parkinson's**			**Thyroid**		
	CSA	**HHO**	**TSA**	**CSA**	**HHO**	**TSA**	**CSA**	**HHO**	**TSA**	**CSA**	**HHO**	**TSA**
W1	0.99955	0.68342	0.02798	0.29578	0.0	0.0	0.0	0.0	0.0	0.0	0.0	0.0
W2	0.99926	0.48179	0.48179	0.74054	0.28513	0.67698	0.0	0.03168	0.0	0.0	0.0	0.06567
W3	1.0	1.0	0.37077	0.37931	0.0	0.34710	0.0	0.0	0.0	0.0	0.0	0.03777
W4	0.99963	1.0	0.62532	0.52302	0.0	0.32596	0.0	0.0	0.27688	0.0	0.0	1.0
W5	0.95734	1.0	0.66528	0.00028	0.0	0.05182	0.0	1.0	1.0	0.0	0.0	0.27827
W6	0.99987	1.0	0.84918	0.99960	0.73997	0.77061	1.0	0.0	1.0	0.0	0.0	0.07903
W7	0.88161	1.0	1.0	0.60541	0.28964	0.72123	0.0	1.0	0.30304	0.0	0.0	0.34065
W8	0.95635	1.0	0.86321	0.98806	0.39522	0.83784	1.0	1.0	0.0	0.0	0.0	0.94969
W9	0.99971	1.0	0.83405	N/A	N/A	N/A	0.0	0.0	0.90080	0.00136	0.0	1.0
W10	0.99922	0.53874	0.15785	N/A	N/A	N/A	0.0	0.0	0.09686	0.47101	0.0	0.76311
W11	0.99999	1.0	0.69349	N/A	N/A	N/A	1.0	0.18872	0.21580	0.0	0.0	0.17567
W12	0.99974	0.30981	1.0	N/A	N/A	N/A	0.0	1.0	0.21538	0.0	0.0	0.21051
W13	0.99955	0.65322	0.57133	N/A	N/A	N/A	0.0	0.0	0.11129	0.0	0.0	0.0
W14	0.99967	1.0	0.83357	N/A	N/A	N/A	0.80071	1.0	0.63166	0.0	0.0	0.84297
W15	1.0	1.0	0.99547	N/A	N/A	N/A	1.0	1.0	0.41264	1.0	0.0	0.42849
W16	0.99962	0.61753	0.46498	N/A	N/A	N/A	0.0	0.0	0.01859	0.04365	0.0	0.0
W17	0.99988	0.70193	0.52315	N/A	N/A	N/A	0.0	1.0	0.20289	0.0	0.00513	0.79203
W18	0.99925	0.29884	0.95313	N/A	N/A	N/A	1.0	0.0	0.47236	0.0	0.0	0.95175
W19	0.99922	0.85027	0.41822	N/A	N/A	N/A	1.0	0.48010	0.07504	0.0	0.0	0.97276
W20	1.0	1.0	0.11431	N/A	N/A	N/A	1.0	1.0	0.75772	0.18877	0.0	0.47394
W21	0.99916	1.0	0.12406	N/A	N/A	N/A	1.0	1.0	0.16217	1.0	0.0	0.99125
W22	0.02495	1.0	0.85538	N/A	N/A	N/A	1.0	0.21911	0.18336	N/A	N/A	N/A
W23	1.0	1.0	0.0	N/A	N/A	N/A	N/A	N/A	N/A	N/A	N/A	N/A
W24	0.02037	1.0	0.0	N/A	N/A	N/A	N/A	N/A	N/A	N/A	N/A	N/A
W25	0.99949	1.0	0.19679	N/A	N/A	N/A	N/A	N/A	N/A	N/A	N/A	N/A
W26	0.74203	1.0	1.0	N/A	N/A	N/A	N/A	N/A	N/A	N/A	N/A	N/A
W27	0.99938	1.0	0.58594	N/A	N/A	N/A	N/A	N/A	N/A	N/A	N/A	N/A
W28	0.99986	1.0	0.80334	N/A	N/A	N/A	N/A	N/A	N/A	N/A	N/A	N/A
W29	0.55448	0.19703	1.0	N/A	N/A	N/A	N/A	N/A	N/A	N/A	N/A	N/A
W30	0.99974	1.0	0.82548	N/A	N/A	N/A	N/A	N/A	N/A	N/A	N/A	N/A
W31	0.99993	1.0	0.76806	N/A	N/A	N/A	N/A	N/A	N/A	N/A	N/A	N/A
W32	0.99995	0.43120	0.36214	N/A	N/A	N/A	N/A	N/A	N/A	N/A	N/A	N/A
W33	0.0	1.0	0.42506	N/A	N/A	N/A	N/A	N/A	N/A	N/A	N/A	N/A
W34	0.0	0.04693	0.05681	N/A	N/A	N/A	N/A	N/A	N/A	N/A	N/A	N/A

Table 4. Comparison of fitness values and running times of hybrid algorithms

Dermatology Dataset	**Diabetes Dataset**	**Parkinson's Dataset**	**Thyroid Dataset**

	H-CSA	H-HHO	H-TSA	H-CSA	H-HHO	H-TSA	H-CSA	H-HHO	H-TSA	H-CSA	H-HHO	H-TSA
Best Fitness	96.2616	**97.1962**	95.3271	**73.4782**	**73.4782**	73.0434	79.3103	79.3103	**81.0344**	96.2962	**96.9907**	90.3703
Worst Fitness	**93.4579**	**93.4579**	**93.4579**	**69.5652**	**69.5652**	**69.5652**	67.2413	**70.6896**	**70.6896**	86.2962	**94.9537**	87.3611
Average Fitness	**95.9532**	95.0934	94.4859	71.4565	71.5217	**71.6086**	72.5000	74.3965	**77.3275**	90.3842	**95.5671**	88.0092
Standard Deviation	1.0677	1.0879	**0.7365**	1.2238	1.2418	**0.8707**	3.6883	**2.3913**	3.0266	3.9746	**0.5241**	1.0684
Mean Runtime(ms)	**1.6550**	3.0765	11.8207	**1.0888**	1.9590	7.3823	**0.4759**	0.8472	3.2175	**12.4584**	22.1137	87.0473

Table 5. Fitness values and runtime scores of the K-Means Algorithm for medical data sets

	Dermatology Dataset	Diabetes Dataset	Parkinson's Dataset	Thyroid Dataset
Best Fitness	0.051248	0.040272	0.037009	0.022738
Mean Runtime (ms)	44.8598%	61.7391%	68.9655%	43.4259%

Table 6. Performance results of hybrid algorithms and K-Means algorithm for Dermatology dataset (Acc:Accuracy, Rcl:Recall, Spc:Specificity, Pre:Precision, F1s:F1-Score)

	H-CSA Train Score: 99.6015% Test Score: 96.2616%						H-HHO Train Score: 98.8047% Test Score: **97.1962**%						H-TSA Train Score: 100.0% Test Score: 95.3271%						K-Means Algorithm Train Score: 45.0199% Test Score: 44.8598%					
	Psoriasis	**Seboreic Dermatitis**	**Lichen Planus**	**Pityriasis Rosea**	**Chronic Dermatitis**	**Pityriasis Rubra Pilaris**	**Psoriasis**	**Seboreic Dermatitis**	**Lichen Planus**	**Pityriasis Rosea**	**Chronic Dermatitis**	**Pityriasis Rubra Pilaris**	**Psoriasis**	**Seboreic Dermatitis**	**Lichen Planus**	**Pityriasis Rosea**	**Chronic Dermatitis**	**Pityriasis Rubra Pilaris**	**Psoriasis**	**Seboreic Dermatitis**	**Lichen Planus**	**Pityriasis Rosea**	**Chronic Dermatitis**	**Pityriasis Rubra Pilaris**
Acc(%)	**1.0**	0.9626	**1.0**	0.9626	**1.0**	**1.0**	**1.0**	**0.9813**	0.9906	**0.9719**	**1.0**	**1.0**	**1.0**	0.9532	**1.0**	0.9532	**1.0**	**1.0**	0.8411	0.7102	0.6635	0.9158	0.9158	0.8504
Rcl (%)	**1.0**	0.8500	**1.0**	**0.9090**	**1.0**	**1.0**	**1.0**	**0.9500**	0.9545	**0.9090**	**1.0**	**1.0**	**1.0**	0.8000	**1.0**	**0.9090**	**1.0**	**1.0**	0.4687	0.2500	0.5454	0.2727	0.3076	**1.0**
Spc (%)	**1.0**	**0.9885**	**1.0**	0.9687	**1.0**	**1.0**	**1.0**	**0.9885**	**1.0**	**0.9791**	**1.0**	**1.0**	**1.0**	**0.9885**	**1.0**	0.9583	**1.0**	**1.0**	**1.0**	0.8160	0.6941	0.9895	**1.0**	0.8367
Pre(%)	**1.0**	0.9444	**1.0**	0.7692	**1.0**	**1.0**	**1.0**	**0.9500**	**1.0**	**0.8333**	**1.0**	**1.0**	**1.0**	0.9411	**1.0**	0.7142	**1.0**	**1.0**	**1.0**	0.2380	0.3157	0.7500	**1.0**	0.3600
F1s(%)	**1.0**	0.8947	**1.0**	0.8333	**1.0**	**1.0**	**1.0**	**0.9500**	0.9767	**0.8695**	**1.0**	**1.0**	**1.0**	0.8648	**1.0**	0.8000	**1.0**	**1.0**	0.6382	0.2439	0.400	0.4000	0.4705	0.5294

The test dataset results for the dermatology classification of disease types were evaluated separately for each disease type. Algorithms that make more successful classification are shown in green for Psoriasis, blue for Seborrheic Dermatitis, red for Lichen Planus, purple for Pityriasis Rosea, orange for Chronic Dermatitis, and brown for Pityriasis Rubra Pilaris. The H-HHO algorithm was more successful than the H-CSA and H-TSA algorithms, with a 97% success rate for the Dermatology dataset. The H-HHO algorithm has the highest accuracy rate in 5 disease types: Seborrheic Dermatitis, Psoriasis, Chronic Dermatitis, Pityriasis Rosea, and Pityriasis Rubra Pilaris. In Lichen Planus disease, it has a very high accuracy rate, with a value of 0.9719, close to 1. H-CSA and H-TSA algorithms have an accuracy score of 1 in diagnosing Lichen Planus disease. It has succeeded in diagnosing Psoriasis, pityriasis rubra, and chronic dermatitis diseases with an accuracy of 1.0 in all three algorithms. When the test metrics are evaluated, although the H-HHO algorithm finds relatively more successful scores in 6 disease types than the H-CSA and H-TSA algorithms, the test metrics of all three optimization algorithms are high and can be used successfully to diagnose this disease. The test score of the K-Means algorithm was examined, and a low success rate of approximately 45% was found. The success rate increased significantly when the K-Means algorithm was used in a hybrid way with optimization algorithms. It was approximately 95% for all three optimization algorithms. In Figure 3, matrices of dermatology dataset confusion of the four algorithms are given.

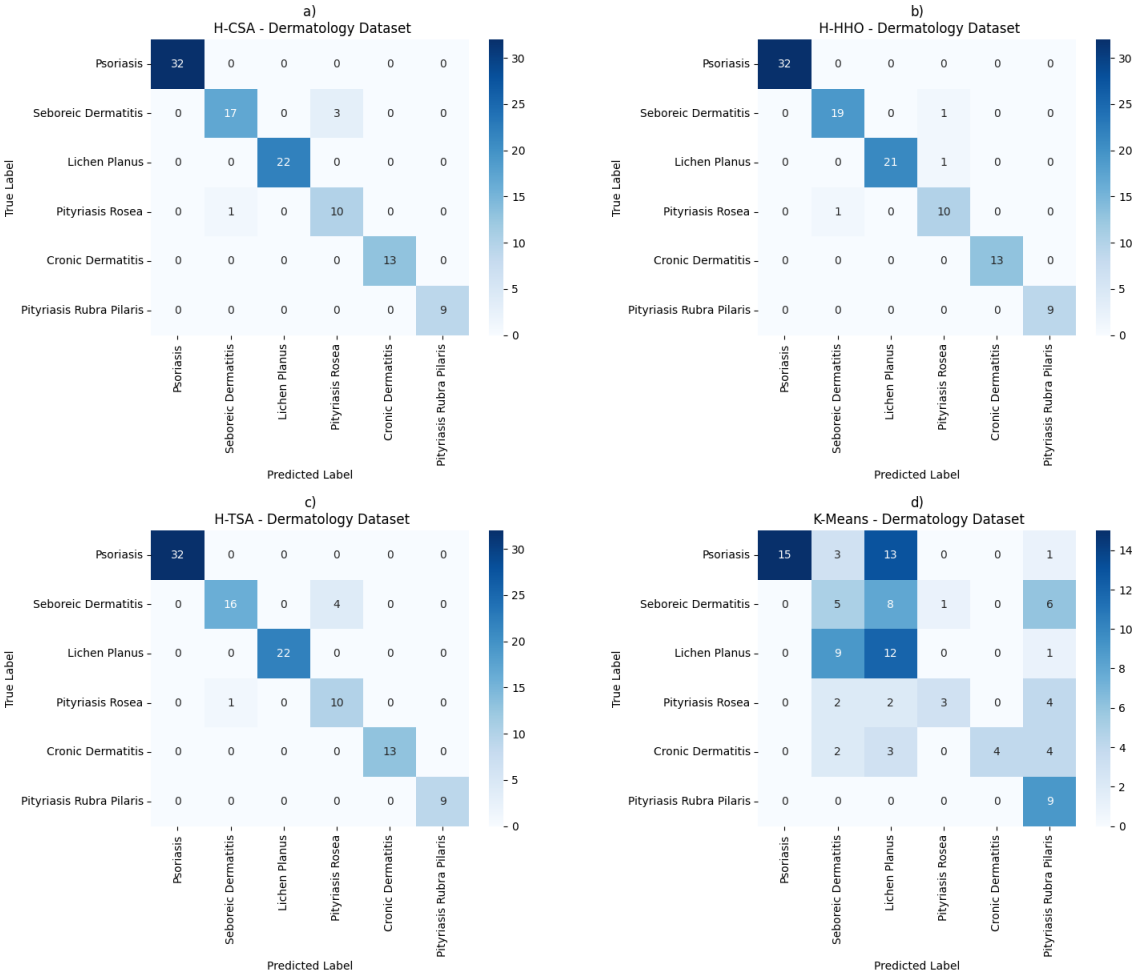

Figure 3. Confusion matrix results of hybrid algorithms and K-Means algorithm for Dermatology dataset

Compared to the optimization algorithms, the disease classification performance of the K-Means algorithm is weak. Hybrid algorithms achieved high performance in classifying all disease types compared to K-Means. Diabetes test results are given in Table 7 as follows. Algorithms with more successful classifications are shown in bold.

Table 7. Performance results of hybrid algorithms and K-Means algorithm for Diabetes dataset

	H-CSA	H-HHO	H-TSA	K-Means Algorithm
Algorithm	Train Score: 81.7518% Test Score: 79.3103%	Train Score: 81.7518% Test Score: 79.3103%	Train Score: 81.7518% Test Score: **81.0344**%	Train Score: 73.7226% Test Score: 68.9655%
Accuracy (%)	0.7931	0.7931	**0.8103**	0.6896
Recall (%)	**1.0**	0.8333	0.8333	0.6875
Specificity (%)	0.7391	0.7826	**0.8043**	0.6904
Precision (%)	0.5	0.5	**0.5263**	0.4583
F1-Score (%)	**0.6666**	0.6250	0.6451	0.5500

H-CSA and H-HHO algorithms achieved the same result in classifying diabetes disease and produced more successful results than H-TSA. The proposed H-CSA and H-HHO models correctly classified diabetes with approximately 74% accuracy. Compared to the other two optimization algorithms, the H-TSA algorithm is also classified with very close accuracy. Accordingly, the H-TSA model is also classified with approximately 73% accuracy. However, the H-CSA and H-HHO algorithms achieved higher performance than the H-TSA algorithm according to accuracy, specificity, precision, and F1-score values. The hybrid algorithms performed about 20% more accomplished classifications than the K-Means algorithm. In Figure 4, confusion matrices taken using the diabetes dataset are shown.

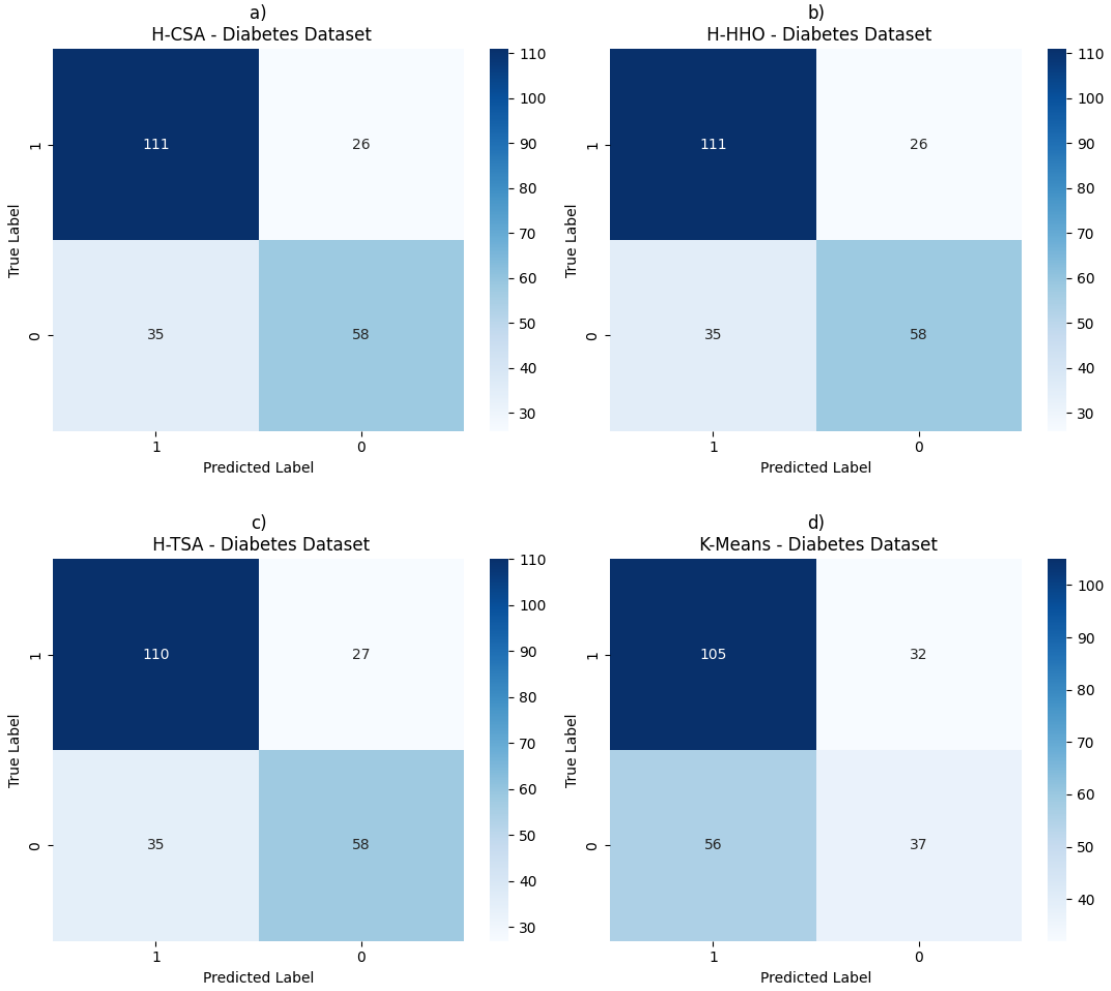

Figure 4. Confusion matrix results of hybrid algorithms and K-Means algorithm for Diabetes dataset

Parkinson's Dataset test results are given in Table 8. Algorithms with more successful results are shown in bold.

Table 8. Performance results of hybrid algorithms and K-Means algorithm for Parkinson's dataset

	H-CSA	H-HHO	H-TSA	K-Means Algorithm
Algorithm	Train Score: 81.7518% Test Score: 79.3103%	Train Score: 81.7518% Test Score: 79.3103%	Train Score: 81.7518% Test Score: **81.0344**%	Train Score: 73.7226% Test Score: 68.9655%
Accuracy (%)	0.7931	0.7931	**0.8103**	0.6896
Recall (%)	**1.0**	0.8333	0.8333	0.6875
Specificity (%)	0.7391	0.7826	**0.8043**	0.6904
Precision (%)	0.5	0.5	**0.5263**	0.4583
F1-Score (%)	**0.6666**	0.6250	0.6451	0.5500

The H-TSA algorithm achieved the highest performance in the Parkinson's dataset, with an accuracy of about 81%. In addition, the H-TSA algorithm received the highest scores in the specificity and precision metrics. The H-TSA algorithm was followed by the H-CSA and H-HHO algorithms with a 79% accuracy score. According to the recall and F1-score metrics, the H-CSA algorithm is ahead of other algorithms. In summary, all three hybrid algorithms achieved a successful classification with scores close to each other. On the other hand, the K-Means algorithm lags far behind the hybrid algorithms, with an accuracy rate of about 68%. In Figure 5, confusion matrices obtained using the Parkinson's dataset are given.

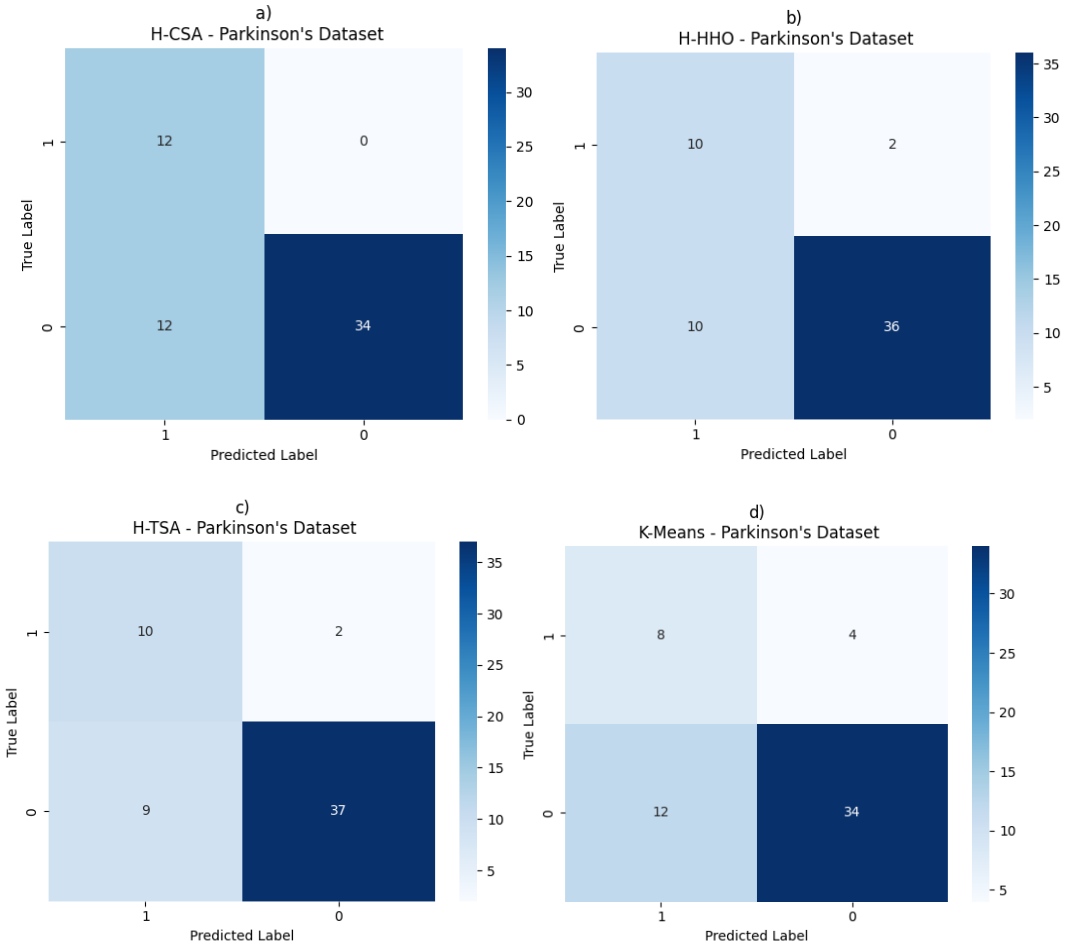

Figure 5. Confusion matrix results of hybrid algorithms and K-Means algorithm for Parkinson's dataset

In Table 9, error metrics results for the Thyroid dataset are shown.

Table 9. Performance results of hybrid algorithms and K-Means algorithm for Thyroid dataset

	H-CSA			H-HHO			H-TSA			K-Means Algorithm		
Algorithm	Train Score: 96.9444% Test Score: 96.2962%			Train Score: 97.8373% Test Score: **96.9907**%			Train Score: 92.0238% Test Score: 90.3703%			Train Score: 43.1151% Test Score: 43.4259%		
Status	**Not Hyperthyroid**	**Hyper Function**	**Subnormal Function**	**Not Hyperthyroid**	**Hyper Function**	**Subnormal Function**	**Not Hyperthyroid**	**Hyper Function**	**Subnormal Function**	**Not Hyperthyroid**	**Hyper Function**	**Subnormal Function**
Accuracy (%)	**0.9847**	0.9652	0.9759	**0.9847**	**0.9722**	**0.9828**	**0.9847**	0.9097	0.9129	0.9171	0.4986	0.4527
Recall (%)	**0.5423**	0.8750	0.9803	**0.5423**	**0.9732**	**0.9824**	**0.5423**	0.3839	0.9436	0.3389	0.6160	0.4268
Specificity (%)	**0.9971**	0.9702	0.9239	**0.9971**	**0.9721**	**0.9883**	**0.9971**	0.9384	0.5555	0.9333	0.4921	0.7543
Precision (%)	**0.8421**	0.6163	0.9933	**0.8421**	**0.6566**	**0.9989**	**0.8421**	0.2544	0.9610	0.1250	0.0622	0.9528
F1-Score (%)	**0.6597**	0.7232	0.9868	**0.6597**	**0.7841**	**0.9906**	**0.6597**	0.3060	0.9523	0.1826	0.1130	0.5895

Types of thyroid disease were examined in the Not Hyperthyroid, Hyperfunction, and Subnormal Function categories. The successful algorithms were shown in green, blue, and red according to the diseases, respectively. H-CSA, H-HHO, and H-TSA algorithms produced the same value with 0.9847 accuracy in classifying not-hyperthyroid disease. The H-HHO algorithm succeeded in diagnosing hyperfunction and Subnormal Function disease types. It achieved high success in all disease types with an accuracy rate exceeding 90% in all three algorithms. For the Thyroid dataset, the H-HHO algorithm with the highest scores in all measurement metrics is relatively more successful than the other two hybrid algorithms. When the H-HHO algorithm is compared with the K-Means algorithm, the accuracy of the H-HHO algorithm is about 7% more successful in classifying Hyperthyroid disease, 97% in classifying Hyper Function disease, and 117% in classifying Subnormal Function disease. In Figure 6, confusion matrices taken using the thyroid dataset are given.

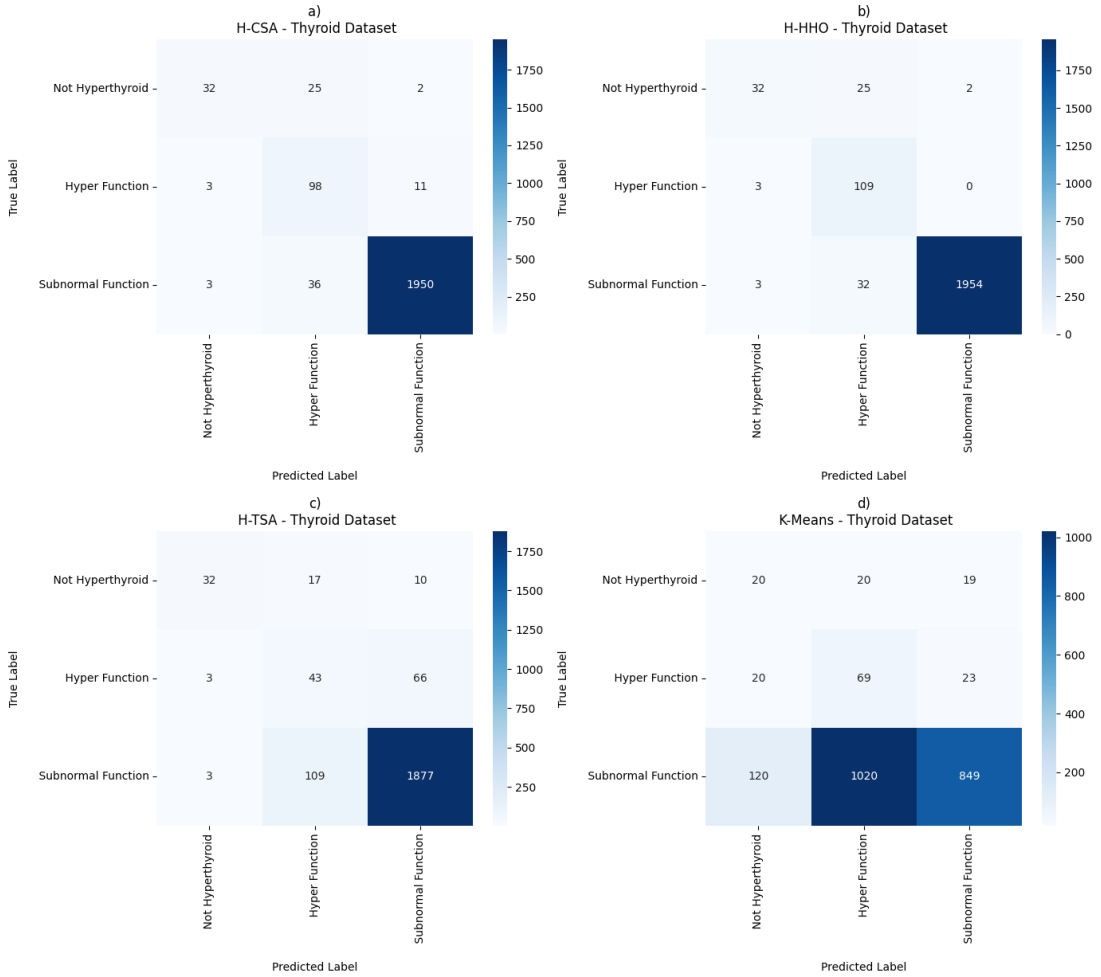

Figure 6. Confusion matrix results of hybrid algorithms and K-Means algorithm for Thyroid dataset

4. Conclusion and Discussion

In the present study, we address the local optimum issue caused by randomly generated initial centroid values in the clustering process of the K-Means algorithm, as well as provide a solution to the challenges in handling large files. We enhance the clustering accuracy by utilizing a metaheuristic algorithm to determine the parameter values for disease diagnosis. In other words, the study aimed to achieve a more precise diagnosis by adjusting the significance level of highly influential parameters. In addition, it sought to prevent false diagnoses by reducing the weight of parameters with minimal impact on the disease diagnosis, with the goal of eliminating false diagnoses by minimizing the effect of irrelevant parameters. By optimizing the coefficients, we aimed to address the issue of the K-Means approach getting trapped in the local optimum and enhance the clustering technique's precision.

The study utilized a hybridized framework that integrated the CSA, TSA, and HHO algorithms and the K-Means method. This approach successfully detected diseases using four distinct medical datasets: dermatology, diabetes, Parkinson's, and thyroid. Additionally, we statistically evaluated the performance measures of the three hybrid algorithms (H-CSA, H-HHO, and H-TSA) and the K-Means algorithm. Among the datasets and optimization algorithms we used in our H-HHO study, the H-HHO algorithm generally achieved higher performance than other algorithms in Diabetes, Dermatology, and Thyroid datasets. On the other hand, the H-CSA achieved the same success rate as H-HHO in the diabetes dataset, although H-HHO produced close results. On the other hand, the H-TSA achieved the highest performance only in the Parkinson's dataset compared to other algorithms. However, H-TSA, in other datasets, is in the last place. We found that the H-CSA algorithm is the fastest of all four data sets used for mean runtime. Despite this, we have concluded that all three algorithms are consistent by producing results that are similar to each other.

The suggested hybrid three metaheuristic algorithm in the Dermatology dataset was detected with 100% success in Psoriasis, Pityriasis Rubra Pilaris, and Chronic Dermatitis disease types. In other disease types in this group (Lichen Planus, Seborrheic Dermatitis, and Pityriasis Rosea), the H-HHO algorithm has been the most successful in the Dermatology dataset, which has six disease types since it has the lowest error value. Test results with the K-Means algorithm demonstrated that the hybrid models were almost half as successful. The results of all three metaheuristic algorithms proposed in the diabetes dataset were determined with the lowest success rate (an average of 73%) compared to the results of other datasets. We predict that this situation is due to the structure of the dataset and the number of input parameters. The H-CSA and H-HHO algorithms produced the same detection value in this dataset and became equivalent algorithms. On the other hand, the K-Means algorithm achieved less success than about 20% of our suggested hybrid algorithms. In the Parkinson's dataset, the H-TSA algorithm, which had a low success rate in other datasets, was the algorithm that produced the most successful diagnosis result. The H-CSA and H-HHO algorithms detected the equal disease in this dataset. In addition, the K-Means algorithm has achieved less success than approximately 12% of the hybrid algorithms we recommend.

The three metaheuristic algorithms proposed in detecting disease Not Hyperthyroid, the subcategory of thyroid disease, achieved the same result with a success rate of 98%. In diagnosing disease types of Hyper Function and Subnormal Function, the H-HHO algorithm achieved higher diagnostic success. Besides, the K-Means algorithm achieved half the diagnostic success of the algorithms we suggested in diseases Hyper Function and Subnormal Function, excluding disease Not Hyperthyroid. The presented study offers significant advantages such as test accuracy rate, staff workload, test costs, and waiting time for the test results detection of different types of diseases in medical datasets. In future research, new studies can be carried out using datasets of different diseases in the health field and different metaheuristic algorithms or deep learning methods.

Conflict of Interest Statement

The authors declare that there is no conflict of interest

References

[1] I. Zheliznyak, Z. Rybchak, and I. Zavuschak, "Analysis of clustering algorithms.," in *Advances in Intelligent Systems and Computing: Selected Papers from the International Conference on Computer Science and Information Technologies, September 6-10 , 2017. Lviv, Ukraine.* Springer, 2017, pp. 305–314.

[2] D. Karaboga and C. Ozturk, "A novel clustering approach: Artificial Bee Colony (ABC) algorithm.," *Applied soft computing*, vol. 11, no. 1, pp. 652–657, 2011. doi.org/10.1016/j.asoc.2009.12.025

[3] M. Ren, J. Zhang, L. Khoukhi, H. Labiod, and V. Vèque, "A unified framework of clustering approach in vehicular ad hoc networks.," *IEEE Transactions on intelligent transportation systems*, vol. 19, no. 5, pp. 1401–1414, 2017. doi.org/10.1109/TITS.2017.2727226

[4] M.M. Rahman and D.N. Davis, "Addressing the class imbalance problem in medical datasets.," *International Journal of Machine Learning and Computing*, vol. 3, no. 2, p. 224, 2013. doi.org/10.7763/IJMLC.2013.V3.307

[5] S. Ding, H. Jia, M. Du, and Y. Xue, "A semi-supervised approximate spectral clustering algorithm based on HMRF model," *Information Sciences*, vol. 429, pp. 215–228, 2018. doi.org/10.1016/j.ins.2017.11.016

[6] M.W. Berry, A. Mohamed, and B.W. Yap, "Supervised and unsupervised learning for data science," Springer, 2019.

[7] C. Fraley and A.E. Raftery, "How many clusters? Which clustering method? Answers via model-based cluster analysis," *The computer journal*, vol. 41, no. 8, pp. 578–588, 1998. doi.org/10.1093/comjnl/41.8.578

[8] A. Saxena, M. Prasad, A. Gupta, et al., "A review of clustering techniques and developments," *Neurocomputing*, vol. 267, pp. 664–681, 2017. doi.org/10.1016/j.neucom.2017.06.053

[9] T. Yi, M. Shi, and H. Zhu, "Medical data publishing based on average distribution and clustering," *CAAI Transactions on Intelligence Technology*, vol. 7, no. 3, pp. 381–394, 2022. doi.org/10.1049/cit2.12094

[10] J. Si, Z. Tian, D. Li, et al., "A multi-modal clustering method for traditonal Chinese medicine clinical data via media convergence," *CAAI Transactions on Intelligence Technology*, p. 2023. doi.org/10.1049/cit2.12230

[11] S. Dörterler, "KANSER HASTALIĞI TEŞHİSİNDE ÖLÜM OYUNU OPTİMİZASYON ALGORİTMASININ ETKİS," *Mühendislik Alanında Uluslararası Araştırmalar VIII*, p. 15, 2023.

[12] S. Dörterler, H. Dumlu, D. Özdemir, and H. Temurtaş, "Hybridization of K-means and Meta-Heuristics Algorithms for Heart Disease Diagnosis," *in NEW TRENDS IN ENGINEERING AND APPLIED NATURAL SCIENCES*, pp. 55. Duvar Publishing (2022).

[13] S. Dörterler, H. Dumlu, D. Özdemir, and H. Temurtaş, "Melezlenmiş K-means ve Diferansiyel Gelişim Algoritmaları ile Kalp Hastalığının Teşhisi," in *International Conference on Engineering and Applied Natural Sciences*, May 10-12, 2022. Konya, Turkey, ICEANS 2022. pp. 1840–1844.

[14] A. Tekerek and M. Dörterler, "The adaptation of gray wolf optimizer to data clustering," *Politeknik Dergisi*, p. 1, 2020. doi.org/10.2339/politeknik.778630

[15] J. Cui, Z. Ding, P. Fan, and N. Al-Dhahir, "Unsupervised machine learning-based user clustering in millimeter-wave-NOMA systems," *IEEE Transactions on Wireless Communications*, vol. 17, no. 11, pp. 7425–7440, 2018. doi.org/10.1109/TWC.2018.2867180

[16] F. Hu, H. Chen, and X. Wang, "An Intuitionistic Kernel-Based Fuzzy C-Means Clustering Algorithm With Local Information for Power Equipment Image Segmentation," *IEEE Access*, vol. 8, pp. 4500–4514, 2020. doi.org/10.1109/ACCESS.2019.2963444

[17] J. Maia, C.A.S. Junior, F.G. Guimarães, et al., "Evolving clustering algorithm based on mixture of typicalities for stream data mining," *Future Generation Computer Systems*, vol. 106, pp. 672–684, 2020. doi.org/10.1016/j.future.2020.01.017

[18] R.M. Alguliyev, R.M. Aliguliyev, and L. V Sukhostat, "Efficient algorithm for big data clustering on single machine," *CAAI Transactions on Intelligence Technology*, vol. 5, no. 1, pp. 9–14, 2020. doi.org/10.1049/trit.2019.0048

[19] Y. Li, J. Qi, X. Chu, and W. Mu, "Customer Segmentation Using K-Means Clustering and the Hybrid Particle Swarm Optimization Algorithm," *The Computer Journal,* p. 2022. doi.org/10.1093/comjnl/bxab206

[20] S.H. Shihab, S. Afroge, and S.Z. Mishu, "RFM based market segmentation approach using advanced k-means and agglomerative clustering: a comparative study," in *2019 International Conference on Electrical, Computer and Communication Engineering (ECCE). February 7-9, 2019*. IEEE , pp. 1–4.

[21] A. Fallah Tehrani and D. Ahrens, "Modified sequential k-means clustering by utilizing response: A case study for fashion products," *Expert Systems,* vol. 34, no. 6, p. e12226, 2017. doi.org/10.1111/exsy.12226

[22] O. Akman, T. Comar, D. Hrozencik, and J. Gonzales, "Data clustering and self-organizing maps in biology," in *Algebraic and Combinatorial Computational Biology*, pp. 351–374. Elsevier (2019). doi.org/10.1016/B978-0-12-814066-6.00011-8

[23] J.P.L. Johnson, "Clustering statistics, roughness feedbacks, and randomness in experimental step-pool morphodynamics," *Geophysical Research Letters*, vol. 44, no. 8, pp. 3653–3662, 2017. doi.org/10.1002/2016GL072246

[24] L. Wen, K. Zhou, and S. Yang, "A shape-based clustering method for pattern recognition of residential electricity consumption," *Journal of cleaner production*, vol. 212, pp. 475–488, 2019. doi.org/10.1016/j.jclepro.2018.12.067

[25] K.P. Sinaga and M.-S. Yang, "Unsupervised K-means clustering algorithm," *IEEE Access*, vol. 8, pp. 80716–80727, 2020. doi.org/10.1109/ACCESS.2020.2988796

[26] R.-Q. Liu, Y.-C. Lee, and H.-L. Mu, "Customer Classification and Market Basket Analysis Using K-Means Clustering and Association Rules: Evidence from Distribution Big Data of Korean Retailing Company," *Knowledge Management Research*, vol. 19, no. 4, pp. 59–76, 2018. doi.org/10.15813/kmr.2018.19.4.004

[27] M. Mehrazma and B. Mahboobi, "Customer Clustering by Combining the Particle Swarm And K-Means Algorithms and Analyzing Their Behavior on Commercial Websites," *Signal Processing and Renewable Energy*, vol. 5, no. 2, pp. 83–97, 2021. dorl.net/dor/20.1001.1.25887327.2021.5.2.6.7

[28] Y. Tang, Y. Guo, Q. Sun, et al., "Industrial polymers classification using laser-induced breakdown spectroscopy combined with self-organizing maps and K-means algorithm," *Optik*, vol. 165, pp. 179–185, 2018. doi.org/10.1016/j.ijleo.2018.03.121

[29] J. Fonseca, G. Douzas, and F. Bacao, "Improving Imbalanced Land Cover Classification with K-Means SMOTE: Detecting and Oversampling Distinctive Minority Spectral Signatures," *Information,* vol. 12, no. 7, p. 266, 2021. doi.org/10.3390/info12070266

[30] M.R. Kanthan and S.N. Sujatha, "Rain drop detection and removal using k-means clustering," in *2015 IEEE International Conference on Computational Intelligence and Computing Research (ICCIC). pp. 1–5. IEEE ,10-12 December 2015, Madurai, India*. doi.org/10.1109/ICCIC.2015.7435707

[31] D. Yu, X. Zhou, Y. Pan, Z. Niu, and H. Sun, "Application of Statistical K-Means Algorithm for University Academic Evaluation," *Entropy,* vol. 24, no. 7, p. 1004, 2022. doi.org/10.3390%2Fe24071004

[32] J. Heil, V. Häring, B. Marschner, and B. Stumpe, "Advantages of fuzzy k-means over k-means clustering in the classification of diffuse reflectance soil spectra: A case study with West African soils." *Geoderma*, vol. 337, pp. 11–21, 2019. doi.org/10.1016/j.geoderma.2018.09.004

[33] N. Xiaoying, X. Liya, and Z. Xiaoyu, "Classification of Rice According to the Geographic Origin Based on K-Means Cluster and Hierarchinal Cluster [J]," *Journal of Agricultural Mechanization Research,* vol. 6, p. 2012.

[34] T.K. Anderson, "Kernel density estimation and K-means clustering to profile road accident hotspots," *Accident Analysis & Prevention,* vol. 41, no. 3, pp. 359–364, 2009. doi.org/10.1016/j.aap.2008.12.014

[35] F. Bação, V. Lobo, and M. Painho, "Self-organizing maps as substitutes for k-means clustering," in *International Conference on Computational Science, 22-25 May 2005,* pp. 476–483. Springer, Atlanta, USA. doi.org/10.1007/11428862_65

[36] S. Chakraborty, N.K. Nagwani, and L. Dey, "Weather forecasting using incremental K-means clustering," *arXiv preprint arXiv:1406.4756*. p. 2014. doi.org/10.48550/arXiv.1406.4756

[37] D.E. Kurniawan and A. Fatulloh, "Clustering of Social Conditions in Batam, Indonesia Using K-Means Algorithm and Geographic Information System," *International Journal of Earth Sciences and Engineering (IJEE),* vol. 10, no. 05, pp. 1076–1080, 2017. doi.org/10.31227/osf.io/qc342

[38] J. Zhou and L.C. Le Liang, "Geographic profiling based on multi-point centrography with K-means clustering," p. 2012. doi.org/10.5281/zenodo.1058785

[39] R.S. Evans, J.F. Lloyd, G.J. Stoddard, J.R. Nebeker, and M.H. Samore, "Risk factors for adverse drug events: a 10-year analysis," *Annals of Pharmacotherapy*, vol. 39, no. 7–8, pp. 1161–1168, 2005. doi.org/10.1345/aph.1e642

[40] E.R. Vickers, H. Boocock, R.D. Harris, et al., "Analysis of the acute postoperative pain experience following oral surgery: identification of 'unaffected','disabled'and 'depressed, anxious and disabled'patient clusters," *Australian dental journal*, vol. 51, no. 1, pp. 69–77, 2006. doi.org/10.1111/j.1834-7819.2006.tb00404.x

[41] D.M. Falkenbach, E.E. Reinhard, and M. Zappala, "Identifying psychopathy subtypes using a broader model of personality: An investigation of the five factor model using model-based cluster analysis," *Journal of interpersonal violence*, vol. 36, no. 15–16, pp. 7161–7184, 2021. doi.org/10.1177/0886260519831388

[42] H. Kim, B. Kim, S.H. Kim, C.H.K. Park, E.Y. Kim, and Y.M. Ahn, "Classification of attempted suicide by cluster analysis: A study of 888 suicide attempters presenting to the emergency department," *Journal of affective disorders*, vol. 235, pp. 184–190, 2018. doi.org/10.1016/j.jad.2018.04.001

[43] R. Shai, T. Shi, T.J. Kremen, et al., "Gene expression profiling identifies molecular subtypes of gliomas," *Oncogene*, vol. 22, no. 31, pp. 4918–4923, 2003. doi.org/10.1038/sj.onc.1206753

[44] F. Bertucci, P. Finetti, J. Rougemont, et al., "Gene expression profiling identifies molecular subtypes of inflammatory breast cancer," *Cancer research*, vol. 65, no. 6, pp. 2170–2178, 2005. doi.org/10.1158/0008-5472.can-04-4115

[45] K. Ushizawa, C.B. Herath, K. Kaneyama, et al., "cDNA microarray analysis of bovine embryo gene expression profiles during the pre-implantation period," *Reproductive Biology and Endocrinology*, vol. 2, no. 1, pp. 1–16, 2004. doi.org/10.1186/1477-7827-2-77

[46] E. Şahin, D. Özdemir, and H. Temurtaş, "Multi-objective optimization of ViT architecture for efficient brain tumor classification," *Biomedical Signal Processing and Control*, vol. 91, p. 105938, 2024. doi.org/10.1016/j.bspc.2023.105938

[47] N. Yagmur, İ. Dag, and H. Temurtas, "Classification of anemia using Harris hawks optimization method and multivariate adaptive regression spline," *Neural Computing and Applications*, pp. 1–20, 2024. doi.org/10.1007/s00521-023-09379-y

[48] N.N. Arslan, D. Ozdemir, and H. Temurtas, "ECG heartbeats classification with dilated convolutional autoencoder," *Signal, Image and Video Processing*, vol. 18, no. 1, pp. 417–426, 2024. doi.org/10.1007/s11760-023-02737-2

[49] N. Yagmur, I. Dag, and H. Temurtas, "A new computer-aided diagnostic method for classifying anaemia disease: Hybrid use of Tree Bagger and metaheuristics," *Expert Systems*, p. e13528, 2023. doi.org/10.1111/exsy.13528

[50] F. Aydemir and S. Arslan, "Covid-19 pandemi sürecinde çocukların el yıkama alışkanlığının nesnelerin interneti tabanlı sistem ile izlenmesi," *Mühendislik Bilimleri ve Araştırmaları Dergisi,* vol. 3, no. 2, pp. 161–168, 2021. doi.org/10.46387/bjesr.949311

[51] N. Yağmur, H. Temurtaş, and İ. Dağ, "Anemi hastalığının yapay sinir ağları yöntemleri kullanılarak sınıflandırılması," *Journal of Scientific Reports-B,* no. 008, pp. 20–34, 2023.

[52] A.M. Ikotun, M.S. Almutari, and A.E. Ezugwu, "K-Means-Based Nature-Inspired Metaheuristic Algorithms for Automatic Data Clustering Problems: Recent Advances and Future Directions," *Applied Sciences,* vol. 11, no. 23, p. 11246, 2021. doi.org/10.3390/app112311246

[53] M. Delattre and P. Hansen, "Bicriterion cluster analysis.," IEEE Transactions on Pattern Analysis and Machine Intelligence. no. 4, pp. 277–291, 1980. https://doi.org/10.1109/TPAMI.1980.4767027

[54] A.K. Jain, M.N. Murty, and P.J. Flynn, "Data clustering: a review," *ACM computing surveys (CSUR),* vol. 31, no. 3, pp. 264–323, 1999. doi.org/10.1145/331499.331504

[55] A.G.D.Ç. TAŞKIN and G.G. Emel, "Veri Madenciliğinde Kümeleme Yaklaşimlari Ve Kohonen Ağlari İle Perakendecilik Sektöründe Bir Uygulama," *Süleyman Demirel Üniversitesi İktisadi ve İdari Bilimler Fakültesi Dergisi,* vol. 15, no. 3, pp. 395–409, 2010.

[56] L. Zhang, M. Jin, and S.-J. Yoo, "A clustering detector with graph theory for blind detection of spatial modulation systems," *Wireless Networks,* vol. 27, no. 2, pp. 1193–1201, 2021. doi.org/10.1007/s11276-020-02508-8

[57] M. Sharma, G.N. Purohit, and S. Mukherjee, "Information retrieves from brain MRI images for tumor detection using hybrid technique K-means and artificial neural network (KMANN)," in *Networking communication and data knowledge engineering*, pp. 145–157, Springer (2018). doi.org/10.1007/978-981-10-4600-1_14

[58] J. Estupiñán Ricardo, J.J. Domínguez Menéndez, I.F. Barcos Arias, J.M. Macías Bermúdez, and N. Moreno Lemus, "Neutrosophic K-means for the analysis of earthquake data in Ecuador," *Neutrosophic Sets and Systems,* vol. 44, no. 1, p. 29, 2021.

[59] M. Roberto e Souza, A. Carlos Sousa e Santos, and H. Pedrini, "A Hybrid Approach Using the k-means and Genetic Algorithms for Image Color Quantization," *Recent Advances in Hybrid Metaheuristics for Data Clustering*, pp. 151–171, 2020. doi.org/10.1002/9781119551621.ch9

[60] S. Kumar, V.K. Solanki, S.K. Choudhary, A. Selamat, and R. González Crespo, "Comparative Study on Ant Colony Optimization (ACO) and K-Means Clustering Approaches for Jobs Scheduling and Energy Optimization Model in Internet of Things (IoT)," *International Journal of Interactive Multimedia & Artificial Intelligence*, vol. 6, no. 1, p. 2020. doi.org/10.9781/ijimai.2020.01.003

[61] A.K. Abasi, A.T. Khader, M.A. Al-Betar, S. Naim, Z.A.A. Alyasseri, and S.N. Makhadmeh, "A novel hybrid multi-verse optimizer with K-means for text documents clustering," *Neural Computing and Applications*, vol. 32, no. 23, pp. 17703–17729, 2020. doi.org/10.1007/s00521-020-04945-0

[62] A. Kaur, S.K. Pal, and A.P. Singh, "Hybridization of Chaos and Flower Pollination Algorithm over K-Means for data clustering," *Applied Soft Computing*, vol. 97, p. 105523, 2020. doi.org/10.1016/j.asoc.2019.105523

[63] J. Chen, X. Qi, L. Chen, F. Chen, and G. Cheng, "Quantum-inspired ant lion optimized hybrid k-means for cluster analysis and intrusion detection," *Knowledge-Based Systems*, vol. 203, p. 106167, 2020. doi.org/10.1016/j.knosys.2020.106167

[64] S. Aggarwal and P. Singh, "Cuckoo and krill herd-based k-means++ hybrid algorithms for clustering," *Expert Systems,* vol. 36, no. 4, p. e12353, 2019. doi.org/10.1111/exsy.12353

[65] Markelle Kelly, Rachel Longjohn, and Kolby Nottingham, *The UCI Machine Learning Repository*. USA, 2022.

[66] H. Naz and S. Ahuja, "Deep learning approach for diabetes prediction using PIMA Indian dataset," *Journal of Diabetes & Metabolic Disorders*, vol. 19, no. 1, pp. 391–403, 2020. doi.org/10.1007%2Fs40200-020-00520-5

[67] M. Little, P. McSharry, E. Hunter, J. Spielman, and L. Ramig, "Suitability of dysphonia measurements for telemonitoring of Parkinson's disease," *Nature Precedings*, p. 1, 2008. doi.org/10.1109%2FTBME.2008.2005954

[68] M. Hosseinzadeh, O.H. Ahmed, M.Y. Ghafour, et al., "A multiple multilayer perceptron neural network with an adaptive learning algorithm for thyroid disease diagnosis in the internet of medical things," *The Journal of Supercomputing*, vol. 77, no. 4, pp. 3616–3637, 2021. doi.org/10.1007/s11227-020-03404-w

[69] H.A. Güvenir, G. Demiröz, and N. Ilter, "Learning differential diagnosis of erythemato-squamous diseases using voting feature intervals," *Artificial intelligence in medicine*, vol. 13, no. 3, pp. 147–165, 1998. doi.org/10.1016/s0933-3657(98)00028-1

[70] M. Ahmed, R. Seraj, and S.M.S. Islam, "The k-means algorithm: A comprehensive survey and performance evaluation," *Electronics,* vol. 9, no. 8, p. 1295, 2020. doi.org/10.3390/electronics9081295

[71] A.A. Heidari, S. Mirjalili, H. Faris, I. Aljarah, M. Mafarja, and H. Chen, "Harris hawks optimization: Algorithm and applications," *Future generation computer systems*, vol. 97, pp. 849–872, 2019. doi.org/10.1016/j.future.2019.02.028

[72] M.S. Kiran, "TSA: Tree-seed algorithm for continuous optimization," *Expert Systems with Applications*, vol. 42, no. 19, pp. 6686–6698, 2015. doi.org/10.1016/j.eswa.2015.04.055

[73] M. Aslan, M. Beskirli, H. Kodaz, and M.S. Kiran, "An improved tree seed algorithm for optimization problems," *Int J Mach Learn Comput*, vol. 8, no. 1, pp. 20–25, 2018. doi.org/10.18178/ijmlc.2018.8.1.657

[74] A. Beşkirli, D. Özdemir, and H. Temurtaş, "A comparison of modified tree–seed algorithm for high-dimensional numerical functions," *Neural Computing and Applications*, vol. 32, no. 11, pp. 6877–6911, 2020. doi.org/10.1007/s00521-019-04155-3

[75] A. Askarzadeh, "A novel metaheuristic method for solving constrained engineering optimization problems: crow search algorithm," *Computers & Structures,* vol. 169, pp. 1–12, 2016. doi.org/10.1016/j.compstruc.2016.03.001

[76] Y. Li and H. Wu, "A clustering method based on K-means algorithm," *Physics Procedia*, vol. 25, pp. 1104–1109, 2012. doi.org/10.1016/j.phpro.2012.03.206

[77] J.M. Pena, J.A. Lozano, and P. Larranaga, "An empirical comparison of four initialization methods for the k-means algorithm," *Pattern recognition letters,* vol. 20, no. 10, pp. 1027–1040, 1999. doi.org/10.1016/S0167-8655(99)00069-0

[78] A. Ucan, M. Dörterler, and E. Akçapınar Sezer, "An emotion analysis scheme based on Gray Wolf optimization and deep learning," *Concurrency and Computation: Practice and Experience*, vol. 33, no. 13, p. e6204, 2021. doi.org/10.1002/cpe.6204

[79] H. Karamollaoğlu, İ.A. Doğru, M. Dörterler, A. Utku, and O. Yıldız, "Sentiment analysis on Turkish social media shares through lexicon based approach," in *2018 3rd International Conference on Computer Science and Engineering (UBMK). September 20-23, 2018*. IEEE, pp. 45–49.

[80] F. Aydemir and S. Arslan, "A System Design With Deep Learning and IoT to Ensure Education Continuity for Post-COVID," *IEEE Transactions on Consumer Electronics*, p. 2023. doi.org/10.1109/TCE.2023.3245129

This is an open access article under the CC-BY license

GAZİ
JOURNAL OF ENGINEERING SCIENCES

Charpy Impact Test in 3D-FDM and Optimization with Artificial Intelligence

Mehmet Altuğ[*a]

Submitted: 22.11.2023 Revised: 26.12.12023 Accepted: 17.01.2024 doi:10.30855/gmbd.0705N02

Keywords: FDM, Charpy impact test, Build orientation, Notch, Deep learning, Extreme learning machines

[a*]Inonu University, Malatya OIZ Vocational School, Malatya / Türkiye
Orcid: 0000-0002-4745-9164
*e mail: mehmet.altug@inonu.edu.tr

ABSTRACT

In the study, the rates of impact energy absorption of Acrylonitrile Butadiene Styrene (ABS) fractures produced by the Fused Deposition Modeling (FDM) method were examined. Charpy impact test results were determined using layer thickness, printing speed, support angle, build orientation, notch type, and unfill type. Box-behnken experimental design design in the study. Notch impact samples are produced on an ABS Three-dimensional Printer (3DP). Then, charpy impact tests were performed on the impact test device. Data were evaluated using the Minitab 21 program. Later, Deep Learning (DL) and Extreme Learning Machines (ELM) file models were created based on this development. The best results were obtained as 0.844 kJ/m^2 with a layer thickness of 0.09 mm. At 60 mm/s printing speed and 30° support angle, the impact energy absorption is 0.803 kJ/m^2. The extinction edge of the highest impact energy is 0.841 kj/m^2. The most effective impact absorption was obtained as 0.827 kJ/m^2 in the U notch type. In the full infill type, impact energy absorption is obtained as 0.777 kJ/m^2. In DL, man is the programming and tanh is the activation function. DL, Mean Squared Error (MSE) value was calculated as 0.000923, r^2 was calculated as 0.97427. In ELM, the activation function is sigmoidal at the input and linear at the output.

3D-FDM'de Charpy Darbe Testinin Yapay Zekâ ile Optimizasyonu

Anahtar Kelimeler: FDM, Charpy darbe testi, Konumlandırma, çentik tipi, Derin öğrenme, Aşırı öğrenme makineleri

ÖZ

Çalışmada FDM yöntemiyle üretilen ABS parçaların darbe enerjisi emilim oranları incelenmiştir. Charpy darbe testi sonuçları, katman dağılımı, yazdırma hızı, destek açısı, yapı yönü, çentik tipi ve dolgu tip kullanılarak belirlendi. Çalışmada Box-behnken deneysel tasarım tasarımı kullanıldı. Çentik darbe numuneleri 3D yazıcıda ABS malzemeden üretildi. Daha sonra darbe test cihazında charpy darbe testleri yapıldı. Veriler Minitab 21 programı kullanılarak değerlendirildi. Daha sonra bu sonuçlara dayanarak DL ve ELM modelleri oluşturuldu. En iyi sonuçlar 0,09 mm katman kalınlığında 0,844 kJ/m^2, 60 mm/s baskı hızında ve 30° destek açısında darbe enerjisi emilimi 0,803 kJ/m^2 olarak belirlendi. En yüksek darbe enerjisinin edge yönünde 0,841 kj/m^2, U çentik tipinde 0,827 kJ/m^2, full dolgulu tipinde 0,777 kJ/m^2 olarak elde edildi. DL'de adam optimizasyon algoritması, tanh ise aktivasyon fonksiyonudur. DL, MSE değeri 0,000923, r^2 ise 0,97427 olarak hesaplandı. ELM'de aktivasyon fonksiyonu girişte sigmoid, çıkışta ise doğrusaldır.

To cite this article: M. Altug, "Charpy Impact Test in 3D-FDM and Optimization with Artificial Intelligence," *Gazi Journal of Engineering Sciences,* vol. 10, no. 1 pp. 12-26, 2024. doi:10.30855/gmdb.0705N02

1. Introduction

There are ma1ny researchers and studies working on Additive Manufacturing (AM) and Reverse Engineering (RE) related issues. Three-dimensional (3D) printing has brought some advantages in its own way. These are design flexibility, high precision and less material usage. FDM and polyjet are widely used in 3D printing methods. Since the mechanical, and rheological properties of the parts in additive manufacturing are relatively low, their printing potential is quite weak [1–4].

Pattnaik et al. He evaluated the advantages and disadvantages of the limitations in production sound in AM. Thus, it has been observed that high costs and long periods of time have been reduced in some critical sectors [5]. Anwer and his colleagues developed simulations with computer-aided tolerance systems to model the effects of tolerances [6]. Chiu et al minimized the time required for repeatability fabrications by optimizing 3D fabrication parameters [7]. Alvarez et al. studied the effect of filler density on the impact and tensile strength of ABS samples [8]. Martinez-Garcia et al. surveyed the effect of different AM techniques on the mechanical properties of polymer parts. Some other researchers have investigated the dimensional and shape changes in Polyjet samples printed by different techniques [9]. In their study, Aroca and colleagues introduced 3D parts with a robot to enable low-cost mass production [10]. Cheng et al. They conducted a theoretical and experimental study for efficient optimization of the density of the cellular structure in AM [11].

Harynska et al. With the outstanding printability of Polylactic acid (PLA)/TPS, they investigated the characterization of self-produced bio-based PLA and TPS tailored for 3D printing technology [12]. Castro et al. They examined the mechanical properties of sandwich panels produced by AM [13]. Andrzejewski et al. investigated that the addition of TPS and PBAT greatly improved impact strength and elongation [14]. Tanveer et al. They studied the effect of filler density on the impact and tensile strength of PLA samples [15]. Caminero et al. They examined the effect of layer thickness on impact performance in nylon samples [16]. According to Feket et al., rubber was used to increase the ductility of PLA filaments and provide deformability compared to samples prepared using 3DPAR filler [17]. Korga et al. They studied the relationship between the percentage filling of the sample and the absorbed energy in AM [18]. Hadid et al. P430 investigated the effect of layer-by-layer shot peening on the low-speed impact properties of ABS parts and demonstrated high toughness and impact strength [19]. Sood et al. The effect of production parameters such as layer thickness and scanning angle on the mechanical properties of 3D parts produced by the FDM method was investigated and it was stated that they had an effect on the strength [20]. Ameri et al. the fracture behavior of 3D printed structures under dynamic loading conditions was investigated [21]. Hetrick et al. Investigated the effect of AM fabricated Kevlar fiber reinforced Onyx composites on impact energy absorption [22]. Kontárová et al. He worked on improving the mechanical and thermal properties of PLA-PHB mixtures [23]. Leon et al. Charpy tested polycarbonate and nylon+carbon fiber samples. According to the results, they found that the absorbed energy was higher for PA+CF material [24]. Velarde et al. They found that adding agave fibers to the filaments improved their crystallinity, impact strength and absorption values [25]. Ning et al. Tensile strengths of carbon fiber reinforced plastic composite parts produced by FDM method were examined and the effect of layer thickness on yield and tensile strength was examined [26]. Sa'ude et al. He investigated the mechanical properties of copper powder added ABS materials produced by FDM method and revealed that they had a significant positive effect [27]. Also ABS etc. There are other studies examining mechanical tests using polymer filaments [28”–30]. These were made with different 3D printers and the results regarding mechanical properties were compared [31,32].

In the literature, there are many Deep Artificial Neural Network (ANN) studies involving convolutional neural networks (CNNs) created in computer vision and image recognition [33], [34] [35]. Ma et al. trained a deep convolutional neural network based on DeepLab. In their study, they applied a symmetric overlap-square strategy and a local processing method based on symmetric correction to increase the accuracy of the results with 3D information [36]. Oborski and Wysocki (2022) examined the quality control system with DL and revealed that the neural network created for visual quality control worked with 99.820% accuracy [37]. Lin et al. investigated to achieve high accuracy prediction performance using one-dimensional convolutional neural network, Fast Fourier Transform Long Short-Term Memory Network and Fast Fourier Transform-Deep Neural Networks. [38]. Pan et al. They worked on the accuracy rate of estimating surface roughness with deep learning [39]. Li et al. introduced a modeling approach to predict the ra (surface roughness) of AM-produced parts. It has shown that 3D printed components can predict the surface roughness with high accuracy [40].

Dimitriou et al. they propose a system that automates diagnostics with ANN [41]. Yun et al. (2020) established a vision-based defect inspection system using defect images obtained from the metal production line. They stated that the proposed method showed an effective performance [42]. Zhang et al. presented a data-based prediction model with deep learning in the FDM method and stated that it performed better than other machine learning techniques [43]. Essien and Giannetti worked on the model consisting of DL and Deep convolutional LSTM encoder-decoder architecture [44]. Serin et al. have tried to monitor the team status with the DL method [45]. Wang et al. worked on a DL model for welding processes [46]. Cardoso et al. They stated that with the Machine Learning approach, useful results can be produced that will assist in providing appropriate resources, decision-making and operation of the system [47]. Klein et al. used random forests (RF) machine learning to estimate the size and surface quality characteristics of holes [48].

ELM was first introduced as a learning scheme for single-layer feedforward networks (SLFNs) and was stated to be able to estimate nonlinear function through random hidden neurons. In particular, the parameters of hidden neurons occur randomly and the activation function is a nonlinear continuous function. ELM was originally designed to solve the supervised learning problem. Later it is used in regression and classification problems [49–53]. The equation of a single hidden layer and feedforward neural network with n number of hidden nodes is shown as in Eq 2. The ai and bi in the equation are the learning parameters. Bi, i. are the weights of the hidden node. G(x) is the activation function [49,50].

f_N (x)=∑_(i=1)^NB_i ,G((a_i,b_i,x),xϵ R,a_i ϵ R) (1)

Looking at the literature, ABS etc. There are also studies examining the mechanical properties of filaments. In this study, notch impact specimens were produced from ABS material in a 3D printer using the experimental design box behnken-RSM method in the first stage. Then, charpy tests were carried out on the AOB impact tester and statistical analyzes of all data obtained were performed in the Minitab 21 program. A model was created with DL and ELM methods through the data obtained in the second stage.

When the literature is examined, there are studies examining the mechanical properties of ABS etc. filaments. In the first stage of this study, notch impact specimens were produced from ABS material on a 3D printer. In the production of these specimens, the Response Surface Methodology (RSM)-Box behnken method, which is rarely encountered in the literature on the mechanical properties of filaments, was used as an experimental design. In addition, another important point that stands out differently from the literature is that AI models were created with DL and ELM methods depending on the data obtained in the experimental results.

2. Material and Methods

Box-Behnken RSM method, one of the surface response methods, was used in the study. Box-Behnken presents a data-driven relationship between the independent variable and the response function. In this context, the model is a first-order model if it shows a predictive result on the response surface as a linear func. of the independent variables (Equation 2). In case of degree of curvature in the response surface, it is a second-order model as in Equation 3.

$$y = \beta_0 + \beta_1 x_1 + \beta_2 x_2 + \cdots + \beta_k \beta_k + \varepsilon \quad (2)$$

$$y = \beta_0 \sum_{i=1}^{n} \beta_i X_i + \sum_{i=0}^{n} \beta_{ii} X_i^2 + \sum_{i=0}^{n} \sum_{j=1}^{n} \beta_{ij} X_i X_j + \varepsilon_0 \quad (3)$$

(Table 1) below presents additive manufacturing parameters and levels. The results were analysed in Minitab 21 software. Sample production according to the parameters was made using the FDM method on a Zortrax M200 (Figure 1) 3D printer. Charpy impact specimens were fabricated using layer thickness, print speed, support angle as continuous factors and build orientation, notch type and filler type as categorical factors (Table 1). Here, the levels of 0.09 mm, 0.14 mm and 0.19 mm were selected for layer thickness on the 3D printer. For printing speed, 40, 60 and 80 mm/s, for support angle 20, 30 and 40 were selected. These choices were made by considering the literature. In the same way, flat, edge and upright production build orientation were selected for build orientation (Fig. 2a). The notch type, which is another important parameter of the study, was selected as U, V and Kh (Figure 2b), and full and mesh methods were selected for the fill type. ABS was used as the filament material. Charpy

impact test specimens (Figure 2) were produced in conformity with ASTM 6110 standard. Charpy impact energy were performed 1J on the AOB impact test device (Figure 3a) and the test sample and post-test sample status are given (Figure 3b).

Table 1. Box-behnken parametres and levels

Continuous Factors	**Level values**	
	Low	**High**
Layer thickness (mm)	*0,09*	*0,19*
Print speed (mm/s)	*40*	*80*
Support angle (°)	*20*	*40*

Categorical Factors	**Level values**		
	1.	**2.**	**3.**
Build Orientation	*Flat*	*Edge*	*Upright*
Notch type	*V*	*U*	*Kh*
Infill type	*Full*	*Mesh*	

After obtaining the experimental data, artificial intelligence based DL and ELM models were tried to be created. recommended prediction model was created with ELM and DL for the Charpy impact test data. Artificial intelligence based analyses of the results were realised in Anaconda-Python 3.9.

Figure 1. 3D printer in the study

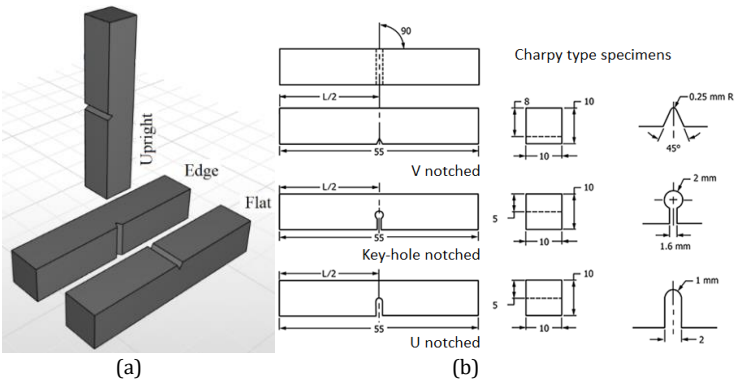

(a) (b)

Figure 2. Charpy impact test specimens a) build orientations b) notch type

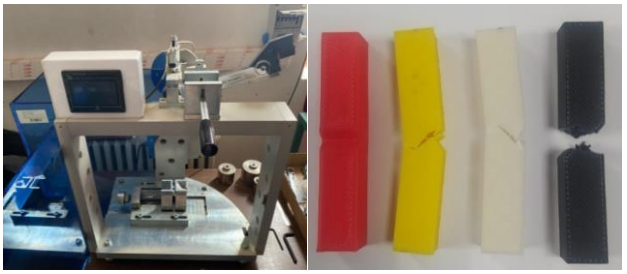

(a) (b)

Figure 3. a) Charpy impact test device in the study and b) samples

3. Results and Discussion

3.1 Response surface method (RSM)

This study, which was measured with the RSM method, the Box behnken method was used as the design of experiment (DOE). In accordance with this experimental design, notch impact samples were produced on the 3D printer. Charpy tests were performed on a Shimadzu brand impact tester and all the data obtained were processed (Table 2). The data achieved after the charpy test were analyzed in Minitab-21 software. Box-benhken analysis and Analysis of Variance (ANOVA) test were performed here. Additionally, figures and graphs were drawn to explain this study more effectively.

Table 2. Box-behnken design and results

Run Order	Pt Type	Blocks	Layer thickness (mm)	Print speed (mm/s)	Support angle (°)	Build orientation	Notch type	Infill type	Data (kj/m²)
1	2	1	0,19	80	30	Edge	V	Mesh	0,539
2	2	1	0,14	40	20	Upright	Kh	Mesh	0,451
3	2	1	0,09	60	40	Edge	Kh	Full	0,951
4	2	1	0,14	40	20	Edge	V	Full	0,660
5	2	1	0,09	60	20	Edge	V	Mesh	0,724
6	2	1	0,09	80	30	Edge	V	Mesh	0,736
7	2	1	0,19	60	40	Upright	U	Mesh	0,636
.	.	.	.	.	.	.	.	.	.
.	.	.	.	.	.	.	.	.	.
.	.	.	.	.	.	.	.	.	.
264	2	1	0,19	60	20	Flat	U	Mesh	0,657
265	2	1	0,09	60	20	Edge	Kh	Full	0,973
266	2	1	0,14	80	40	Upright	Kh	Full	0,517
267	2	1	0,09	40	30	Edge	U	Mesh	1,081
268	2	1	0,14	80	40	Upright	U	Full	0,622
269	2	1	0,14	40	40	Flat	U	Mesh	0,726
270	2	1	0,09	80	30	Edge	Kh	Full	0,984

The effects of continuous and categorical parameters on the charpy impact test are demonstrate in (Figures 4&5). The impact strength data is inversely proportional to the layers thickness. It was concluded that the main reason behind this is that the smaller the diameter of the filament at the nozzle exit, the stronger the adhesion will be, as the surface area of adhesion to the previous layers will increase. Also, a thinner filament will create a tighter texture. In terms of charpy impact energy absorption, the high-odrer value charpy impact energy absorption was achieved with a layer thickness of 0.09 mm. In terms of layer thickness, the lowest impact energy absorption values were obtained at a layer thickness of 0.19 mm. The highest impact energy value absorption was obtained as 0.844 kj/m2 at 0.09 mm layer thickness. The results regarding the layer thickness are compatible with the searches in the literature [32,54,55].

When the effects of print speed on the charpy impact test data were commented and seen that most noteworthy results was at the median value of 60 mm/s. It was concluded that the main reason behind this is that the slow and fast writing process affects the adhesion and therefore the impact test value due to the cooling of the surface. The maximal charpy impact energy absorption was obtained as 0.803 kj/m2 at 60 mm/s printing speed. The results regarding the layer thickness are compatible with the

searches in the literature [54,55].

When the support angle values were commented and seen that the best outcomes were achieved at 30° degrees. The difference between the support angle of 20° and 40° with the filament reveals the fact that the adhesion decreases. The highest charpy impact energy absorption was obtained as 0.803 kj/m2 at 60 mm/s printing speed.

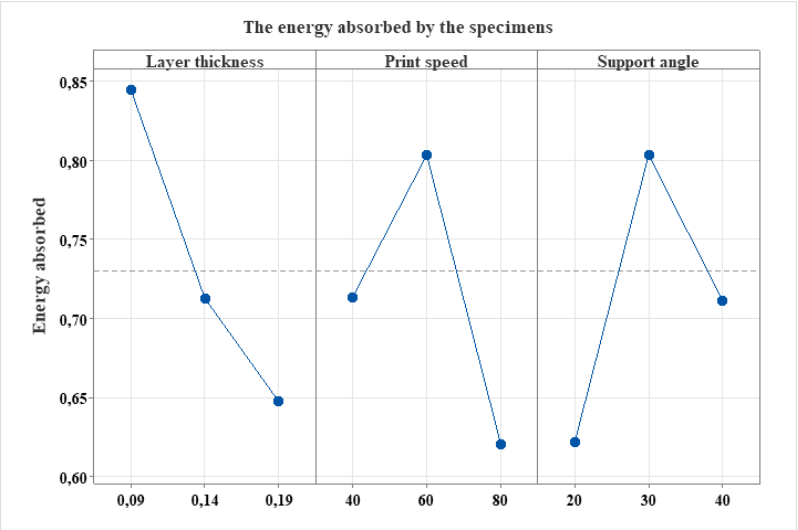

Figure 4. Main effects plot for continious parameters

When the effect of categorical parameters is examined in Fig. 5, it gave extremely good results on the edge charpy impact test data from the build orientation values. Here, when the build orientation is considered together with the notch type, the edge gave good results because it is the surface that meets the impact load. Flat positioning followed this. Upright, where the samples were produced vertically, gave the weakest impact values due to both the oscillations during production and the elevation on a low cross-sectional area. The maximal charpy impact energy absorption was obtained as 0.841 kj/m^2 at edge position. The results regarding the build orientation are compatible with the searches in the literature [22,29,56].

When notch type was examined, the highest charpy impact values were obtained in U type samples. This result can be explained as U-section absorbs the impact force by spreading it over a wide surface. The keyhole cutout also gave relatively good results. Again, the section where the impact force is distributed has gained importance here as well. The highest impact energy absorption was obtained as 0.827 kj/m^2 at U notch type. The results regarding the layer thickness are compatible with the searches in the literature [18].

When the filling type is examined, as expected, the full filling type revealed the best results compared to the mesh filling type. The highest impact energy absorption was obtained as 0.777 kj/m^2 at full infill type. The results regarding the layer thickness are compatible with the searches in the literature [18,22].

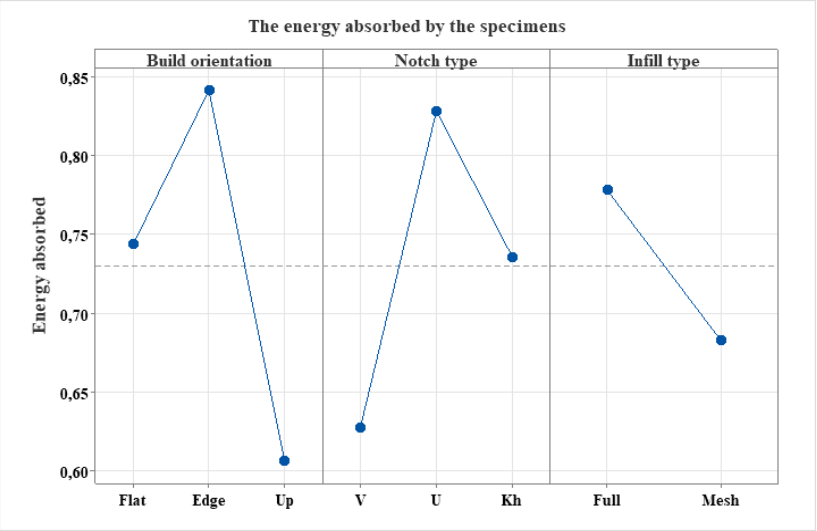

Figure 5. Main effects plot for categorical parameters

The r^2 value of the model emerging with the Box-behnken method is 0.9529. However, the estimated and adjusted r^2 values were revealed as 0.9454 and 0.9377. These numerical results demonstrated that there is a statistical highly remarkable fit in the box behnken model (Table 3).

Table 3. Model R results

S	R:sq	R:sq(adj)	R:sq(pred)
0,0453935	95,29%	94,54%	93,77%

ANOVA after charpy test is presented in (Table 4). The F result of the model obtained in ANOVA was 126.81 and a remarkable effect rate of 95.29% was obtained. In addition, with p values of the model being <0.05, it was unveiled that the model was statistically significant in terms of both linear and square values, with all continuous and categorical variables. According to ANOVA, the most effective parameters on the charpy results were build direction (24.69%) and notch type (17.81%).

Table 4. ANOVA for Process Parameters

Source	DF	Adj:SS	Adj:MS	F:Value	P:Value	Contribution
Model.	37	9,6682	0,26130	126,81	0,000	95,29%
Linear.	8	6,9118	0,86398	419,29	0,000	68,12%
Layer thickness	1	1,3926	1,39260	675,83	0,000	13,73%
Print speed	1	0,3111	0,31109	150,97	0,000	3,07%
Support angle	1	0,2878	0,28783	139,69	0,000	2,84%
Build orientation	2	2,5055	1,25277	607,97	0,000	24,69%
Notch type	2	1,8066	0,90331	438,38	0,000	17,81%
Infill type	1	0,6081	0,60814	295,13	0,000	5,99%
Square	3	2,7054	0,90179	437,64	0,000	26,66%
*Layer thickness*Layer thickness*	1	0,0100	0,00995	4,83	0,029	0,73%
*Print speed*Print speed*	1	1,4164	1,41642	687,39	0,000	11,96%
*Support angle*Support angle*	1	1,4178	1,41777	688,05	0,000	13,97%
2-Way Interaction	26	0,0510	0,00196	0,95	0,536	0,50%
Layer thickness Print speed*	1	0,0003	0,00028	0,14	0,713	0,00%
Layer thickness Support angle*	1	0,0023	0,00235	1,14	0,287	0,02%
Layer thickness Build orientation*	2	0,0019	0,00096	0,46	0,629	0,02%
Layer thickness Notch type*	2	0,0009	0,00044	0,21	0,807	0,01%
*Layer thickness*Infill type*	1	0,0000	0,00000	0,00	0,975	0,00%
*Print speed*Support angle*	1	0,0046	0,00462	2,24	0,135	0,05%
*Print speed*Build orientation*	2	0,0061	0,00307	1,49	0,227	0,06%
*Print speed*Notch type*	2	0,0118	0,00590	2,86	0,059	0,12%
*Print speed*Infill type*	1	0,0024	0,00236	1,15	0,286	0,02%
*Support angle*Build orientation*	2	0,0034	0,00169	0,82	0,441	0,03%
*Support angle*Notch type*	2	0,0004	0,00020	0,10	0,907	0,00%
*Support angle*Infill type*	1	0,0006	0,00059	0,29	0,592	0,01%
*Build orientation*Notch type*	4	0,0012	0,00030	0,15	0,965	0,01%
*Build orientation*Infill type*	2	0,0133	0,00667	3,24	0,041	0,13%
*Notch type*Infill type*	2	0,0017	0,00086	0,42	0,659	0,02%
Error	232	0,4781	0,00206			4,71%
Lack-of-Fit	196	0,3451	0,00176	0,48	0,999	3,40%
Pure Error	36	0,1329	0,00369			1,31%
Total	269	10,1462				100,00%

3.2 Optimization with artificial intelligence (AI)

Using these experimental data, ELM and DL prediction models were created. Before starting the analysis, dependent variables were not normalized, but independent variables were normalized in the [0,1] range. Normalization was applied to the data in both methods (DL and ELM). Sigmoid was applied as activation function in ELM. In ELM, the number hidden layer is set as 1. Eight different values were set for the number of neurons in the hidden layers (Table 5). 90% of the data was utilised for training the models and the of those who remain 10% was reserved for testing (Table 5). In DL, adam and rmsprop were applied as optimization algorithms, tanh, sigmoid and relu were applied as activation functions. In DL, the number of hidden layer is 3 and the number neurons in each hidden layer is 6 and 12. In DL, as in ELM, 90% of the data was utilised for training the models and the of those who remain 10% was reserved for testing. Epochs was set to 1000 (Table 5).

Table 5. DL and ELM parameters

AI Parameters	**DL**	**Basic ELM**	**P/ELM**	**OP/ELM**
Optimization Algorithms	Adam and Rmsprop	-	-	-
Normalization method	Min/Max Scaling	Min/Max Scaling	Min/Max Scaling	Min/Max Scaling
Activation Function for Input Layer	Relu, tanh, sigmoid	sigmoid	sigmoid	sigmoid
Activation Function for Output Layer	-	linear	linear	linear
Input Layer Neurons	6	6	6	6
Output Layer Neurons	1	6	6	6
Hidden Layers	3	1	1	1
Hidden-1 Layer Neurons	6;12	6;12;18;24	30;60;90;120	30;60;90;120
Hidden-2 Layer Neurons	6;12	-	-	-
Hidden-3 Layer Neurons	6;12	-	-	-
DL Learning Rate	0,001			
Batch Size	16			
Training data size	0,9	0,9	0,9	0,9
Test data size	0,1	0,1	0,1	0,1
Epochs for DL	1000	-	-	-

In this AI analysis, 96 trial runs were performed with DL parameters and 45 trial runs were performed with ELM parameters. The architectures of the AI (DL and ELM) models proposed as a result of these runs are presented in (Figures 6&7).

The max. dynamic results of DL were determined by the mean square error. Here, the best results were obtained under the following conditions. Adam as the optimization algorithm, tanh as the activation function, the number of hidden layers 3 and the number of neurons 6, 6 and 6. The architectural design of the DL model is shown in (Figure 6).

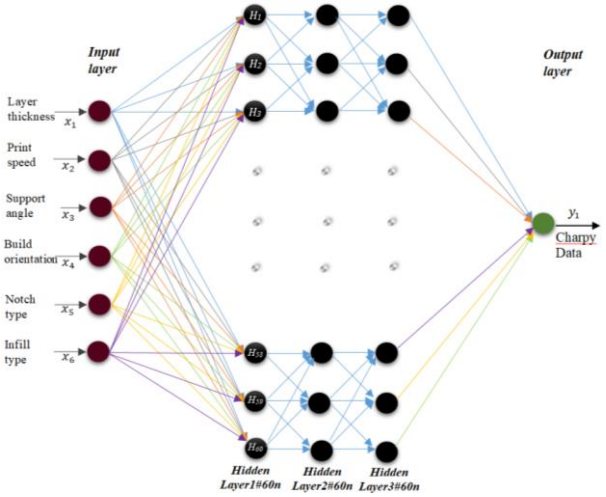

Figure 6. DL architecture of this study

The ELM model used in the research is demonstrated in (Figure 7). In ELM, the activation function is sigmoid at the input layer and linear at the output. In ELM, the best MSE results were obtained with 180 neurons in the hidden layer Optimally Pruned Extreme Learning Machine (OP-ELM).

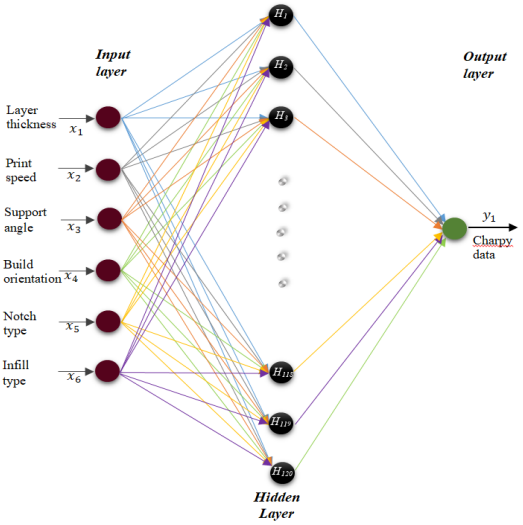

Figure 7. ELM architecture of this study

In this study, prediction models for ELM and DL were created using the Charpy test. The optimal MSE value in ELM was calculated as 0.00173 and r squared value as 0.96178. These results were obtained by using OP-ELM as the optimization algorithm and sigmoid as the activation function. The best MSE value in DL was calculated as 0.000923, and the r^2 as 0.974274. These results were obtained using adam as the optimization algorithm and tanh as the activation function. Some of the other activation functions were also tried in ELM. However, since remarkable results are usually obtained in the sigmoid function, the results of other activation functions were not taken into account. Therefore, sigmoid was included in all ELM trials. All results are demonstrated in (Table 6).

For the models presented in this study, it is demonstrated that both DL and ELM give very successful prediction results as efficient optimization, although DL results are relatively better. The proper choice of model for further research and analyses will vary depending on the data set and print parameters.

Depending on the results obtained, it has revealed that that different artificial intelligence optimization practice can be applied in optimizing the outputs obtained with different parameters. More importance, it has become clear that AI-based optimizations give remarkable predictions as all the results obtained in additive manufacturing.

Table 6. Result of DL and ELM

	Method	Optimization algorithms	Neuron Number	Activation function	MSE Training	MSE Test	r^2
Charpy data (kj/m²)	Deep Learning	Adam	(6,6,6)	Relu, Relu, Relu	0,014889	0,008906	0,78231
				Sigm., Sigm., Sigm.	0.018986	0.014021	0.609101
				tanh, tanh, tanh	0.001104	0.000923	***0.974274***
			(6,12,12)	Relu, Relu, Relu	0,001835	0,004677	0,88568
				Sigm., Sigm., Sigm.	0.01895	0.013402	0.626372
				tanh, tanh, tanh	0.001177	0.001948	0.945683
			(12,6,6)	Relu, Relu, Relu	0,00273	0,006389	0,84384
				Sigm., Sigm., Sigm.	0.015924	0.012803	0.643054
				tanh, tanh, tanh	0.00096	0.001744	0.951383
			(12,12,12)	Relu, Relu, Relu	0,001431	0,005228	0,87221
				Sigm., Sigm., Sigm.	0.017581	0.012305	0.656941
				tanh, tanh, tanh	0,000768	0,001786	0,95020
		RmsProp	(6,6,6)	Relu, Relu, Relu	0,009848	0,011644	0,7154
				Sigm., Sigm., Sigm.	0.018496	0.014314	0.60093
				tanh, tanh, tanh	0.003434	0.003451	0.903795
			(6,12,12)	Relu, Relu, Relu	0,008579	0,010829	0,73532
				Sigm., Sigm., Sigm.	0.01887	0.014302	0.601273
				tanh, tanh, tanh	0.002399	0.00294	0.918035
			(12,6,6)	Relu, Relu, Relu	0,002074	0,003994	0,90237
				Sigm., Sigm., Sigm.	0.017955	0.012302	0.657039
				tanh, tanh, tanh	0.001972	0.002593	0.927714
			(12,12,12)	Relu, Relu, Relu	0,002517	0,010966	0,73196
				Sigm., Sigm., Sigm.	0.019488	0.01361	0.620579
				tanh, tanh, tanh	0,003791	0,004205	0,88277
	Extreme Learning Machines	Basic ELM	6	Sigmoid	0.014242	0.012677	0.646567
			12		0.012794	0.012072	0.663446
			18		0.007343	0.003898	0.891334
			24		0.009754	0.010598	0.704544
			48		0.001341	0.002177	***0.94304***
		P-ELM	30	Sigmoid	0.006035	0.007112	0.801723
			60		0.001037	0.002518	0.929812
			90		0.001004	0.002458	***0.94548***
			120		0.001161	0.003248	0.909447
			180		0.002334	0.003001	0.916346
		OP-ELM	30	Sigmoid	0.006506	0.00452	0.873975
			60		0.001254	0.002273	0.936618
			90		0.000908	0.004553	0.873054
			120		0.000539	0.002201	0.938638
			180		0.000563	0.00173	***0.96178***

Comparisons of the predicted values achieved in the ELM and DL models with the values achieved in the experiments are displayed in (Figures 8&9). In the graphs, Red-dashed line demonstrate the predicted data of the best model, and black-solid line demonstrate the actual data. When figures are analyzed in detail, the data of the proposed models revealed results very close to the original data.

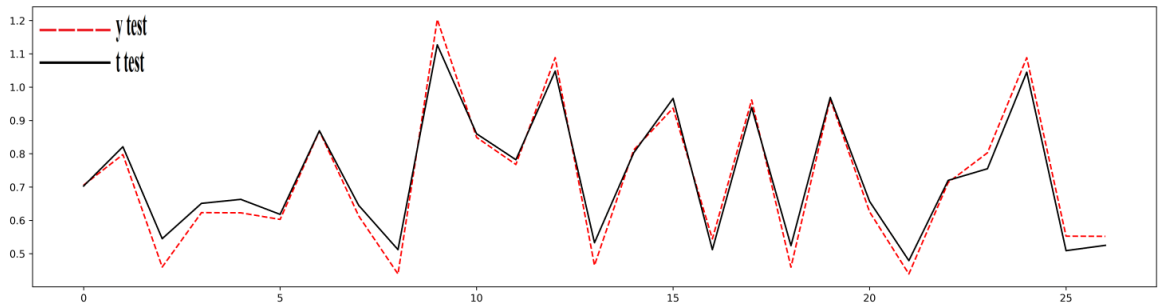

Figure 8. DL's original data vs. model output comparison chart in terms of best test MSE Value

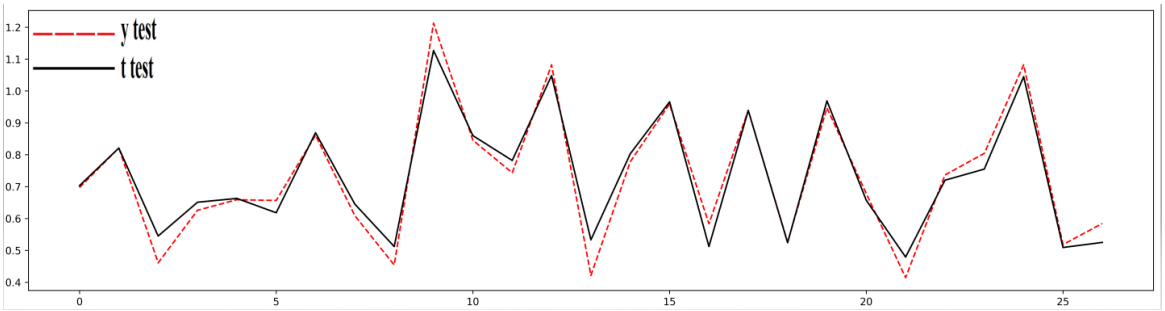

Figure 9. OP-ELM's original data vs. model output comparison chart in terms of best test MSE Value

4. Conclusion

In the study, charpy impact tests were investigated out to determine the energy absorption of the specimens produced by the 3D-FDM method. In this study, notch impact specimens were produced from ABS material in a 3D printer using the experimental design box behnken RSM method in the first stage. Then, charpy tests were performed on the AOB brand impact tester and all the data achieved were analyzed in the Minitab-21 software program. In the context of these conclusions achieved in the next stage, a model is presented with DL and ELM methods from these data. All the conclusions of the research are as follows;

• Charpy impact test data decreased with the increase in layer thickness values. A thinner filament is expected to produce a tighter texture. Among all experiments, the maximal charpy impact energy absorption was obtained as 0.844 kj/m^2 at a layer thickness of 0.09 mm.

• The effects of printing speed on the charpy impact test data were analysed and It has been seen that the best impressive result was obtained at 60 mm/s. It is thought that the slow and fast printing process affects the adhesion and thus the impact test value due to the cooling of the surface. The maximal charpy impact energy absorption was obtained as 0.803 kj/m^2 at 60 mm/s printing speed.

• Support angle values were analysed and the optimal results were achieved at 30°. The maximal charpy energy absorption was obtained as 0.803 kj/m^2 at 30° support angle.

• Build orientation values showed extremely effective results on edge charpy impact test data. When the build orientation is considered together with the notch type, the good results of the edge can be explained more because it is the surface that meets the impact load. The maximal charpy impact energy absorption was obtained as 0.841 kj/m^2 at edge position.

• When Notch type was examined, the highest charpy values were obtained in U type samples. The keyhole cut out also gave relatively good results. The maximal charpy impact energy absorption was obtained as 0.827 kj/m^2 at U notch type.

• As the filling type, the full filling type showed the best results compared to the mesh filling type. The maximal charpy impact energy absorption was obtained as 0.777 kj/m^2 at full infill type.

• In DL, adam was applied as the optimization algorithm and tanh as the activation func. The number

of hidden layer in the runs that gave good results in the analysis was 3. 10% of the data was used for testing. DL, MSE value was calculated as 0.000923 and r square value as 0.97427.

• The activation func. utilized in ELM is sigmoid for input and linear for output. In ELM, the best (MSE) results were obtained with 180 neurons in the hidden layer (OP-ELM). In ELM, the best MSE result was calculated as 0.00173 and r^2 value as 0.96178. The results showed that the OP-ELM optimization algorithm resulted in an effective ELM model when the activation function was in the sigmoid.

• For the models put forward this study, although the DL results are relatively better, it shows that both DL and ELM give very successful prediction results as the effective optimization. It is concluded that different artificial intelligence methods can be applied to optimize the outputs obtained with different parameters in each case.

Acknowledgements

Due to the great earthquakes that occurred in Turkey on February 6 and turned our lives upside down; I would like to express my gratitude and gratitude to the Deanship and management of 19 Mayıs University Faculty of Engineering for the academic working environment and opportunities they provided us.

Conflict of Interest Statement

The authors declare that there is no conflict of interest

Data availability

All the raw data of analysis are available as supplementary data. Any other data generated or analyzed during this study are available from the corresponding authors on reasonable request.
https://docs.google.com/spreadsheets/d/1cixYHjxhKUULWqhSZXMj9zqqpahjtSH9/edit?usp=sharing&ouid=104439447976128858155&rtpof=true&sd=true

References

[1] G. D. Goh, S. Agarwala, G. L. Goh, V. Dikshit, S. L. Sing, and W. Y. Yeong, "Additive manufacturing in unmanned aerial vehicles (UAVs): Challenges and potential," *Aerospace Science and Technology,* vol. 63, pp. 140–151, 2017, doi:10.1016/j.ast.2016.12.019

[2] M. D. Monzón, Z. Ortega, A. Martínez, and F. Ortega, "Standardization in additive manufacturing: activities carried out by international organizations and projects," *The International Journal of Advanced Manufacturing Technology,* vol. 76, no. 5–8, pp. 1111–1121, 2015, doi:10.1007/s00170-014-6334-1

[3] C. Palanisamy, R. Raman, and P. kumar Dhanraj, "A review on mechanical properties of polyjet and FDM printed parts," *Additive Manufacturing,* vol. 79, no. 9. Springer Berlin Heidelberg, 2022. doi:10.1007/s00289-021-03899-0

[4] S. Singh, S. Ramakrishna, and R. Singh, "Material issues in additive manufacturing: A review," *Journal of Manufacturing Processes.*, vol. 25, pp. 185–200, Jan. 2017. doi:10.1016/j.jmapro.2016.11.006

[5] S. Pattnaik, P. K. Jha, and D. B. Karunakar, "A review of rapid prototyping integrated investment casting processes," *Proceedings of the Institution of Mechanical Engineers, Part L: Journal of Materials: Design and Applications,* vol. 228, no. 4, pp. 249–277, Oct. 2014. doi:10.1177/1464420713479257

[6] N. Anwer, B. Schleich, L. Mathieu, and S. Wartzack, "From solid modelling to skin model shapes: Shifting paradigms in computer-aided tolerancing," *CIRP Annals - Manufacturing Technology*, vol. 63, no. 1, pp. 137–140, 2014. doi:10.1016/j.cirp.2014.03.103

[7] S. H. Chiu, K. T. Chen, S. T. Wicaksono, J. R. Tsai, and S. H. Pong, "Process parameters optimization for area-forming rapid prototyping system," *Rapid Prototyping Journal*, vol. 21, no. 1, pp. 70–78, Jan. 2015. doi:10.1108/RPJ-12-2012-0114

[8] K. L. Alvarez C., R. F. Lagos C., and M. Aizpun, "Investigating the influence of infill percentage on the mechanical properties of fused deposition modelled ABS parts," *Ingenieria e Investigacion*, vol. 36, no. 3, pp. 110–116, 2016. doi:10.15446/ing.investig.v36n3.56610

[9] P. Mantada, R. Mendricky, and J. Safka, "Parameters influencing the precision of various 3D printing technologies," *MM Science Journal,* vol. 2017, no. December, pp. 2004–2012, 2017. doi:10.17973/MMSJ.2017_12_201776

[10] R. V. Aroca, C. E. H. Ventura, I. De Mello, and T. F. P. A. T. Pazelli, "Sequential additive manufacturing: automatic manipulation of 3D printed parts," *Rapid Prototyping Journal,* vol. 23, no. 4, pp. 653–659, Jun. 2017. doi:10.1108/RPJ-02-2016-0029

[11] L. Cheng, P. Zhang, E. Biyikli, J. Bai, J. Robbins, and A. To, "Efficient design optimization of variable-density cellular structures for additive manufacturing: theory and experimental validation," *Rapid Prototyping Journal*, vol. 23, no. 4, pp. 660–677, Jun. 2017. doi:10.1108/RPJ-04-2016-0069

[12] A. Haryńska, H. Janik, M. Sienkiewicz, B. Mikolaszek, and J. Kucińska-Lipka, "PLA-Potato Thermoplastic Starch Filament as a Sustainable Alternative to the Conventional PLA Filament: Processing, Characterization, and FFF 3D Printing," *ACS Sustainable Chemistry and Engineeering,* vol. 9, no. 20, pp. 6923–6938, 2021. doi:10.1021/acssuschemeng.0c09413

[13] B. D. de Castro, F. de C. Magalhães, T. H. Panzera, and J. C. Campos Rubio, "An Assessment of Fully Integrated Polymer Sandwich Structures Designed by Additive Manufacturing," *Journal of Materials Engineering and Performance*, vol. 30, no. 7, pp. 5031–5038, 2021. doi:10.1007/s11665-021-05604-8

[14] J. Andrzejewski, K. Grad, W. Wiśniewski, and J. Szulc, "The use of agricultural waste in the modification of poly(Lactic acid)-based composites intended for 3d printing applications. the use of toughened blend systems to improve mechanical properties," *Journal of Composites Science*, vol. 5, no. 10, 2021. doi:10.3390/jcs5100253

[15] M. Q. Tanveer, A. Haleem, and M. Suhaib, "Effect of variable infill density on mechanical behaviour of 3-D printed PLA specimen: an experimental investigation," *SN Applied Science,* vol. 1, no. 12, p. 1701, Dec. 2019. doi:10.1007/s42452-019-1744-1

[16] M. A. Caminero, J. M. Chacón, I. García-Moreno, and G. P. Rodríguez, "Impact damage resistance of 3D printed continuous fibre reinforced thermoplastic composites using fused deposition modelling," *Composites Part B: Engineering,* vol. 148, no. April, pp. 93–103, 2018. doi:10.1016/j.compositesb.2018.04.054

[17] I. Fekete, F. Ronkay, and L. Lendvai, "Highly toughened blends of poly(lactic acid) (PLA) and natural rubber (NR) for FDM-based 3D printing applications: The effect of composition and infill pattern," *Polymer Testing,* vol. 99, 2021. doi:10.1016/j.polymertesting.2021.107205

[18] S. Korga, M. Barszcz, and L. Zgryza, "The effect of the 3D printout filling parameter on the impact strength of elements made with the FDM method," *IOP Conference Series: Materials Science and Engineering,,* vol. 710, no. 1, 2019. doi:10.1088/1757-899X/710/1/012027
[19] H. Hadidi et al., "Low velocity impact of ABS after shot peening predefined layers during additive manufacturing," *Procedia Manufacturing,* vol. 34, pp. 594–602, 2019. doi:10.1016/j.promfg.2019.06.169

[20] A. K. Sood, R. K. Ohdar, and S. S. Mahapatra, "Improving dimensional accuracy of Fused Deposition Modelling processed part using grey Taguchi method," *Materials and Design*, vol. 30, no. 10, pp. 4243–4252, Dec. 2009. doi:10.1016/j.matdes.2009.04.030

[21] B. Ameri, F. Taheri-Behrooz, and M. R. M. Aliha, "Mixed-mode tensile/shear fracture of the additively manufactured components under dynamic and static loads," *Engineering Fracture Mechanics*, vol. 260, no. July 2021. p. 108185, 2022, doi:10.1016/j.engfracmech.2021.108185

[22] D. R. Hetrick, S. H. R. Sanei, O. Ashour, and C. E. Bakis, "Charpy impact energy absorption of 3D printed continuous Kevlar reinforced composites," *Journal of Composite Materials*, vol. 55, no. 12, pp. 1705–1713, 2021. doi:10.1177/0021998320985596

[23] S. Kontárová et al., "Printability, mechanical and thermal properties of poly(3-hydroxybutyrate)-poly(lactic acid)-plasticizer blends for three-dimensional (3D) printing," *Materials (Basel).,* vol. 13, no. 21, pp. 1–28, 2020. doi:10.3390/ma13214736

[24] R. A. García-León, M. Rodríguez-Castilla, and W. Quintero-Quintero, "Experimental Analysis of Impact Resistance of 3D Polycarbonate and Nylon + Carbon Fiber Specimens," *Journal of Materials Engineering and Performance*, vol. 30, no. 7, pp. 4837–4847, 2021. doi:10.1007/s11665-020-05422-4

[25] V. Figueroa-Velarde et al., "Mechanical and physicochemical properties of 3d-printed agave fibers/poly(Lactic) acid biocomposites," *Materials (Basel).,* vol. 14, no. 11, 2021. doi:10.3390/ma14113111

[26] F. Ning, W. Cong, Y. Hu, and H. Wang, "Additive manufacturing of carbon fiber-reinforced plastic composites using fused deposition modeling: Effects of process parameters on tensile properties," *Journal of Composite Materials*, vol. 51, no. 4, pp. 451–462, 2017. doi: 10.1177/0021998316646169

[27] N. Sa'ude, S. H. Masood, M. Nikzad, and M. Ibrahim, "Dynamic Mechanical Properties of Copper-ABS Composites for FDM Feedstock," *Int. J. Eng. Res. Appl.,* vol. 3, no. 3, pp. 1257–1263, 2013. [Online]. Available: http://scholar.google.com/scholar?hl=en&btnG=Search&q=intitle:Dynamic+Mechanical+Properties+of+Copper-ABS+Composites+for+FDM+Feedstock#0

[28] M. Samykano, S. K. Selvamani, K. Kadirgama, W. K. Ngui, G. Kanagaraj, and K. Sudhakar, "Mechanical property of FDM printed ABS: influence of printing parameters," *The International Journal of Advanced Manufacturing Technology*, vol. 102, no. 9–12, pp. 2779–2796, 2019. doi:10.1007/s00170-019-03313-0

[29] S. Abid, R. Messadi, T. Hassine, H. Ben Daly, J. Soulestin, and M. F. Lacrampe, "Optimization of mechanical properties of printed acrylonitrile butadiene styrene using RSM design," *The International Journal of Advanced Manufacturing Technology*, vol. 100, no. 5–8, pp. 1363–1372, 2019. doi:10.1007/s00170-018-2710-6

[30] A. Garg, A. Bhattacharya, and A. Batish, "Chemical vapor treatment of ABS parts built by FDM: Analysis of surface finish and mechanical strength," *The International Journal of Advanced Manufacturing Technology,* vol. 89, no. 5–8, pp. 2175–2191, 2017. doi:10.1007/s00170-016-9257-1

[31] S. Khabia and K. K. Jain, "Comparison of mechanical properties of components 3D printed from different brand ABS filament on different FDM printers," *Materials Today: Proceedings*, vol. 26, pp. 2907–2914, 2019. doi:10.1016/j.matpr.2020.02.600

[32] S. Khabia and K. K. Jain, "Influence of change in layer thickness on mechanical properties of components 3D printed on Zortrax M 200 FDM printer with Z-ABS filament material & Accucraft i250+ FDM printer with low cost ABS filament material," *Materials Today: Proceedings*, vol. 26, pp. 1315–1322, 2019. doi:10.1016/j.matpr.2020.02.268

[33] C. Szegedy *et al.*, "Going deeper with convolutions," *2015 IEEE Conference on Computer Vision and Pattern Recognition (CVPR)*, Boston, MA, USA, 2015, pp. 1-9, doi: 10.1109/CVPR.2015.7298594.

[34] J. Redmon, S. Divvala, R. Girshick and A. Farhadi, "You Only Look Once: Unified, Real-Time Object Detection," *2016 IEEE Conference on Computer Vision and Pattern Recognition (CVPR)*, Las Vegas, NV, USA, 2016, pp. 779-788, doi: 10.1109/CVPR.2016.91.

[35] H. Tercan and T. Meisen, "Machine learning and deep learning based predictive quality in manufacturing: a systematic review," *Journal of Intelligent Manufacturing*, vol. 33, no. 7, pp. 1879–1905, Oct. 2022. doi:10.1007/s10845-022-01963-8

[36] B. Ma, X. Ban, H. Huang, Y. Chen, W. Liu, and Y. Zhi, "Deep Learning-Based Image Segmentation for Al-La Alloy Microscopic Images," *Symmetry (Basel).*, vol. 10, no. 4, p. 107, Apr. 2018. doi:10.3390/sym10040107

[37] P. Oborski and P. Wysocki, "Intelligent Visual Quality Control System Based on Convolutional Neural Networks for Holonic Shop Floor Control of Industry 4.0 Manufacturing Systems," *Advances in Science and Technology Research Journal, vol. 16,* no. 2, pp. 89–98, Apr.2022.doi:10.12913/22998624/145503

[38] W.-J. Lin, S.-H. Lo, H.-T. Young, and C.-L. Hung, "Evaluation of Deep Learning Neural Networks for Surface Roughness Prediction Using Vibration Signal Analysis," *Applied Sciences*, vol. 9, no. 7, pp. 1462, Apr. 2019. doi:10.3390/app9071462

[39] Y. Pan, R. Kang, Z. Dong, W. Du, S. Yin, and Y. Bao, "On-line prediction of ultrasonic elliptical vibration cutting surface roughness of tungsten heavy alloy based on deep learning," *Journal of Intelligent Manufacturing*, vol. 33, no. 3, pp. 675–685, Mar. 2022. doi:10.1007/s10845-020-01669-9

[40] Z. Li, Z. Zhang, J. Shi, and D. Wu, "Prediction of surface roughness in extrusion-based additive manufacturing with machine learning," *Robotics and Computer-Integrated Manufacturing*, vol. 57, no. October 2018, pp. 488–495, Jun. 2019. doi:10.1016/j.rcim.2019.01.004

[41] N. Dimitriou et al., "Fault Diagnosis in Microelectronics Attachment Via Deep Learning Analysis of 3-D Laser Scans," *IEEE Transactions on Industrial Electronics*, vol. 67, no. 7, pp. 5748–5757, Jul. 2020. doi:10.1109/TIE.2019.2931220

[42] J. P. Yun, W. C. Shin, G. Koo, M. S. Kim, C. Lee, and S. J. Lee, "Automated defect inspection system for metal surfaces based on deep learning and data augmentation," *Journal of Manufacturing Systems,* vol. 55, no. May 2019, pp. 317–324, Apr. 2020. doi:10.1016/j.jmsy.2020.03.009

[43] J. Zhang, P. Wang, and R. X. Gao, "Deep learning-based tensile strength prediction in fused deposition modeling," *Computers in Industry,* vol. 107, pp. 11–21, May 2019. doi:10.1016/j.compind.2019.01.011

[44] A. Essien and C. Giannetti, "A Deep Learning Model for Smart Manufacturing Using Convolutional LSTM Neural Network Autoencoders," *IEEE Transactions on Industrial Informatics*, vol. 16, no. 9, pp. 6069–6078, Sep. 2020. doi:10.1109/TII.2020.2967556

[45] G. Serin, B. Sener, A. M. Ozbayoglu, and H. O. Unver, "Review of tool condition monitoring in machining and opportunities for deep learning," *The International Journal of Advanced Manufacturing Technology,* vol. 109, no. 3–4, pp. 953–974, Jul. 2020. doi:10.1007/s00170-020-05449-w

[46] Q. Wang, W. Jiao, P. Wang, and Y. Zhang, "A tutorial on deep learning-based data analytics in manufacturing through a welding case study," *Journal of Manufacturing Processes,* vol. 63, pp. 2–13, Mar. 2021, doi:10.1016/j.jmapro.2020.04.044

[47] L. Cardoso Silva et al., "Benchmarking Machine Learning Solutions in Production," in *2020 19th IEEE International Conference on Machine Learning and Applications (ICMLA)*, pp. 626–633, Dec. 2020. doi:10.1109/ICMLA51294.2020.00104

[48] S. Klein, S. Schorr, and D. Bähre, "Quality Prediction of Honed Bores with Machine Learning Based on Machining and Quality Data to Improve the Honing Process Control," *Procedia CIRP,* vol. 93, pp. 1322–1327, 2020. doi:10.1016/j.procir.2020.03.055

[49] G. Huang, T. Liu, Y. Yang, Z. Lin, S. Song, and C. Wu, "Discriminative clustering via extreme learning machine," *Neural Networks,* vol. 70, pp. 1–8, Oct. 2015. doi:10.1016/j.neunet.2015.06.002

[50] G. Huang, G. Bin Huang, S. Song, and K. You, "Trends in extreme learning machines: A review," *Neural Networks*, vol. 61, pp. 32–48, 2015. doi:10.1016/j.neunet.2014.10.001

[51] T. Liu, C. K. Liyanaarachchi Lekamalage, G. Bin Huang, and Z. Lin, "Extreme Learning Machine for Joint Embedding and Clustering," *Neurocomputing*, vol. 277, pp. 78–88, 2018. doi:10.1016/j.neucom.2017.01.115

[52] Y. Wang, Z. Xie, K. Xu, Y. Dou, and Y. Lei, "An efficient and effective convolutional auto-encoder extreme learning machine network for 3d feature learning," *Neurocomputing*, vol. 174, pp. 988–998, 2016. doi:10.1016/j.neucom.2015.10.035

[53] Z. Chen, D. Li, and W. Zhou, "Process parameters appraisal of fabricating ceramic parts based on stereolithography using the Taguchi method," *Proceedings of the Institution Mechanical Engineers, Part B: Journal Engineering Manufacture,* vol. 226, no. 7, pp. 1249–1258, Jul. 2012. doi:10.1177/0954405412442607

[54] C. Palanisamy, R. Raman, and P. kumar Dhanraj, "Additive manufacturing: a review on mechanical properties of polyjet and FDM printed parts," *Polymer Bulletin,* vol. 79, no. 9, pp. 7065–7116, Sep. 2022. doi:10.1007/s00289-021-03899-0

[55] M. Ramesh and K. Panneerselvam, "Mechanical investigation and optimization of parameter selection for Nylon material processed by FDM," *Materials Today: Proceedings,* vol. 46, pp. 9303–9307, 2019. doi:10.1016/j.matpr.2020.02.697

[56] K. Raney, E. Lani, and D. K. Kalla, "Experimental characterization of the tensile strength of ABS parts manufactured by fused deposition modeling process," *Materials Today: Proceedings*, vol. 4, no. 8, pp. 7956–7961, 2017. doi:10.1016/j.matpr.2017.07.132

This is an open access article under the CC-BY license

Conference Paper/Konferans Bildirisi

GAZİ
JOURNAL OF ENGINEERING SCIENCES

An Attempt for Price Comparison System

Emre Özakyıldız[a], Oğuzhan Menemencioğlu[*b], Adib Habbal[c]

Submitted: 20.11.2023 Revised: 25.12.2023 Accepted: 27.12.2023 doi:10.30855/gmbd.2023.0705N03

ABSTRACT

In the current landscape, product prices exhibit significant variations across diverse e-commerce platforms. Numerous price comparison websites have emerged to aid users in finding their desired products at the best prices. However, these systems face challenges such as irrelevant search results, outdated product prices, and accuracy issues. This study seeks to address these challenges by developing a user-friendly system. Our system comprises two components. JSoup is employed for data collection, while TF-IDF, SVD, and Cosine Similarity are integrated for product offerings. The proposed platform gathers data from reputable retailers, analyzes it to extract product information, and presents the findings to consumers. We evaluated the system's performance using real data obtained from various marketplaces. The results demonstrate that our system achieved an acceptable accuracy rate when compared to similar industrial solutions and relevant literature. Consequently, users are empowered to make more informed purchasing decisions, leveraging the capabilities provided by the proposed system.

Keywords: Price Comparison Website, Product Matching, Crawler, Scraper, User Centric, Web Application.

[a] Karabük University, Engineering Faculty, Dept. of Computer Engineering 78050 - Karabük, Türkiye
Orcid: 0009-0004-1568-4465
e mail: emreozakyildiz@gmail.com

[b,*] Karabük University, Engineering Faculty, Dept. of Computer Engineering 78050 - Karabük, Türkiye
Orcid: 0000-0002-4343-6563
e mail: omenemencioglu@karabuk.edu.tr

[c] Karabük University, Engineering Faculty, Dept. of Computer Engineering 78050 - Karabük, Türkiye
Orcid: 0000-0002-3939-2609

*Corresponding author: omenemencioglu@karabuk.edu.tr

Fiyat Karşılaştırma Sistemi Girişimi

ÖZ

Mevcut ortamda, ürün fiyatları çeşitli e-ticaret platformlarında önemli farklılıklar göstermektedir. Kullanıcıların istedikleri ürünleri en iyi fiyatlarla bulmalarına yardımcı olmak için çok sayıda fiyat karşılaştırma web sitesi ortaya çıkmıştır. Ancak bu sistemler alakasız arama sonuçları, güncel olmayan ürün fiyatları ve doğruluk sorunları gibi zorluklarla karşı karşıyadır. Bu çalışma, kullanıcı dostu bir sistem geliştirerek bu zorlukların üstesinden gelmeyi amaçlamaktadır. Sistemimiz iki bileşenden oluşmaktadır. Veri toplama için JSoup kullanılırken, ürün teklifleri için TF-IDF, SVD ve Kosinüs benzerliği entegre edilmiştir. Önerilen platform, saygın perakendecilerden veri toplamakta, ürün bilgilerini çıkarmak için analiz etmekte ve bulguları tüketicilere sunmaktadır. Sistemin performansını çeşitli pazar yerlerinden elde edilen gerçek verileri kullanarak değerlendirdik. Sonuçlar, sistemimizin benzer endüstriyel çözümler ve ilgili literatürle karşılaştırıldığında kabul edilebilir bir doğruluk oranına ulaştığını göstermektedir. Sonuç olarak, kullanıcılar önerilen sistem tarafından sağlanan yeteneklerden yararlanarak daha bilinçli satın alma kararları verme konusunda güçlendirilmiştir.

Anahtar Kelimeler: Fiyat Karşılaştırma Web Sitesi, Ürün Eşleştirme, Arama Robotu, Veri Toplayıcı, Kullanıcı Merkezli, Web Uygulama

To cite this article: E. Ozakyildiz, O. Menemencioglu and A. Habbal, "An Attempt for Price Comparator System" *Gazi Journal of Engineering Sciences,* vol.10, no.1, pp. 27-37, 2024. doi:10.30855/gmbd.0705N03

1. Introduction

When it comes to buying products from e-commerce websites, it can be a troublesome for customers to find the cheapest product across various markets. In recent years, many Price Comparison Websites (PCW) have appeared to make this task easier. In Türkiye, there are a few examples of PCW: while Akakce [1] and Cimri [2] compare e-commerce products, Trivago [3] offers the cheapest hotel prices worldwide. Both Akakce and Cimri provide various recommendation options, including unit price sorting, trends and top-rated offerings, to ensure customer satisfaction.

In order to PCW to provide such services, they need to gather up-to-date product data from several sources. The accuracy of product data, covering stock availability, the precision of price information, and exact matching of requested products, is of utmost importance. Additionally, the website's search mechanism holds a major role in its successful operation. Furthermore, tracking the price trends of products over time, allowing users to observe price changes across months, enhances the user experience.

The prominent tools such as web scrappers and web crawlers are used to gather current product information as raw data. In prior studies, diverse approaches have been employed both for web scraping and product matching. For web scraping, researchers such as Nagaraj et al., Shah et al., and Asawa et al. utilized the effective web scraping library BeautifulSoup4 [4-6]. Alternatively, Alam et al. employed the Python library Scrapy [7].

Table 1. Popular Scraper/Crawler Libraries

Library	Programming Language	Type	Strengths	Weaknesses
Scrapy	Python	Crawler	+ Full featured web crawling library. + Has detailed crawling abilities like spiders and link extractors.	- limited capability with Javascript (JS)
Apache Nutch	Java	Crawler	+ Comprehensive web crawling framework + Has its own data structure called Apache Hadoop. + Can work with additional related Apache libraries.	- Setting up an Apache Nutch project is complicated when compared with other Java crawlers.
Crawler4J	Java	Crawler	+ Has some of the crawling methods	- Required additional developer written code in demand. - Not up to date.
Puppeteer	Node.js	Scraper	+ JS based scraper so easily can be implemented in JS projects if there's no backend.	- focuses on JS only - there are unofficial ports for Python and PHP
Simple HTML DOM	PHP	Scraper	+ A simple parser for PHP projects. + quick and easy manipulation of HTML elements on small amount of element	- slow when working with large documents or many elements
Beautiful Soup	Python	Scraper	+ HTML/XML Parser library for Python with additional scraping features. + Has its own data structure to manipulate scraped data.	- It doesn't have any crawling ability.
Jaunt/Jauntium	Java	Scraper	+ A simple HTML parser for Java projects. + Jauntium version can handle pages with Javascript using Selenium (actually it is same but built in).	- No crawling features. - Not up to date.
Jsoup	Java	Scraper	+ Has detailed parsing abilities. It uses Document Object Model (DOM).	- Less selector support compared to other scraper libraries. - It doesn't have any crawling abilities.

Prasetyo opted for the Java library Jaunt for the scraping process and utilized the collected data in a K-means algorithm with varying cluster numbers. Notably, the use of ten clusters yielded superior results compared to five clusters [8]. Wang et al. harnessed Jsoup to collect web data, subsequently applying Pearson correlation to the scraped data, although, yielding a weak correlation [9]. In later works, Harikirshnan et al. studied Support Vector Machine (SVM) and compared their performance against Decision Trees and Random Forest algorithms [10]. Additionally, some studies explored alternative data delivery methods for web scraping and product similarity discovery, as demonstrated by Julian et al. [11]. Table 1 includes a comprehensive comparison of the common web scraping and crawler approaches. After analyzing the pros and cons, we conclude that the JSoup is most suitable Scraper library to integrate into our system when we consider the target market and amount of retrieved data.

Existing PCWs, exhibit shortcomings in providing accurate product information to users. Our testing revealed instances where the products offered by the seller market were either unavailable in source PCW or substantially differed from the user's expectations. Furthermore, when a user searches for a certain product, PCWs might list the wrong item, an item with a different price from the original market, or they might list sold-out products, as shown in Figure 1. Therefore, for PCW, there are certain open challenges namely irrelevant search results, outdated product prices, and accuracy issues that should be addressed in future work.

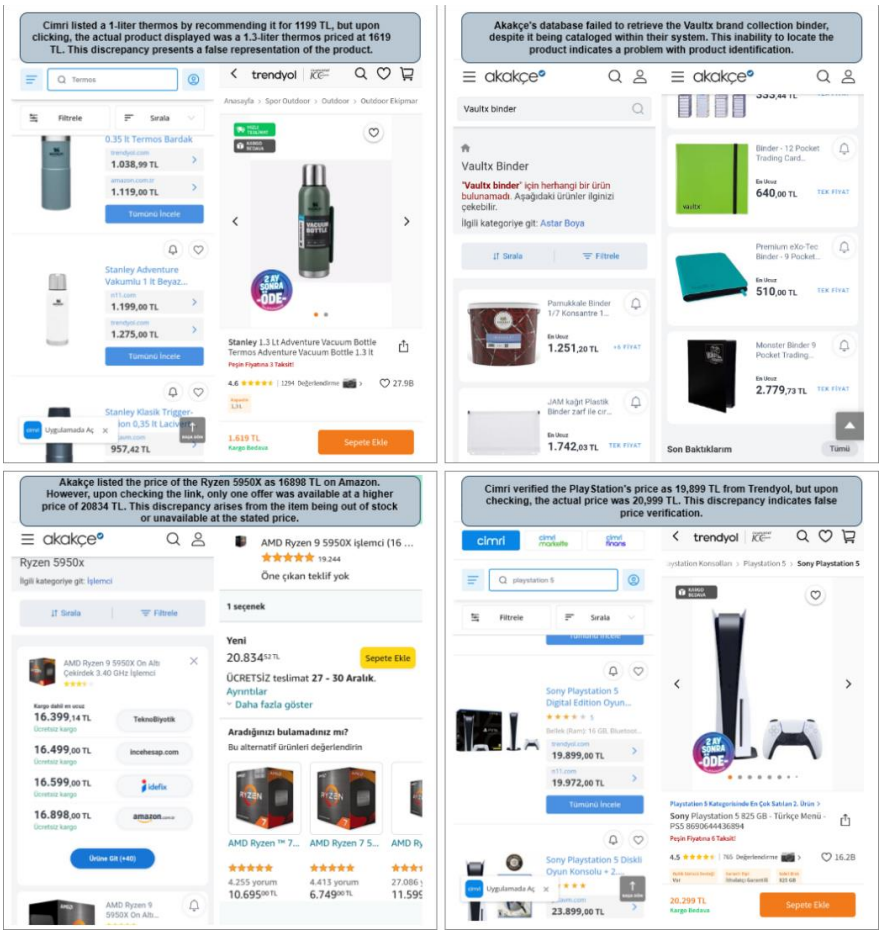

Figure 1. Issue for current PCWs in tested December 2023

The main goal of this study is to address the prevalent deficiencies observed in existing platforms. These deficiencies encompass inaccurate product availability listings, substantial discrepancies between listed and actual products, and the presentation of unreliable trend prices, all which compromise user confidence and satisfaction. In particular, we aim to develop a user-friendly price comparison system that provides accurate product information, an in-depth product trend analysis and ensures user satisfaction through the provision of precise product offerings.

2. Methods

In the design of the proposed system, there are two phases: Data Collection and Product Offering. Data collection process is handled by Java Spring backend. Meanwhile, the product offering is achieved by using Term Frequency - Inverse Document Frequency (TF-IDF), Singular Value Decomposition (SVD), and cosine similarity. The overall structure of the system from scraping process to product offering level is presented in the following subsections.

2.1. Data Collection

We used Jsoup to scrape products from three popular e-commerce websites: Trendyol (www.trendyol.com), A101 (www.a101.com.tr) and Migros (www.migros.com.tr). The pseudo code of our scraping service is stated in algorithm 1.

JSoup is used to index the categories and subcategories of each market. After the indexing process is completed, scraping is applied to extract products from subcategory pages. Each market has its own CSS selectors for product cards, which is why the scraper code is implemented individually for each market.

Since Migros and Trendyol heavily utilize JavaScript on their websites, JSoup was insufficient for scraping product information from the pages that had been crawled because such markets load price information by using frontend programming, which makes it hard to get price data from the website without running JavaScript code before the scrapping process. JSoup does not have a built-in web driver to run JS code. In that scenario, Selenium was used to execute JavaScript code on the page sources, and JSoup was employed to retrieve the page content afterward.

Algorithm 1: Web Scraping Pseudo Code

```
for each market in markets do
    for each category in market.categories do
        for each sub-category in category.subCategories do
            page <- JSoup.connect(market)
            products <- page.select(market.productCardCssSelectror)
            for each product in sub-category.products do
                new Product();
                Product.setProductName(product.select(marketSpecificNameSelector));
                Product.setProductLink(product. select(marketSpecificLinkSelector));
                Product.setProductPrice(product. select(marketSpecificPriceSelector));
                Product.setProductImage(product. select(marketSpecificImgSelector));
                Product.setSubCategory(sub-category);
                Product.setTimestamp(currentTimestamp);
                Product.save(Products);
            end for
        end for
    end for
end for
```

The Data Access Layer utilizes Java Persistence API (JPA) to efficiently store product information within the PostgreSQL database. This integration ensures effective data management and retrieval. Figure 2 is the database diagram that provides a visual representation of the project's data structure, illustrating the relationships and organization of the stored information.

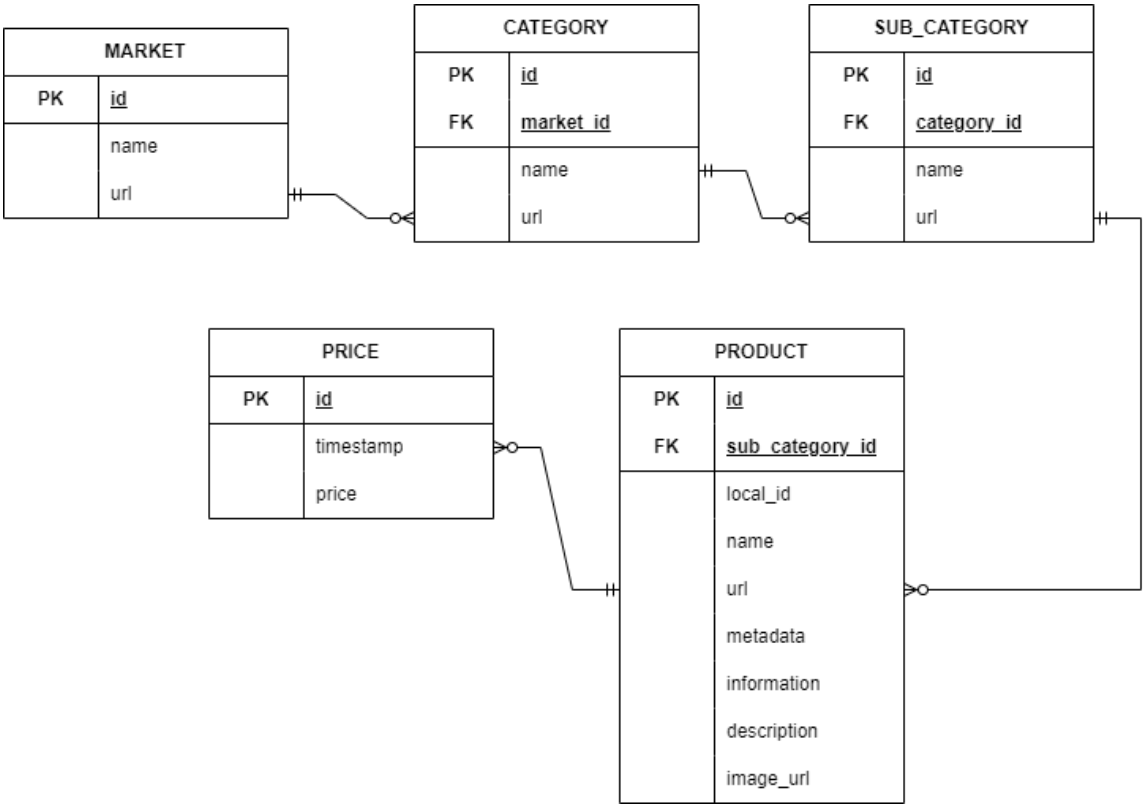

Figure. 2 ER Diagram of proposed system

2.2. Product Offering

The offering phase initiates with a product request submitted by the user. The requested product ID is subsequently forwarded to the Python backend, which in turn retrieves the top 10 similar items associated with the requested product.

Algorithm 2: Recommendation Pseudo Code

```
TFIDF = fit(product_data_with_features)
svd= SVD.fit(TFIDF,10)
similarities = cosine_similarity(svd)
sorted = sort(similarities)
for i, product in enumerate(products):
    similarProducts = GetTopSimilarIndices(sorted, 20)
    top10[product] = similarProducts
return top10
```

The product offering described in Algorithm 2, utilizes, TF-IDF and SVD [12]. TF-IDF is employed to convert product information, including product names, prices, and categories, into numerical representations. The obtained numerical representations are then used to calculate similarities and identify the top 10 most similar products in the database by SVD and cosine similarity [13].

To compute similarities, the Cosine Similarity Metric [14] is favored for its proven effectiveness in handling high-dimensional textual data. Its inherent capability to evaluate similarities while adjusting for variations in scale within product descriptions establishes it as an efficient measure for product matching tasks. The proficiency of this metric in identifying similarities based on orientation rather than magnitude in numerical representations aligns seamlessly with the diverse nature of product attributes.

```
Product:Pınar Yarım Yağlı Süt 1 L


TF-IDF

  (0, 2656)     0.5839952101471663
  (0, 1122)     0.23355711457321554
  (0, 2393)     0.3926840133402722
  (0, 2684)     0.4107172056757372
  (0, 2126)     0.5305763954288694


Singular Value Decompositon

[ 0.2564603  -0.15208331 -0.01131369 -0.1037611  -0.14633315  0.0254556
  0.12080375 -0.00366323  0.08429878 -0.21742818]



 productid                                        product_name  product_price
       676          Teksüt Süt Yarım Yağlı (%1,5 Yağlı) 1 L          15.90
      4043          Teksüt Süt Yarım Yağlı (%1,5 Yağlı) 1 L          15.90
       673 Yörükoğlu Yarım Yağlı Süt (En az %1,5 Yağlı) 1 L          16.90
      4040 Yörükoğlu Yarım Yağlı Süt (En az %1,5 Yağlı) 1 L          16.90
       659                                Pınar Süt Yağlı 1 L          21.50
       714                          Pınar Yarım Yağlı Süt 1 L          71.99
       723                          Pınar Yarım Yağlı Süt 1 L          71.99
       706                     Pınar Yarım Yağlı Süt 4 x 1 L         153.99
       715                     Pınar Yarım Yağlı Süt 4 x 1 L         153.99
       724                     Pınar Yarım Yağlı Süt 4 x 1 L         153.99
```

Figure 3. Product offering process using TF-IDF and SVD

An example of this process is illustrated in Figure 3 with real data. To retrieve best match, TF – IDF calculates numerical metrics for "Pınar Yarım Yağlı 1 Lt Süt" milk, then SVD weights the most important part of the product and cosine finds the similarities between the grabbed products within the system. We prefer only 10 matches to test. It is worth noting that increasing the pool size may lead to improved results in specific cases. However, in general, it can result in irrelevant product offerings due to the variations of product description.

2.3. System Architecture

The architecture is illustrated in Figure 4. The proposed system incorporates two distinct backend systems. In the initial step, Java is responsible for gathering product data from various markets and storing this data in the database. This process iterates until all market data has been collected, ensuring the continuous updating of product information.

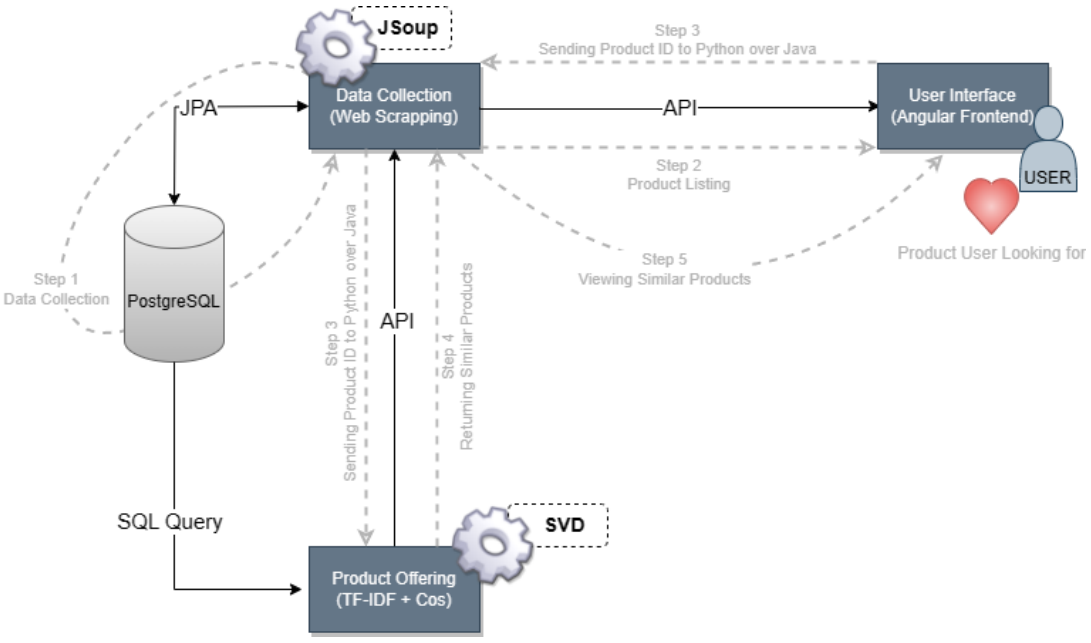

Figure. 4 Proposed system architecture

Meanwhile, users engage with the front end to search for a product. In the second step, products retrieved by the backend are presented to the user. In the third step, the selected product's identifier is transmitted to Python via a Java API.

Python, in the fourth step, Python is used to develop our data offering algorithm to recommend products that are similar to the previously selected item. The identifiers of these generated products are returned to Java. Subsequently, in the fifth step, the product information for these similar products is gathered and then relayed to the frontend. So, a user finds intended products list.

The front-end portal showcased in Figure 5 represents the result of the user search. Our system offers users access to both price trends and the identification of the most cost-effective products available.

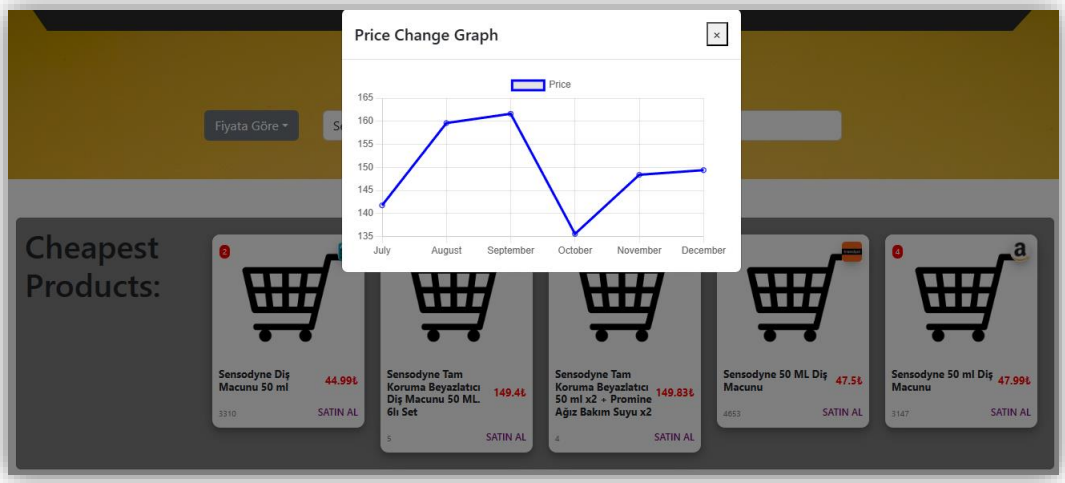

Figure 5. User interface

3. Results and Discussion

The proposed system was evaluated through a comparative performance analysis with two of Türkiye's most popular PCWs, namely Akakçe and Cimri. For testing purposes, we selected Amazon's top-selling products list from September 18th to September 24th and conducted individual product searches on each of the websites.

For our evaluation, distinct performance metrics were measured to gauge the effectiveness of our system compared to Akakçe and Cimri. These metrics encompassed several key aspects:

- the "first place match," denoting when a product recommended by the platform appeared as the primary suggestion;
- "match," indicating any instance of product alignment across search result pages;
- "outdated product," evaluating discrepancies in product information such as stock availability or pricing accuracy; and
- "missing product," signifying products untraceable on the platform.

Figure 6 illustrates that the product matching algorithms employed by both Akakçe and Cimri yield very close matching ratios, in contrast to our system. This outcome was derived from human testing, involving the manual search for selected products on each comparison website. While Akakçe exhibits the highest first-place product matching rate, exceeding 75 percent, all systems maintain a nearly 90 percent matching rate.

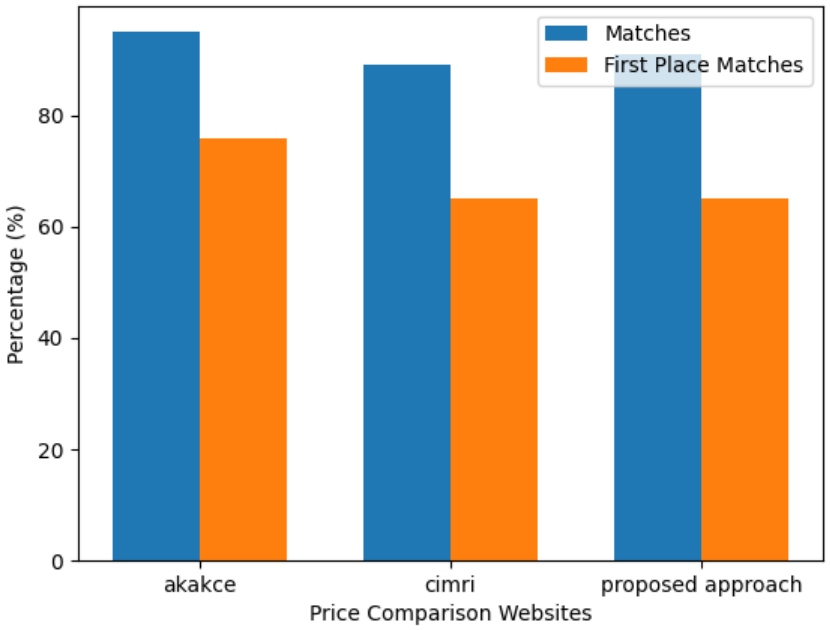

Figure 6. Matching Rates

Table 2 has success rates of previous studies. Those rates stand for the system's overall performance. Success rate in this study is the match rate of the searched products.

Table 2. Success rate comparison of previous studies

Author	Success Rate (%)
Ketki Gupte et al. [10]	68.34
Vincentius Riandaru Prasetyo [5]	73.80
Evan Shieh et al. [12]	83.00
Zhixiang Lin et al. [11]	90.12
Harikirshnan K. Et al. [7]	93.00
Proposed approach	84.00

Upon examining the timeliness and accuracy of product data from previously matched products (as shown in Figure 7), our system consistently provides the most recent and accurate product information, minimizing false directives. However, we should note that our system has data from only three markets while others have over ten suppliers.

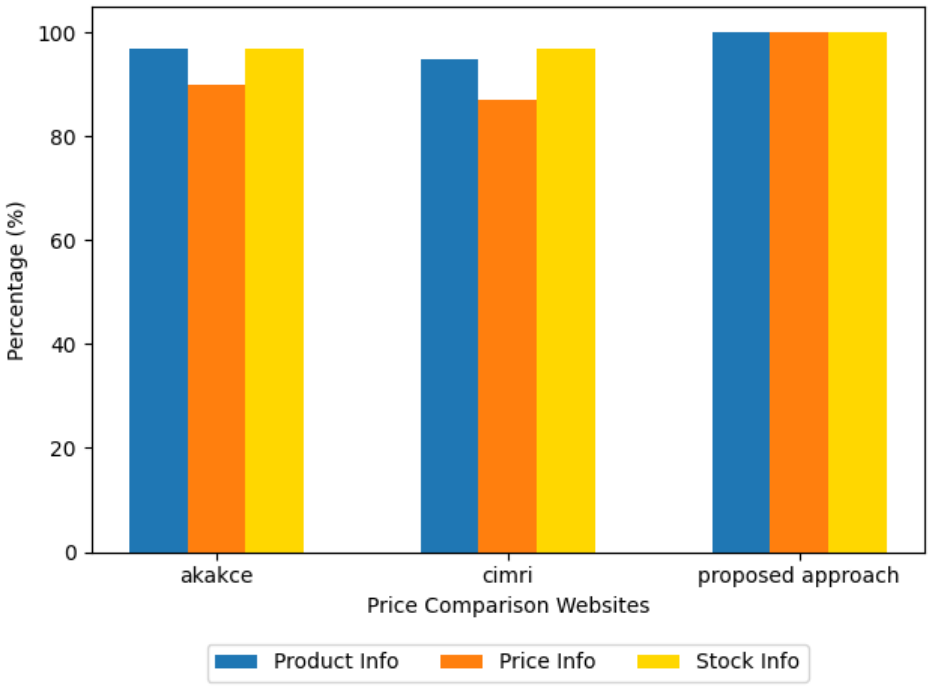

Figure 7. Data Accuracy

To address mismatched products, we further investigated whether these items were included in the respective comparison websites or were absent from their databases. Figure 8 reveals that 17.5 percent of the mismatched items in Cimri were present in their system but remained undiscoverable by users.

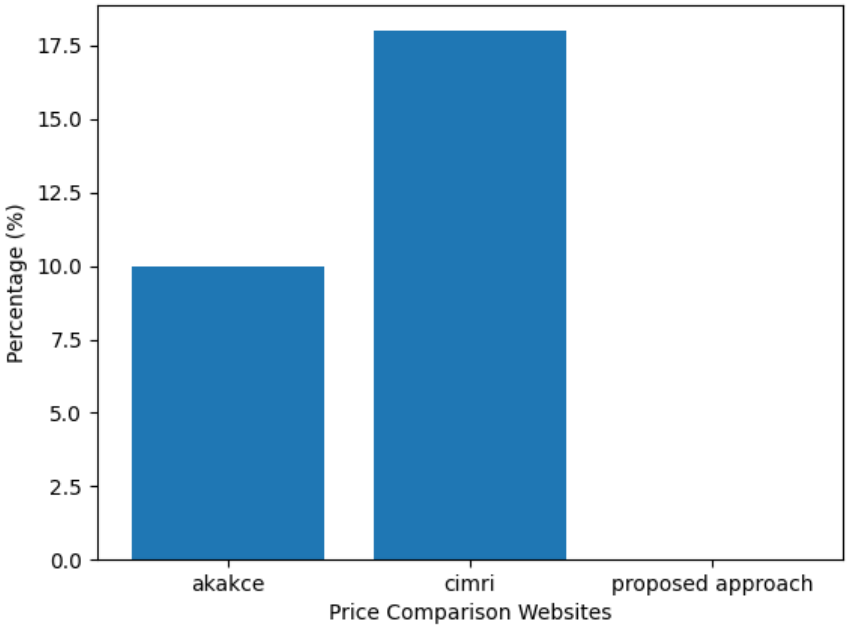

Figure 8. Outdated Data Results

Finally, Figure 9 presents an assessment of the system's efficiency which is calculated by comparing the price shown on PCW and on the actual website of the market, specifically its ability to identify the most cost-effective products. As depicted, our system's performance falls between that of Akakçe and Cimri.

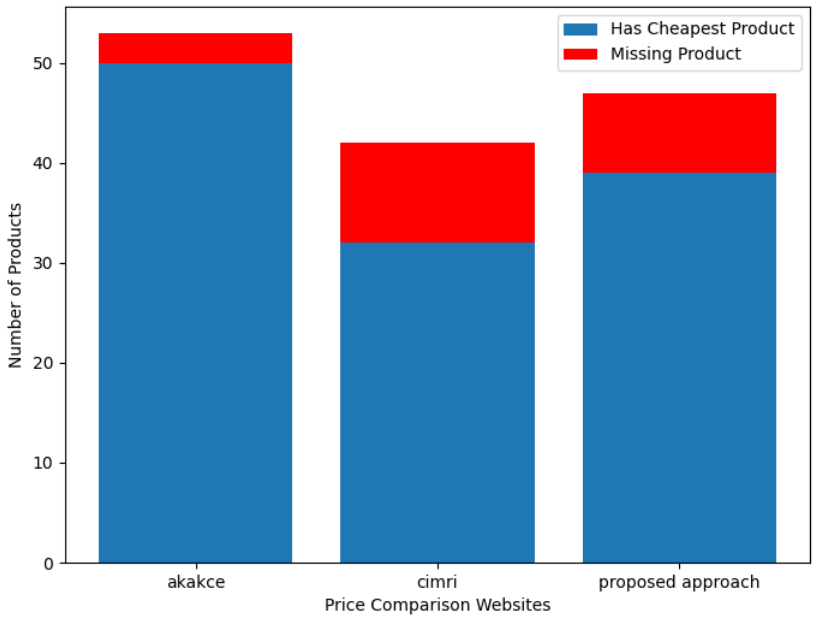

Figure 9. Cheapest Product Rate

While the results affirm the competitiveness of the proposed approach against its counterparts, further research may lead to clarify its strengths and identify areas for enhancement. The initial objective entails an expanded product database and market inclusion, prioritizing user-centric objectives. This strategic expansion aims to ensure a comprehensive product availability, thereby enhancing the overall user experience within the PCW. Another crucial facet of future works involves augmenting the product matching algorithms. The envisaged increase in market diversity, and subsequently in product volume, may poses a challenge to the current SVD modelling. As a response, alternative algorithms, such as Random Forest, will be explored to ascertain their viability and comparative performance against the existing models.

4. Conclusion

This study introduced an alternative price comparison system. Our proposed system consists of two main components, data collection and product offering. The former deploys Jsoup scraper library and the later integrates TF – IDF, SVD, and cosine similarity. The proposed system was evaluated, and its performance compared with existing academic research and industrial PCWs. When it is compared with literature, the success rate reached 84% percentage which is reasonable. Furthermore, our system achieved acceptable efficiency and accurate product offering compared to Akakçe and Cimri.

While our system demonstrates promising results in delivering current and accurate product information, it indicates opportunities for enhancing its performance from different aspects. Future research endeavors aim to verify the system's strengths by diversifying the market, including more products, and exploring alternative matching algorithms, such as Random Forest. These strategies will be pivotal in enhancing the system's competitiveness and user-centric functionality within the price comparison landscape.

Acknowledgement

This paper improves Emre Özakyıldız and Fatma Birel B.Sc. thesis research at Karabuk University in 2023, supervised by Dr. Oğuzhan Menemencioğlu. Fatma Birel's work was separately supported by the Scientific and Technological Research Council of Turkey (TÜBİTAK) under TÜBİTAK 2209-A Science Fellowships and Grant Programmes and the Project ID is: 1919B012218690.

Conflict of Interest Statement

The authors declare that there is no conflict of interest

References

[1] "Akakçe." [Online]. https://www.akakce.com. [Accessed Dec. 23, 2023].

[2] "Cimri." [Online]. https://www.cimri.com. [Accessed Dec. 23, 2023].

[3] "Trivago." [Online]. https://www.trivago.com.tr. [Accessed Dec. 23, 2023].

[4]P. Nagaraj, V. Muneeswaran, A. V. S. R. Pavan Naidu, N. Shanmukh, P. V. Kumar, and G. S. Satyanarayana, "Automated E-Commerce Price Comparison Website using PHP, XAMPP, MongoDB, Django, and Web Scrapping," in *2023 Int. Conf. Comput. Commun. Informatics, ICCCI 2023*, no. Iccci, pp. 1–6, 2023, doi:10.1109/ICCCI56745.2023.10128573

[5] R. Shah, K. Pathan, A. Masurkar, S. Rewatkar, and N. Vengurlekar, "Comparison of E-commerce Products using web mining," *Int. J. Sci. Res. Publ.*, vol. 6, no. 5, p. 640, 2016.

[6] A. Asawa, S. Dabre, S. Rahise, M. Bansode, K. T. Talele, and P. Chimurkar, "Co-Mart - A Daily Necessity Price Comparison Application," in *Proc. - Int. Conf. Appl. Artif. Intell. Comput. ICAAIC 2022*, no. Icaaic, pp. 1076–1080, 2022, doi:10.1109/ICAAIC53929.2022.9792935

[7] A. Alam, A. A. Anjum, F. S. Tasin, M. R. Reyad, S. A. Sinthee, and N. Hossain, "Upoma: A Dynamic Online Price Comparison Tool for Bangladeshi E-commerce Websites," in *2020 IEEE Reg. 10 Symp. TENSYMP 2020*, no. June, pp. 194–197, 2020, doi:10.1109/TENSYMP50017.2020.9230862.

[8] V. R. Prasetyo, "Searching Cheapest Product on Three Different E-Commerce Using K-Means Algorithm*," in Proceeding - 2018 Int. Semin. Intell. Technol. Its Appl. ISITIA 2018*, pp. 239–244, 2018, doi:10.1109/ISITIA.2018.8711043.

[9] J. Wang, S. Yang, Y. Wang, and C. Han, "The crawling and analysis of agricultural products big data based on Jsoup," in *2015 12th Int. Conf. Fuzzy Syst. Knowl. Discov. FSKD 2015*, pp. 1197–1202, 2016, doi:10.1109/FSKD.2015.7382112.

[10] K. Harikirshnan., R. Nagavigneshwar., R. Vignesh., R. Santhosh, and R. Reshma, "Intelligent Online Shopping using ML-based Product Comparison Engine," in 2023 International Conference on Inventive Computation Technologies (ICICT), Apr. 2023, no. Icict, pp. 174–179, doi:10.1109/ICICT57646.2023.10134401

[11] L. R. Julian and F. Natalia, "The use of web scraping in computer parts and assembly price comparison," in 2015 3rd International Conference on New Media (CONMEDIA), Nov. 2015, pp. 1–6, doi:10.1109/CONMEDIA.2015.7449152

[12]S. Brunton and J. Nathan Kutz, "Singular Value Decomposition (SVD)," in Data-Driven Science and Engineering, no. Dmd, Cambridge University Press, 2019, pp. 3–46.

[13] J. Han, M. Kamber, and J. Pei, "Getting to Know Your Data," in Data Min., pp. 39–82, Jan. 2012, doi:10.1016/B978-0-12-381479-1.00002-2

[14]A. R. Lahitani, A. E. Permanasari, and N. A. Setiawan, "Cosine similarity to determine similarity measure: Study case in online essay assessment," in Proc. 2016 4th Int. Conf. Cyber IT Serv. Manag. CITSM 2016, Sep. 2016, doi:10.1109/CITSM.2016.7577578.

This is an open access article under the CC-BY license

Review Article/Derleme

GAZİ
JOURNAL OF ENGINEERING SCIENCES

Various Methods to Improve Energy Efficiency in Industrial Refrigerators

Buğra Şensoy*[a], Mustafa Aktaş[b]

Submitted: 13.10.2023 Revised: 01.11.2023 Accepted: 09.02.2024 doi:10.30855/gmbd.0705N04

ABSTRACT

Effective and efficient energy consumption, environmental sensitivities, climate change, and global warming are significant issues that the world is currently focusing on. Industrial refrigerators are the devices that have significant effects under the mentioned headings. Environmental sensitivities should be valued when improving innovative designs for effective and efficient energy consumption in industrial refrigerators. Moreover, with both international and national regulations recently, designs to be made at this point have become an obligation rather than a necessity. This study aims to use energy effectively and efficiently, creating an energy efficiency factor in industrial refrigerators; various aspects, such as components, insulation, refrigerant, control technique, ambient conditions, cooling cycle, and airflow were studied from different perspectives and grouped, and the outputs obtained as a result of the studies were compiled. The grouped and compiled outputs were presented title-based and optimum solutions in terms of energy efficiency were discussed. The presented outputs will be used as effective design inputs in the studies carried out by researchers and product manufacturers, thus, as a result of innovative studies that create energy efficiency, designs with substantial environmental sensitivity, especially carbon emissions, will emerge. In addition, it thought that innovative and efficient designs would make direct and indirect contributions to the economy.

Keywords: Industrial refrigerator, Energy consumption, Opportunities for energy efficiency, Thermal insulation, Eco design

[a,*] Gazi University, Institute For Graduate Studies In Pure and Applied Sciences, Dept. of Energy Systems Engineering 06560 - Ankara, Türkiye
Orcid: 0000-0002-7350-9540
e mail: bugra.sensoy@gazi.edu.tr

[b] Gazi University, Technology Faculty, Dept. of Energy Systems Engineering 06560- Ankara, Türkiye
Orcid: 0000-0003-1187-5120

*Corresponding author: bugra.sensoy@gazi.edu.tr

Endüstriyel Soğutuculardaki Enerji Verimliliğini Arttırmaya Yönelik Çeşitli Yöntemler

ÖZ

Enerjinin etkin ve verimli kullanılması, çevresel hassasiyetler, iklim değişimi ve küresel ısınma güncel olarak tüm dünyanın üzerinde durduğu önemli başlıklardır. Endüstriyel soğutucular da bahsedilen başlıklar içinde önemli etkilere sahip cihazlardır. Endüstriyel soğutuculardaki enerjinin etkin ve verimli kullanımına ilişkin yenilikçi tasarımlar geliştirirken çevresel hassasiyetler de göz ardı edilmemelidir. Ayrıca, son zamanlarda gerek uluslararası gerekse de ulusal düzenlemelerle bu noktada yapılacak tasarımlar gereklilikten ziyade bir zorunluluk haline gelmiştir. Enerjinin etkin ve verimli kullanılmasını amaç edinen bu çalışmada, endüstriyel soğutuculardaki enerji verimliliği unsuru yaratan; komponentler, yalıtım, soğutucu akışkan, kontrol tekniği, ortam şartları, soğutma çevrimi ve hava akışı bazlı farklı perspektifteki çalışmalar incelenerek gruplandırılmış ve çalışmalar sonucunda ortaya konulan çıktılar derlenmiştir. Gruplandırılan ve derlenen çıktılar başlık temelli sunularak enerji verimliliği açısından optimum çözümler tartışılmıştır. Sunulan çıktılar, araştırmacı ve ürün üreticilerinin gerçekleştirecekleri çalışmalarda etkin tasarım girdileri olarak kullanılacak böylelikle enerji verimliliği yaratan yenilikçi çalışmaların sonucunda da karbon salınımı başta olmak üzere çevresel hassasiyeti güçlü tasarımlar ortaya çıkacaktır. Ayrıca yenilikçi ve verimli olarak geliştirilen tasarımların ekonomiye de doğrudan ve dolaylı katkılar vereceği düşünülmektedir.

Anahtar Kelimeler: Endüstriyel soğutucu, Enerji tüketimi, Enerji verimliliği için fırsatlar, Isı yalıtımı, Eko dizayn

To cite this article: B. Sensoy, and M. Aktas, "Various Methods to Improve Energy Efficiency in Industrial Refrigerators," *Gazi Journal of Engineering Sciences,* vol.10, no.1, pp. 38-59, 2024. doi:10.30855/gmbd.0705N04

1. Giriş (Introduction)

Dünya'da enerji talebi; nüfus artışı, teknoloji gelişimi ve tüketim alışkanlıklarında yaşanan değişime bağlı olarak günden güne artış göstermektedir. Enerji talebinin karşılanabilmesi için de başta fosil yakıtların kullanılması olmak üzere çevreye ciddi boyutta zarar verilmektedir. Bu süreçte, oluşan zararları minimize etmek için; enerjinin etkin ve tasarruflu olarak kullanılabilmesini amaçlayan enerji verimliliği kavramı öne çıkmaktadır.

Enerji tüketimi özellikle endüstride oldukça fazla olduğundan verimlilik çalışmalarında endüstriyel cihazlara ayrıca önem verilmesi gerekir. Soğutma sektöründe kullanılan endüstriyel soğutucular da dünya enerji tüketiminde ciddi paya sahip cihazlardır. Salehy ve arkadaşları tarafından yapılan çalışmada (2020), soğutma sistemlerinin dünyadaki enerji talebinin yaklaşık %17'sini tükettiği ve yine bu sistemlerin dünya sera gazı emisyonunun yaklaşık %8'inden sorumlu olduğu belirtilmiştir [1].

Soğutma sistemleri içerisinde yer alan endüstriyel soğutucular, ürünlerin muhteviyatlarına göre, özelliklerini koruyarak belirli bir sıcaklık ve nem altında muhafaza edilmesini sağlayan sistemlerdir. Endüstriyel soğutucular, depolama veya teşhir amaçlı tasarlanırken konuya ilişkin detaylı sınıflandırma *TS EN ISO 23953* numaralı standart uyarınca yapılmaktadır. İlgili standart dahilinde endüstriyel soğutucular içerisinde; chiller grupları, soğutmalı vitrin ve teşhir dolapları, profesyonel kullanım için şok soğutucular, dondurma tezgâhları, soğutmalı otomatlar, buz yapıcılar gibi birçok farklı ürün gamı bulunmaktadır. Endüstriyel soğutucular; soğutma amacı, ortama bağlı gereklilikler, düşük ya da orta sıcaklık uygulamaları gibi kriterlere göre seçilirken, soğutma yükü ihtiyacı doğrultusunda çok geniş ürün yelpazesine sahip ürünlerdir.

Endüstriyel soğutucuların oldukça geniş yer bulduğu konumlardan birisi de süpermarketlerdir. Süpermarketler içerisinde özellikle teşhir tipi endüstriyel soğutucular sıklıkla tercih edilmekte olup bu soğutucu çeşidi, muhafaza sıcaklığına göre sınıflara ayrılmaktadır. Tablo 1.'de teşhir tipi endüstriyel soğutucuların sıcaklık sınıflandırılmasına yer verilmiştir [2].

Tablo 1. Teşhir tipi endüstriyel soğutucuların sınıflandırma parametreleri [2] (Classification parameters of industrial display refrigerator)

Soğutucu Sınıfı	En sıcak ürün paketinin en yüksek değeri, (°C)	En soğuk ürün paketinin en düşük değeri, (°C)	En sıcak ürün paketinin en düşük sıcaklık değeri, (°C)
L1	-15	-	-18
L2	-12	-	-18
L3	-12	-	-15
M1	+5	-1	-
M2	+7	-1	-
H1	+10	+1	-
H2	+10	-1	-
S		Özel sınıflandırma	

Endüstriyel soğutucu kullanımına doğrudan etkisi olan süpermarketler ile alakalı, sektörel araştırmalar yapan bir firmanın verilerine göre; 2010-2017 yılların arasında discount marketlerin mağaza sayısı %285, şube sayısı en az 5 ve üzeri olan market zincirlerinin toplam mağaza sayısı %178 ve yerel market zincirlerine ait mağaza sayısı %77 oranında artış göstermiştir. Ayrıca Türkiye'de organize zincir market sayısının 2024 yılı sonunda, 44 bin adete ulaşması beklenmektedir [3]. Günümüzde süpermarket sayısında yaşanan artış birlikte ulusal enerji tüketiminde de ciddi talep artışları meydana gelmektedir. Dünya genelinde sayıları git gide artan süpermarketler de ulusal enerji tüketiminde önemli bir tüketim noktası olarak karşımıza çıkmaktadır. Bu konuda; Kauko ve arkadaşları yapmış oldukları çalışmada (2017), dünya genelinde üretilen toplam enerjinin yaklaşık %3-4'ünün süpermarketlerde kullanıldığını ortaya koymuşlardır [4].

Süpermarket sayısında yaşanan artış beraberinde teşhir tipi endüstriyel soğutucuların sayısının da artmasını sağlamaktadır. Süpermarketlerde yer alan teşhir tipi endüstriyel soğutucuların, süpermarketlerin toplam enerji tüketiminin büyük bir kısmından sorumlu olduğu yapılan çalışmalarda görülmektedir. Bu konuda; M.R. Braun ve arkadaşları (2014), İngiltere'nin kuzeyinde orta ölçekli bir süpermarketi referans alarak yapmış

oldukları çalışmada, süpermarketin elektrik enerjisi tüketiminin yaklaşık %66'sının soğutma sistemlerinden kaynaklandığı sonucuna ulaşmıştır [5]. Tassou ve arkadaşları tarafından yapılan başka bir çalışmada (2011), Birleşik Krallık'ta bulunan süpermarketlerin enerji tüketimlerinden kaynaklı olarak, ülkedeki sera gazı emisyonlarının yaklaşık %1'inden sorumlu oldukları ortaya konulmuştur. Bununla birlikte; bu bölgede toplam elektrik tüketiminin, %3-5 arası süpermarketlerden kaynaklandığı, endüstriyel soğutucuların ise süpermarketlerin toplam elektrik enerjisi tüketiminin yaklaşık %35-50'sini oluşturduğunu belirtmişlerdir [6]. Yapılan çalışmalar, özellikle süpermarketlerde bulunan teşhir tip endüstriyel soğutucuların ulusal elektrik enerjisi tüketimi ve sera gazı emisyonuna olan etkisini açıkça göstermektedir.

Yapılan bu çalışma ile;

• Teşhir tip endüstriyel soğutucularda etkinlik katsayısının yükseltilmesini sağlayan, enerji verimliliği arttıran ve karbon salınımını azaltan bazı önemli çalışmalar incelenip derlenmesi,

• Yeni yapılacak tasarımlar için enerji verimliliği açısından girdi oluşturacak parametrelerin sunulması,

• Araştırmacı ve endüstriyel soğutucu üreticilerinin faydalanabileceği farklı perspektiflerden beslenen bir kaynak ortaya çıkartılması amaçlanmıştır.

2. Endüstriyel Soğutucularda Yapılan Çeşitli İyileştirme Çalışmaları (Various Improvement Studies on Industrial Refrigerators)

Endüstriyel soğutucularda; tasarım, sistem komponenti, soğutucu akışkan ve dış ortam şartları baz alınarak bilimsel çalışmalarda yapılan çeşitli iyileştirmeler sonucunda ortaya konan çıktılar başlık bazında sunulmuştur.

2.1. Endüstriyel soğutucularda komponent bazlı çalışmalar (Component based studies on industrial refrigerators)

Endüstriyel soğutucular, buhar sıkıştırmalı soğutma çevrimi dahilinde çalışmaktadır. Bu çevrimin en temel bileşenleri; kompresör, kondenser, genleşme valfi ve evaporatördür. Bu kısımda komponentlerde gerçekleştirilen çeşitli iyileştirme ve çevrimde yapılan eklemelere ait çalışmalara yer verilmiştir.

Shaban ve arkadaşları (2020), teşhir tipi endüstriyel soğutucularda enerji ve ekserji verimliliğine yönelik bir çalışma gerçekleştirmişlerdir. Gerçekleştirilen çalışmada iki ayrı sistem kıyas edilmiş olup; birinci sistemde sabit hızlı klasik aç/kapa kompresör ve mekanik genleşme valfi kullanılırken ikinci sistemde değişken hızlı kompresör ve elektronik genleşme valfi kullanılmıştır. Yapılan yeni tasarım sonucunda konvansiyonel sisteme göre, %32 oranında enerji verimliliği sağlanırken ekserji yıkımı %76 oranında azalmıştır [7].

Ünal ve arkadaşları (2016), Şekil 1.'de tasarım şeması sunulan, çift buharlaştırıcıya sahip bir soğutma sistemine ejektör entegre ederek yeni nesil bir tasarım ortaya koymuşlardır. Yapılan tasarımda, R134a akışkanı ve bu akışkana muadil olarak geliştirilen R1234yf akışkanı kullanılmıştır. Gerçekleştirilen analiz çalışması sonucu ejektör entegreli sistemin klasik sisteme göre R134a akışkanı için %15, R1234yf için ise %17 daha fazla etkinlik katsayısına sahip olduğunu tespit etmişlerdir. Ayrıca çalışmada sistemde genleşme vanası yerine ejektör kullanıldığı durumda ekserji kaybında da azalma meydana geldiği görülmüştür. Bu kaybın azalma miktarının, R134a soğutkanı için %17, R1234yf akışkanı için ise %19 olduğu hesaplanmıştır [8].

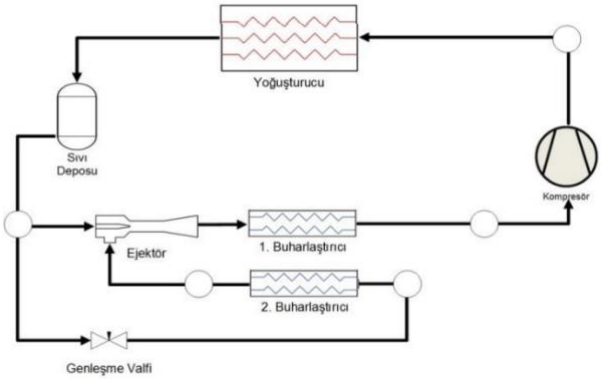

Şekil 1. İki buharlaştırıcılı ejektörlü soğutma sistemi [8]
(Cooling system with ejector and two evaporators)

Ocak ve arkadaşları (2023), yapmış oldukları çalışmada teşhir tipi endüstriyel soğutucularda kompresör seçiminin enerji tüketimine olan etkisini araştırmışlardır. Bunun için, R290 soğutucu akışkanına sahip iki özdeş soğutma sisteminin birinde sabit devirli kompresör kullanılırken diğerinde değişken hızlı kompresör seçimi yapılmıştır. Yapılan deneysel çalışma sonucunda; 1.sistemin elektrik enerjisi tüketimi 11,2 kWh/gün olurken 2. sistem 8,3 kWh/gün elektrik enerjisi tüketmiştir. Kompresör seçiminin etkisiyle, enerji tüketiminin %25,9 azalmasıyla birlikte soğutma sisteminin enerji etiketi değeri "C" seviyesinden "B" seviyesine yükselmiştir [9].

Bilir Sag ve arkadaşları (2015), yapmış oldukları çalışmada soğutma çevriminde aynı ortam şartlarında, genleşme valfi yerine ejektör kullanmanın COP ve ekserji yıkımı üzerine etkisini incelemişlerdir. Yapılan çalışma neticesinde sisteme ejektör entegre edilmesiyle birlikte COP değeri %7,34-12,87 oranında, ekserji verimi ise %6,6-11,24 oranında artmıştır [10].

Knabben ve arkadaşları (2020), soğutma sistemlerinde elektronik genleşme valfi kullanımının enerji tüketimine etkisini araştırmışladır. Yapılan çalışma sonucunda, soğutma sistemlerinde kapiler boru yerine elektronik genleşme valfi kullanımının toplam enerji tüketimini %4-9 oranında azalttığı sonucuna ulaşılmıştır [11].

Doğan ve arkadaşları (2021) yapmış oldukları çalışmada, soğutucularda enerji tüketimi ve soğutucu akışkan şarjını azaltmak amacıyla yeni bir kondenser tasarımı gerçekleştirmişlerdir. Soğutucu tasarımında, Şekil 2.'de görselleri sunulan, geleneksel telli borulu tip kondenser yerine mini kanallı kondenser kullanmışlardır. Çalışmada yapılan kıyaslama esnasında 2800, 3300 ve 3800 mm uzunluklarında üç farklı uzunlukta kapiler boru kullanılmıştır. Çalışmada en iyi sonuç, yeni nesil kondenser tasarımı kullanımıyla birlikte 3300 mm uzunluğundaki kapiler boru kullanımıyla; %5,7 oranında enerji tasarrufu sağlanarak ve soğutkan şarjında %10,7 oranında azalma yaşanarak gerçekleştirilmiştir [12].

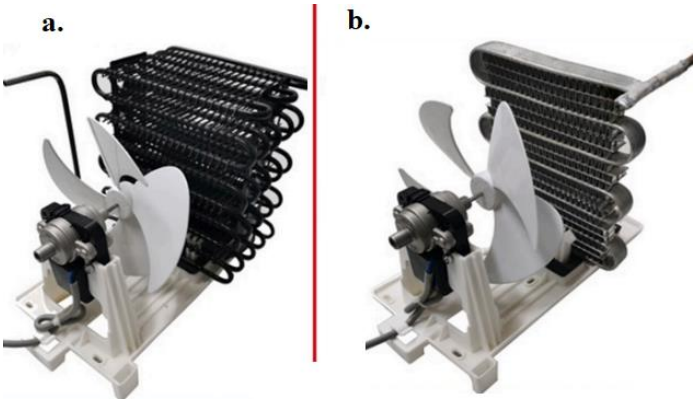

Şekil 2. a-Telli borulu tip kondenser, b- Mikro kanallı kondenser [12]
(a-wire tube condenser, b- micro channel condenser)

Patil (2012), bir soğutma sisteminde performans katsayısını arttırmak amacıyla kondenser tasarımına ilişkin çalışmalarda bulunmuştur. Yapılan çalışmada; soğutma sisteminde U tip bir kondenser yerine mikro telli kondenser kullanılmıştır. Çalışma sonucunda, soğutma kapasitesi %10 artarken COP değerinde ise %17'lik bir artış gerçekleşmiştir [13].

Zhang ve arkadaşları (2017), evaporatör ünitesine kurutucu entegre karlanma yaşanmayan bir soğutma kabini tasarımı gerçekleştirmişlerdir. Bu yenilikçi ısı değiştirici sadece karlanmayı önlemekle kalmamakla birlikte aynı zamanda yüksek verimliliğe de sahip yapıdadır. Yüksek verimli olmasının temel sebebi de ortam havasına atılan yoğuşma ısısı yoluyla kurutucunun verimli bir şekilde çalışmasından kaynaklanmaktadır. Sistemde evaporatör dönüş hava sıcaklığı ve bağıl nem sırasıyla 12 °C ve 0,6 iken günlük elektrik enerjisi tüketimi 3,1 kWh ve sistem COP değeri 3,2 olarak hesaplanmaktadır. Çalışmada ayrıca evaporatör dönüş havası ve bağıl nem değişiminin COP değeri üzerinde önemli bir etkisi olduğu da vurgulanmıştır. Bu noktada evaporatör dönüş havası sıcaklığı 8°C'den 14 °C'ye çıktığında COP değeri %115; bağıl nem 0,5 ten 0,8 e çıktığında ise COP değeri %35 artmıştır [14].

Vidrih (2014), alışveriş merkezlerinde kullanılan teşhir tipi endüstriyel soğutucuların elektrik tüketiminin düşürülmesi amacıyla bir çalışma gerçekleştirmiştir. Çalışmada, yapılan bütünsel stratejilerle elektrik tüketiminde %30,2 düşüş gerçekleşmiştir. Bu stratejiler incelendiğinde; elektrik tüketimini düşüren en büyük etkenin %10,7 ile endüstriyel soğutucuya kapı takılması olmuştur. Bunu, %7,7 düşüş ile kapaklara ısıtıcı entegresi, %4 ile sıcak gaz ile defrost yöntemine geçilmesi, %3,6 ile LED aydınlatma kullanımı, %2,23 ile çevredeki hareketlere göre aydınlatma sisteminin optimize edilmesi ve %2,0 ile kabin içerisinde oluşan ısıyı yansıtan üst yüzey kaplaması takip etmiştir [15].

Heidinger ve arkadaşları (2016), kapalı teşhir tip soğutucularda kapılar arası boşluk olan ve olmayan durumlarda, elektromanyetik ve elektronik fanlarla deneysel bir çalışma gerçekleştirmişlerdir. Çalışmada, kapılar arasında hava boşluğu kaldığı durumda ısı yükü yaklaşık %10 oranında artmıştır. Ayrıca çalışmada, elektromanyetik fan kullanıldığında ısı yükü elektronik fan kullanılma durumuna göre %4 artmıştır. Çalışma sonucunda, kapılar arası boşluklar bırakılmaması ve elektronik fan kullanımı ısı yükünün azaltılmasını sağladığı görülmektedir [16].

IIR tarafından 42. Soğutma Teknolojileri konferansında oluşturulan bilgilendirme notunda (2021), endüstriyel soğutma sistemlerinde yağ gerektirmeyen kompresör kullanımının öneminden bahsedilmiştir. Yağlama yağlarının, ısı transferini zayıflatabileceği, sistem performansını düşürebileceği ve sistem konfigürasyonunu karmaşık hale getirebileceği vurgulanmıştır. Yağlama yağı gerektirmeyen kompresörler ise; manyetik yatak, gaz yatağı ve seramik yatak kompresörler olarak üçe ayrılmakta her birinin kapasitesi ve uyumlu olduğu akışkanlar çalışmada ifade edilmiştir [17].

Rauss ve arkadaşları (2008), teşhir tipi endüstriyel soğutucularda aydınlatma sistemlerinin enerji tüketimine etkisini incelemişlerdir. Yapılan çalışmada, soğuk katotlu floresan, LED ve fiber optik aydınlatma sistemlerinin enerji tüketim tahminleri kıyas edilmiştir. Hesaplamada teşhir tipi soğutucunun 24 saat tam yükte çalışacağı baz alınmıştır. Bu doğrultuda, soğuk katotlu floresan, LED ve fiber optik aydınlatma sistemleri için sırasıyla soğutucu başına yıllık enerji tüketimleri; 444 kWh, 314 kWh ve 556 kWh olarak tahmin edilmiştir [18].

IIR tarafından 42.Soğutma Teknolojileri konferansında oluşturulan bilgilendirme notunda (2021), iklim değişikliği süreçlerinde soğutucu akışkan miktarının azaltılmasını belirten eylem planlarına uyum sağlamak için soğutma sistemlerinde Şekil 3'te gösterilen düşey film evaporatör tipinin kullanılması önerilmektedir. Bu evaporatör çeşidi, diğer evaporatörlere göre daha yüksek ısı transfer katsayısına sahipken çevreye olan zararının da düşük olduğu vurgulanmıştır. Çalışmada, Midea Grup tarafından tanıtılan bir sistemde, düşen film evaporatör kullanılmasıyla soğutucu şarj miktarında %40 azalma meydana geldiği vurgulanmıştır [17].

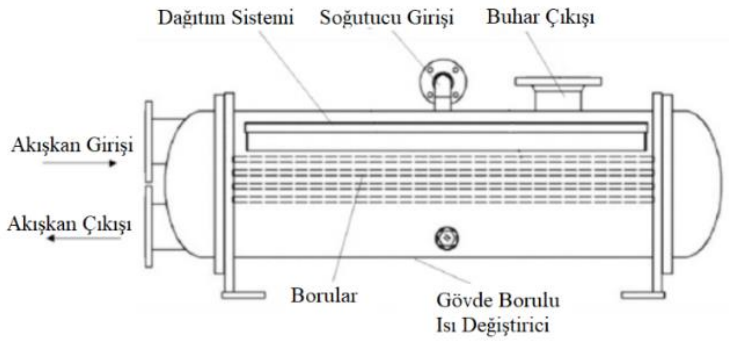

Şekil 3. Düşey film evaporatör yapısı [17]
(Falling film evaporatör structure)

2.2. Endüstriyel soğutucularda yalıtım bazlı çalışmalar (Insulation based studies on industrial refrigerators)

Sıcak ya da soğuk havanın ısı köprüleri vasıtasıyla sistemin içine girmesini ya da dışına çıkmasını engellemek amacıyla yapılan işler bütününe yalıtım denir. Enerji verimliliği sürecinin en kritik noktalarından birisi olan yalıtım, endüstriyel soğutma sistemleri verimi için de oldukça önemlidir. Bu kısımda endüstriyel soğutma sistemlerinde gerçekleştirilen yalıtım çalışmalarına ait çıktılara yer verilmiştir.

Jadhav ve arkadaşları (2021) yaptıkları çalışmada, açık teşhir tip bir endüstriyel soğutucuda PVC şerit perde kullanılmıştır. Yapılan çalışmada, Şekil 4.'te gösterilen PVC şerit perde kullanımı, kabin sıcaklığını -2°C ila +6°C arasında, gıda ürün sıcaklığını ise 0°C ila 6°C arasında tutmuştur. PVC perde kullanılmadığı durumda ise, kabin sıcaklığı +6°C ila +9 °C arasında, gıda ürünü sıcaklığı +12°C ila +22°C arasında kalmıştır. Kabin ile hava arasında yapay bir kapı görevi üstlenen PVC şerit sayesinde enerji tüketimi 1,63 kWh/gün değerinden 1,12 kWh/gün değerine düşmüştür [19].

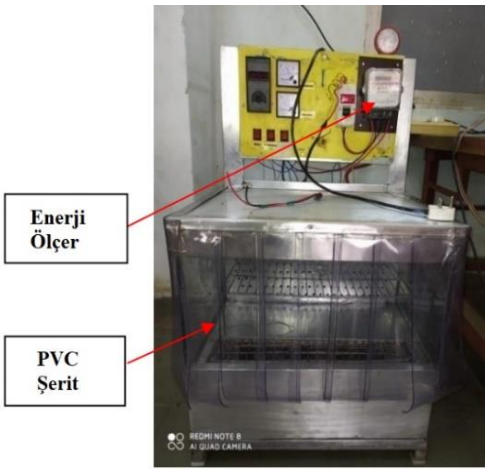

Şekil 4. PVC şerit ile donatılan endüstriyel soğutucu [19]
(Industrial refrigerator equipped with PVC strip)

Orlandi ve arkadaşları (2015), kapalı teşhir tip endüstriyel soğutuculardа yapmış olduğu simülasyon analizi ile, soğutucuda enerji tüketimi dağılımlarını ortaya koymuştur. Yapılan çalışmada, kapı arası boşluğun termal yüke, soğutucunun fazla kullanılmadığı gece anlarında %23, yoğun kullanımda ise %15 gibi büyük bir oranda etki ettiğini ortaya koymuştur. Bu anlamda yapılacak tasarımlarda, termal yükün ve dolayısıyla enerji tüketiminin azaltılması amacıyla boşluk miktarı olabildiğince azaltılması gerekmektedir [20].

Liu ve arkadaşları (2021), kapalı tip endüstriyel soğutucularda contanın ısı yalıtımı için oldukça önemli olduğuna dikkat çeken bir çalışma gerçekleştirmişlerdir. Bazı tasarımlarda, conta kaynaklı ısı sızıntısının, toplam ısı yükünün %15-20'sini oluşturduğu vurgulanan çalışmada, 2019 senesi baz alınarak conta tasarımlarında yapılacak iyileştirmeler sayesinde; 2025 yılında %3, 2030 yılında ise %5'e kadar enerji tasarrufu

sağlanacağı hedeflendiği belirtilmiştir. Belirlenen hedefin gerçekleşebilmesi için çeşitli kriterler belirlenmiştir. Bunlar incelendiğinde; soğutucu özelinde conta tasarımı yapılması, düşük sıcaklığa dayanıklı PVC conta üretimi, yüksek esnekliğe sahip termoplastik elastomer kullanımı, contaların doğru termal-mekanik bağlantı simülasyonu modellemesinin yapılması gibi kriterler sıralanmıştır [21].

Agaro ve arkadaşları (2021), dikey teşhir tip endüstriyel soğutucu kapaklarında kullanılan anti-fog kaplamaların açıya bağlı olarak buğulanmayı önleme durumlarını araştırmışlardır. Kullanılan anti-fog filmin camla temas açısını 90°'den 30°'ye düşüren film sayesinde cam kapaklarda oluşan yoğuşmanın %50'ye kadar azaldığı tespit edilmiştir. Ayrıca, 30 saniyelik kapı açılma süresinden sonra buğu giderme işleminin tamamlanması için gereken süre, anti-fog filmli camda çıplak camın ihtiyaç duyduğu süreden yaklaşık %30 daha az olduğu çalışmada vurgulanmıştır [22].

Ander tarafından yapılan bir araştırmada (2014), özellikle çalışma saatleri dışında endüstriyel soğutucuların üzerinin alüminyum perde ile kaplanması önerilmiştir. Şekil 5.'te açıklandığı üzere; alüminyum kaplamanın yüksek yansıtıcılığı ve iyi ısı yalıtımına sahip olması, radyasyon ve iletim yoluyla oluşan ısı transferinin azalmasını sağlamaktadır. Yapılan çalışmada 3 farklı senaryo üzerinde durulmuş, ilk senaryoda marketin açık ve kapalı olduğu hiçbir saatte alüminyum perde kullanılmamış, ikinci senaryoda marketin kapalı olduğu 6 saatlik periyotta alüminyum perde kullanılmış ve üçüncü senaryoda ise marketin tatil olduğu bir günde sürekli alüminyum perde kapalı tutulmuştur. Çalışma neticesinde; soğutma yükleri ilk senaryoya göre, ikinci senaryoda %8,5, üçüncü senaryoda ise %41 oranında azalmıştır. Enerji tüketimleri ilk senaryoya göre; ikinci senaryoda %9, üçüncü senaryoda ise %36 oranında düşüş göstermiştir [23].

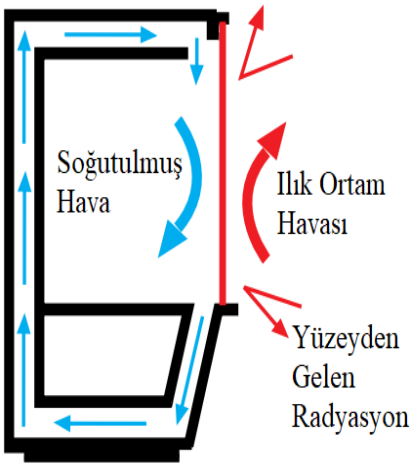

Şekil 5. Soğutulan alanda ışınım ve iletkenle ısı transferinin azaltılması [23]
(Reducing radiation and conductive heat transfer to the cooled area)

Chaomuanga ve arkadaşları (2019), yapmış oldukları çalışmada kapalı teşhir tip soğutucuların çalışma koşulları hakkında bir araştırma yapmışlardır. Yapılan çalışmada, kapalı tip kabinler sayesinde, soğutuculardan dış ortama daha az soğuk hava yayıldığı ve bu durumun mağaza termal konfor şartları açısından da olumlu olduğu vurgulanmıştır. Bunun yanında çalışma içerisinde, kapalı tip kabinlerin %20-70 arasında enerji verimliliği sağladığı ve hava sızma sorununu önlediği belirtilmiştir ve kapalı kabinlerin tüm bu olumlu özellikleriyle birlikte sayılarının arttığı bahsedilmiştir [24]. Fransa'da, devlet otoriteleri ile büyük süpermarket üreticileri arasında yapılan anlaşma doğrultusunda, açık tip kabinlerin %75'inin kapalı tip kabinlere dönüştürülmesi amaçlanmıştır [25].

Pedersen ve arkadaşları (2018), kabin yalıtımıyla ilgili bir çalışma gerçekleştirmişler ve kabin yalıtım kalınlığının arttırılmasının ısı köprüsü oluşumunu azalttığını vurgulamışlardır. Çalışmada, bir endüstriyel soğutucuya 2 cm daha poliüretan köpük yalıtım malzemesi eklemenin ısı köprüsü oluşumunu %95 oranında azalttığı sonucuna ulaşmışlardır [26].

Humar ve arkadaşları (2022), kapalı teşhir tip soğutucu dolap kapaklarında oluşan buğulanmayı önlemek amacıyla kullanılan ısıtıcılarla ilgili araştırmalarda bulunmuşlardır. Çalışmada, dolap kapağı ve çerçevelere ısıtıcı entegresi sayesinde çiğ noktası sıcaklığının değişmesi, enerji tüketiminde %84,6 azalma sağlanacağı bu ısıtıcının doğrudan cama takılması durumunda ise, enerji tüketiminin ısıtıcı olmayan duruma göre %90,1 oranında azalacağı ifade edilmiştir [27].

2.3. Endüstriyel soğutucularda soğutkan bazlı çalışmalar (Refrigerant based studies on industrial refrigerators)

Soğutkanlar, endüstriyel soğutuculardа hem sistemin termodinamik özelliklerine uyum ve soğutucu verimliliği açısından hem de çevresel hassasiyetler açısından oldukça önemli bir parametredir. Bu kısımda endüstriyel soğutma sistemlerinde soğutkanlar hususunda yapılan çalışmalara yer verilmiştir.

Gil ve Kasperski (2018), R134a kullanılan ejektörlü bir soğutma sistemine yeni nesil alternatif soğutkan entegre etmek amacıyla çalışmalarda bulunmuşlardır. Çalışmada, 3 farklı buharlaşma-yoğuşma sıcaklığı ikilisi üzerinden çalışılmış olup (0°C-25 °C, 6°C-30°C ve 9°C-40°C) bu sıcaklıklarda maksimum COP değerleri sırasıyla e 0.35, 0.365, ve 0.22 olarak hesaplanmıştır. Çalışmada en büyük verim HFO-1243zf ve HFO 1234ze(E) akışkanlarından alınmasına karşın bu akışkanların geniş enjektör sıcaklıklarında çalışmaya uygun olmadığı vurgulanmış, HFO-1233zd(E) ve HFO-1224yd(Z) akışkanların optimum çalışabilmeleri için 130 °C'nin üzerinde buharlaşma sıcaklarına ihtiyaç bulunduğu, HFO-1243zf'nin kullanıldığında ise, düşük buharlaşma sıcaklıklarının (yaklaşık 60 °C'den 88 °C'ye) soğutma kapasitesini arttıracağı vurgulanmıştır [28].

Yıldırım ve Şahin (2020), yapmış olduğu çalışmada iki kademeli soğutma sistemi için farklı akışkanlar kullanarak sistemin analizlerini gerçekleştirmiştir. R32, R290, R410A, R245fa, R717, R407C, R507A, R1234yf ve R1234ze soğutucu akışkanlarının kullanıldığı çalışmada, Şekil 6.'da sunulduğu üzere COP değerleri hesaplanmıştır. Hesaplamada, en yüksek COP değeri R717 akışkanı ile 5,358 olarak hesaplanırken en düşük COP değeri ise R407C soğutkanı ile 4,165 olarak hesaplanmıştır. Ekserji analizlerinin de yapıldığı çalışmada en yüksek ekserji verimi 0,7069 değeri ile R717 soğutkanı ile sağlanırken en düşük ekserji verimi ise 0,5496 değeri ile yine R407C akışkanı kullanıldığında hesaplanmıştır. Sistem komponentlerinin ekserji analizine bakıldığında ise, en yüksek ekserji yıkımının %80 ile evaporatörde en düşük ekserji yıkımının ise ara soğutucu ünitesinde gerçekleştiği tespit edilmiştir [29].

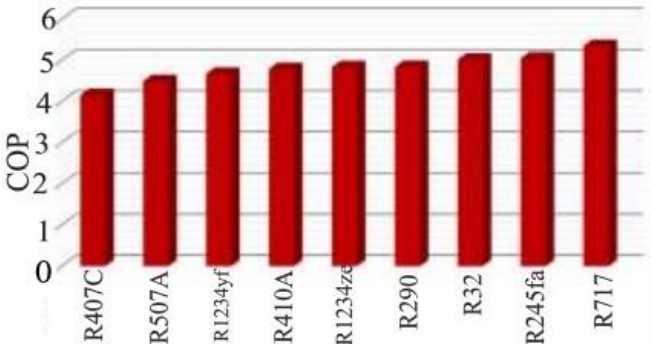

Şekil 6. Çalışmada kullanılan soğutucu akışkanların COP değerleri karşılaştırılması [29]
(COP values comparison of refrigerants used in the study)

Katırcıoğlu ve arkadaşları (2020), soğutma sistemlerinde performans katsayısının belirlenmesi esnasında kızılötesi görüntü işleme teknikleri kullanmış ve soğutma sisteminde, R22 soğutkanına alternatif olarak R438A ve R417A soğutucu akışkanlarını incelemiş, ticari soğutma sistemleri için her iki akışkanın analizini gerçekleştirmişlerdir. Soğutma sisteminde kızılötesi kamera ile gerçekleştirilen performans katsayısı analizleri soncunda; R22, R438A ve R417A akışkanlarının COP değerleri sırasıyla, 3,623, 3,565 ve 2,961 olarak hesaplanmıştır. Bu bağlamda kullanımı önce sınırlandırılıp daha sonra yasaklanan HCFC grubu soğutkanlar içerisinde en çok kullanılan akışkanlardan birisi olan R22 soğutkanına, ticari soğutma sistemlerinde, termodinamik özellikler bakımından R438A akışkanının iyi bir alternatif olacağı ortaya konulmuştur [30].

Banjo ve arkadaşları (2020), soğutma sistemlerinde KIP ve ODP değeri düşük olan soğutkanların kullanımına yönelik bir çalışma gerçekleştirmişlerdir. Bu bağlamda R134a kullanılan bir sisteme alternatif olarak R606a akışkanı kullanarak deneysel bir çalışma gerçekleştirmişlerdir. Soğutma sisteminde 46 gram R606a ve 70 gram R134a soğutkanı ile yapılan kıyaslama sonucunda; COP değerinin %32,2 arttığı ve enerji tüketiminin %4,5 oranında azaldığı görülmüştür. Ayrıca -21°C'lik buharlaşma sıcaklığına R606a akışkanı 1 saatte ulaşırken, R134a akışkanında bu süre 2 saat 15 dakikayı bulmuştur [31].

Sethi ve arkadaşları (2016), endüstriyel soğutuculardа düşük KIP değerine sahip, 3943 KIP değerine sahip R404A soğutkanına alternatif bir soğutucu akışkan kullanımını geliştirmek amacıyla bir çalışma gerçekleştirmişlerdir. Çalışmada, KIP değeri 1273 olan ve yanıcı olmayan R448A soğutkanı ile KIP değeri 146 olan ve hafif yanıcı soğutucu R455A soğutkanı üzerinde durulmuştur. Deneysel süreç, piyasada R404A akışkanına uygun olarak satılan bir soğutucu kullanarak yapılmış olup alternatif olarak görülen her iki akışkan da termodinamik olarak R404A ya benzer özellikler göstermiştir. Kompresörün çalışma süreleri incelendiğinde; R448A soğutkanına sahip sistemin kompresörü %9, R455A soğutkanına sahip sistemin kompresörü ise %6 daha az çalışmıştır. Bu durum hem doğrudan hem de dolaylı emisyonları azaltan bir faktör olarak görülmüştür. Testler ayrıca, bir gömme soğutucu için de R448A ve R404A soğutkanları kullanılarak kıyaslandı. Kıyaslama sonucunda, R448A soğutkanını, dış ortam sıcaklığına bağlı olarak yaklaşık %9'dan %20'ye kadar daha fazla enerji tasarrufuyla sonuçlandığı vurgulanmıştır [32].

Besagni ve arkadaşları (2018), soğutma sistemlerinde düşük küresel ısınma potansiyeline sahip alternatif akışkanlar belirlemek amacıyla çalışmalarda bulunmuşlardır. Çalışmalar sonucunda; düşük sıcaklık uygulamalarında, R32 soğutkanının yüksek COP değerlerine ulaştığı, R290, R152a ve R1243yf geniş çalışma koşulları aralığına sahip olduğu ve bu aralıkta R152a soğutkanının R290 ve R1234yf ile karşılaştırıldığında daha yüksek performans gösterdiği, R1234yf'ni iyi bir performans gösteren bir soğutkan olduğu, R152a ve R290 ile karşılaştırıldığında daha az yanıcı olduğu ve R152a ile karşılaştırıldığında daha düşük KIP' a sahip olduğu sonuçlarına ulaşılmıştır. Ayrıca çalışmada, soğutkandan bağımsız olarak jeneratör ve evaporatör sıcaklıklarının yükselmesinin COP değerini arttırdığı, kondenser sıcaklığı artışının ise enjektörlü soğutma sistemlerinde enjektör performansını düşürdüğü belirtilmiştir [33].

Hmood ve arkadaşları (2021), F-Gaz yönetmeliği doğrultusunda KIP değeri 150'den büyük olan soğutkanların kullanımdan aşamalı olarak kaldırılmasına yönelik, soğutma sistemlerinde R134a'nın yerine geçme olanakları olan çevre dostu soğutucu akışkanlar konusunda çalışma gerçekleştirmişlerdir. Çalışmada, yeni sistem tasarımı anında kullanılabilecek alternatifler, mevcut kullanılan sistemlerde soğutucu akışkanın değiştirilmesi gibi parametreler düşünülmüştür. Çalışmalar sonucunda; R134a soğutkanına en uygun muadil olabilecek çevre dostu akışkanların R1234yf, R152a, R450A ve R513A olduğunu görülmüştür. R290, R600 ve R600a, soğutkanlarının ise yanıcılık sorununun üstesinden gelinerek yani mevcut soğutma sistemi tasarımında bazı değişiklikler yapılarak R134a'nın yerini alabileceği vurgulanmıştır [34].

Oh ve arkadaşları (2016), endüstriyel soğutuculardа saf bir soğutkan yerine birden fazla soğutkan kullanımına olanak sağlayan bir tasarım üzerinden enerji verimliliği miktarını simülasyon çalışması üzerinden incelemişlerdir. Yapılan çalışmada, mevcut sistemde önemli yapısal değişiklikler yapılmasına gerek olmadan soğutucu akışkan karışımı ile enerji tasarrufu sağlanabileceği görülmüş olup farklı tasarımlar üzerinden, %16,3-27,2 arasında enerji verimliliği sağlanabileceği sonucuna ulaşılmıştır [35].

Yılmaz ve Erdinç (2019), farklı soğutucu akışkanlar kullanarak ejektör entegre edilen bir sistemde aşırı soğutma prosesini de içeren bir tasarım gerçekleştirmişlerdir. Yedi farklı soğutucu akışkanın kullanıldığı (R32, R1234yf, R290, R134a, R717, R600a ve R245fa) sistemde her bir soğutkan için enerji ve ekserji analizleri gerçekleştirilmiştir. Gerçekleştirilen yenilikçi tasarımın, klasik soğutma tasarımına göre en iyi performans arttırdığı akışkan R1234yf olmuştur. R1234yf soğutkanı ile çalışan yenilikçi tasarımda konvansiyonel tasarıma göre COP değeri %21, ekserji değeri ise %18 artmıştır. Meydana gelen artışın önemli sebeplerinden birisinin sistemde genleşme valfi yerine ejektör kullanılması olduğu vurgulanmıştır. Ayrıca, yeni tasarımda en yüksek COP ve ekserji değeri R245fa soğutucu akışkanı ile sağlanmıştır. Konvansiyonel sistemde en yüksek COP ve

ekserji değeri ise R717 soğutkanı ile sağlanmıştır [36].

2.4. Endüstriyel soğutucularda ortam şartları ve kontrol tekniği bazlı çalışmalar (Environmental conditions and control techniques based studies on industrial refrigerators)

Endüstriyel soğutucular ortam şartlarından kolayca etkilenebilmekte ve bu durum verimliliklerine yansımaktadır. Ayrıca, endüstriyel soğutucular için yapılan optimizasyonların doğru ve etkin yapılması da verimliliklerini etkileyen bir başka unsurdur. Bu kısımda hem ortam şartları hem de kontrol parametrelerinin endüstriyel soğutuculara olan etkilerini belirten çalışmalar sunulmuştur.

Belman-Flores ve arkadaşları (2019), teşhir tipi soğutucuya ait dolap kapağı ve kompresör hızı arasındaki ilişkiyi bulanık mantık yöntemiyle analiz eden bir kontrol yöntemi tasarlamışlardır. Araştırmacılar, bu tasarımı yaparken soğutucu içerisindeki gıda maddelerinin sıcaklığını olabildiğince referans değerlerde sabit tutmak isterken aynı zamanda enerji tasarrufu sağlamayı amaçlamışlardır. Çalışma sonucunda toplam elektrik enerjisi tüketiminde %3'lük bir tasarruf sağlanırken besin maddelerinin sıcaklıkları daha stabil kalmıştır [37].

Kasera ve arkadaşları (2020), R290 akışkanı kullanan bir endüstriyel soğutucuda, fotovoltaik paneller ile beslenen değişken hıza uyum sağlayabilen DC kompresörü deneysel olarak test etmişlerdir. Güneş enerjisi desteğine tam uyum gösteren bu kompresör maksimum güçte ve değişken devirde kıyaslanmıştır. Sistem maksimum güçte iken 210,9 W enerji harcarken değişken hızda bu değer 162,5 W seviyelerine kadar düşmüştür. Deneysel çalışmalar sonucunda, değişken hızda kontrol edilen kompresörün yaklaşık %30 oranında daha az enerji tükettiği ortaya konulmuştur [38].

Yu ve Chan (2008), soğutma sistemlerinde COP artışı için optimum kondenser fanı kontrolüne ilişkin bir çalışma gerçekleştirmişlerdir. Geliştirilen kontrol mekanizması sayesinde; sistem kompresörleri ve kondenser fanlarının optimize edilmiş güç ilişkileri ile yoğuşma sıcaklığının optimum ayar noktasının belirlenmesini ve kondenserlerin hava akışının ve ısı transfer alanının arttırılması amaçlanmıştır. Ortam ve yük koşullarına bağlı olarak kontrol mekanizması istenildiği gibi çalıştığında COP artışının %11,4–237,2 arasında gerçekleşebileceği modellenmiştir [39].

Jensen ve arkadaşları (2021) yaptıkları çalışmada, endüstriyel soğutuculardaki kompresör kontrol stratejilerinin enerji verimliliğine olan etkisini araştırmışlardır. Çalışmada, yedi farklı tasarım çeşidiyle aç-kapa, değişken hızlı kompresör ve adaptif enerji optimizasyonu modelleri ile araştırmalar yapılmıştır. Kompresör boyutunda yaşanan küçülme güç tüketimini azaltırken, ortalama ürün sıcaklık değerini de düşürmüştür. Adaptif enerji optimizasyonu yöntemi de çalışmalarda boyutu küçük bir kompresör davranışları göstermiştir. Hem değişken hızlı kompresör yöntemi de adaptif enerji optimizasyonu modeli aç-kapa kompresörlere göre enerji tüketiminde önemli azalmalar yaşatmış fakat bu yöntemler ürün sıcaklığında bazı dalgalanmaların oluşmasına da neden olmuştur [40].

Bahman ve arkadaşları (2012), teşhir tipi endüstriyel soğutucuların operasyonel koşullarda iklimlendirme verilerinin soğutucu davranışlarına olan etkilerini incelemişlerdir. Normal koşullarda açık teşhir tip soğutucular 24 °C ve %55 bağıl nemde derecelendirilmektedir. Yapılan çalışmada, bağıl nem oranı yaklaşık %5 azaltılarak %51 seviyelerinde tutulmuş ve diğer koşullar sabit bırakılmıştır. Bunun sonucunda, kabin soğutma yükünün %9,25 oranında azaldığı ve bunun toplam mağaza enerji yükünde %4,84'lük bir azalmayı beraberinde getirdiği ortaya konulmuştur [41].

Koşan ve arkadaşları (2022), R290A soğutucu akışkanı kullanan bir endüstriyel soğutma sisteminde fan kontrol tekniği ile enerji verimlilik indeksi değerini arttırıcı, çevre dostu bir tasarım gerçekleştirmişlerdir. Yapılan yeni kontrol tasarımında hem evaporatör hem de kondenser fanları kontrol edilmiş bu sayede enerji tüketiminde %25,2'lik bir azalma yaşanırken, enerji verimlilik etiketi "E" sınıfından "D" sınıfına düşmüştür [42].

Cirera ve arkadaşları (2020), endüstriyel soğutma sistemlerinde stokastik yük davranışını optimize eden veriye dayalı tahminlerde bulunan bir yük yönetim sistemi geliştirmişlerdir. Deneysel olarak yapılan çalışma sonucunda geliştirilen bu yöntem ile birbirine paralel olarak bağlı çalışan kompresörlerin çalışma süresi %77 oranında azalmış, bu azalma da %17 oranında elektrik enerjisi tasarrufunu beraberinde getirmiş ve bunun yanında kompresörlerin çalışma saatinin azaltılması da sistem kullanım ömrünü uzatan bir gelişme yaratmıştır [43].

Ben-Abdallah ve arkadaşları (2020), endüstriyel soğutma sistemlerine faz değiştirici madde entegresi ve PV paneller kullanarak soğutma sisteminin enerji tüketim durumunu incelemişlerdir. Ayrıca çalışma içerisinde ortam sıcaklığı ve fan gücü tasarım parametreleri de incelenmiştir. Tasarımda fan gücü 25 W'tan 70 W seviyesine yükselince kabinlere dışarıdan hava girişi azalarak infiltrasyon olayı azalmış; ortam sıcaklığının 16 ◦C'den 26 ◦C'ye artması ise faz değiştirici madde için, %20 daha fazla şarj süresi gerektirmiş ve %50 daha az deşarj süresi oluşturmuştur. Faz değiştirici madde entegresi, tasarımda PV panel kullanılmadığı durumlarda enerji talebini %8 azaltırken PV panellerin kullanıldığı durumlarda bu azalmanın oranı %13 olarak belirtilmiştir [44].

2.5. Endüstriyel soğutucularda soğutma çevrimi bazlı çalışmalar (Cooling cycle based studies on industrial refrigerators)

Endüstriyel soğutucularda sistem büyüklüğüne, buhar sıkıştırmalı soğutma çevriminde yapılacak çeşitli ekleme ve değişiklikler ile tasarım yapıları değişebilmektedir. Bu kısımda, endüstriyel soğutucu tasarımında gerçekleştirilen çeşitli çalışmalar sunulmuştur.

Zubair (1990), soğutma sistemlerinde enerji verimliliği kapsamında gerçekleştirmiş olduğu çalışmada, aşırı soğutma uygulaması yapmış ve sistem performansının yoğunlaşma ve buharlaşma sıcaklıkları arasında alt doyma noktasında zirve yaptığını belirtmiştir. Gerçekleştirilen simülasyonlarda, yüksek yoğuşma sıcaklıklarının olduğu dönemlerde sistem performansının aşırı soğutma sistemi kullanılarak %20'ye kadar artabileceğini ve klasik çevrime göre, yüksek sıcaklıklı ve düşük sıcaklıklı soğutma sistemlerinde sırasıyla %20-40 arasında enerji tasarrufunun sağlanabileceği belirtilmiştir [45].

Sánchez ve arkadaşları (2018), R134A akışkanı kullanılan direk soğutmalı bir sistemin iki döngülü ve ikincil sistemde R134a, R152a ve R1234ze(E) akışkanlarının kullanıldığı bir sisteme dönüştürülmesinin enerji tüketimine etkisini araştırıldığı bir çalışma gerçekleştirmişlerdir. Deneysel olarak gerçekleşen çalışmada kapalı tip endüstriyel soğutucu kabinin sıcaklığı 25 °C ve bağıl nemi %55'te sabit tutulmuştur. Tasarımda gerçekleştirilen bu değişim sayesinde; enerji tüketimi değerleri ikincil sistemde kullanılan soğutkana göre; R134a akışkanı için %21,8, R152a akışkanı için %18,7 ve son olarak R1234ze(E) akışkanı için ise, %27,2 azalmıştır. Ayrıca tasarım değişikliği sayesinde; soğutucu akışkana şarj miktarı, ikincil sistem akışkanına göre; R134a için %42,5, R152a için %62,0 ve son olarak R1234ze(E) için %52,3 oranında azalmıştır [46].

Llopis ve arkadaşları (2016), transkritik çevrimin mekanik aşırı soğutma çevrimi ile kombinasyonunu yaparak bir çalışma gerçekleştirmiştir. Ana soğutma çevriminde CO_2, aşırı soğutma çevriminde ise R1234yf soğutkanı kullanılarak 0 °C ve 10 °C evaporatör sıcaklıkları ile 24,0 °C, 30,2°C ve 40,0 °C kondenzasyon sıcaklıklarında sistem optimize edilmeye çalışılmış ve veriler deneysel olarak kıyaslanmıştır. Sistemde aşırı soğutma çevrimi kullanılmasıyla birlikte; ölçülen maksimum COP koşullarında kapasitedeki artışlar, 0,0 °C buharlaşma seviyesinde %23,1 ile %39,4 arasında ve -10,0 °C'de %24,2 ile %55,7 arasında artış göstermiştir [47].

Roy ve Mandal (2018), aşırı soğutma çevrimiyle entegre edilmiş buhar sıkıştırmalı soğutma çevrimi tasarımı gerçekleştirmişler, bu sistemin enerji ve ekserji analizlerini yapmışlar sonrasında ise bu sistemi geleneksel buhar sıkıştırmalı soğutma çevrimi ile kıyaslamışlardır. Aşırı soğutma kullanılan ve kullanılmayan her iki sistemde de soğutkan olarak R134a akışkanı kullanılmıştır. Aşırı soğutma çevrimi kullanıldığında, sistemin soğutma yükü yaklaşık %11 artmıştır. Sistemin COP artışı, aşırı soğutma ile evaporatör sıcaklıkları 0 ˚C ve -10 ˚C olduğunda sırasıyla %11,4 ve %16 olarak hesaplanmıştır. Aşırı soğutma entegresi ile, ekserji yıkımı ise belirtilen evaporatör sıcaklıkları için sırasıyla %17,8 ve %8,8 oranında azalmıştır [48].

Yu ve arkadaşları (2009), merkezi soğutma sistemleri ile plug-in soğutma sistemleri kıyaslanmıştır. Yapılan çalışmada, merkezi sistem tasarımıyla hava perdesi hızı kontrolünün daha kolay sağlandığı, kabin iç yapısının daha rahat tasarlanabildiği, kabin içerisinde karlanmanın azaldığı, buna bağlı olarak defrost süre aralıklarının arttırılarak, 6 saatten 9 saate çıkarabileceği, maksimum ürün sıcaklık farkının 3 ˚C'den 2 ˚C'ye düşürülebileceği sonuçlarına ulaşılmıştır [49].

Gullo (2019), Dünya'da çevresel hassasiyetler sonucu çıkan regülasyonların etkisiyle endüstriyel soğutma sistemlerinde yenilikçi tam entegre R744 soğutkanını kullanan bir tasarım gerçekleştirmiştir. Yapılan tasarımda, doğrudan alan ısıtma ve soğutma, kabinlerde ürün soğutması yapılarak çok enjektörlü CO_2 soğutkanına tam entegre bir yapı oluşturulmuş ve bu sayede süpermarketlerde yaygınlaşması düşünülen bir yapı kurgulanmıştır. Çalışmada, bu yöntemin özellikle hava sıcaklığı yüksek olan şehirlerde, HFC temelli sistemlere göre enerji tüketiminde ve karbon ayak izinde meydana getireceği düşüşün; sırasıyla %33,3 ve %89,5 olacağı tahmin edilmiştir [50].

Sun ve Wang (2022), endüstriyel soğutuculardа kaskad tip soğutma tasarımıyla enerji verimliliğini arttırmak amacıyla bir çalışma gerçekleştirmişlerdir. Yapılan çalışmada, R1150/R717 soğutucu akışkanlarını kullanan iki döngülü bir endüstriyel soğutucu ile R1150/R41/R717 soğutucu akışkanlarını kullanan üç döngülü bir endüstriyel soğutucu sistem tasarımı kıyaslanmıştır. Çin'e ait 5 farklı iklim bölgesinde yapılan kıyaslama çalışması sonrasında; iki döngülü sistemin kompresörünün giriş gücünün üç döngülü sisteme göre 1,45-1,61 kW daha düşük olduğu, iki döngülü sistemin COP değerlerinin üç döngülü sisteme göre her bölgede daha yüksek olduğu ve iki döngülü sistemin enerji tüketiminin üç döngülü sisteme göre bölgesel bazda yıllık %8,6-10,2 oranında yüksek olduğu hesaplanmış ve iki döngülü sistemi üç döngülü sistem yerine kullanılmasının daha fizibil olduğu tespit edilmiştir [51].

Karampour ve Sawalha tarafından (2017), İsveç'te yer alan bir süpermarketteki entegre CO_2 transkritik sisteminin enerji verimliliği değerlendirmesi gerçekleştirilmiştir. Çalışmada, ortam ve sıcak su ısıtma, ortam soğutma (klima) ve teşhir tipi dolaplarda ürün soğutma uygulaması gerçekleştirildiği komplike bir sistem tasarımı yapılmıştır. Yapılan tasarımın enerji verimliliği açısından gerçekleştirilen simülasyon temelli değerlendirmesinde; sistemin, Kuzey Avrupa'da ürün soğutma, ısıtma ve klima için bağımsız geleneksel HFC çözümlerine kıyasla yaklaşık %11 daha düşük miktarda elektrik enerjisi tüketeceği tahmin edilmiştir [52].

2.6. Endüstriyel soğutuculardа hava akışı bazlı çalışmalar (Airflow based studies on industrial refrigerators)

Endüstriyel soğutuculardа özellikle gıda maddelerinin istenilen sıcaklıkta, homojen sıcaklık gradyanıyla muhafaza edilmesi hem ürün sağlığı hem de ürün dayanımı için oldukça önemlidir. Sıcaklık dağılımının soğutma kabini içerisinde dengeli dağılımı, istenilen ürün muhafaza sıcaklıklarının en verimli şekilde korunabilmesi amacıyla hava perdesi ve kabin geometrisi temelli yapılan çalışmalar bu kısımda sunulmuştur.

Yuan ve arkadaşları (2022), açık teşhir tip bir endüstriyel soğutucuya kanatçık entegresinin sistem performansı ve enerji tüketimine etkisini deneysel olarak incelemişlerdir. Yapılan çalışmada, kabinin kanatçıklı şekilde tasarlanmasıyla, kabin içerisindeki maksimum sıcaklık farkı 0.6˚C azalmış, ısı sürüklenme faktörü %38,7-50 oranında düşmüş ve toplam enerji tüketiminde ise %21,7 oranında azalma sağlanarak faydalı bir tasarım ortaya konulmuştur [53].

Lin ve arkadaşları (2023), açık teşhir tipi bir soğutucunun kabin geometrisinin, soğutma performansı üzerine olan etkisini incelemişlerdir. Çalışmada, soğutma kabini arka panelinde yer alan hava deliklerinin soğutucu kabin içerisindeki hava akışına etkisi araştırılmıştır. Hava deliklerinin soğutma kabinin alt kısmına doğru yerleştirilmesinin paketli gıdaların sıcaklık kontrolü için daha uygun olacağı sonucuna ulaşılmıştır. Ayrıca çalışmada gıda ambalajlarının kullanıldığı malzemelerin hava akışı için önemli bir etken olduğundan da bahsedilmektedir [54].

Tsamos ve arkadaşları (2019), açık teşhir tipi endüstriyel soğutucu raflarının ön yüzeyinde hava yönlendirici

kanatçıklar kullandıkları yeni nesil bir tasarım ile geleneksel tasarımı simülasyon ortamında kıyasladıkları bir çalışma gerçekleştirmişlerdir. Geleneksel tasarım 42 kWh/gün enerji harcarken gerçekleştirilen kanatçıklı tasarımın enerji tüketimi 25,3 kWh/gün olmuştur. Bu bağlamda kabine yapılan bu entegre sayesinde yaklaşık %60 oranında enerji tasarrufu gerçekleştirilmiştir [55].

Li ve arkadaşları (2022), açık teşhir tip endüstriyel soğutucularda bir hava perdesi yerine iki hava perdesi kullanarak bir çalışma gerçekleştirmişlerdir. Çalışmada, hava perdesi hızının kontrolsüz artışının operasyon için olumsuz olduğu, kabinin hava tahliye ızgarası açısının tasarım için önemli olduğu açıklanmış ve buna göre farklı operasyonlar gerçekleştirilmiştir. Çalışmaların sonucunda, çift hava perdeli soğutucu tek hava perdeli soğutucuya göre her zaman daha iyi performans sergilemiş ve yapılan çalışmalarda, %29-41,6 arasında enerji tasarrufu sağlandığı hesaplanmıştır [56].

Wu ve arkadaşları (2014), dikey açık teşhir tipi endüstriyel soğutucularda kabinin arka panel yapısının akış ve ısı transferi üzerine etkisini inceledikleri bir çalışma gerçekleştirmişlerdir. Çalışmada, arka panelde yer alan deliklerin sayısı ve farklı konumlara yerleştirilmesi sonucunda arka panel ve hava perdesi akışı arasındaki karakteristik incelenmiştir. Çalışmada, %3'ten daha az gözenekli yapının akış için olumlu olduğu, delik konumlarının ise ürünlerin sıcaklık dağılımı üzerine küçük bir etkisi olduğu belirtilmiştir. Raflardaki gözenekli yapının optimizasyonu sayesinde ürünler arasındaki maksimum sıcaklık farkı sapması %49'a kadar iyileştirilmiştir [57].

Nikitin (2020), açık teşhir tip bir endüstriyel soğutucuda tek hava perdesi yerine iki hava perdesi kullandığı çalışma verilerini kıyaslamıştır. Eklenen hava perdesinin çok büyük bir tasarımsal değişiklik gerektirmediği ve tasarım maliyetini fazla arttırmadığı belirtilen çalışmada, yapılan simülasyon sonucunda, iki hava perdeli tasarımın, kullanılabilir etkin hacmi %13 oranında arttırabileceği belirtilmiştir [58].

Hammond ve arkadaşları (2016), teşhir tipi endüstriyel soğutucularda kullanılan hava perdesi yaklaşımlarına ilişkin bir çalışma gerçekleştirmişlerdir. Yapılan çalışmada, geleneksel teşhir tipi dolaplarında bulunan tek sütun şeklinde dağılan hava perdesi yerine Şekil 7.'de görsel tasarımı sunulan raflar arasına kısa mesafeli hava perdesi tasarımı yaklaşımı ortaya konulmuştur. Kısa hava perdesinin sıcaklık dağılımının daha homojen olmasını sağlama ve daha verimli bir soğutma ortaya koyacağı düşünülerek gerçekleştirilen çalışmada, enerji tüketimi 47,63 kWh/gün'den 30,54 kWh/gün değerine düşmüş ve sıcaklık stabilitesinin %67 oranında daha fazla geliştirildiği sonuçlarına ulaşılmıştır [59].

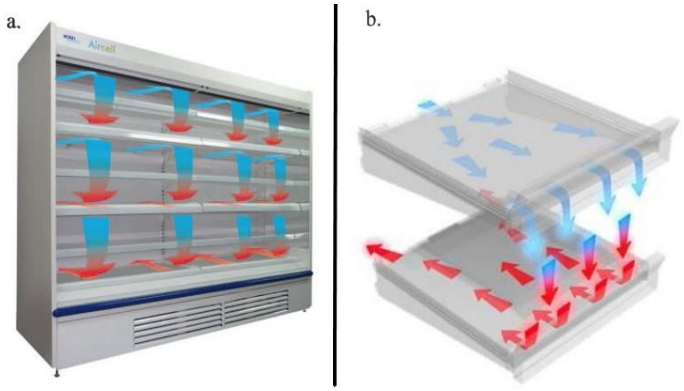

Şekil 7. a- Kısa mesafeli hava perdesi tasarımı, b- Raflar arasındaki hava akışı detayı [59] (a- Short distance air curtain design, b- Air flow detail between shelves)

XueHong ve arkadaşları (2017), açık teşhir tip bir soğutucu içerisinde faz değiştirici madde geçen yeni nesil kompozit bir raf tasarlamışlar ve bunu geleneksel raflarla kıyaslamışlardır. Kompozit raflarda geleneksel raflara göre ürünlerin daha homojen sıcaklık eğilimi gösterdiği ve maksimum sıcaklık farklarının %13.7–32 oranında düştüğü, defrost süreci boyunca ise raflarda bulunan besinlerin sıcaklık dalgalanmalarının %53,3–83,3 oranında azaldığı ortaya konulmuştur [60].

Jouhara ve arkadaşları (2017) açık teşhir tip soğutucu raflarına, düz ısı borusu teknolojisiyle yeni bir tasarım gerçekleştirmişler ve tasarımın enerji tüketimi, gıda muhafaza koşullarına olan etkisini araştırmışlar, konvansiyonel ticari raflarla bu raf tipini belirtilen değişkenler üzerinden kıyaslamışlardır. Deneysel çalışmalarda, ısı borulu yenilikçi raflarının kullanımının, ürünlerin sıcaklık profilini homojenleştirdiği ve raflar ile ürünler arasındaki ısı transferini iyileştirebildiği göstermiştir. Bunun yanında bu yenilikçi tasarım sayesinde endüstriyel soğutucunun enerji tüketimi yaklaşık %12 oranında azalmıştır [61].

Chaomuanga ve arkadaşları (2019), kapalı tip endüstriyel soğutucuları açık tip soğutucularla kıyasladıkları bir çalışma gerçekleştirmişlerdir. Endüstriyel soğutuculardaki kabinlerin ön kısmı daha yüksek sıcaklığa sahipken arka taraflarda sıcaklık daha düşük olmaktadır. Bu durum sıcaklık heterojenliğine yol açarken, soğutucularda kapı kullanmanın bu duruma etkisi gözlemlenmek istenmiştir. Yapılan deneysel çalışmada, kapı kullanılan durumlarda kabinin muhtelif yerleri arasındaki maksimum sıcaklık farkları 2,1 °C iken kapı kullanılmadığı durumlarda ise bu fark 4,9 °C'e kadar çıkmıştır. Bu yönden ürün sıcaklıklarının homojenliği kapı kullanılarak daha iyi bir noktaya çıkarılmıştır. Ayrıca çalışmada, kabinin yüklenme durumunun hava akışına etkisi de incelenmiş ve yükleme yüzdesinin, delikli plakadan geçen hava akış hızını önemli ölçüde etkilemediği vurgulanmıştır [62].

Sun ve arkadaşları (2017), açık teşhir tip soğutucularda hava akışının sağlıklı olabilmesi maksadıyla yaptıkları yeni tasarıma simülasyon analizleri gerçekleştirmişlerdir. Yapılan çalışmada, Şekil 8.'de gösterildiği üzere endüstriyel soğutucuda hava kılavuz şeritleri kullanmanın, hava perdesi etkisini dikey olarak kuvvetlendirdiği ve ortam havasının kabin içerisine sızmasını önlediği, şerit kullanımının kabindeki hava sıcaklığını 4,9 °C düşürdüğü ve bu düşüşün gerekli soğutma kapasitesini %34 oranında azalttığı sonuçlarına ulaşılmıştır [63].

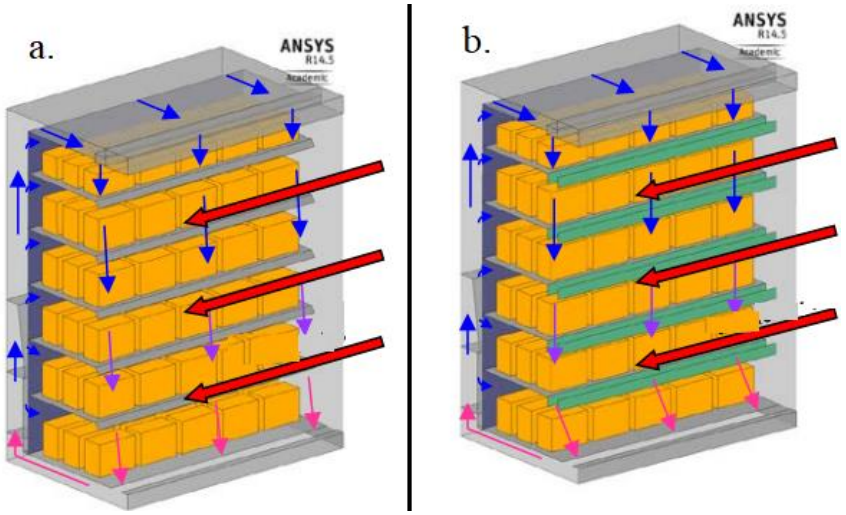

Şekil 8. a- Geleneksel soğutma kabini yapısı, b- Yenilikçi kabin yapısı [63] (Traditional cooling cabinet structure, b- Innovative cabinet structure)

Wang ve arkadaşları (2021), çift sıcaklıklı açık teşhir tip endüstriyel soğutucular üzerine bir çalışma gerçekleştirmiştir. Yapılan çalışmada ortaya konulan tasarımla, teşhir tip soğutucu depolanan ürünlerin hem soğutulmasını hem de ısıtılmasını sağlayabilmektedir. Çalışma esnasında, çift sıcaklıklı açık tip endüstriyel soğutucunun arka panel deliklerinin yüksekliği ve fan boyutlandırılması temel alınarak tasarım optimize edilmeye çalışılmıştır. Çalışmada, açık teşhir tip endüstriyel soğutuculardaki büyük bir fan kullanmanın yalnızca hava perdesi akış hızını arttıracağı bunun dışında hava perdesi yapısına bir etkide bulunmayacağı belirtilmiştir. Bunun yanında soğutma havasının yaklaşık %25'i arka panellerdeki deliklerden sağlandığından, deliklerin konumu ve yüksekliği hava perdesine ciddi oranda etki ettiği ve bunların her bir dolap özelinde optimize edilmesinin oldukça önemli olduğu belirtilmiştir [64].

3. Tartışma (Discussion)

Endüstriyel soğutucuların dünya genelindeki enerji tüketimine bakıldığında, dünyada tüketilen elektrik enerjisinin %6'sı gibi ciddi bir orana sahip oldukları görülmektedir [65]. Bu oranın ekonomik yansımaları hem son tüketici bazında işletmelere hem de ulusal bazda devletlere azımsanmayacak bir maliyet çıkarmaktadır. Bunun yanında gerek küresel boyutta yapılan uluslararası sözleşmeler gerekse de lokal düzenlemeler endüstriyel soğutucuların hem elektrik enerjisi tüketimi hem de soğutkan salınımı yönlerinden çevreye olan etkilerinin azaltılmasını gerekli hale getirmiştir.

Günden güne sayıları artan süpermarketlerin içerisinde yer alan endüstriyel soğutucuların verimliliklerinin artmasının ve çevreye olan tahribatlarının azaltılmasının kümülatif faydalarının olacağı çok açıktır. Bu sebeple, endüstriyel soğutucu tasarımlarında ve soğutucuların operasyon koşullarında gerçekleştirilecek her iyileştirme sürdürülebilirliğe katkı sağlayacaktır.

Gerçekleştirilen bu çalışmada, endüstriyel soğutma sistemlerinde yapılabilecek iyileştirmeler gruplandırılarak sürece olabildiğince farklı perspektiflerden bakılmaya çalışılmıştır. Bu bağlamda; endüstriyel soğutucu komponentleri, yalıtım çalışmaları, endüstriyel soğutucuların dış ortam şartları ve soğutucularda kontrol yöntemleri, kullanılan soğutkan çeşitleri, soğutma çevriminde yapılan iyileştirmeler ve hava akışı konularında gerçekleştirilen önemli çalışmalar incelenerek, çıktıları sunulmuştur.

Endüstriyel soğutucular içerisinde yer alan komponentlerin her birinin son teknolojik gelişmelere uyum sağlayabilmeleri, verimliliklerinin yüksek olması ve uzun süre kullanılma imkanına sahip olmaları oldukça önemlidir. Bu başlık altında dikkat çeken en önemli sistem bileşenlerinden birisi şüphesiz kompresörlerdir. Kompresörler, soğutma sistem ekipmanları içerisinde en fazla enerji tüketimine sahip olduklarından, yapılacak iyileştirmeler sistemin bütününe olumlu katkılar vermektedir. Kompresörler özelinde, aç/kapa tip kompresörler yerine değişken devirli kompresör kullanımın, kompresörlerde doğru yağlama yağları seçimi yapılmasının, soğutma kapasitesine uygun tipte bir kompresör seçimi gerçekleştirmenin, kompresör gücü ve kompresör sayısının soğutma yüküne uygun olmasının, kompresörlerin olabildiğince sabit basınç ve sıcaklık değerleri üzerinden çalışmasının ve sistemde kullanılan soğutkanın termodinamik olarak kompresöre uygun olmasının enerji tüketimi açısından oldukça fazla önemi olduğu görülmektedir.

Endüstriyel soğutma sistemlerinde kullanılan önemli diğer ekipman kondenserdir. Tasarımlarda kullanılan kondenserlerin mikro kanal yapıda tercih edilmesi genellikle ısı transferi sürecini olumlu hale getirmektedir. Bunun yanında bu tip kondenserlerin kirli ortamlarda kullanımı mikro kanallar içerisine biriken çeşitli partiküller sebebiyle çevrime zarar da verebilmektedir. Kondenser seçimi yapılırken soğutucu akışkan şarjı miktarını minimum değere indirebilecek tasarımlar yapılmalı, tasarımlarda ısı iletim katsayısı yüksek malzemeler kullanılmalı, ekipman temizliği düzenli olarak sağlanmalı, gerektiğinde ve özellikle mevsim geçişi zamanlarında sisteme olumlu katkılar verecek dinamik kondenzasyon uygulaması tercih edilmelidir.

Soğutma çevriminde kullanılan bir diğer ekipman da genleşme valfleridir. Endüstriyel soğutma sistemlerinde verim arttırıcı çalışmalar esnasında; kontrol sistemlerine daha iyi adapte olması nedeniyle mekanik genleşme valfi ve kapiler borular yerine elektronik genleşme valfi kullanımı, genleşme valfi yerine ise kompresör yükünün küçültmesini sağlamanın yanında daha küçük evaporatör ve kondenser boyutları kullanımına imkân sağlaması sebepleriyle ejektör kullanımı sıkça görülmektedir. Bunun yanında soğutucu şarjı ve elektrik enerjisi tüketimi açısından genleşme işleminde kullanılan kapiler boru uzunluğu dikkat edilmesi gereken bir başka nokta olarak karşımıza çıkmaktadır.

Soğumanın fiziksel olarak hissedildiği sistem bileşeni olan evaporatör ünitesi tasarımında da önemli noktalar bulunmaktadır. Evaporatörlerde dikkat edilmesi gereken en önemli nokta karlanmanın kısa sürede defrost işlemiyle çözülmesi işlemidir. Karlanmanın yanında kirlenmenin önlenmesi için evaporatörlerin temizliği planlı şekilde yapılmalıdır. Sistem tasarımında ısıl iletkenlik katsayısı yüksek, kanatçıklı yapıda evaporatör tasarımı ısı transferini kolaylaştıracaktır.

Bunun yanında endüstriyel soğutuculardа aydınlatma sistemleri hem estetik açısından hem de işlevsel açıdan oldukça kritiktir. Aydınlatma sistemleri olarak enerji tasarruf özelliği yüksek ve estetik açıdan güçlü LED ışık kaynağı tasarımları enerji tüketimini azaltmanın yanında dikkat çekici görüntüler sunması nedeniyle satışlar açısından ticari olarak da tercih sebebi olmaktadır.

Değerlendirme yapılan bir diğer konu başlığı da endüstriyel soğutucuların yalıtımıdır. Endüstriyel soğutuculardа en önemli yalıtım yöntemi açık tip soğutuculara kapak takılmasıdır. Enerji tüketimini ciddi oranda azalmasını sağlayan kapalı tip endüstriyel soğutucular süpermarket içerisindeki havalandırma sisteminin kontrolü açısından da daha avantajlıdır.

Endüstriyel soğutuculardа bir diğer yalıtım yöntemi açık tip soğutuculardа kullanılan gece perdesidir. Süpermarketin açık olmadığı zamanlarda ve satışın olmadığı saatlerde kullanılan gece perdeleri sayesinde, endüstriyel soğutucuya dışarıdan hava girişi miktarı azalmakta ve soğutucu daha uzun süre stabil sıcaklığa sahip olabilmektedir.

Yalıtım sürecinde dikkat edilmesi gereken bir başka nokta da kapalı tip soğutucu kapaklarında kullanılan contaların büyüklüğünün kapakla uyum göstermesi ve hava kaçaklarının minimum düzeye inmesidir. Bunun yanında kapak conta bakımlarının düzenli olarak yapılması da enerji verimliliği için oldukça önemli bir parametredir.

Enerji verimliliği yüksek tasarımlardа kullanılan bir diğer yöntem ise dolap kapaklarının anti-fog malzeme ile kaplanarak çiylenme noktası sıcaklığını arttırmak veya kapak çerçeve kenarları ve camları üzerine rezistans ekleyerek kapaklardа oluşan buğulanmayı önlemektir. Oluşan buğulanmayı önlemek sadece enerji verimliliği açısından değil aynı zamanda ticari olarak, ürün görülebilirliği ve satışlar açısından da önemlidir.

Endüstriyel soğutucuların karbon salımı konusunda soğutkanlar büyük sorumluluğa sahiptir. Soğutkan seçimi yalnızca soğutkanın doğrudan çevreye karbon salımı noktasında değil, tüm sistemin verimliliği noktasında da önemli bir etken olduğundan, endüstriyel soğutma sistemi ile termodinamik ve fiziksel olarak tam uyum gösteren bir soğutucu akışkan seçimi yapmak tasarım esnasında oldukça kritiktir. Tasarım ile uyum içerisinde çalışan bir soğutkan enerji verimliliği yaratabileceğinden kullanılan elektrik enerjisi miktarı düşecek ve dolaylı olarak da çevreye pozitif anlamda katma değer yaratan bir süreç gerçekleşmiş olacaktır. Özellikle son 20 senede kullanılan soğutkanlara ilişkin küresel ölçekte ve yerel düzeyde birçok düzenleme gerçekleştirilmiştir. Bu düzenlemeler ile; CFC gazların tüketimi yasaklanmış daha sonrasında ise, HCFC gazlarının kullanımı önce sınırlandırılmış ardından tamamen yasaklanmıştır. Mevcut durumda, bazı HFC grubu gazların da kullanımı sınırlandırılmıştır. Bu yasaklama ve sınırlandırmanın en büyük sebebi, ilgili gazların KIP ve ODP potansiyellerinin oldukça yüksek olması olmuştur. Endüstriyel soğutma sistemlerinin tasarım aşamasında, çevresel tahribat açısından KIP ve ODP değerleri düşük akışkan seçimi gerçekleştirilmelidir. Bununda yanında seçilecek olan akışkan, yapılacak olan tasarıma uyumlu termodinamik muhteviyatta olmalı ve fiziksel açıdan da kullanım ortamına uygun özellikler barındırmalıdır.

Endüstriyel soğutuculardа sıklıkla tercih edilen R134a akışkanının kullanımının son zamanlarda sınırlandırılmaya başlamasıyla birlikte bu akışkana muadil olarak benzer termodinamik özellikler göstermenin yanında daha çevreci özelliklere sahip olan R1234ze ve R1234yf akışkanları tasarımlarda tercih edilmektedir. Yine geçmiş dönemde sıkça kullanılan R22 akışkanına alternatif olarak ise, R438A ile R417A akışkanlarının kullanımı yaygınlaşmaktadır. Bunun yanında tasarımlarda; R410A, R290A ve R404A akışkanlarının da sıklıkla tercih edildiği görülmektedir. Ayrıca çalışmalarda, akışkan seçiminin tasarım bazlı ve çalışma koşullarına göre yapılması gerektiği açıkça vurgulanmaktadır.

Endüstriyel soğutma sistemlerinde verimlilik arttırıcı unsurlarda incelenen bir diğer başlık da sistemin kontrol edilebilir tasarıma sahip olması ve ortam şartlarıdır. Endüstriyel soğutuculardа kullanılan sistem bileşenleri belirli sınırlar dahilinde çalışan cihazlardır. Bu cihazların şartlara ve zamana bağlı olarak, zaman zaman sınır noktalarının daraltılabilmesi sistemin daha az enerji tüketmesini sağlamaya imkân tanır. Özellikle

sistem kompresörü ve fanların belirli bir algoritma doğrultusunda çalışmalarının optimize edilmesi enerji verimliliği açısından son derece olumlu sonuçlar vermektedir. Ayrıca endüstriyel soğutucular ve özellikle soğutma kabinleri ortam şartlarından son derece kolay şekilde etkilenebilmektedir. Bu nedenle, ortam sıcaklığı ve bağıl nem başta olmak üzere soğutma sistemlerinin konumlandırıldığı ortamın fiziksel özelliklerinin yapılan tasarım kriterlerine uygun ve olabildiğince stabil olması sistem verimliliği açısından olumlu olacaktır.

Buhar sıkıştırmalı çevrimi kullanılan endüstriyel soğutma sistemlerinde verimliliğinin arttırılması amacıyla çevrime eklemeler yapılabilmekte ve tasarım tipleri değişebilmektedir. Buhar sıkıştırmalı soğutma çevrimine en yaygın entegre edilen yöntemler, aşırı soğutma ve aşırı kızdırma uygulamalarıdır. Aşırı soğutma uygulamasıyla, soğutkanın kondenser çıkışında aşırı soğutularak evaporatörde daha fazla ısı çekmesi sağlanır ve böylelikle sistemin COP değeri artar. Ayrıca aşırı soğutma uygulaması, kondenserden çıkan soğutucu akışkanın buhar kabarcıkları şeklini alarak genleşme valfine girmesi, genleşme valfi kapasitesinin düşmesi ve buharlaştırıcıya giren soğutucu akışkan miktarının azalması gibi etkileri de engellenmektedir. Evaporatör çıkışında gerçekleşen aşırı kızdırma uygulaması ise, soğutulan ortamdan daha çok ısı enerjisi çekilmesini ve böylelikle COP değerinin arttırılmasını amaçlar. Bunun yanında bu uygulama sayesinde, kompresöre sıvı fazda soğutkan girmesi de önlenir. Her iki yöntem de sistem performansını doğrudan etkilemekte, soğutma kapasitesi ve enerji verimliliğinde önemli oranda artış sağlanabilmektedir.

Bunun yanında soğutma yüküne, soğutulacak malzeme çeşidi, büyüklüğü ve soğutma amacına göre farklı tasarım çeşitleri bulunmaktadır. Özellikle süpermarketlerde, bakım maliyetleri düşük olan ve hareket özgürlüğü sağlayan plug-in endüstriyel soğutma sistemleri fazlaca kullanılırken, evaporatör ünitesinde soğutulan havanın çekilen tesisatla, borulama yardımıyla, dağıtıldığı merkezi soğutma sistemleri de yüksek soğutma talebine ihtiyaç duyulan noktalarda sıklıkla kullanılabilmektedir. Ayrıca, soğutma yükünün daha az olduğu durumlarda merkezi endüstriyel soğutma sistemlerine alternatif olarak geliştirilen, evaporatörlerin soğutucu kabinlere nispeten daha yakın konumlandırıldığı, bölünmüş tip endüstriyel soğutma sistemleri de son zamanlarda yaygın şekilde perakendecilik sektöründe yerini almaktadır.

Endüstriyel soğutucu tasarımlarında üzerinde durulan son başlık hava akışı olmuştur. Soğutma dolaplarında saklanan ürünlerin maksimum sıcaklık farklarının olabildiğince az ve homojen olması, enerji tüketimi ve ürün sağlığı açısından oldukça değerlidir. Hava akışının sağlıklı olabilmesi için ve ürün sıcaklık dağılımlarında homojenliğin sağlanabilmesi açısından; endüstriyel soğutma kabinlerinde kompozit malzemeler ve kanatçık kullanımı son dönemde oldukça yaygınlaşmıştır. Bunun yanında soğutucu kabinlerin arkasında yer alan hava deliklerinin konumu ve sayısının doğru belirlenmesi, arka panelde kullanılan malzemenin yapısının gözenekli olması, raflar arasında kısa mesafeli hava perdesi tasarımları, kompozit malzeme içerikli raf tasarımları, çift hava perdesi kullanılan tasarımlar gibi birçok yöntem tasarım bazlı kullanılmış ve hava akışına farklı oranlarda önemli katkılar sağlanmıştır.

Küresel ve yerel bazda alınan karbon salınımı önlemleri, son kullanıcılar ve ülkelerin enerji tüketimlerinde verimlilik arayışı, buna bağlı olarak son kullanıcıların girdi maliyetlerini azaltma çabaları, ülkelerin bahsedilen regülasyonlara uyma zorunluluğu, yoğunlukla enerji ithalatçısı ülkelerin enerji tüketimlerinde yer alan verimsiz yönleri bir an önce azaltarak cari açıklarını azaltmak istemeleri, özellikle Avrupa ülkelerinde enerji verimliliği süreçlerine yönelik ürün satışını kısıtlayıcı standartların oluşması gibi birçok sebep endüstriyel soğutma sistemlerinde enerji verimliliği çalışmalarını hız kazandırmıştır. Bu konuda özellikle, AB üyesi ülkelerde 2019 senesinde yürürlüğe girmiş olan "Eko Tasarım" gereklilikleri soğutucu cihazlar için de çeşitli zorunluluklar getirmiştir. Saklanan ürünün muhteviyatı ve tasarlanan dolabın özelliklerine göre tasarım gereklilikleri ayrıntılı şekilde açıklanan düzenlemede, A ve G arasında yapılan sınıflandırma ile enerji verimlilik endeks değeri belirlenmektedir. Piyasaya yeni sürülecek olan endüstriyel soğutucular için ilgili düzenlemeyle, 1 Mart 2021'den itibaren enerji verimliliği endeksi değerinin 100 değerinden küçük olma zorunluluğu, 1 Eylül 2023'ten itibaren ise 80 değerinden küçük olma zorunluluğu getirilmiştir. Gerek AB üyesi ülkelerde bulunan gerekse de bu ülkelere ihracatçı konumunda olan ve piyasaya ürün satmak isteyen üreticilerin belirtilen enerji etiketi değerine ve eko tasarım gerekliliklerine uygun hareket etmesi ticari olarak

zorunluluk oluşturmuştur.

Çevresel olarak bahsedilen gereklilikler yanında daha uzun vadeli ve geniş kapsamlı olarak çevreci yaklaşımların da geliştirilmesi değerlidir. Bu noktada, piyasaya sunulan endüstriyel soğutucuların LCCP analizlerinin gerçekleştirilerek termodinamik ve eko tasarım gereklilikleri göz ardı edilmeden; malzeme seçimi, soğutkan seçimi, enerji tüketimi, operasyonel koşullar ve ürünün kullanım ömrü tamamlandığında yapılacak bertaraf çalışmaları da dahil birçok parametre dikkate alınarak mümkün olan en çevreci tasarım ortaya konulmalıdır. Bu yönüyle LCCP analizlerinin de uygulandığı bir tasarım, yalnızca sera gazı emisyonunu azaltmayacak aynı zamanda dünyanın daha sürdürülebilir ve yaşanabilir bir alan olması amacına da hizmet edecektir.

Çalışmada başlıklar halinde sunulan ve bu kısımda tartışılan yöntemlerin bir kısmının uygulanması dahi, bu cihazların enerji verimliliğini yükselterek enerji etiket değerlerinin düşmesini sağlayacaktır. Dünya genelinde milyonlarca bulunan bu cihazlarda sağlanacak en küçük verimlilik dahi küresel enerji tüketiminin azaltılmasını sağlayarak çevresel süreçlere olumlu katkılar verecektir. Ülkelerin karbon vergisi çalışmalarını hızlandırdığı bu dönemde, daha verimli endüstriyel soğutucu kullanımı perakende sektöründe yer alan zincir marketler başta olmak üzere, birçok son kullanıcıyı doğrudan ve olumlu yönde etkileyecektir. Bunun yanında, ülke enerji tüketiminde yaşanacak tasarruf ile aynı miktar kurulu güç ve elektrik enerjisi üretimiyle daha fazla sistem çalışacağından ülkelerin gelişmişlik düzeyinin göstergesi olan enerji verimliliği konusunda ülke genelinde önemli bir gelişim yaşanabilecek ve bunun doğrudan ve dolaylı yansımaları da katma değer oluşturacaktır.

4. Sonuç (Result)

Gerçekleştirilen bu çalışma ile, endüstriyel soğutucularda enerji verimliliğini arttıran, performans katsayısının yükselmesini sağlayan ve çevreci yaklaşımlar içeren çeşitli çalışmalar incelenerek derlenmiş, farklı bakış açılarıyla endüstriyel soğutucularda enerji verimliliği yaratan yöntemler, araştırmacı ve ürün üreticilerine tasarım girdisi olması maksadıyla sunulmuştur. Çalışmada sunulan bu girdiler dikkate alınarak gerçekleştirilecek yeni nesil tasarımlar ile daha az enerji kullanımı sağlayan ve buna bağlı daha fazla performans gösteren verimli endüstriyel soğutucular üretilebilecek ve bu sayede daha çevreci, doğaya karbon salınımı azalmış, ürün grupları oluşturulabilecektir.

Çıkar Çatışması Beyanı (Conflict of Interest Statement)

Yazarlar tarafından herhangi bir çıkar çatışması bildirilmemiştir.

Kaynaklar (References)

[1] Y. Salehy, H. M. Hoang, F. Cluzel, Y. Leroy, A. Delahaye, L. Fournaison, and B. Yannou, "Energy performances assessment for sustainable design recommendations: Case study of a supermarket's refrigeration system," *Procedia CIRP*, vol. 90, pp. 328-333, January 2020. doi:10.1016/j.procir.2020.01.102

[2] M. Aktaş, S. Erten, E. Demirci, E. Kılıç ve F. N. Erdoğmuş, *Teknoloji ve Mühendislik Bilimlerine Güncel Bakış: Doğrudan Satış İşlevli Endüstriyel Soğutma Sistemlerinde Enerji Verimliliğinin Arttırılması ve Çevresel Etkilerin Azaltılmasına Yönelik Yapılan Çalışmalar*, Ankara, Türkiye: İksad Yayınevi, 2021, 49-99.

[3] N. Kuduz ve S. Bürhan, "Süpermarketler tarafından yapılan satış geliştirme faaliyetlerinin cinsiyet açısından değerlendirilmesi," *Güncel Pazarlama Yaklaşımları ve Araştırmaları Dergisi*, vol. 1, no. 2, pp. 68-86, December 2020.

[4] H. Kauko, K. H. Kvalsvik, N. Masson, C. Noel, S. Minetto, A. Rossetti, S. Marinetti, D. Thalheim, K. Martens, M. Karampour, S. Piscopiello, N. Fidorra, B. G. Frontera, A. Saez de Guinoa, L. M. Toledo, S. Ciconkov, V. Ciconkov, "Proposal for the Development of the EU Ecolabel Criteria for Food Retail Stores," ec.europa.eu, January 18, 2019. Available: https://ec.europa.eu/research/participants/documents/downloadPublic?documentIds=080166e5c2381d34&appId=PPGMS. [Accessed: 13 Oct. 2023].

[5] M. R. Braun, H. Altan H., and S. B. M. Beck, "Using regression analysis to predict the future energy consumption of a supermarket in the UK", *Applied Energy*, vol. 130, pp. 305-313, October 2014. doi:10.1016/j.apenergy.2014.05.062

[6] S. A Tassou, Y. Ge, A. Hadawey, and D. Marriott, "Energy consumption and conservation in food retailing," *Applied Thermal Engineering*, vol. 31, no. 2–3, pp. 147–156, February 2011. doi:10.1016/j.applthermaleng.2010.08.023

[7] N. A. Shaban, I. Nasser, J. Al Asfar, S. Al-Qawabah, and A. N. Olimat, "Thermodynamic and economic analysis of a refrigerator display cabinet equipped with a DC compressor and electronic expansion valve," *International Journal of Heat and Technology*, vol. 38, no. 2, pp. 432-438, June 2020. doi:10.18280/ijht.380219

[8] Ş. Ünal, M. T. Erdinç ve Ç. Kutlu, "Çift buharlaştırıcılı ve ejektörlü bir soğutma sisteminin termodinamik analizi," *Gazi Üniversitesi Mühendislik Mimarlık Fakültesi Dergisi*, vol. 31, no.4, pp. 1039-1047, Aralık 2016. doi:10.17341/gazimmfd.278459

[9] C. Ocak, M. Koşan, S. Erten, F. N Erdoğmuş, and M. Öder, "Comparison of different compressor technologies for refrigerated display cabinet: Experimental study," *Materials Today: Proceedings*, vol. 81, no. 1, pp. 74-80, 2023. doi:10.1016/j.matpr.2023.01.213

[10] N. Bilir Sag, H. K. Ersoy, A. Hepbasli, and A. S. Halkaci, "Energetic and exergetic comparison of basic and ejector expander refrigeration systems operating under the same external conditions and cooling capacities," *Energy Conversion and Management*, vol. 90, pp. 184-194, January 2015. doi:10.1016/j.enconman.2014.11.023

[11] F. T. Knabben, A. F. Ronzoni, and C. J. L. Hermes, "Application of electronic expansion valves in domestic refrigerators," *International Journal of Refrigeration*, vol. 119, pp. 227-237, November 2020. doi:10.1016/j.ijrefrig.2020.07.029

[12] B. Doğan, M. M. Ozturk, T. Tosun, M. Tosun, and L. B. Erbay, "A novel condenser with offset strip fins on a mini channel flat tube for reducing the energy consumption of a household refrigerator," *Journal of Building Engineering*, vol. 44, pp. 102932, December 2021. doi:10.1016/j.jobe.2021.102932

[13] P. A. Patil, "Performance analysis of HFC-404A vapor compression refrigeration system using shell and u-tube smooth and micro-fin tube condensers," *A Journal of Thermal Energy Generation, Transport, Storage, and Conversion*, vol. 25, no. 2, pp. 77-91, March 2012. doi:10.1080/08916152.2011.562343

[14] L. Zhang, T. Fujinawa, and M. Saikawa, "Theoretical study on a frost-free refrigerated display cabinet," *International Journal of Refrigeration*, vol. 74, pp. 95-104, February 2017. doi:10.1016/j.ijrefrig.2016.09.027

[15] Š. Vidrih, "Strategije za optimizacijo stroškov porabe električne energije hladilne tehnike v nakupovalnih središčih," Magistrsko Delo, Univerza v Ljubljani, Fakulteta za Elektrotehniko, Ljubljani, Slovenija, 2014.

[16] G. G. Heidinger, S. M. Nascimento, P. D. Gaspar, and P. D. Silva, "Relevant parameters on the energy efficiency of closed refrigerated multideck display cases," *WIT Transactions on Ecology and the Environment*, vol. 205, pp. 71-81, January 2016. doi:10.2495/EQ160071

[17] B. Wang, and X. Li, "State of the art of new technologies applied to chillers," in *42nd Informatory Note on Refrigeration Technologies, 30 March 2021, Paris, France*, [Online]. Available: IIR/IIF, https://www.iifiir.org. [Accessed: 13 Oct. 2023].

[18] D. Rauss, S. Mitchell, and R. Faramarzi, "Cool retrofit solutions in refrigerated display cases," *ACEEE Summer Study on Energy Efficiency in Buildings*, vol. 9, pp. 233-244, 2008.

[19] S. Jadhav, S. Panchal, P. Kulkarni, T. Firake, R. Melwanki, and U. Asolekar, "Design of an innovative refrigerated display cabinet," *International Journal Of Engineering Research & Technology (IJERT)*, vol. 9, no. 3, pp. 638-643, February 2021. doi:10.17577/IJERTCONV9IS03133

[20] M. Orlandi, F. M. Visconi, and S. Zampini, "CFD assisted design of closed display cabinets," in *2nd IIR International Conference on Sustainability and the Cold Chain, 2-4 April 2013, Paris, France* [Online]. Available: IIR/IIF, https://www.iifiir.org. [Accessed: 13 Oct. 2023].

[21] G. Liu, G. Yan G., and J. Yu, "A review of refrigerator gasket: Development trend, heat and mass transfer characteristics, structure and material optimization," *Renewable and Sustainable Energy Reviews*, vol. 144, pp. 110975, July 2021. doi:10.1016/j.rser.2021.110975

[22] P. D'Agaro, G. Croce, and N. Suzzi, "CFD simulation of anti-fogging coatings performance in refrigerated display cabinets," *Journal of Physics: Conference Series*, vol. 1868, pp. 012002, September 2021. doi:10.1088/1742-6596/1868/1/012002

[23] G. D. Ander, "Display case shields reduce supermarket energy use," econofrost.com, March 24, 2005. Available: https://econofrost.com/acrobat/SouthernCaliforniaEdison.pdf. [Accessed: 13 Oct. 2023].

[24] N. Chaomuang, D. Flick, A. Denis, and O. Laguerre, "Influence of operating conditions on the temperature performance of a closed

refrigerated display cabinet," *International Journal of Refrigeration*, vol. 103, pp. 32-41, July 2019. doi:10.1016/j.ijrefrig.2019.03.031

[25] N. Chaomuang, O. Laguerre, and D. Flick, "A simplified heat transfer model of a closed refrigerated display cabinet," *Thermal Science and Engineering Progress*, vol. 17, pp. 100494, June 2020. doi:10.1016/j.tsep.2020.100494

[26] P. H. Pedersen, J. K. Jensen, N. P. Reinholdt, W. B. Markussen, and M. L. Hansen, "Energy efficient professional counter cabinet," in *13th Gustav Lorentzen Conference, 18-20 June 2018, Valencia, Spain*, [Online]. Available: IIR/IIF, https://www.iifiir.org. [Accessed: 13 Oct. 2023].

[27] I. Humar, U. Hudomalj, A. Marinšek, and M. Umberger, "Optimizing the power usage of anti-sweat heaters in glass-door refrigerators according to the dew point," *Energies*, vol. 15, no. 13, pp. 4601, June 2022. doi:10.3390/en15134601.

[28] B. Gil, and J. Kasperski, "Efficiency evaluation of the ejector cooling cycle using a new generation of HFO/HCFO refrigerant as a R134a replacement," *Energies*, vol. 11, no. 8, pp. 2136, August 2018. doi: 10.3390/en11082136

[29] B. Şahin Yıldırım ve A. Şencan Şahin, "Farklı akışkanların kullanıldığı iki kademeli soğutma sisteminin enerji ve ekserji analizi," *Teknik Bilimleri Dergisi*, vol. 10, no. 2, pp. 37-41, Temmuz 2020. doi:10.35354/tbed.722878

[30] F. Katırcıoğlu, Z. Cingiz, Y. Çay, A. T. Gürel, S. Sarıdemir ve A. Kolip, "R22 ve Alternatifleri R438A ile R417A Soğutucu Akışkanları için Kızılötesi Görüntü İşleme Teknikleri Kullanarak, Soğutma Sistem Performansının İncelenmesi," *Academic Platform Journal of Engineering and Science*, vol. 8, no. 3, pp. 500-513, Eylül 2020. doi:10.21541/apjes.726624

[31] O. Banjo, B. Bolaji, O. Ibhadode, O. Fayomi, I. Sunday, O. B. Fakehinde, P. A. Olayiwola, S. Oyedepo, and N. Udoye, "Experimental analysis of the performance characteristic of an eco-friendly HC600a as a retrofitting refrigerant in a thermal system," *Journal of Physics: Conference Series*, vol. 1378, pp. 042033, December 2019. doi:10.1088/1742-6596/1378/4/042033

[32] A. Sethi, G. Pottker, and S. Y. Motta, "Experimental evaluation and field trial of low global warming potential R404A replacements for commercial refrigeration," *Science and Technology for the Built Environment*, vol. 22, no. 8, pp. 1175-1184, July 2016. doi:10.1080/23744731.2016.1209032

[33] G. Besagni, L. Croci, and R. Nesa, "A screening of low-GWP refrigerant for ejector refrigeration," *Chemical Engineering Transactions*, vol. 70, pp. 1291-1296, July 2018. doi:10.3303/CET1870216

[34] K. S. Hmood, V. Apostol, H. Pop, V. Badescu, and E. Pop, "Drop-in and retrofit refrigerants as replacement possibilities of R134a in domestic/commercial refrigeration and automobile air conditioner applications," *Journal of Thermal Engineering*, vol. 7, no. 7, pp. 1815-1835, November 2021. doi:10.18186/thermal.1027435

[35] J. S. Oh, M. Binns, S. Park, and J. K. Kim, "Improving the energy efficiency of industrial refrigeration systems," *Energy*, vol. 112, pp. 826-835, October 2016. doi:10.1016/j.energy.2016.06.119

[36] T. Yilmaz, and M. T. Erdinç, "Energetic and exergetic investigation of a novel refrigeration system utilizing ejector integrated subcooling using different refrigerants," *Energy*, vol. 168, pp. 712-727, February 2019. doi:10.1016/j.energy.2018.11.081

[37] J. M. Belman-Flores, S. Ledesma, D. A. Rodríguez-Valderrama, and D. Hernández-Fusilier, "Energy optimization of a domestic refrigerator controlled by a fuzzy logic system using the status of the door," *International Journal of Refrigeration*, vol. 104, pp. 1-8, May 2019. doi:10.1016/j.ijrefrig.2019.04.025

[38] S. Kasera, R. Nayak, and S. C. Bhaduri, "Energy efficiency analysis of variable speed DC compressor using R290," in *5th IEEE International Conference on Recent Advances and Innovations in Engineering (ICRAIE), 1-3 December 2020, Jaipur, India*, [Online]. Available: IEEE Xplore, http://www.ieee.org [Accessed: 13 Oct. 2023].

[39] F. W. Yu, and K. T. Chan, "Optimizing condenser fan control for air-cooled centrifugal chillers," *International Journal of Thermal Sciences*, vol. 47, pp. 942-953, July 2008. doi:10.1016/j.ijthermalsci.2007.07.018

[40] J. K. Jensen, M. R. Kærn, P. H. Pedersen, and W. B. Markussen, "Comparison of compressor control strategies for energy efficient refrigerated counters," *International Journal of Refrigeration*, vol. 126, pp. 1-11, February 2021. doi:10.1016/j.ijrefrig.2021.02.008

[41] A. Bahman, L. Rosario, and M. M. Rahman, "Analysis of energy savings in a supermarket refrigeration/HVAC system," *Applied Energy*, vol. 98, pp. 11-21, October 2012. doi:10.1016/j.apenergy.2012.02.043

[42] M. Koşan, Y. Dilber, S. Erten, E. M. Bahar, F. N. Erdoğmuş, M. Aktaş, and M. Öder, "Investigation of the effects of fan control technique on energy consumption in industrial refrigerated display cabinet: An experimental study," *Proceedings of the Institution of Mechanical Engineers, Part E: Journal of Process Mechanical Engineering*, November 2022. doi:10.1177/09544089221141360

[43] J. Cirera, J. A. Carino, D. Zurita, J. A. Ortega, "Improving the energy efficiency of industrial refrigeration systems by means of data-

driven load management," *Processes*, vol. 8, no. 9, pp. 1106, September 2020. doi:10.3390/pr8091106

[44] R. Ben-Abdallah, D. Leducq, A. Delahaye, L. Fournaison, O. Pateau, B. Ballot-Miguet, H. M. Hoang, "Analysis of phase change material integration in retail display cabinets for energy management," *Applied Thermal Engineering*, vol. 187, pp. 116459, December 2021. doi:10.1016/j.applthermaleng.2020.116459

[45] S. M. Zubair, "Improvement of refrigeration/air-conditioning performance with mechanical sub-cooling," *Energy*, vol. 15, no. 5, pp. 427-433, May 1990. doi:10.1016/0360-5442(90)90039-5

[46] D. Sánchez, R. Cabello, R. Llopis, J. Catalán-Gil, and L. Nebot-Andrés, "Energy assessment of an R134a refrigeration plant upgraded to an indirect system using R152a and R1234ze(E) as refrigerants," *Applied Thermal Engineering*, vol. 139, pp. 121-134, July 2018. doi:10.1016/j.applthermaleng.2018.04.114

[47] R. Llopis, L. Nebot-Andrés, R. Cabello, D. Sánchez, and J. Catalán-Gil, "Experimental evaluation of a CO_2 transcritical refrigeration plant with dedicated mechanical subcooling," *International Journal of Refrigeration*, vol. 69, pp. 361-368, June 2016. doi:10.1016/j.ijrefrig.2016.06.009

[48] R. Roy, and B. K. Mandal, "Thermodynamic analysis of a vapour compression refrigeration system integrated with a subcooler cycle," *International Journal of Renewable Energy Technology*, vol. 8, no. 3-4, pp. 334-345, January 2017. doi:10.1504/IJRET.2017.088982

[49] K. Yu, G. Ding, and T. Chen, "Experimental investigation on a vertical display cabinet with central air supply," *Energy Conversion and Management*, vol. 50, no. 9, pp. 2257-2265, September 2009. doi:10.1016/j.enconman.2009.05.012

[50] P. Gullo, "Innovative fully integrated transcritical R744 refrigeration systems for a HFC-free future of supermarkets in warm and hot climates," *International Journal of Refrigeration*, vol. 108, pp. 283-310, December 2019. doi:10.1016/j.ijrefrig.2019.09.001

[51] Z. Sun, and Y. Wang, "Comprehensive performance analysis of cascade refrigeration system with two-stage compression for industrial refrigeration," *Case Studies in Thermal Engineering*, vol. 39, pp. 102400, September 2022. doi:10.1016/j.csite.2022.102400

[52] M. Karampour, and S. Sawalha, "Energy efficiency evaluation of integrated CO_2 trans-critical system in supermarkets: A field measurements and modelling analysis," *International Journal Of Refrigeration*, vol. 82, pp. 470-486, August 2017. doi:10.1016/j.ijrefrig.2017.06.002

[53] P. Yuan, Q. H. Zeng, Y. X. Wu, Y. L. Lu, C. L. Hu, H. C. Sun, and W. Q. Tao, "Experimental study of using aerofoils in a refrigerated display cabinet," *International Journal of Thermofluids*, vol. 14, pp. 100140, May 2022. doi:10.1016/j.ijft.2022.100140

[54] C. H. Lin, P. S. Cheng, C. H. Hsieh, Y. M. Li, and P. Y. Yu, "Investigations on predictions of cooling capacity for open refrigerated display cabinet using CFD approach with different positions of perforated back panels," *Thermal Science and Engineering Progress*, vol. 43, pp. 102018, August 2023. doi:10.1016/j.tsep.2023.102018

[55] K. M. Tsamos, H. Mroue, J. Sun, S. A Tassou, N. Nicholls, and G. Smith, "Energy Savings Potential in Using Cold-shelves Innovation for Multi-deck Open Front Refrigerated Cabinets," *Energy Procedia*, vol. 161, pp. 292-299, March 2019. doi:10.1016/j.egypro.2019.02.094

[56] X. Li, Z. Zhang, H. Liu, X. Hu, S. Liu, Z. Xu, and Q. Wang, "Performance of an open refrigerated display cabinet with two air curtains," *Applied Thermal Engineering*, vol. 212, pp. 118549, July 2022. doi:10.1016/j.applthermaleng.2022.118549

[57] X. Wu, Z. Chang, P. Yuan, Y. Lu, Q. Ma, and X. Yin, "The optimization and effect of back panel structure on the performance of refrigerated display cabinet," *Food Control*, vol. *40*, pp. 278-285, June 2014. doi:10.1016/j.foodcont.2013.12.009

[58] M. N. Nikitin, "Numerical analysis of refrigerated display designs in terms of cooling efficiency," *International Journal of Thermal Sciences*, vol. 148, pp. 106157, February 2020. doi:10.1016/j.ijthermalsci.2019.106157

[59] E. Hammond, C. Marques, and L. P. Ketteringham, "Application of short air curtains in retail display refrigerators," in *4th IIR International Conference on Sustainability and the Cold Chain, 7-9 April 2016, Aukland, New Zealand*, [Online]. Available: IIR/IIF, https://www.iifiir.org. [Accessed: 13 Oct. 2023].

[60] W. XueHong, L. WeiPing, W. Yanling, C. ZhiJuan, W. ChunXu, and D. Chang, "Experimental investigation of the performance of cool storage shelf for vertical open refrigerated display cabinet," *International Journal of Heat and Mass Transfer*, vol. 110, pp. 789-795, July 2017. doi:10.1016/j.ijheatmasstransfer.2017.03.071

[61] H. Jouhara, T. Nannou, H. Ghazal, R. Kayyali, S. A Tassou, and S. Lester, "Temperature and energy performance of open refrigerated display cabinets using heat pipe shelves," *Energy Procedia*, vol. 123, pp. 273-280, September 2017. doi:10.1016/j.egypro.2017.07.240

[62] N. Chaomuang, D. Flick, A. Denis, and O. Laguerre, "Experimental analysis of heat transfer and airflow in a closed refrigerated display cabinet," *Journal of Food Engineering*, vol. 244, pp. 101-114, March 2019. doi:10.1016/j.jfoodeng.2018.09.009

[63] J. Sun, K. M. Tsamos, and S. A Tassou, "CFD comparisons of open-type refrigerated display cabinets with/without air guiding strips," *Energy Procedia*, vol. 123, pp. 54-61, September 2017. doi:10.1016/j.egypro.2017.07.284

[64] Y. Wang, S. Qian, J. Xu, L. Li, X. Dou, X. Li, G. Yan, and J. Yu, "Numerical study on the air curtain characteristics of a dual-temperature open display cabinet," *International Journal of Refrigeration*, vol. 126, pp. 23-34, June 2021. doi:10.1016/j.ijrefrig.2021.02.007

[65] C. Melo, and L. W. Silva, "A perspective on energy savings in household refrigerators," in *Sustainable Refrigeration and Heat Pump Technology Conference, Stockholm, Sweden, 13-16 June 2010.*

This is an open access article under the CC-BY license

Research Article/Araştırma Makalesi

GAZİ
JOURNAL OF ENGINEERING SCIENCES

A Study on the Effects of Test Frequency on the Fatigue Life of PLA Parts Manufactured by Additive Manufacturing

Yusuf Ayan*[a]

Submitted: 08.09.2023 Revised: 03.12.2023 Accepted: 31.01.2024 doi:10.30855/gmbd.0705N05

ABSTRACT

Fatigue tests of materials require longer time than most other mechanical tests when the enitre process is considered. One of the most critical factors affecting the test time is the test frequency. In this study, fatigue tests at different test frequencies were applied to the PLA parts produced by the additive manufacturing (AM) technique, and the effects of test frequency were investigated. In the fatigue tests, four different stress levels were applied, and the tests were carried out at four different frequencies: 2 Hz, 4 Hz, 6 Hz, and 8 Hz. The fatigue life of the samples changed according to the applied stress levels at varying test frequencies. There was an approximately 44% decrease in the fatigue life with increasing test frequency at the 1st stress level. Fatigue life showed an increasing trend at and after the 3rd stress level. At the 4th stress level, fatigue life increased by 45% when the test frequency was changed from 2 Hz to 8 Hz. In general, after a specific fatigue life, it was observed that increasing test frequency tended to increase the fatigue life.

Keywords: Polymer, additive manufacturing, fatigue, frequency

[a,*] Karabuk University,
Technology Faculty,
Dept. of Mechatronics Engineering
78050 - Karabük, Türkiye
Orcid: 0000-0002-0045-3777
e mail: yusufayan@karabuk.edu.tr

*Corresponding author:
yusufayan@karabuk.edu.tr

Eklemeli İmalat ile Üretilen PLA Parçaların Yorulma Ömründe Test Frekansının Etkileri Üzerine Bir Çalışma

ÖZ

Malzemelerin yorulma testleri, tüm süreç dikkate alındığında diğer birçok mekanik teste göre daha uzun süre gerektirmektedir. Test süresini etkileyen en önemli faktörlerden biri yorulma test frekansıdır. Bu çalışmada Eİ tekniğiyle üretilen PLA parçalara farklı test frekanslarında yorulma testi uygulanmış ve test frekansının etkileri araştırılmıştır. Yorulma testlerinde dört farklı gerilme seviyesi uygulanmış ve testler 2 Hz, 4 Hz, 6 Hz ve 8 Hz olmak üzere dört farklı frekansta gerçekleştirilmiştir. Uygulanan gerilme seviyelerine göre değişen test frekanslarında farklı yorulma ömürleri bulunmuştur. 1. Gerilme seviyesinde artan test frekansıyla yorulma ömründe yaklaşık %44 azalma görülmüştür. 3. Gerilme seviyesi ve sonrası yorulma ömrü artan trend göstermiştir. 4. Gerilme seviyesinde test frekansı 2 Hz'den 8 Hz'e değiştirildiğinde yorulma ömrü %45 artmıştır. Genel olarak, belirli yorulma ömür değerinden sonra artan test frekansının yorulma ömrünü arttırma eğiliminde olduğu görülmüştür.

Anahtar Kelimeler: Polimer, eklemeli imalat, yorulma frekans

To cite this article: Y. Ayan, "A Study on the Effects of Test Frequency on the Fatigue Life of PLA Parts Manufactured by Additive Manufacturing," *Gazi Journal of Engineering Sciences,* vol.10, no.1, pp. 60-71, 2024. doi:10.30855/0705N05

1. Introduction

In recent years, interest in additive manufacturing (AM) systems has increased in academic and industrial fields [1]. The capabilities of the AM method, such as performing fast production, reducing design limitations, and reducing material consumption [2], have contributed to this situation. In today's manufacturing industry, the increasing demand for more specialized and highly complex components has led to advances in AM technologies [3]. Different materials such as polymer, ceramic, metal, and composite can be processed with the AM method. Polymers are a type of material commonly used in the AM process [4]. The development of polymers has led to their use in various structural and load-bearing applications [5]. Polymers have recently been preferred in many industrial applications, and replacing metallic alloys with polymers has become very important in new technological machines and systems [6]. The fact that polymers are light in weight, easy to manufacture, and have good mechanical properties such as abrasion resistance [7] can be shown among the reasons that may contribute to this change.

Different production techniques and methods are used in the AM method. One of them is the fused deposition modeling (FDM) and its use has increased with the widespread use of 3D printers [8]. Poly lactic acid (PLA) is one of the most widely used polymers in FDM [9]. PLA can be used in many sectors, such as medical, biomedical, packaging, agriculture, and automotive industries [10]. Since this material has a common usage area, it is important to determine the mechanical properties of this material to provide the desired working performance. The mechanical properties of the polymer parts produced with AM are highly dependent on the production parameters. Nozzle temperature and speed [11] infill pattern type, build orientation, and raster angle [12] are examples of these parameters. Although a target part produced in different parameters with a 3D printer physically provides the same geometric properties in its final form, mechanical properties may vary due to differences in production parameters. In this respect, studies on the mechanical properties of parts produced with AM have attracted great interest in recent years [13].

Kaygusuz and Özerinç [9] investigated the effect of printing temperature and infill density on the produced PLA structure. Noting that these two printing parameters significantly affect the mechanical properties, they found that increasing printing temperature increased the tensile strength. They attributed this increase to reducing voids in the structure due to high temperature. Kam et al. [14] investigated the effects of vibrations in the 3D printer on the surface roughness of the produced part. They found that the full honeycomb was the best result among the parts produced in six different infill structures. With this study, it is understood that the 3D printer system can also directly affect the properties of the produced part. İstif [7] investigated the wear behavior of PLA parts produced with FDM. Different wear behavior was observed in two different sample types produced in vertical and horizontal orientations, indicating that layer orientation plays a vital role in the wear mechanism. Yavuz et al. [15] applied a three-point bending test to PLA, ABS, and PETG structures produced in different topologies by 3D printing. They stated that the ABS structure is more ductile than the PLA structure, and although the PLA structure can withstand higher loads, it exhibits a more brittle behavior by showing less displacement as a result of bending. In a similar study, Kamer et al. [13] investigated the flexural properties of structures produced with ABS and PLA at different nozzle and bed temperature parameters. While the effect of these two parameters on the flexural strength of the samples produced with ABS is less than in PLA, the table temperature affected the flexural strength very little in the PLA samples. However, the change in the printing temperature affected the flexural strength.

Parts produced with FDM are affected by mechanical failures throughout their service life. Fatigue is one of these failures that can cause the component to crack and fracture even at low cyclic stress values [16]. In addition, fatigue is responsible for 90% of the damage caused by the working of the machine components [17]. If PLA components produced with AM are used in engineering applications, they should provide sufficient accuracy and safety regarding fatigue strength [18]. Considering that PLA components produced with AM can take on a task in structural applications, it is necessary to know these components' fatigue properties. Gomez-Gras et al. [19] applied a fatigue test to PLA samples produced in different parameters

with FDM. They stated that infill density had the most significant effect on fatigue performance, followed by nozzle diameter and layer height. They also found that printing speed had little effect. Azadi et al. [20] applied a fatigue test to circular cross-section PLA samples produced with FDM in horizontal and vertical build orientations. They found that at low-stress levels, the effect of the build orientation is greater, and the fatigue life of specimens produced in the vertical orientation is lower. Bakhtiari et al. [16] conducted a review study investigating the effect of 3D printing parameters on fatigue properties. Their study discussed the effects of production parameters according to the fatigue test type. They stated that it is difficult to deduce the overall effect of each parameter due to the few parametric studies on FDM products in the literature. They also mentioned that each production parameter can negatively or positively affect fatigue properties depending on the change in material or load type. Safai et al. [21] stated that the synergy between all printing parameters, such as build orientation, raster angle, layer height, and infill density, makes it difficult to determine the best parameters regarding the best fatigue strength.

When the studies in the literature are evaluated, the effects of 3D printing parameters on mechanical properties have been investigated in general according to the tests applied. Studies about the fatigue properties were found to be less in number than other studies. It was also stated by some researchers that the studies on the fatigue properties of AM and PLA materials are few [18,19,22,23]. Considering the operation of polymer structures under cyclic loading conditions, it is important to determine their fatigue strength. Since the test parameters are directly effective in evaluating the results, the test conditions can be considered another important factor, like 3D printing parameters, in determining mechanical properties. Some basic test parameters applied in fatigue tests are ambient temperature, applied stress level, and test frequency. Each of these parameters is a factor that can directly change the test results. The most critical factor affecting test times is fatigue test frequency. Since varying levels of loads must be applied to the test material in determining the fatigue strength, many samples are used, and thus, the test times can be very long depending on the applied load. This study investigated the effects of fatigue test frequency on the PLA structure produced by 3D printing. Fatigue tests at varying test frequencies were applied to the samples produced under the same conditions. Fatigue tests were carried out with a test machine applying planar bending stress. Investigating the effects of fatigue test frequency and applying the fatigue test are among the differences in this study. This study examined both the effects of fatigue test frequency and the fatigue life of PLA structure at different stress levels.

2. Materials and Methods

The study consist of three stages: specimen production, tensile test, and fatigue test. FDM technique was used in production, and Ender 6 brand-model 3D printer was used. 1.75 diameter white colored ESUN brand PLA+ filament was used. Printing parameters were kept constant in all productions. The printing parameters used in the processes are given in Table 1. Two different types of specimens were printed for tensile and fatigue tests. The printing process is shown schematically in Fig. 1.

Table 1. Printing parameters

Filament diameter (mm)	1.75
Nozzle diameter (mm)	0.4
Nozzle temperature (°C)	205
Bed temperature (°C)	60
Printing speed (mm/s)	80
Layer height (mm)	0.2
Infill density (%)	100
Raster angle (°)	0°

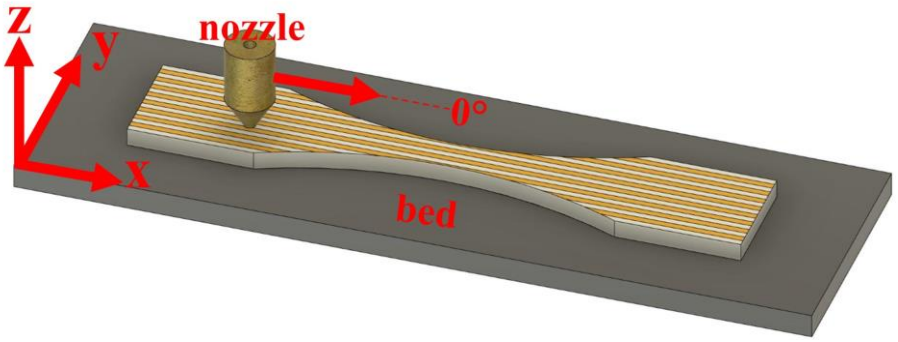

Figure 1. Schematic representation of the printing process

Tensile tests were applied to determine the tensile strength of PLA structures and specify the load levels for fatigue tests. Tensile test specimens were printed according to the ASTM D638 type IV standard [24]. The tests were carried out with a Shimadzu AG 50 kN test machine at a fixed cross head speed of 5 mm/min at room temperature, and three samples were tested. Tensile test specimen dimensions is given in Fig. 2

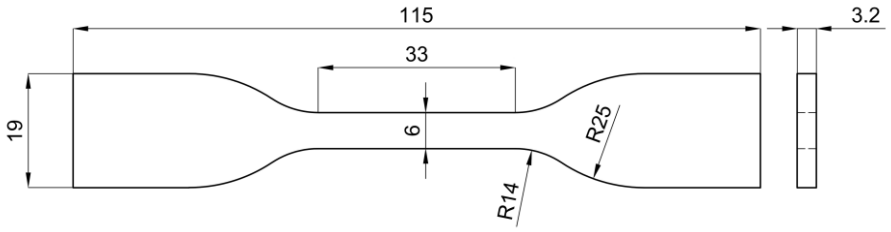

Figure 2. Tensile test specimen dimensions (mm)

Fatigue tests were carried out with a test machine applying planar bending stress. Figure 3 shows the fatigue testing machine and the test scheme. The fatigue test machine is custom designed and manufactured. The test specimen is mounted to one end fixed jaw and the other end movable jaw. The movable jaw moves up and down at a certain frequency (range 0-20 Hz), forcing the specimen to bend. There is a 200 kg capacity load-cell below the fixed jaw. Load cell performs instant load measurement during the test and the measured value is read from the screen on the machine instantly. The machine also has a counter that calculates the total cycle of the sample during testing. By connecting the machine to a computer, instantaneous load changes over time can be monitored and the data obtained throughout the test is recorded. Samples of different dimensions can be tested by changing the jaws on the machine or using the existing jaws. The tests were conducted at room temperature, with all other conditions being the same except for the fatigue test frequency. Since the study aims to investigate the effect of fatigue test frequency, the tests were applied at four different test frequencies: 2 Hz, 4 Hz, 6 Hz, and 8 Hz. Four different stress levels and three specimens for each test frequency were used for each level. A total of 48 fatigue test specimens were tested for four different stress values, four different test frequencies, and three replications. Fatigue test specimen dimensions is given in Fig. 4.

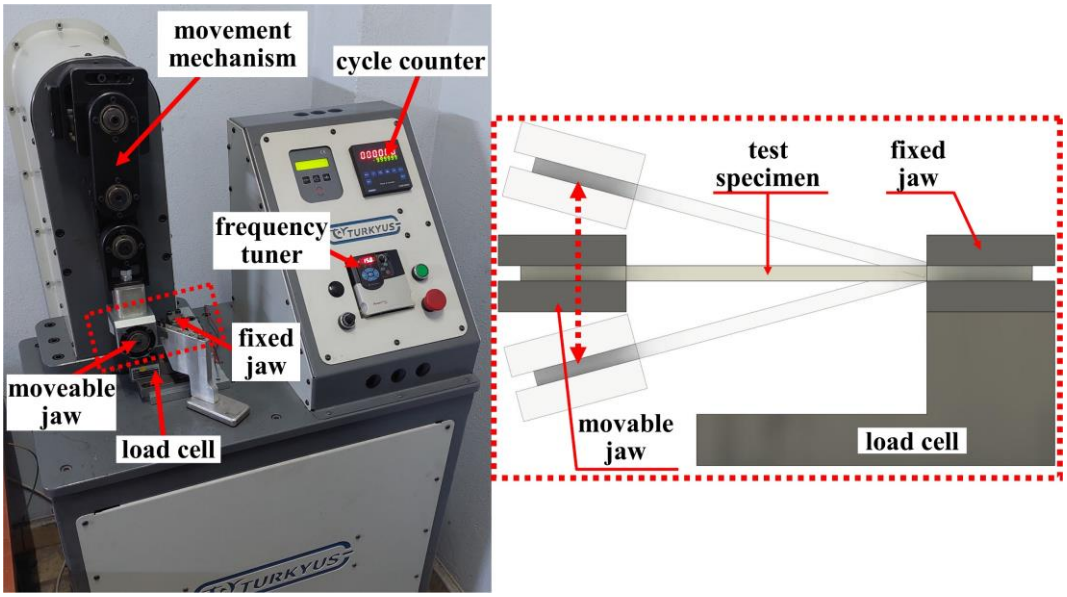

Figure 3. Fatigue test machine and application principle

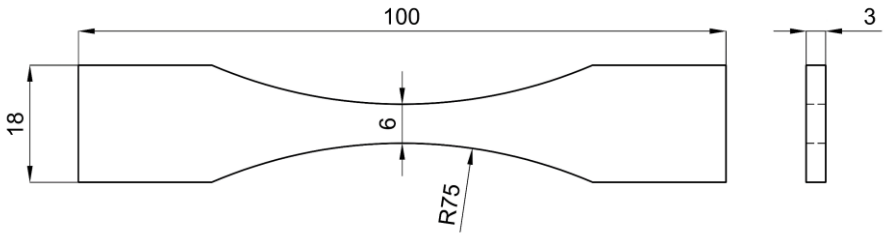

Figure 4. Fatigue test specimen dimensions (mm)

3. Results and Discussions

3.1. Tensile test results

Figure 5 shows the samples after the tensile test. When the rupture regions of the samples are examined, it is seen that all of them were damaged from a similar region. This failure type is the case with specimens printed at a 0° raster angle. In the sample printed at this angle, the orientation of deposited material is in the same direction as the load applied in the tensile test. The stress is concentrated in the region where the flat area on the specimen ends, the rounding begins, and thus, the rupture occurs in this region.

Figure 5. Specimens after the tensile test

The stress-strain curves obtained from the tensile tests are given in Fig. 6. Three specimens subjected to the tensile test showed very similar results in terms of tensile strength and elongation. This situation indicates that the 3D printing process and the applied test are performed correctly under equal conditions. The average tensile strength has been calculated as approximately 45 MPa. The tensile strength of 3D-printed PLA parts is directly related to the printing parameters. In another study, the tensile strength of the PLA part produced with similar parameters was found to be very close [25]. Since the primary purpose of the tensile test is to determine the amount of load to be applied in the fatigue test, there was no need for a more detailed evaluation of the results.

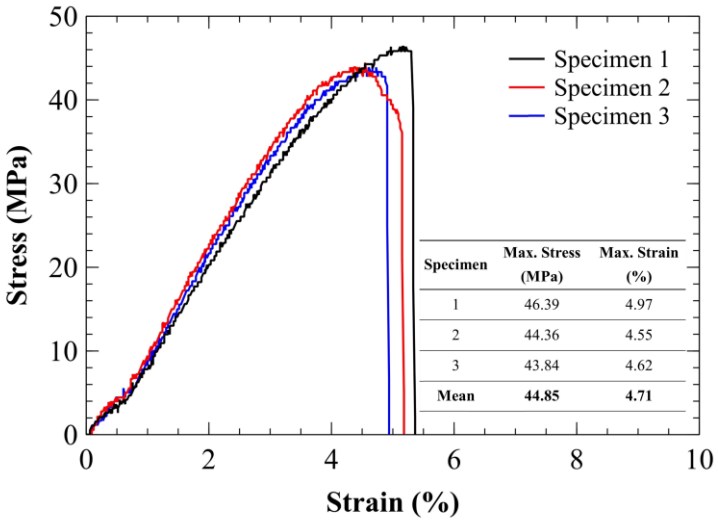

Specimen	Max. Stress (MPa)	Max. Strain (%)
1	46.39	4.97
2	44.36	4.55
3	43.84	4.62
Mean	**44.85**	**4.71**

Figure 6. The stress-strain curves of the specimens

3.1. Fatigue test results

Figure 7 shows the specimens after the fatigue test. Factors such as the applied stress magnitude, temperature, frequency and manufacturing defects in the sample affect the test results [20]. When Figure 7 is examined, it can be seen that the samples were damaged in approximately the same area at all the test frequencies. In this case, when evaluating the test results, it can be said that there is no manufacturing defect that adversely affects the results.

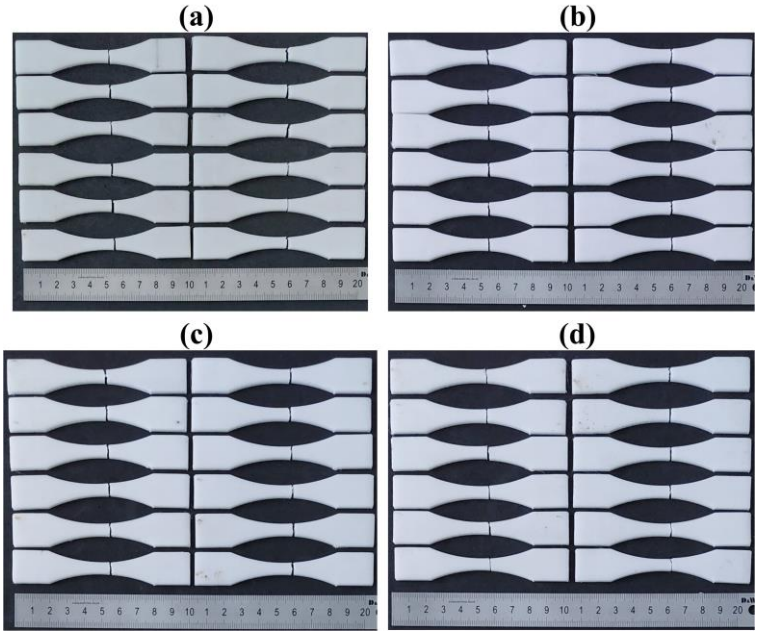

Figure 7. Specimens after the fatigue test a) 2 Hz, b) 4 Hz, c) 6 Hz and d) 8 Hz

In the fatigue tests, four different stress amplitudes of approximately 0.30, 0.45, 0.60, and 0.70 times the average tensile strength (≈45 MPa), calculated according to the results of the tensile tests, were applied. The cycle numbers obtained as a result of the tests at these stress levels are given in Table 2. Two different stress-numbers of cycle graphs were created with these values. The first is the graph obtained with the results of all samples in the fatigue test shown in Figure 8. The graph in Fig. 9 is obtained with the average number of cycles at each fatigue test frequency and each stress level. While calculating the average number of cycles, the total cycle values of the two closest samples were used.

Table 2. Fatigue test results

Stress Level	Applied Stress (MPa)	Test Frequency (Hz)	Specimen	Number of Cycle	Mean Number of Cycle	Stress Level	Applied Stress (MPa)	Test Frequency (Hz)	Specimen	Number of Cycle	Mean Number of Cycle
			1	1072					1	11656	
		2	2	1184	1180			2	2	7552	11024
			3	1176					3	10392	
			1	1136					1	12128	
		4	2	1104	1120			4	2	12176	12152
			3	1368					3	9336	
1	30.2		1	1096		**3**	18.6		1	18096	
		6	2	904	1112			6	2	14424	14952
			3	1128					3	15480	
			1	864					1	15816	
		8	2	624	656			8	2	13200	16004
			3	688					3	16192	
			1	4040					1	27008	
		2	2	2880	2692			2	2	28160	27584
			3	2504					3	31384	
			1	2664					1	34920	
		4	2	2816	2740			4	2	29144	28444
			3	3008					3	27744	
2	25.9		1	2832		**4**	14.3		1	36672	
		6	2	3040	2936			6	2	25624	37576
			3	6016					3	38480	
			1	2656					1	38392	
		8	2	2864	2820			8	2	43424	40908
			3	2776					3	30640	

Note: In calculating the mean number of cycles, the cycle number of the 2 closest samples were used.

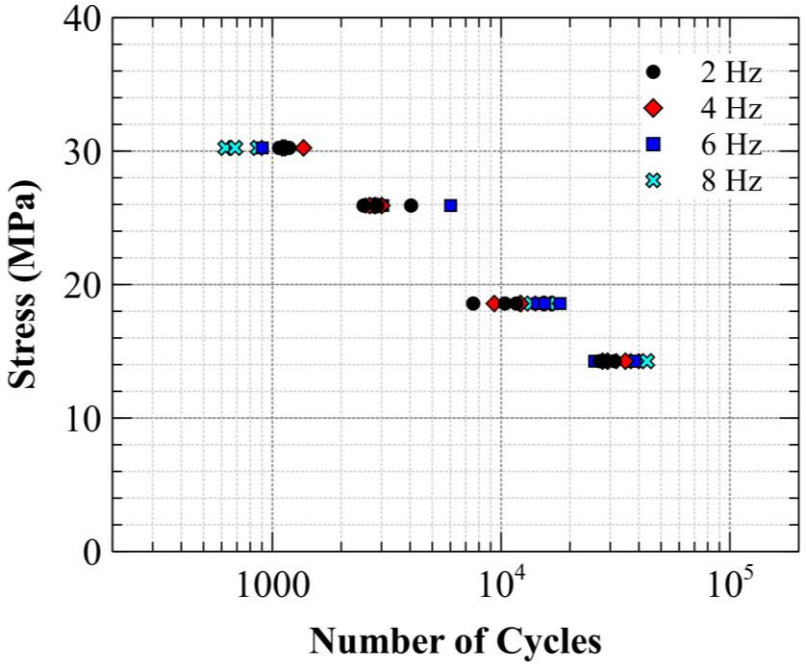

Figure 8. Graph generated by fatigue test results (all samples)

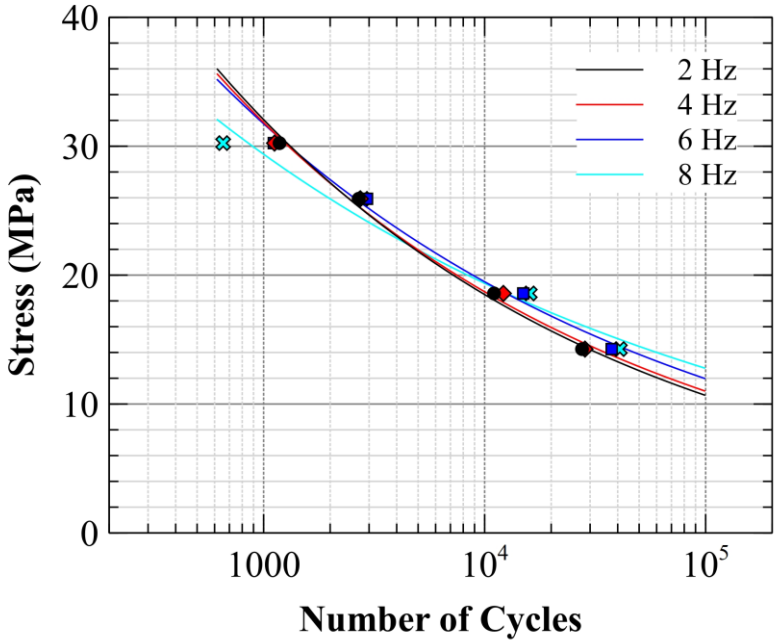

Figure 9. Stress-Average Number of Cycles plot based on test frequency

When the graph shown in Fig. 9 is examined, it is observed that the fatigue life decreases in general with the increase of the fatigue frequency at the highest stress level. At the highest stress level, excluding the 8 Hz test frequency curve, the distance between the curves decreased with increasing test frequency. At the highest stress value, the fatigue life of the specimens applied with a frequency of 8 Hz remained below 1000. With the fatigue test frequency decreasing at the highest stress, the fatigue life exceeded 1000, and the highest fatigue life was obtained at 2 Hz test frequency. When the lowest and highest frequency values are compared at the 1st stress level, approximately a 44% decrease in fatigue life has been calculated.

When Table 2 and Fig. 9 are examined, it is seen that the average fatigue life with the varying test frequency at the 2nd stress level is generally close to each other. However, in the graph in Fig. 9, although the number

of cycles at the 2nd stress level is seen to be coincident, a slight difference in the fatigue life was found. At this stress level, the mean fatigue life at 4 different frequencies was calculated as 2797 ± 107. Besides, the lowest fatigue life was found in specimens with a test frequency of 2 Hz and the highest in specimens with a test frequency of 6 Hz. When the test frequencies applied at this level were compared, an approximately 9% difference in fatigue life was found. It was observed that the fatigue life increased with increasing fatigue test frequency at the 3rd stress level. Fatigue life increased by approximately 45% when the test frequency increased from 2 Hz to 8 Hz. When the curves in the graph shown in Fig. 9 are examined, the distances between the curves have increased significantly towards the applied low-stress levels, and it has been observed that the fatigue life tends to increase with increasing test frequency. At the 4th level, where the lowest stress was applied, the highest average fatigue life was 40908 when the test frequency was 8 Hz. The lowest fatigue life was obtained at a test frequency of 2 Hz, with an average of 27584. By increasing the fatigue test frequency by 3 times, an increase of approximately 48% in the fatigue life value was observed. According to the trend of the curves depending on the test frequency, it was deduced that this increase will continue if lower stress is applied.

The above evaluations were based on the fatigue life results obtained at each stress level. When the test results obtained in fatigue tests were generally evaluated, the increased test frequency at high-stress value decreased the fatigue life. When the applied stress value decreases, with increasing test frequency, the fatigue life found intersects at a point on the graph and then shows an increasing trend. It was observed that the linear variation of the fatigue test frequency does not tend to increase/decrease the fatigue life linearly. In the graph in Fig. 9, after the fatigue life of 10^4, the effect of test frequency change on the fatigue life is more apparent.

According to the results obtained in the fatigue test, it has been observed that at high-stress levels (≈0.60-0.70 x σ_{max}) applied, generally close results can be obtained with varying test frequency in fatigue life. At low-stress levels, it was observed that increasing test frequency generally increased the fatigue life. It has been mentioned that high test frequency increases the temperature of the test specimen. In this case, it decreases the fatigue life by causing material flow with increased ductility [26]. Selecting a test frequency of less than 5 Hz is also recommended to reduce high heat generation [21]. Magri et al. [27] applied a tensile-tensile type fatigue test at 10 Hz, 40 Hz, and 80 Hz frequencies to the 3D-produced PLA-Graphen sample. During the test, they measured the sample temperature with a thermal camera and observed a decrease in the fatigue life due to the heating in the material at an 80 Hz frequency. Ueki [28], conducted a study on fatigue testing of composite materials. The researcher stated that if the sample temperature is controlled, close results can be found in the fatigue tests at 1 Hz and 230 Hz frequencies. The researcher also mentioned the possibility of applying external cooling to the sample. Apart from the mentioned literature results, in this study, when the fatigue test results at increasing test frequencies were evaluated, there was no decrease in fatigue life in general. In this case, it was thought that the increased test frequency applied in the study, ranging from 2 Hz to 8 Hz, did not cause a heating that would reduce fatigue life. Increased fatigue life at high frequency compared to low frequency: This could be attributed to prolonging the duration of action of low-frequency repetitive stretching and increasing fatigue damage accumulation under the same stress level [29].

In the literature, it is mentioned that the increasing fatigue test frequency causes heating in polymer materials. Thus, the tests should be carried out at low frequencies. However, within the parameters used in this study, it was not concluded that increasing test frequency influenced reducing fatigue life in general. It has been understood that the frequency values chosen in the study do not cause heating, which reduces the fatigue strength of the samples, or a different adverse effect that will reduce the fatigue life. In a fatigue test where the test frequency is chosen as 2 Hz and 8 Hz, there is a difference of approximately 3 times in the total test time until the same number of cycles is reached. For example, the number of cycles in 4 hours for a test performed at a frequency of 2 Hz will be reached in 1 hour with a frequency of 8 Hz. Considering the conditions, such as the test method and material used in the study, in terms of shortening the fatigue tests: In similar fatigue tests, it has been understood that applying a test frequency of 8 Hz will not have a negative effect and will significantly accelerate the fatigue test process. However, the possibility of frequency variation causing a change in fatigue life should be considered in the fatigue test

3. Conclusions

The general outcomes of this study, in which the bending fatigue test was applied at different test frequencies to the 3D-printed PLA structure produced with AM, are listed below.

- The average tensile strength of the specimens produced at 0° raster angle was calculated as 45 MPa.
- In the fatigue tests, the damage occurred in approximately the same area in all samples; in this case, it was concluded that there was no production-related fault in the samples.
- When the test frequency was increased from 2 Hz to 8 Hz at the highest stress level, a 44% decrease in fatigue life was observed. Depending on the increase in frequency, fatigue life started to increase after the 2nd stress level.
- Fatigue life increased with increasing test frequency, except for the highest stress level applied in fatigue tests since the specimen is subjected to stress in less time at high frequency. When the test frequency was increased from 2 Hz to 8 Hz at the lowest stress level, a 48% increase in fatigue life was observed.
- With increasing fatigue test frequency, there was no decrease in fatigue life due to the heating effect mentioned in the literature.
- It has been concluded that 8 Hz test frequency can be used for tests to be carried out under similar conditions where fatigue tests need to be applied faster or achieve quicker results.

Conflict of Interest Statement

The author declares that there is no conflict of interest.

References

[1] G. Akıncıoğlu and E. Aslan, "Investigation of tribological properties of amorphous thermoplastic samples with different filling densities produced by an additive manufacturing method," *Gazi Journal of Engineering Sciences*, vol. 8, no. 3, pp. 540–546, Dec. 2021. doi:10.30855/gmbd.0705041

[2] M. S. Kamer, Ş. Temiz, H. Yaykaşlı, and A. Kaya, "3 Boyutlu yazıcı ile farklı renklerde ve farklı dolgu desenlerinde üretilen çekme test numunelerinin mekanik özelliklerinin incelenmesi," *Uludağ University Journal of The Faculty of Engineering*, pp. 829–848, Dec. 2021. doi:10.17482/uumfd.887786

[3] B. Sağbaş, and B. Gavcar, "Biyomedikal uygulamalar için titanyum alaşımlarının eklemeli imalatı," *Uluborlu Mesleki Bilimler Dergisi*, vol. 5, no. 1, pp. 54–74, 2022.

[4] I. Jasiuk, D. W. Abueidda, C. Kozuch, S. Pang, F. Y. Su, and J. McKittrick, "An overview on additive manufacturing of polymers," *JOM*, vol. 70, no. 3, pp. 275–283, Mar. 2018. doi:10.1007/s11837-017-2730-y

[5] V. Shanmugam, O. Das, K. Babu, U. Marimuthu, A. Veerasimman, D.J. Johnson, R.E. Neisiany, M.S. Hedenqvist, S. Ramakrishna, and F. Berto, "Fatigue behaviour of FDM-3D printed polymers, polymeric composites and architected cellular materials," *International Journal of Fatigue*, vol. 143, p. 106007, Feb. 2021. doi:10.1016/j.ijfatigue.2020.106007

[6] S. Karabeyoğlu, B. Ergene, and Ç. Bolat, "An experimental study on wear performance of electrolytic multilayer Cu-Ni-Cr coated ABS under different test forces," *El-Cezeri Fen ve Mühendislik Dergisi*, Mar. 2021. doi:10.31202/ecjse.862808

[7] İ. İstif, "Eriyik yığma modelleme ile üretilen PLA parçalarının kuru sürtünmeli aşınma davranışlarının tanılanması," *Dicle Üniversitesi Mühendislik Fakültesi Mühendislik Dergisi*, Feb. 2021. doi:10.24012/dumf.855768

[8] O. Doğan and M. S. Kamer, "Farklı üretim parametreleri kullanılarak 3B yazıcı ile üretilen test numunelerinin sürünme davranışlarının deneysel olarak incelenmesi," *Gazi Üniversitesi Mühendislik Mimarlık Fakültesi Dergisi*, vol. 38, no. 3, pp. 1839–1848, Jan. 2023. doi:10.17341/gazimmfd.1122973

[9] B. Kaygusuz, and S. Özerinç, "3 boyutlu yazıcı ile üretilen PLA bazlı yapıların mekanik özelliklerinin incelenmesi," *Makine Tasarım ve İmalat Dergisi*, vol. 16, no. 1, pp. 1–6, 2018.

[10] N.-A.A.B. Taib, M.R. Rahman, D. Huda, K.K. Kuok, S. Hamdan, M.K.B. Bakri, M.R.M.B. Julaihi, and A. Khan, "A review on poly lactic acid (PLA) as a biodegradable polymer," *Polymer Bulletin*, vol. 80, no. 2, pp. 1179–1213, Feb. 2023. doi:10.1007/s00289-022-04160-y

[11] M.-H. Hsueh, C.-J. Lai, S.-H. Wang, Y.-S. Zeng, C.-H. Hsieh, C.-Y. Pan, and W.-C. Huang, "Effect of printing parameters on the thermal and mechanical properties of 3D-printed PLA and PETG, using fused deposition modeling," *Polymers*, vol. 13, no. 11, p. 1758, May 2021. doi:10.3390/polym13111758

[12] M.-H. Hsueh, C.-J. Lai, C.-F. Chung, S.-H. Wang, W.-C. Huang, C.-Y. Pan, Y.-S. Zeng, and C.-H. Hsieh, "Effect of printing parameters on the tensile properties of 3D-printed polylactic acid (PLA) based on fused deposition modeling," *Polymers*, vol. 13, no. 14, p. 2387, Jul. 2021. doi:10.3390/polym13142387

[13] M. S. Kamer, O. Doğan, Ş. Temïz, and H. Yaykaşlı, "3 Boyutlu yazıcı ile farklı yazdırma parametreleri kullanılarak üretilen eğme test numunelerinin mekanik özelliklerinin incelenmesi," *Çukurova Üniversitesi Mühendislik Fakültesi Dergisi*, vol. 36, no. 3, pp. 835–846, Sep. 2021. doi:10.21605/cukurovaumfd.1005909

[14] M. Kam, H. Saruhan, and A. İpekçi, "Investigation the effect of 3D printer system vibrations on surface roughness of the printed products," *Düzce Üniversitesi Bilim ve Teknoloji Dergisi*, vol. 7, no. 2, pp. 147–157, Mar. 2019. doi:10.29130/dubited.441221

[15] G. Acar Yavuz, B. Gören Kıral, S. Katre, and D. Atilla, "Effects of topology and material on mechanical properties of structures produced by the additive manufacturing method," *Dokuz Eylül Üniversitesi Mühendislik Fakültesi Fen ve Mühendislik Dergisi*, vol. 23, no. 69, pp. 755–765, Sep. 2021. doi:10.21205/deufmd.2021236905

[16] H. Bakhtiari, M. Aamir, and M. Tolouei-Rad, "Effect of 3D printing parameters on the fatigue properties of parts manufactured by fused filament fabrication: a review," *Applied Sciences*, vol. 13, no. 2, p. 904, Jan. 2023. doi:10.3390/app13020904

[17] A. Şık, A. Atak, C. Yavuz, and V. Özdemir, "The design of fatigue strength machine being one of the methods for determining the mechanical properties of the materials used in the industry," *Gazi University Journal of Science Part A: Engineering and Innovation*, vol. 5, no. 2, pp. 79–88, 2018.

[18] O. H. Ezeh and L. Susmel, "Fatigue strength of additively manufactured polylactide (PLA): effect of raster angle and non-zero mean stresses," *International Journal of Fatigue*, vol. 126, pp. 319–326, Sep. 2019. doi:10.1016/j.ijfatigue.2019.05.014

[19] G. Gomez-Gras, R. Jerez-Mesa, J. A. Travieso-Rodriguez, and J. Lluma-Fuentes, "Fatigue performance of fused filament fabrication PLA specimens," *Materials & Design*, vol. 140, pp. 278–285, Feb. 2018. doi:10.1016/j.matdes.2017.11.072

[20] M. Azadi, A. Dadashi, S. Dezianian, M. Kianifar, S. Torkaman, and M. Chiyani, "High-cycle bending fatigue properties of additive-manufactured ABS and PLA polymers fabricated by fused deposition modeling 3D-printing," *Forces in Mechanics*, vol. 3, p. 100016, Sep. 2021. doi:10.1016/j.finmec.2021.100016

[21] L. Safai, J. S. Cuellar, G. Smit, and A. A. Zadpoor, "A review of the fatigue behavior of 3D printed polymers," *Additive Manufacturing*, vol. 28, pp. 87–97, Aug. 2019. doi:10.1016/j.addma.2019.03.023

[22] C. W. Ziemian, R. D. Ziemian, and K. V. Haile, "Characterization of stiffness degradation caused by fatigue damage of additive manufactured parts," *Materials & Design*, vol. 109, pp. 209–218, Nov. 2016. doi:10.1016/j.matdes.2016.07.080

[23] J. A. Travieso-Rodriguez, M. D. Zandi, R. Jerez-Mesa, and J. Lluma-Fuentes, "Fatigue behavior of PLA-wood composite manufactured by fused filament fabrication," *Journal of Materials Research and Technology*, vol. 9, no. 4, pp. 8507–8516, Jul. 2020. doi:10.1016/j.jmrt.2020.06.003

[24] ASTM D638-14, "Standard test method for tensile properties of plastics", (2014).

[25] P. Yadav, A. Sahai, and R. S. Sharma, "Experimental studies on the mechanical behaviour of three-dimensional PLA printed parts by fused filament fabrication," *Journal of The Institution of Engineers (India): Series D*, vol. 104, no. 1, pp. 233–245, Jun. 2023. doi:10.1007/s40033-022-00403-4

[26] M. F. Afrose, S. H. Masood, P. Iovenitti, M. Nikzad, and I. Sbarski, "Effects of part build orientations on fatigue behaviour of FDM-processed PLA material," *Progress in Additive Manufacturing*, vol. 1, no. 1–2, pp. 21–28, Jun. 2016. doi:10.1007/s40964-015-0002-3

[27] A. El Magri, S. Vanaei, M. Shirinbayan, S. Vaudreuil, and A. Tcharkhtchi, "An investigation to study the effect of process parameters on the strength and fatigue behavior of 3D-printed PLA-graphene," *Polymers*, vol. 13, no. 19, p. 3218, Sep. 2021. doi:10.3390/polym13193218

[28] Y. Ueki, "High-speed bending-fatigue testing of composite materials," *IOP Conference Series: Materials Science and Engineering*, vol. 388, p. 012008, Jul. 2018. doi:10.1088/1757-899X/388/1/012008

[29] W. Hu, W. Huang, Y. Sun, W. Zhang, L. Tan, S. Zhang, G. Ma, D. Zhang, and Q. Wang, "Influence of load frequency and corrosive environments on fatigue behavior of as-extruded Mg–Zn–Zr–Nd alloy," *Journal of Materials Research and Technology*, vol. 22, pp. 2627–2640, Jan. 2023. doi:10.1016/j.jmrt.2022.12.114

This is an open access article under the CC-BY license

Research Article/Araştırma Makalesi

GAZİ
JOURNAL OF ENGINEERING SCIENCES

Image Based Web Page Classification by Using Deep Learning

Muhammed Mutlu YAPICI*[a]

Submitted: 26.10.2023 Revised: 15.11.2023 Accepted: 22.11.2023 doi:10.30855/gmbd.0705N06

ABSTRACT

The internet holds a significant role in all aspects of our lives, and its importance continues to grow each day. Therefore, the usability of the Internet holds great significance. Low data quality and disinformation severely impact the usability of the internet. Consequently, people face challenges in obtaining accurate and clear information. In the present day, websites predominantly feature image-based content like pictures and videos, as opposed to text-based content. The classification of such content holds immense importance for search engines. As a result, the classification of web pages stands as a crucial research area for scholars. This study focuses on the classification of image-based web pages. A deep learning-based approach is proposed to categorize web pages into four main groups: tourism, machinery, music, and sports. The suggested method yielded the most favourable outcomes when utilizing the Stochastic Gradient Descent (SGD) optimization method, achieving an accuracy of 0.9737, a recall of 0.9474, an F1 score of 0.9474, and an Area Under the ROC Curve (AUC) value of 0.9649. Furthermore, the utilization of Deep Learning (DL) led to achieving the most advanced results in web page classification within the existing literature, particularly on the WebScreenshots dataset.

Keywords: Deep learning, web page classification, DenseNet, optimization methods

[a,*] Ankara University, Elmadag Vocational School, Dept. Of Computer Technologies 06780 - Ankara, Türkiye
Orcid: 0000-0001-6171-1226
e mail: mutluyapici@ankara.edu.tr

*Corresponding author: mutluyapici@ankara.edu.tr

Derin Öğrenme Kullanarak Görüntü Tabanlı Web Sayfası Sınıflandırma

ÖZ

İnternet hayatımızın her alanında önemli bir yere sahip ve önemi her geçen gün artmaya devam ediyor. Bu nedenle internetin kullanılabilirliği büyük önem taşımaktadır. Düşük veri kalitesi ve dezenformasyon, internetin kullanılabilirliğini ciddi şekilde etkilemektedir. Bu nedenle insanlar doğru ve temiz bilgiye ulaşma konusunda zorluklarla karşılaşmaktadır. Günümüzde web sitelerinde metin tabanlı içerik yerine ağırlıklı olarak resim ve video gibi görsel tabanlı içerikler daha çok yer almaktadır. Bu tür içeriklerin sınıflandırılması arama motorları için büyük önem taşımaktadır. Sonuç olarak web sayfalarının sınıflandırılması bilim insanları için önemli bir araştırma alanı olarak karşımıza çıkmaktadır. Bu çalışma görsel tabanlı web sayfalarının sınıflandırılmasına odaklanmaktadır. Web sayfalarını turizm, makine, müzik ve spor olmak üzere dört ana grupta sınıflandırmak için derin öğrenmeye dayalı bir yöntem önerilmiştir. Önerilen yöntem, 0,9737 accuracy, 0,9474 recall, 0,9474 F1-score ve 0,9649 AUC değeriyle en iyi sonuçları Stokastik Gradyan İnişi (SGD) optimizasyon yöntemi ile elde etmiştir. Ayrıca, Derin Öğrenmenin (DL) kullanılması, web sayfası sınıflandırmasında, özellikle WebScreenshots veri kümesinde, mevcut literatürdeki en iyi sonuçların elde edilmesini sağlamıştır.

Anahtar Kelimeler: Derin öğrenme, Web sayfası sınıflandırma, Densenet,Optimizasyon yöntemleri

To cite this article: M. M. Yapici, "Image Based Web Page Classification by Using Deep Learning," *Gazi Journal of Engineering Sciences*, vol.10, no.1, pp. 72-83, 2024. doi:10.30855/gmbd.0705N06

1. Introduction

The field of the Internet has been profoundly impacted by the advancement of technology. Internet technology, officially introduced in 1968 and laid out in 1969 as ARPANET, reached a milestone with the integration of emails into our lives and rapidly expanded worldwide[1,2]. Currently, these advancements and expansions continue to grow exponentially, permeating nearly every aspect of human life[3]. Another pivotal moment in the history of the internet was the global proliferation of social media platforms, the integration of the internet into mobile devices, and the interconnection of all electronic devices through the Internet of Things (IoT). Presently, the internet holds vital importance across various domains, including health, education, commerce, and entertainment[4]. Furthermore, it is anticipated that the next significant breakthrough in the internet realm will involve the Internet of Humans (IOH), further solidifying its crucial role[5].

The usability of internet technology, which is progressively becoming more significant for individuals, is growing more challenging due to the escalating data volume and the prevalence of misinformation. Users often encounter difficulties when searching for specific information or products on the internet. Moreover, numerous companies aiming to establish a presence in the online market face challenges in attracting customers to their web pages. It is important to be able to access quickly the required web pages. Text based search approaches fail to list the web pages users are searching for. Therefore, image-based web page searching, and classification models are important to address the problem. Consequently, the classification of web pages has emerged as a complex research area. Although there are attempts within the literature to address this issue, the number of studies in this field remains relatively limited.

Web pages possess numerous attributes, including URL addresses, text content, hyperlinks, images, domain names, server information, HTML tags, and semantic web tags. Consequently, the classification methods developed by researchers are built upon these attributes. In the literature, research on web page classification appears to be divided primarily into two main categories based on the classification data type: 1) text-based classification and 2) image-based classification. Text-based classification methods utilize data such as website content, HTML tags, and domains as inputs for the classification process. Conversely, image-based methods employ screenshots captured from website pages as inputs [6]. Within these classification groups, three notable challenges pose difficulties for researchers. The primary challenge revolves around the rapid expansion of data, rendering analysis increasingly complex. Many classification techniques prove inadequate and slow in handling this data complexity. Another significant obstacle stems from the abundance of attributes present on web pages, particularly in text-based classification. Web pages are essentially text files composed of HTML tags, where both content and design are defined by these tags. The task of segregating content from design, deciphering the page's language, and eliminating extraneous words demands meticulous attention and intricate analysis. Inconsistencies between textual and raw data attributes further complicate the classification of web pages. Lastly, a critical issue pertains to extracting meaningful data for the classification process. On occasion, the content of a web page might not align with the site's purpose, posing a significant challenge for accurate classification. This discrepancy, whether intentional or inadvertent, contributes to the classification problem.

Text-based classifiers are subject to various limitations arising from data complexity and language-related problems. Given that images possess universal attributes, image-based methods offer a more effective and globally applicable solution. Additionally, in contemporary times, websites predominantly feature image-based content such as pictures and videos, as opposed to text-based content. The classification of these media elements bears immense significance for search engines. In light of the inadequacies of text-based classification methods, this study adopts a deep learning approach, a method with established success in various domains, to classify websites using image data. The proposed classification technique is rooted in a convolutional neural network (CNN) architecture for image analysis. The principal distinction of this novel model from existing methods in the literature lies in its training and testing using three distinct optimization

methods. This approach aims to address the challenges of feature extraction and data complexity, which represent the most formidable obstacles in web page classification. Contributions of the study are listed below:

1- Proposing a image based approach for web page classification,
2- Addressing to limitations of searching and classification of text based approaches,
3- It guides researchers to choose the best optimization method by comparing image-based classification methods,
4- It improves the literature results in the field of image-based web page classification.

2. Literature Review

Web page classification is the process of assigning a web page to one of the predetermined categories. These categories may be two categories such as malignant or benign, or they may consist of multiple categories such as e-commerce, education, entertainment etc. The increment of use of web pages and the desire to quickly access valuable data sought on the internet have made the problem of web page classification an important research topic. In order to overcome this problem, many researchers have tried to find solutions using different models and techniques. The studies about web page classification the literature going on two main groups according to the input data used by the researchers. These are 1) text-based, 2) image-based classification, as mentioned in the previous section. However, it is seen that text-based classification is also divided into 3 groups depending on the data type. First one is textual classification which is trying to classify the input data that consists of page contents, titles, HTML tags, domain name. Second one is graph-based classification, and it uses structural relationships of links and back linked web pages. Last one is named as other classification types and this types use server information and, semantic web data as input data[6-9].

When the studies are examined, it is seen that the most popular classification type for web page classification is text-based classification. The large number of features to be used has led researchers to prefer text-based classification methods. Many studies have been carried out to distinguish between adult and child-oriented sites by using text-based classification. Alvari et al.[10] used support vector machines to classify adults and children oriented web page with 12 different textual features. Likewise, Ahmadi et al.[11] used the decision tree structure for classification of pornographic web pages. Some researchers used both textual and graph-based data for web page classification. To address web page classification problem, Sun et al.[12], Qi et al.[13], Tian et al.[14] proposed a system by using support vector machines and, Kwon and Lee[15], Celado et al.[16] proposed other one by using K-nearest neighbor algorithms. Xia et al.[8] used HTML tag, header information and URL as input data for classification. They tried to classify five different web page categories which composed of health to sports. At last decades Deep Learning (DL) methods, which have been achieved state-of-arts results in many fields[17-22] were also used in web page classification. Lin[23] performed web page classification with combination of graph-based and text-based data by using recurrent neural networks (RNN) and deep residual neural networks (ResNet). Buber and Diri [24] reported that they achieved 85% success on RNNs. Evolution-based genetic algorithms and fuzzy logic methods are other robust methods which presented in the literature for text-based web page classification problem[25-28]. One of the biggest limitations of text-based classification methods is that the web page contents are differ according to the languages of the countries and even local regions. So, this makes language the main problem of the text-based classification.

Especially at last decades, image data is used as much as text data in web page classification approaches. In the literature it is seen that image features such as histogram, color information, edge detection and some other features obtained via image filter, are primarily preferred for classification process. De Boer et al. [29] used image features such as histogram, color beam, edge histogram information, Gabor filter and Tamura attributes to classify websites in two categories as beautiful and ugly according to their aesthetic appearance. They chose the Naive Bayes method as the classification method and reported that they achieved 83% success. Ugalde [30], which deals with the mobile-based web page classification problem in the thesis study conducted in 2015, used both text-based and image-based features. As image-based features, he also classified web pages

by analyzing histogram, color beam, edge histogram information, Gabor filter and Tamura features on WEKA [30]. In another study which used both text-based and image-based features, the researchers carried out classification by using deep learning method, on their own dataset that created by themselves. The authors encoded the text-based features as images and then classified the images. They used the bag of words method to encode textual data as images and, reported a success rate of 93.7% was achieved [31]. Li et al.[32] captured the web pages by using their own application, and then they used image features to classify web sites of gambling and sexual. The authors classified these features by using support vector machines. Susaki et al.[33] classified the screenshots of the tourism web sites' in order to create a tourism recommendation guide. They made a classification according to the features that obtained by performing color analysis. In other study, Abdali et al. [34] used more than 50 thousand images obtained from 500 different sites for classify web pages by using deep learning network. All this research in literature show that each researcher collected and created their own dataset independently from each and performed web page classification by using their own dataset. Moreover, it is seen that they haven't shared the datasets publicly. Thus, there is no possibility of comparing results of the methods with each other. It is not also possible for the studies carried out in this way to reveal their superior sides by comparing them with each other[7]. Only giving obtained results in the studies proves that they didn't compare the result with other results in the literature. However, Aydos et al.[6] created and shared a new web page dataset composed of 20 thousand sites that obtained from Google searches. Name of the published dataset is WebScreenshots. They tested the dataset by using deep learning methods. The authors reported that they achieved 94.90% classification success on 4 classes. So, in order to compare the success of the proposed method with other studies in the literature and then detect the state-of-art study, the WebScreenshots dataset was used in this study.

3. Proposed Method

In this study, an Artificial Neural Networks (ANN)-based classification system has been proposed for website classification. The system comprises two main components: feature extraction and the classification process from images. Initially, a deep neural network system based on Convolutional Neural Networks (CNN) is utilized to extract image features, followed by the execution of the classification process. While numerous CNN models exist in the literature, three models have emerged as particularly notable: VGG, ResNet, and DenseNet. These models have demonstrated considerable success and find applications in various domains. Research has consistently indicated that the DenseNet model outperforms other CNN models [35]. Therefore, for the classification phase of this study, the DenseNet121 model was chosen.

After the classification phase, in order to enhance the efficacy of the proposed method, three distinct optimization methods were employed during the fine-tuning stage. These optimization techniques encompass Stochastic Gradient Descent (SGD), Adam, and AdaGrad. The architecture of the proposed system is visually represented in Figure 1.

To best of our knowledge, there is no publicly available data set used by researchers in the literature in this field. It is seen that each researcher carries out his studies by creating his own database. In this study, a publicly shared dataset that created by Aydos et al.[6] was used to compare the obtained results and by the way clearly detect the best accurate web page classification system in the literature.

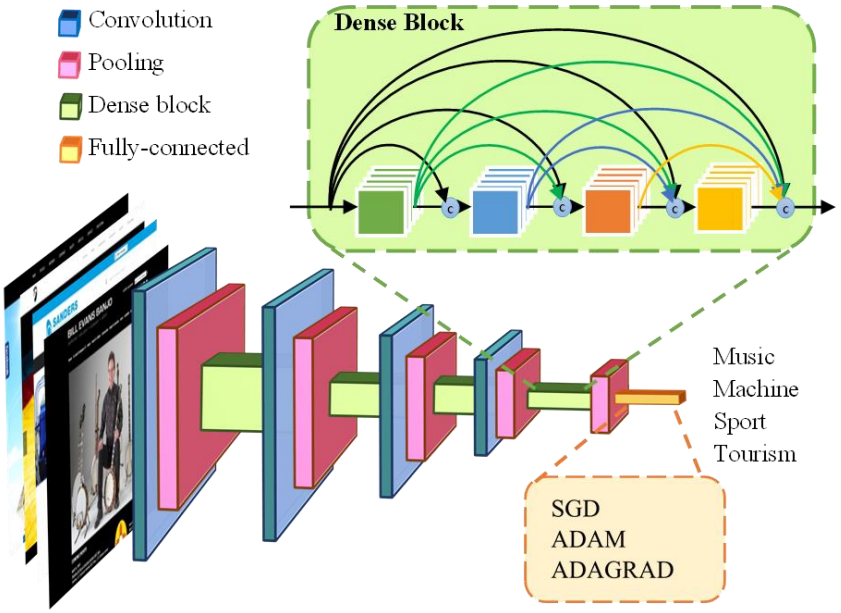

Figure 1. Architecture of proposed web page classification system

In the experiments, the success of the system was measured via 4 different metrics: Accuracy, Recall, F1 score and Area Under Curve (AUC). The classification results were obtained separately for each class. The definitions and equation of the metrics are shown in equation 1, equation 2, equation 3 and equation 4, respectively.

Accuracy: It refers to the proportion of correctly detected data in the entire test dataset. It is defined as in equation 1.

$$Accuracy = \frac{TP+TN}{TP+TN+FP+FN} \quad (1)$$

Recall: It is the ratio of positive samples predicted correctly by the model to all positive samples in the data set. It is defined as in equation 2.

$$Recall = \frac{TP}{TP+FN} \quad (2)$$

F1-Score: It is the harmonic mean of Precision and Recall values. The F1-Score formula is as follows in equation 3.

$$F1 - Score = 2\,x\,\left(\frac{Precision\,x\,Recall}{Precision+Recall}\right) \quad (3)$$

Area Under Curve (AUC): The area under the ROC curve is expressed as AUC. It is defined as in equation 4.

$$AUC = \int_0^1 \frac{TP}{TP+FN}\, d\,\frac{FP}{TN+FP} \quad (4)$$

3.1. Convolutional neural network

The Convolutional Neural Network (CNN), initially introduced by LeCun et al. [36], is an image processing technique characterized by two core attributes: 1) spatially shared weights and 2) spatial pooling. In 1998, the same research group advanced this concept by introducing the LeNet-5 architecture, a 7-layer CNN design, for recognizing handwritten digits on bank check images, which were resized to 32x32 digital images [37].

Presently, CNN stands as the most prevalent deep learning architecture for feature extraction, particularly in tasks such as image classification and object recognition. Fundamentally, CNNs [36] constitute a specialized and enhanced variant of neural networks, boasting multiple layers that have markedly revolutionized the realm of image processing.

A CNN architecture, illustrated in Figure 2, comprises three primary layers: the convolutional layer, the subsampling layer (also referred to as the pool layer), and the fully connected layer. This architecture has ushered in significant advancements in the domain of image processing.

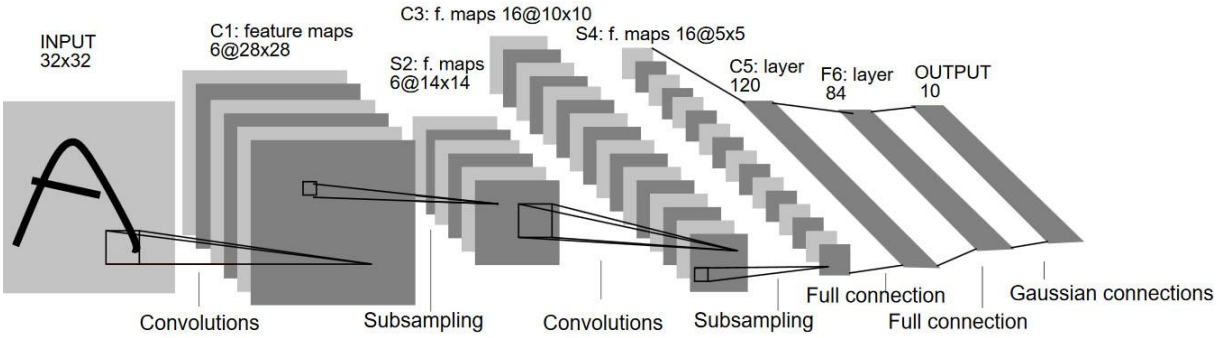

Figure 2. Basic CNN architecture [36]

CNN aims to learn abstract features by applying filters on the input image in the convolution layer and then subsampling the abstracted data in the pool layer. In the convolution layer, the convolution operation is performed by shifting the filter data matrix over the input data matrix. Thus, the features of the input data are obtained. In the first layer, these filters respond and sample edges or spots of color, while in the last layer they begin to sample shapes and parts of objects [38]. The convolution is carried out as a result of the multiplication of the input and output matrices and adding a bias term on the result. Figure 3 shows the basic convolution structure. And the basic formula that represent the convolution process is also given in equation 5. In the equation, the pixels of the filter (kernel), the pixels of the input image, the pixels of the output image, and the bias term are represented by w, x, y and b, respectively.

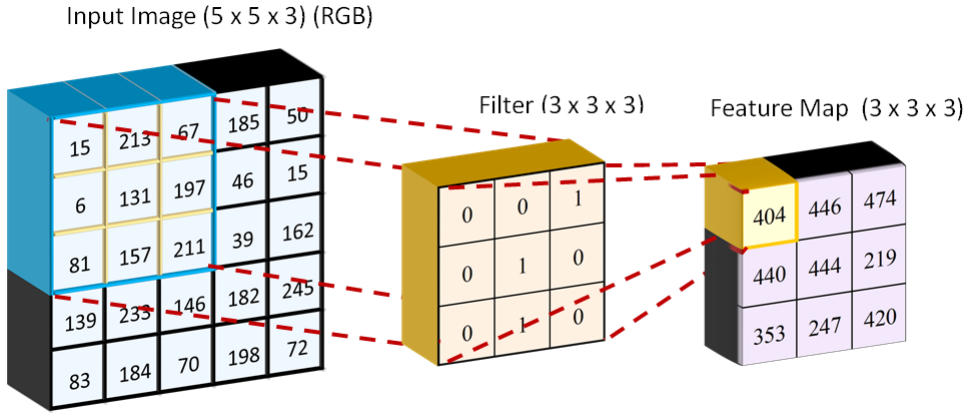

Figure 3. Basic convolution process, the convolution operation is obtained by multiplication of the input data matrix and the filter data matrix and then adding a bias term on it [39]

$$y_n = \sum_{n=1}^{9} (x_n . w_n + b_n) \quad (5)$$

Another layer that CNNs use is the pooling layer, also called the subsampling layer. Pooling [39] is used to reduce the size of feature obtained from the previous layer by moving into subsamples. The pooling layer activation function performs the size reduction process by getting maximum or average value of the obtained

features. The main purpose of the pooling layers is to gradually reduce the feature sizes of the representation and thus reduce the computational cost of the model by reducing the number of parameters [37].

An activation function is added at the end of each layer, and these functions may differ according to preference. Generally, Rectified Linear Unit (ReLU) activation is used at the end of the layer. Activation function aims to normalize result values. The implementation of the ReLU function is that the output of the function will be 0 if the input is less than 0, otherwise the input value will be sent as the output. That is, if the input is greater than 0, the output is equal to the input. The function of the basic process of ReLU is given in equation 6.

$$\mathrm{ReLU(x)} = \begin{cases} 0 & if\ x < 0 \\ x & if\ x \geq 0 \end{cases} \tag{6}$$

The last layer of a CNN is Fully Connected-(FC) layer. In the FC layer, each neuron at the previous layers is connected to every neuron in the next layers. FC layers are the basic building blocks of traditional neural networks. These layers are used to transform the activation feature maps into a one-dimensional feature vector where each value is associated with an object class. End of the FC layer, SoftMax activation function is applied to transform the FC layer results into a probability distribution indicating which class they belong to. By the way, fully connected layers transform the feature map of images into votes that represent the ratio of belongingness of every classes. These rates are expressed as weight or link strength between each value and each class [37,38].

3.2. Densenet

In the traditional CNN architecture, the feature map obtained from each convolutional layer is passed along to the subsequent layer as input. Consequently, every layer can solely glean knowledge from the feature map of the preceding layer. Unfortunately, this setup results in the latter layers being unable to directly access the raw features from the initial layers. This limitation poses challenges in effectively learning input data features and might lead to the loss of numerous features before they ultimately reach the classification layer.

In response to this issue, the ResNet [40] model introduces a novel approach by forwarding the outputs of the two previous convolutional layers as additional inputs to the current layer. By doing so, each layer gains insight from the feature maps of its two predecessors. Nevertheless, even within the ResNet framework, the features of prior layers still struggle to propagate deeply enough, contributing to ongoing feature losses.

In contrast, the DenseNet model refines the structure introduced by ResNet. In the DenseNet model, each layer possesses the capability to harness the feature maps of all preceding layers. This configuration signifies a notable improvement over the ResNet architecture, allowing for more efficient and comprehensive feature utilization across the network.

DenseNet, conceptualized by Huang et al. [41], arose from the insight that classical CNN models could achieve improved accuracy and efficiency through a reimagining of their design, specifically incorporating short connections between each preceding layer and the subsequent layers. Similar to ResNet, DenseNet incorporates these additional short connections, but with a notable distinction: these connections span not only between the current layer and the previous one but also encompass all layers in the network. This fundamental redesign aims to mitigate challenges such as the vanishing gradient problem during weight optimization, while simultaneously enhancing feature extraction, promoting feature reuse, and significantly curtailing the number of parameters involved.

In the classic N-layer CNN model, there exist N connections linking the layers, excluding the input layer. In contrast, the DenseNet model introduces a more intricate connectivity pattern, wherein each layer establishes

connections with all subsequent layers. As a result, every layer receives the feature maps from all preceding layers as input. This approach effectively tackles the vanishing gradient issue, facilitates robust feature extraction, and fosters feature sharing across the network. The DenseNet family encompasses several variations, including models with 121, 169, 201, and 264 layers. For this study, the DenseNet-121 model, comprising 121 dense layers, was selected. The architecture of the DenseNet model is visually presented in Figure 4.

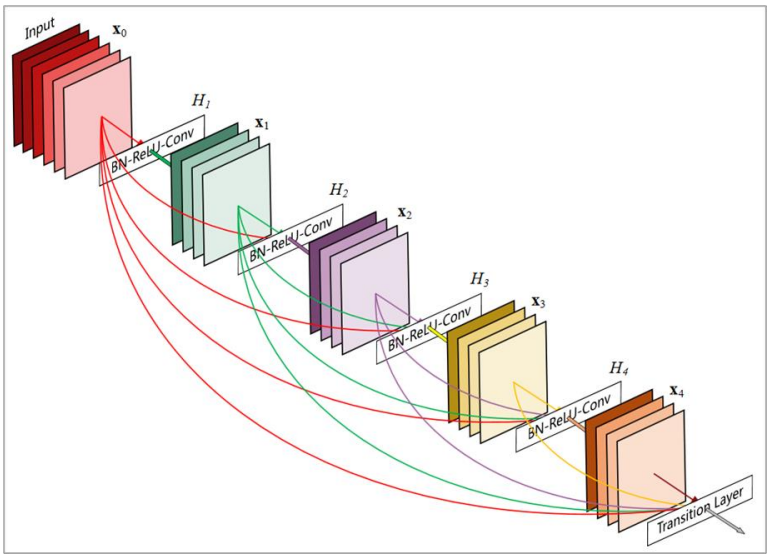

Figure 4. The architecture of the DenseNet [33,35]

4. Experiments and Discussion

This section describes the dataset, experimental setup, training and test phases. Subsequently, the results of the experiments are given and discussed. Finally, the obtained results are compared with the literature.

4.1. Dataset

The WebScreenshots database was developed by Aydos et al.[6] in 2019. The limitation of small databases in web page classification poses challenges in training complex systems like deep learning, which encompass a vast number of learning parameters. Additionally, the dynamic nature of web content over time complicates the comparison of classification results based on search engine-generated search results. To address these issues, researchers introduced the WebScreenshots database, which serves as an extensive collection of web pages.

This database comprises datasets for URL, content, and screenshots categorized into various classes. The screenshot dataset focuses on four distinct classes: machinery, music, sports, and tourism ("machinery," "music," "sport," "tourism"). The process involved listing the web pages from the DMOZ database into classes based on the screenshot dataset's categories and capturing screenshots of these pages. A total of 5000 web pages were captured for each class, culminating in a dataset containing 20,000 instances. Notably, the DMOZ database boasts universality and encompasses diverse web pages in different languages, totaling 44 different languages. Given that the study specifically pertains to image-based classification, solely the screenshots dataset was utilized for the research.

4.2. Results

As mentioned before, in the study, the categories of the web pages are estimated from the screenshots of the web sites. In the study, all experiments were carried out on the WebScreenshots Database, which consists of

20000 data belonging to 4 classes. There are 4 different subsets in the WebScreenshots database named Google10, Google20, Subset10 and Subset20. In this study, Google20, the most comprehensive data set, was used. The Google20 data group consists of 20000 data samples. Screenshots of each class are size of 224X224px. Each image is in RGB format. In the study, data augmentation methods such as rotation, mirroring, shifting, random cropping were used on all data. These methods were used only in the training phase. Data augmentation was not performed on the test data.

In the experiments, all data were split into two groups as 80% training and 20% testing. Each experiment carried out 100 epochs and each epoch consist of 32 batch sizes. The 5-fold cross validation (CV) method was applied in the experiments to reduce randomness and increase reliability. By this way we aimed to tackle of over fitting problem. Final results were obtained by getting average of the CV results. The study was carried out on the NVIDIA TITAN XP graphic card using Keras framework. As stated in the previous section, all experiments were performed on the DenseNet121 model. Experiments were repeated separately for Stochastic Gradient Descent-SGD, Adam and AdaGrad optimization methods. The success of the system was calculated separately for each class and each optimization method by using 4 different metrics: Accuracy, Recall, F1 score and AUC. The obtained results are given in table 1.

Table 1. Experimental results for each class and each optimization method

	Classes	Accuracy	Recall	F1 Score	AUC
SGD	Machinery	0,9754	0,9477	0,9507	0,9662
	Music	0,9685	0,9437	0,9374	0,9602
	Sport	0,9683	0,9329	0,9364	0,9565
	Tourism	**0,9825**	0,9652	**0,9649**	**0,9767**
	Average of SGD	**0,9737**	**0,9474**	**0,9474**	**0,9649**
ADAM	Machinery	0,9118	0,8272	0,8243	0,8836
	Music	0,8784	0,7403	0,7527	0,8323
	Sport	0,8731	0,7862	0,7560	0,8442
	Tourism	0,9361	0,8452	0,8686	0,9058
	Average of ADAM	0,8999	0,7997	0,8004	0,8665
ADAGRAD	Machinery	0,9776	0,9548	0,9552	0,9700
	Music	0,9679	0,9418	0,9361	0,9592
	Sport	0,9669	0,9266	0,9332	0,9534
	Tourism	0,9820	**0,9654**	0,9641	0,9765
	Average of ADAGRAD	0,9736	0,9471	0,9471	0,9648

Upon reviewing the obtained results, it becomes evident that the SGD (Stochastic Gradient Descent) and ADAGRAD optimization methods yielded highly similar outcomes. However, it's noteworthy that the SGD optimization method achieved the most successful result, albeit with a minor disparity. Specifically, the SGD method achieved an average AUC (Area Under the ROC Curve) of 0.9649, while ADAGRAD achieved an average AUC of 0.9648. In contrast, the ADAM optimization method demonstrated the least favorable performance within the WebScreenshots database.

Notably, the Tourism class emerged as the category with the most impressive results across the entire

database. This outcome can be attributed to the high distinctiveness observed within the samples belonging to this particular class. The inherent characteristics of the Tourism class samples appeared to facilitate more accurate and discerning classification outcomes.

Table 2. Comparison of the results with literature results (Elde edilen sonuçların literatür sonuçlarıyla karşılaştırılması)

Paper	Model	Optimization Method	Accuracy	Recall	F1 Score	AUC
Aydos et. al.[6]	VGG16	-	0,9035	-	-	-
Aydos et. al.[6]	DenseNet121	-	0,9300	-	-	-
Aydos et. al. [6]	DenseNet169	-	0,9475	-	-	-
Aydos et. al. [6]	DenseNet201	-	0,94450	-	-	-
Proposed	DenseNet121	Average of SGD	**0,9737**	**0,9474**	**0,9474**	**0,9649**
Proposed	DenseNet121	Average of ADAM	0,8999	0,7997	0,8004	0,8665
Proposed	DenseNet121	Average of ADAGRAD	0,9736	0,9471	0,9471	0,9648

The comparison of the achieved results with those reported in the literature is outlined in Table 2. Upon analyzing the existing literature, it becomes evident that only one study has been conducted on the WebScreenshots database[6]. In this particular study, Aydos et al.[6]attained an accuracy rate of 0.9475 across the four classes. The authors conducted their experiments using a learning rate of 0.00001. However, they did not provide information regarding the optimization method employed in their experiments. Moreover, the authors exclusively presented results based on the accuracy metric, omitting any insights into other evaluation metrics.

Based on the results obtained in the current study, a clear distinction emerges: the proposed system, leveraging the SGD and ADAGRAD optimization methods, outperforms the previous study by Aydos et al. [6]. Notably, the success achieved through the proposed ADAM optimization method falls short of the performance recorded in the literature.

5. Conclusion

In the study, the classification of web page content was conducted using captured website images, totaling 20,000 images across four distinct classes. This classification task was executed employing a deep learning approach. Specifically, the DenseNet121 model, recognized for its success across diverse domains, was selected for the classification process, wherein it was paired with three different optimization methods: SGD, ADAM, and ADAGRAD. To ensure robustness and reliability, a 5-fold cross-validation (CV) methodology was implemented, and the final results were obtained by averaging the outcomes of the CV runs.

Upon analyzing the experimental results, a clear pattern emerges. The SGD optimization method emerged as the most successful, boasting impressive metrics: an Accuracy of 0.9737, a Recall of 0.9474, an F1 score of 0.9474, and an AUC value of 0.9649. These outcomes reflect the superior performance of the proposed approach, particularly with the SGD optimization method. Notably, the proposed system achieved state-of-the-art results within the existing literature concerning the WebScreenshots Database, not only with the SGD method but also with the ADAGRAD optimization method.

Acknowledgments

This work has been supported by the NVIDIA Corporation. All experimental studies were carried out on the TITAN XP graphics card donated by NVIDIA. We sincerely thank NVIDIA Corporation for their supports.

Conflict of Interest Statement

The authors declare that there is no conflict of interest

References

[1] J. McQuillan, I. Richer and E. Rosen, "The New Routing Algorithm for the ARPANET" *IEEE Transactions on Communications*, vol. 28, no. 5, pp. 711-719, May 1980. doi:10.1109/TCOM.1980.1094721

[2] C. P. Berges and V. Schafer, "Arpanet (1969–2019)," *Internet Histories*, vol. 3, no. 1, pp. 1-14, 2019. doi:10.1080/24701475.2018.1560921

[3] M. T. Simsim, "Internet usage and user preferences in Saudi Arabia," *Journal of King Saud University-Engineering Sciences*, vol. 23, no. 2, pp. 101–107, 2011. doi:10.1016/j.jksues.2011.03.006

[4] A. Weinstein and M. Lejoyeux, "Internet Addiction or Excessive Internet Use," *The American Journal of Drug and Alcohol Abuse*, vol. 36, no. 5, pp. 277-283, 2010. doi:10.3109/00952990.2010.491880

[5] K. Chan and W. Fang, "Use of the internet and traditional media among young people," *Young Consumers*, vol. 8, no. 4, pp. 244–256, 2007. doi:10.1108/17473610710838608

[6] F. Aydos, A. M. Özbayoğlu, Y. Şirin, and M. F. Demirci, "Web page classification with Google Image Search results," *arXiv preprint arXiv:2006.00226*, 2020. [Online]. Available https://arxiv.org/abs/2006.00226

[7] X. Qi and B. D. Davison, "Web page classification: Features and algorithms," *ACM computing surveys (CSUR)*, vol. 41, no. 2, pp. 1–31, 2009. doi:10.1145/1459352.1459357

[8] C. Xia and X. Wang, "Graph-Based Web Query Classification," in *2015 12th Web Information System and Application Conference*, WISA, 11-13 Sept. 2015, Jinan, China [Online]. Available: IEEE Xplore, http://www.ieee.org. [Accessed: 04 February 2016].

[9] M. Hashemi, "Web page classification: a survey of perspectives, gaps, and future directions," *Multimed Tools Appl*, vol. 79, no. 17–18, pp. 11921–11945, 2020. doi:10.1007/s11042-019-08373-8

[10] H. Alvari, E. Shaabani, P. Shakarian, H. Alvari, E. Shaabani, and P. Shakarian, "Semi-Supervised Causal Inference for Identifying Pathogenic Social Media Accounts," *Identification of Pathogenic Social Media Accounts: From Data to Intelligence to Prediction*, pp. 51–61, 2021 doi:10.1007/978-3-030-61431-7_5

[11] A. Ahmadi, M. Fotouhi, and M. Khaleghi, "Intelligent classification of web pages using contextual and visual features," *Applied Soft Computting*, vol. 11, no. 2, pp. 1638–1647, 2011. doi:10.1016/j.asoc.2010.05.003

[12] A. Sun, E. P. Lim, and W. K. Ng, "Web classification using support vector machine," in *Proceedings of the 4th international workshop on Web information and data management*, New York, NY, USA, WIDM02, Association for Computing Machinery,2002, pp. 96–99.

[13] X. Qi and B. D. Davison, "Knowing a web page by the company it keeps," in *Proceedings of the 15th ACM international conference on Information and knowledge management*, CIKM06, New York, NY, USA, Association for Computing Machinery, 2006, pp. 228–237.

[14] L. Tian, D. Zheng, and C. Zhu, "Image classification based on the combination of text features and visual features," *International journal of intelligent systems*, vol. 28, no. 3, pp. 242–256, 2013. doi:10.1002/int.21567

[15] O. W. Kwon and J. H. Lee, "Web page classification based on k-nearest neighbor approach," in *Proceedings of the fifth international workshop on Information retrieval with Asian languages*, IRAL00, New York, NY, USA, Association for Computing Machinery, 2000, pp. 9–15.

[16] P. Calado, M. Cristo, E. Moura, N. Ziviani, B. Ribeiro-Neto, and M. A. Gonçalves, "Combining link-based and content-based methods for web document classification," in *Proceedings of the twelfth international conference on Information and knowledge management*, CIKM03, New York, NY, USA , Association for Computing Machinery, 2003, pp. 394–401.

[17] K. Gürkahraman and R. Karakiş, "Brain tumors classification with deep learning using data augmentation," *Journal of the Faculty of Engineering and Architecture of Gazi University*, vol. 36, no. 2, pp. 997–1011, 2021. doi:10.17341/gazimmfd.762056

[18] A. Tekerek, "A novel architecture for web-based attack detection using convolutional neural network," *Computers & Security*, vol.

100, pp. 102096, 2021. doi:10.1016/j.cose.2020.102096

[19] R. Karakis, K. Gurkahraman, G. D. Mitsis, and M. H. Boudrias, "Deep learning prediction of motor performance in stroke individuals using neuroimaging data," *Journal of Biomedical Informatics*, vol. 141, pp. 104357, 2023. doi:10.1016/j.jbi.2023.104357

[20] S. Savaş, N. TOPALOĞLU, Ö. KAZCI, and P. KOŞAR, "Comparison of deep learning models in carotid artery Intima-Media thickness ultrasound images: CAIMTUSNet," *Bilişim Teknolojileri Dergisi*, vol. 15, no. 1, pp. 1–12, 2022, doi:10.17671/gazibtd.804617

[21] M. Kizilgul, R. Karakis, N. Dogan, H. Bostan, M. M. Yapici, U. Gul et al., "Real-time detection of acromegaly from facial images with artificial intelligence," *European journal of endocrinology*, vol. 188, no. 1, pp. 158-165, 2023. doi:10.1093/ejendo/lvad005

[22] S. Savaş, "Detecting the stages of Alzheimer's disease with pre-trained deep learning architectures," *Arabian Journal for Science and Engineering*, vol. 47, no. 2, pp. 2201–2218, 2022. doi:10.1007/s13369-021-06131-3

[23] Y. Lin, "RNN-Enhanced Deep Residual Neural Networks for Web Page Classification," Ph.D. dissertation, University of Calgary, Calgary, Canada, 2016.

[24] E. Buber and B. Diri, "Web page classification using RNN," *Procedia Computer Science*, vol. 154, pp. 62–72, 2019. doi:10.1016/j.procs.2019.06.011

[25] D. Alsaleh and S. Larabi-Marie-Sainte, "Arabic Text Classification Using Convolutional Neural Network and Genetic Algorithms," *IEEE Access*, vol. 9, pp. 91670-91685, 2021. doi:10.1109/ACCESS.2021.3091376

[26] A. P. García-Plaza, V. Fresno, R. M. Unanue and A. Zubiaga, "Using Fuzzy Logic to Leverage HTML Markup for Web Page Representation," in *IEEE Transactions on Fuzzy Systems*, vol. 25, no. 4, pp. 919-933, Aug. 2017. doi:10.1109/TFUZZ.2016.2586971

[27] V. Petridis and V. G. Kaburlasos, "Clustering and classification in structured data domains using Fuzzy Lattice Neurocomputing (FLN)," *in IEEE Transactions on Knowledge and Data Engineering*, vol. 13, no. 2, pp. 245-260, March-April 2001. doi:10.1109/69.917564

[28] C. Haruechaiyasak, Mei-Ling Shyu and Shu-Ching Chen, "Web document classification based on fuzzy association," *Proceedings 26th Annual International Computer Software and Applications*, Oxford, UK, 2002, pp. 487-492.

[29] V. de Boer, M. van Someren, and T. Lupascu, "Web page classification using image analysis features," in *Web Information Systems and Technologies: 6th International Conference*, WEBIST 2010, Valencia, Spain, April 7-10, 2011, pp. 272–285.

[30] D. S. Ugalde, "Android App for Automatic Web Page Classification: Analysis of Text and Visual Features," Ph.D. dissertation, Universidade de Coimbra, Portugal, 2015.

[31] T. Gogar, O. Hubacek, and J. Sedivy, "Deep neural networks for web page information extraction," in *Artificial Intelligence Applications and Innovations*, AIAI 2016, Thessaloniki, Greece, September 16-18 2016, Proceedings 12, 2016, pp. 154–163.

[32] L. Li, G. Gou, G. Xiong, Z. Cao, and Z. Li, "Identifying gambling and porn websites with image recognition," in *Advances in Multimedia Information Processing: 18th Pacific-Rim Conference on Multimedia*, PCM 2017, Harbin, China, September 28-29, 2017, pp. 488–497.

[33] J. Sasaki, S. Li, and E. Herrera-Viedma, "A classification method of photos in a tourism website by color analysis," in *Advances and Trends in Artificial Intelligence. From Theory to Practice: 32nd International Conference on Industrial, Engineering and Other Applications of Applied Intelligent Systems, IEA/AIE 2019*, Graz, Austria, July 9–11, 2019, Proceedings 32, 2019, pp. 265–278.

[34] S. Abdali, R. Gurav, S. Menon, D. Fonseca, N. Entezari, N. Shah and E. E. Papalexakis, "Identifying misinformation from website screenshots," in *Proceedings of the International AAAI Conference on Web and social media*, ICWSM-21, California, USA, June 7-10, 2021, pp. 2–13.

[35] M. M. Yapıcı, A. Tekerek and N. Topaloğlu, "Performance Comparison of Convolutional Neural Network Models on GPU," *IEEE 13th International Conference on Application of Information and Communication Technologies (AICT), 23-25 October 2019*, Baku, Azerbaijan [Online]. Available: IEEE Xplore, http://www.ieee.org. [Accessed: 06 Feb. 2020].

[36] Y. LeCun, B. Boser, J. Denker, D. Henderson, R. Howard, W. Hubbard and L. Jackel, Advances in Neural Information Processing Systems: *Handwritten digit recognition with a back-propagation network*, Morgan-Kaufmann, 1990

[37] Y. LeCun, L. Bottou, Y. Bengio, and P. Haffner, "Gradient-based learning applied to document recognition," *Proceedings of the IEEE*, vol. 86, no. 11, pp. 2278–2324, November 1998. doi:10.1109/5.726791

[38] A. Krizhevsky, I. Sutskever, and G. E. Hinton, "Imagenet classification with deep convolutional neural networks," *Communications of the ACM*, vol. 60, no. 6, pp. 84-90, June 2017. doi:10.1145/3065386

[39] A. Tekerek and M. M. Yapici, "A novel malware classification and augmentation model based on convolutional neural network," *Computer & Security*, vol. 112, pp. 102515, January 2022, doi:10.1016/j.cose.2021.102515

[40] K. He, X. Zhang, S. Ren, and J. Sun, "Deep residual learning for image recognition," in *Proceedings of the IEEE conference on computer vision and pattern recognition*, CVPR 2016, 26-29 June 2016, Las Vegas, USA [Online]. Available: https://cvpr2016.thecvf.com/. [Accessed: 01 July. 2016].

[41] G. Huang, Z. Liu, L. Van Der Maaten, and K. Q. Weinberger, "Densely connected convolutional networks," in *Proceedings of the IEEE conference on computer vision and pattern recognition*, CVPR 2017, 21-26 July 2016, Honolulu, Hawaii [Online]. Available: https://cvpr2017.thecvf.com/, [Accessed: 29 July. 2017].

This is an open access article under the CC-BY license

GAZİ
JOURNAL OF ENGINEERING SCIENCES

Determination of Effects of Point Pollution Sources in Kesikköprü Dam Lake Basin

Olcay Gülçiçek Uysal*[a], Kağan Cebe[b]

Submitted: 01.10.2023 Revised: 29.01.2024 Accepted: 29.02.2024 doi:10.30855/gmbd.2017.0705N07

ABSTRACT

This study aims to examine the effects of pollution coming from point sources within the basin of Kesikköprü dam lake, which is considered a source of drinking water supply for Ankara province, considering the increasing population between 2022 and 2050, and the wastewater. The point sources of pollution in a region include domestic and industrial wastewater and solid waste leachate incoming to the receiving environment. A methodology for calculating total nitrogen (TN), total phosphorus (TP), biochemical oxygen demand (BOD), chemical oxygen demand (COD), and total suspended solids (TSS) loads, which are pollutant loads coming from point sources, is presented and region-specific findings and results are obtained. The study area is divided into 33 sub-basins and point pollution sources in each sub-basin are determined. The loads occurring in these sources are calculated according to unit pollution values. In addition to the pollution loads from point sources existing in the basin in 2022, the change in loads in 5-year periods between 2022 and 2050 is also estimated according to the population projection in the region. Thematic maps showing the spatial distribution of the results are created using ArcGIS 10.8. The calculated point source pollution loads reveal that if no improvement for wastewater treatment is made by 2050, they will increase parallel to the population growth, creating a significant pollution load on the dam lake from which drinking water is supplied, and negatively affecting water quality in the reservoir.

Keywords: Water pollution, point sources of pollution, wastewater, GIS

[a,*] Mersin University,
Faculty of Engineering,
Dept. of Environmental Engineering
33100 - Mersin, Türkiye
Orcid: 0000-0001-9032-4241
e mail: olcayozer@mersin.edu.tr

[b] Ondokuz Mayıs University,
Faculty of Engineering,
Dept. of Civil Engineering
55200 - Samsun, Türkiye
Orcid: 0000-0003-1288-1362

*Corresponding author:
olcayozer@mersin.edu.tr

Kesikköprü Baraj Gölü Havzasındaki Noktasal Kirlilik Kaynaklarının Etkilerinin Belirlenmesi

ÖZ

Bu çalışmada, kentleşme ile birlikte artan nüfus ve beraberinde oluşacak olan evsel atıksu ve kirlilik yükleri dikkate alınarak, Ankara ili için içme suyu kaynağı olarak değerlendirilen Kesikköprü baraj gölü ne havza içerisindeki noktasal kaynaklardan gelen kirliliğin 2022-2050 yılları arasındaki baskı ve etkilerinin incelenmesi hedeflenmiştir. Alıcı ortama gelen evsel ve endüstriyel atıksular ile katı atık sızıntı suları bölgedeki noktasal kaynaklı kirleticileri oluşturmaktadır. Noktasal kaynaklardan gelen kirletici yüklerinden olan toplam azot (TN), toplam fosfor (TP), biyokimyasal oksijen ihtiyacı (BOİ), kimyasal oksijen ihtiyacı (KOI) ve askıda katı madde (AKM) yüklerinin hesaplanması için bir metodoloji sunulmuş ve bölgeye özgü bulgu ve sonuçlar ortaya konulmuştur. Çalışma alanı, 33 alt havzaya ayrılmış ve her alt havzada bulunan noktasal kirlilik kaynakları tespit edilerek, bu kaynaklarda oluşan yükler birim değerlere göre hesaplanmıştır. Havza içerisinde 2022 yılında mevcut olan noktasal kirlilik yükleri yanı sıra, bölge için yapılan nüfus projeksiyonuna göre 2022-2050 yılları arasında 5 yıllık periyotlar ile yüklerinin değişimi de tahmin edilmiştir. Sonuçların, alansal dağılımını gösteren tematik haritalar ise ArcGIS 10.8 yazılımı kullanılarak oluşturulmuştur. Hesaplanan noktasal kaynaklı kirlilik yüklerinin 2050 yılına kadar hiçbir iyileştirme yapılmaz ise nüfus artışına paralel olarak artarak içme suyu temin edilen baraj gölünde kirlilik yükü baskısı oluşturacağını ve su kalitesini olumsuz yönde etkileyeceğini ortaya koymaktadır.

Anahtar Kelimeler: Su kirliliği, noktasal kirletici kaynakları, atıksu, CBS

To cite this article: O. Gulcicek Uysal and K. Cebe, "Determination of Effects of Point Pollution Sources in Kesikköprü Dam Lake Basin," *Gazi Journal of Engineering Sciences*, vol.10, no.1, pp. 84-101, 2024. doi:10.30855/gmbd.0705N07

1. Giriş (Introduction)

Temiz ve kullanılabilir suya ulaşım, Dünya üzerindeki hızlı nüfus artışı, sanayileşme ve kentleşme ile gün geçtikçe zorlaşmaktadır [1]. Su kaynakları üzerindeki gün geçtikçe artan baskıların değerlendirmesi yapıldığında, su kaynaklarının havza ölçeğinde yönetiminin önemli olduğu ortaya çıkmaktadır. Havza, tüm doğal kaynakları içinde barındıran akarsuyun başlangıcından döküldüğü noktaya kadar tüm drenaj alanı kapsayan bir arazi parçası olarak tanımlanmaktadır ve bu bakımdan çoğu zaman idari sınırdan bağımsızdır. Havza yönetimi ise havza içerisindeki tüm kaynakların bütünlük içinde korunmasını sağlayacak yönetim kavramı olarak belirlenmiştir [2].

Havzaların yönetimi, doğru kullanımı, havza içindeki göllerin ve rezervuarlarının ıslahı ve korunması, havzayı besleyen yüzey sularının doğal ekosistemlerin korunması için anahtardır [3]. Bu nedenle havzalarda kirlilik oluşturan kaynakların ortaya konulması ve kontrolü oldukça önemlidir [4]. Kirletici kaynaklarını kirliliğin ortama veriliş şekilleri açısından ikiye ayırmak mümkündür. Bunlar, noktasal kirletici kaynaklar ve yayılı (noktasal olmayan) kirletici kaynaklar olarak adlandırılır. Noktasal kaynaklardan gelen kirlilik yükleri alıcı ortama belli bir noktadan, doğrudan deşarj edilir. Yayılı kaynaklardan gelen kirlilik yükleri ise alıcı ortama yayılarak ulaşmaktadır. Bu bakımdan, noktasal kirlilik kaynaklarının kontrolü ve ıslahı, yayılı kaynaklara göre daha kolaydır. Bu çalışma kapsamında çalışma alanına ait noktasal kirletici kaynakları araştırılmıştır. Noktasal kirletici kaynaklar evsel atıksu arıtma tesisi deşarjlarını, endüstriyel atıksu deşarjlarını ve sabit bir noktadan gelen kirleticileri kapsamaktadır. Avrupa Birliği üye devletleri, nehir havzası yönetim planı doğrultusunda yayınladıkları "Avrupa suları durum değerlendirmesi ve baskılar" adlı raporunda noktasal kirlilik kaynaklarında kentsel atık suların baskın kirlilik kaynağı olduğunu açıklamışlardır [5].

Havza sınırlarında oluşan su kaynaklarının azalması ve kirlenmesi, bitki örtüsü kayıpları, nüfus artışı, noktasal ve noktasal olmayan kirlilik kaynakları havzada müdahale gerektiren olayların varlığını göstermektedir. Havzalarda müdahale gerektiren olaylara hızlı çözüm üretebilmek için havzayı oluşturan tüm parçaların birbirleriyle ilişkisinin ortaya konulması gereklidir [2, 6, 7]. Havzalarda başlıca kirliliğe neden olan unsurların envanter çalışmasının yapılması ile su kalitesini etkileyen kaynakların gözlenmesi ve değerlendirilmesi, havzadaki potansiyel sorunlar tanımlanması açısından oldukça önemlidir [2]. Sınırlayıcı ve düzenleyici faktörler ilkesine göre, belirli ekolojik süreçlerin talebe göre en az arzda bulunan çevresel faktör tarafından kontrol edildiğini belirtir. Bu fikre göre, durgun sularda ve göllerde azot ve özellikle fosfor, sucul ekosistemlerde birincil üretim için sınırlayıcı besin olarak kabul edilmektedir [8]. Araştırmalar, neredeyse tüm tatlı sularda birincil üretimin, fosfat iyonu olarak ortaya çıkan fosforun mevcudiyeti ile sınırlı olduğunu göstermiştir.

Durgun sular ve göllerde en önemli azot kaynaklarından biri de noktasal kirletici kaynaklarından su kütlesine ulaşan kirleticilerdir. Türkiye Cumhuriyeti Tarım ve Orman Bakanlığına (TOB) ait raporda, Yeşilırmak Havza sınırlarındaki yüzey sularının kentsel ve endüstriyel deşarjların neden olduğu önemli baskılardan etkilendiği rapor edilmiş olup, çevresel hedeflere ulaşma riski düşük veya kentsel ve endüstriyel atıksular nedeniyle önemli ölçüde etkilenen 28 su kütlesi hassas su kütleleri olarak kabul edilmiştir [9].

Erdoğan [10] tarafından, Doğu Karadeniz Havzası'nda gerçekleştirilen araştırmada 2017-2040 yılları arasında havza nüfusunun tahmin edildiği ve bu dönemde havza içindeki noktasal ve yaygın kaynaklardan alıcı ortamlara ulaşabilen kimyasal oksijen ihtiyacı (KOİ), toplam azot (TN) ve toplam fosfor (TP) yüklerinin tahmin edilmesi üzerine odaklanılmıştır. Çalışmanın sonuçlarına göre, kirlilik yüklerinin kaynakları şu şekildedir: Noktasal azot yükleri %96 oranında kentsel kirlilikten kaynaklanmakta, %2 oranında endüstriyel kaynaklardan ve %2 oranında ise katı atık sızıntı sularından kaynaklanmaktadır. Noktasal fosfor yükleri açısından ise %99'u kentsel kaynaklardan, %1'i ise endüstriyel kaynaklardan kaynaklanmaktadır. Bursa Uluabat Gölü'nde noktasal kirlilik kaynakları üzerine Hacısalihoğlu ve Karaer tarafından yapılan çalışmada, bu kaynakların gölü önemli ölçüde kirlettikleri belirlenmiştir [11]. Marmara Havzası'nda evsel atıksuların su kaynakları etkileri incelenmiş ve havzadaki kirliliğin baskın olarak daha çok noktasal kaynaklardan geldiği ortaya konmuştur [12].

Bu çalışma ile Türkiye'nin en uzun nehri Kızılırmak üzerinde bulunan, elektrik üretimi ve sulama yanında 2008 yılından itibaren Ankara'nın içme suyunun karşılanması için de kullanılan Kesikköprü baraj gölünün, artan nüfusa bağlı olarak 2022-2050 yılları arasında maruz kalacağı kirlilik yüklerinin ortaya konulması amaçlanmaktadır. Bu amaçla, çalışma alanı 33 alt havzaya ayrılmış ve her alt havzanın noktasal kirlilik kaynakları tespit edilerek, 2022-2050 yılları arasında kirletici yükleri hesaplamaları Atıksu Arıtma Tesisleri Teknik Usuller Tebliği'nde [13] yer alan birim değerlere göre yapılmıştır. Elde edilen sonuçların, alansal dağılımını gösteren tematik haritalar ise ArcGIS v.10.8 yazılımı kullanılarak oluşturulmuştur.

2. Çalışma Alanı (Study area)

Çalışma alanı, Türkiye'nin ikinci en büyük havzası olan Kızılırmak havzasında yer almaktadır. Kızılırmak havzası İç Anadolu Bölgesi'nin doğusunda yer almaktadır. 1.151 km'lik uzunluğu ile Türkiye akarsularının en uzunu olan Kızılırmak, 82.181 km^2'lik bir drenaj alanına sahiptir [14]. Kızılırmak üzerinde bulunan Kesikköprü baraj gölü , Ankara ili Bala ve Şereflikoçhisar ilçeleri ve Kırşehir ili Kaman ilçesi ile Kırıkkale ili Çelebi ilçe sınırları içerisinde bulunmaktadır. Söz konusu Proje alanı Ankara il merkezinin kuş uçuşu yaklaşık 76 km güneydoğusunda ve Kırşehir ilinin yaklaşık 55 km kuzeybatısında yer almaktadır. Proje alanı Kızılırmak Havzası-Orta Kızılırmak Alt Havzası sınırları içerisinde yer almakta olup, havzayı temsil eden Kesikköprü Barajı Gölü'nün orta noktası ED50 UTM Zone 36 536611 D ve 4359527 K koordinatlarında bulunmaktadır. Türkiye 1/25.000 ölçekli pafta bölümlemesinde barajın havza alanı; J30-b2, J30-b3, J30-b4, J30-c1 J30-c2, J31-a1 ve J31-a4 paftaları içerisinde yer almaktadır. Baraj havzasının coğrafi konumunu gösterir harita Şekil 1'de verilmiştir.

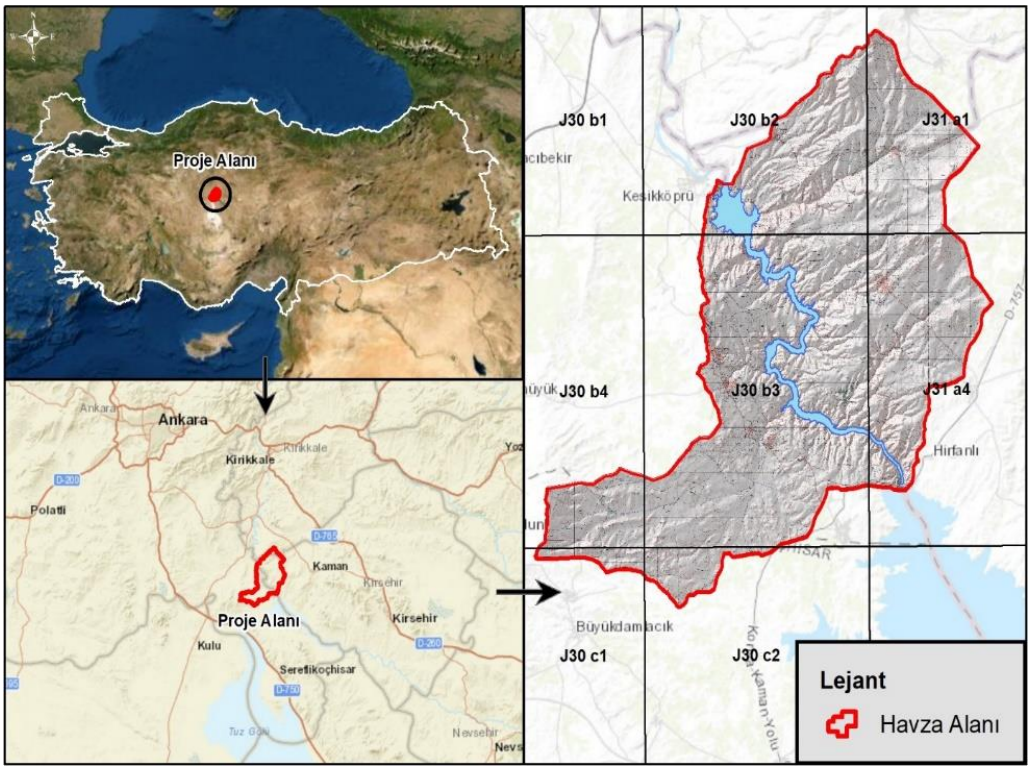

Şekil 1. Kesikköprü baraj gölü havzası coğrafi haritası
(Geographical map of Kesikköprü dam lake basin)

Kızılırmak nehri üzerinde kurulu 11 adet baraj mevcuttur. Bu barajlardan biri olan Kesikköprü Barajı, Ankara'ya 120 km mesafededir. Güncel olarak baraj kullanımı; enerji, tarımsal sulama ve içme suyu amacıyla gerçekleşmektedir. 1995 yılında Ankara ili için gelecekte içme suyu kaynağı olarak önerilen Kapulukaya Barajı'nın su kalitesinin yetersiz olmasından dolayı, 2000 yılında Kesikköprü Barajı'nın içme suyu amacıyla kullanımı kararlaştırılmıştır.

Bu çalışma kapsamında, Kesikköprü baraj gölü havzası, sınırlarındaki akarsu kolları ve baraj gölü temel alınarak 33 alt havzaya ayrılmıştır. Bir coğrafi bilgi sistemi (CBS) yazılımı olan ArcGIS v.10.8 Arc/Hydrology

programı kullanılarak çalışma alanı mikro alt havzalara bölünmüş ve baraj gölünü besleyen ana akarsu kollarının beslenme alanları, membadan mansaba doğru sıralanarak birleştirilmiştir. Oluşturulan alt havzaların (KAH) sınırları Şekil 2'de ve alanları ise Tablo 1'de verilmiştir.

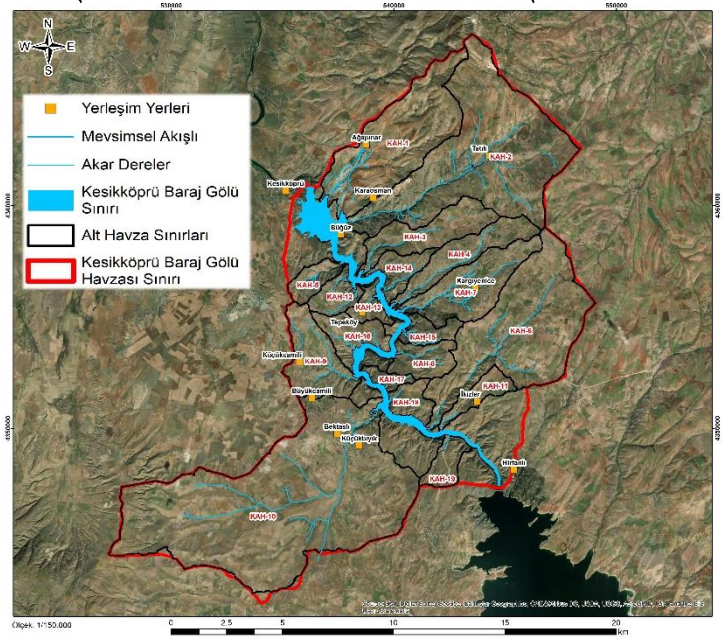

Şekil 2. Kesikköprü baraj gölü alt havzaları
(Kesikköprü dam lake sub-basins)

Tablo 1. Kesikköprü baraj gölü alt havzalarının alanları (Sub-basin areas of Kesikköprü dam lake)

Kod	Alanı (ha)	Kod	Alanı (ha)	Kod	Alanı (ha)	Kod	Alanı (ha)
KAH-1	2.053	**KAH-10**	6.527	**KAH-19**	297	**KAH-28**	102
KAH-2	3.765	**KAH-11**	295	**KAH-20**	271	**KAH-29**	384
KAH-3	800	**KAH-12**	310	**KAH-21**	147	**KAH-30**	386
KAH-4	710	**KAH-13**	208	**KAH-22**	23	**KAH-31**	104
KAH-5	267	**KAH-14**	337	**KAH-23**	131	**KAH-32**	84
KAH-6	2.782	**KAH-15**	261	**KAH-24**	41	**KAH-33**	51
KAH-7	1.084	**KAH-16**	447	**KAH-25**	6		
KAH-8	419	**KAH-17**	132	**KAH-26**	41		
KAH-9	838	**KAH-18**	280	**KAH-27**	87	**TOPLAM**	**24.138**

2. Noktasal Kirlilik Kaynakları (Point sources of pollution)

Kesikköprü baraj gölü havzasında noktasal kirletici kaynaklar; evsel atıksular, endüstriyel atıksular ve katı atıklardan kaynaklı sızıntı suları olarak üç ana başlığa ayrılmıştır. Evsel atıksular, atıksu arıtma tesislerinde arıtılmış ve/veya arıtılmadan doğrudan deşarj edilen sular, merkezi fosseptiklerde depolanan suları içerirken; endüstriyel atıksular ise endüstriyel faaliyetler sonucunda oluşan arıtılmış ve/veya arıtılmamış atık sular olarak sınıflandırılmıştır. Kesikköprü baraj gölü havzasındaki noktasal kirletici kaynaklar Şekil 3'te gösterilmiştir.

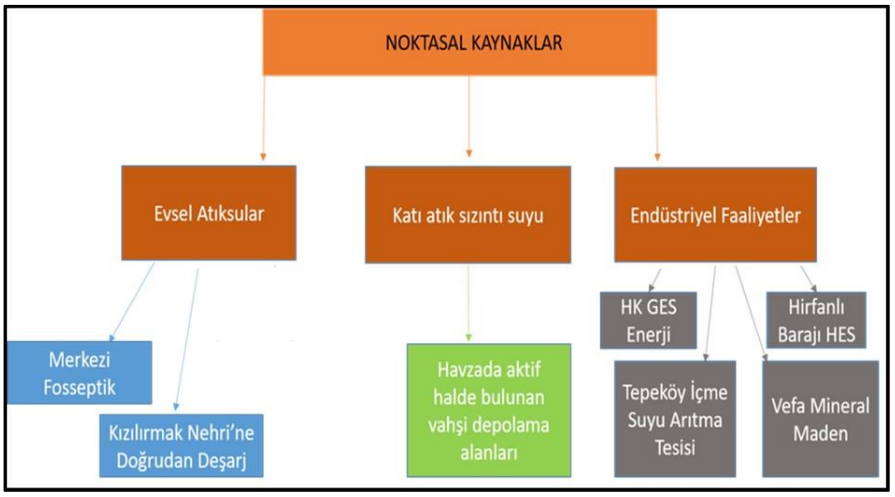

Şekil 3. Kesikköprü baraj gölü havzasındaki başlıca noktasal kirletici kaynakları
(Major Point Pollutant Sources in Kesikköprü Dam Lake Basin)

Noktasal kaynaklardan gelen kirlilik yükü hesapları, Kesikköprü baraj gölü havzasını paylaşan yerleşim yerlerinin dâhil oldukları alt havzalar bazında yapılmıştır (Ağapınar: KAH-1, Tatık, Büğüz KAH-2, Kargınyenice: KAH-7, Küçükcamili: KAH-9, Büyükcamili, Bektaşlı, Küçükbıyık: KAH-10, İkizler: KAH-11, Tepeköy: KAH-13).

Kirlilik yükü hesaplamalarında kişi başına düşen debi ve kirlilik yükü hesaplamaları yapılabilmesi için, çalışma alanındaki yerleşim yerlerinin nüfus değerleri 1985, 1990 ve 2000 yılları için Kızılırmak Havzası Master Planı Nihai Raporu'ndan [15], 2007-2021 yılları arasındaki nüfus verileri ise Adrese dayalı nüfus kayıt sisteminden alınmıştır. 25 yıllık nüfus projeksiyonu hesaplamalarında (2030-2035-2040-2045-2050) İller Bankası nüfus projeksiyon metodu kullanılmıştır.

2.1. İller Bankası metoduna göre nüfus projeksiyonu (Population projection by İller Bankası method)

İller Bankası Yöntemi, artış hızının çoğalma katsayıları ile ifade edildiği ve geometrik artış metodu esasına göre artışın sınırlandırıldığı bir yöntemdir. Çoğalma katsayıları Eşitlik 1 yardımıyla hesaplanmaktadır [16].

$$Ç = \left(a\sqrt{\frac{N_y}{N_e}} - 1\right) x\ 100 \quad (1)$$

Burada, Ç= Çoğalma katsayısı, a=İki nüfus arasında geçen süre (yıl), Ny= Beldenin yeni nüfus değeri, Ne= Beldenin eski nüfus değerini ifade etmektedir. İller Bankası yöntemine göre, nüfus artış oranının aşırı yüksek veya düşük tahmin edilmesinin önüne geçilmesi adına çoğalma katsayısının değeri, Ç>=3 ise Ç=3, Ç<=1 ise Ç=1 olarak alınır. Burada yıllara göre nüfus artış ve düşüş gösterdiğinden her yıl için ayrı ayrı çoğalma katsayısı hesaplanmıştır (Tablo 2).

Tablo 2. İller Bankası Artış Metodu ile nüfus projeksiyonu

Yıllar	**1985**	**1990**	**2000**	**2007**	**2008**	**2009**	**2010**	**2011**	**2012**	**2013**	**2014**	**2015**	**2016**	**2017**	**2018**	**2019**	**2020**	**2021**	**Artış Katsayısı Ortalaması**
Nüfus	9.729	9.986	10.406	4.991	5.012	4.806	4.482	4.674	4.202	4.310	3.943	3.865	4.025	4.573	5.473	4.551	4.146	3.822	
Hesap Dönemi		1990-1985	2000-1990	2007-2000	2008-2007	2009-2008	2010-2009	2011-2010	2012-2011	2013-2012	2014-2013	2015-2014	2016-2015	2017-2016	2018-2017	2019-2018	2020-2019	2021-2020	
Artış Katsayısı		1,03	1,04	0,48	0,42	-4,11	-6,74	4,28	-10,10	2,57	-8,51	-1,98	4,14	13,61	19,68	-16,85	-8,90	-7,81	-1,82

Çoğalma katsayısının yıllara göre değişiklik göstermesi ve ortalama değerinin 1'den küçük olması nedeniyle projeksiyonda Ç=1 olarak alınmıştır. Nüfus hesabı Eşitlik 2 yardımı ile yapılmıştır.

$$N_y = N_e \times \left(1 + \frac{Ç}{100}\right)^n \quad (2)$$

Burada, Ny= Yeni nüfus sayım değeri, Ne= Eski nüfus sayım değeri, Ç= Çoğalma katsayısı, n= İki nüfus arasında geçen süreyi (yıl) ifade etmektedir. Kesikköprü Baraj Gölü Havzası'nda bulunan yerleşim yerlerinin nüfus projeksiyonu, İller Bankası artış metoduna göre hesaplanmıştır (Tablo 3).

Tablo 3. Yerleşimlerin İller Bankası Metodu ile hesaplanan nüfus projeksiyonu

Alt Havza - Yerleşim Yeri / Yıllar	2022	2023	2024	2025	2030	2035	2040	2045	2050
KAH-1 (Ağapınar)	238	246	253	261	302	350	406	471	546
KAH-2 (Tatık-Büğüz)	303	306	310	313	329	346	363	382	401
KAH-7 (Kargınyenice)	824	832	840	849	892	937	985	1036	1088
KAH-9 (Küçükcamili)	402	414	427	440	510	591	685	794	921
KAH-10 (Büyükcamili, Bektaşlı, Küçükbıyık)	963	992	1023	1053	1221	1416	1641	1903	2207
KAH-11 (İkizler)	76	78	80	83	96	111	129	150	174
KAH-13 (Tepeköy)	118	122	125	129	150	173	201	233	271

2.1. Evsel atıksu (Domestic wastewater)

Kesikköprü baraj gölü havzası noktasal kirlilik yükü ve atıksu debisi hesaplamalarında 20.03.2010 tarih ve 27527 sayılı Atıksu Arıtma Tesisleri Teknik Usuller Tebliği'nde yer alan kişi başına düşen birim değerler ve literatürde bugüne kadar yapılmış çalışmalar baz alınarak hesaplamalar yapılmıştır [10, 17, 18]. Atıksu Arıtma Tesisleri Teknik Usuller Tebliği [13] içerisinde bulunan Tablo 2.1 yerleşim yerlerinin nüfusu ile kişi başına düşen ortalama atıksu miktarını göstermektedir. Bu tabloda en düşük nüfus değeri 2000-10.000 kişi değerler arasında olup çalışma alanında 2000 kişi altındaki nüfusa sahip yerleşim yerleri için birim değerler kabulü yapılmıştır. 2022 yılı için hesaplanan kişi başı atıksu oluşumu değerleri 2050 yılına kadar 5 yıllık zaman dilimlerinde kademeli olarak arttırılmıştır.

Hesaplanan atıksu debisi sonuçlarına sızma debisi de ilave edilmiştir. Sızma debisi, yerleşim yerinin sahilde olup olmamasına, yeraltı su seviyesine, zemine, kanalizasyon şebekesinin yeni ya da eski olmasına ve şebekelerdeki kaçak oranı ile değişmekte olup, hesaplamalarda kentsel altyapı sisteminin zamanla iyileştirileceği kabulü ile kademeli olarak azaltılmıştır.

Buna göre; kişi başı atıksu debisi 2022 yılında %50, 2025 yılında %45, 2030 yılında %40, 2035 yılında %35, 2040 yılında %30, 2045 yılında %25 ve 2050 yılında %20 oranında artırılarak toplam atıksu debisi hesaplanmıştır (Tablo 4). Kesikköprü baraj gölü havzası evsel atıksular için kirlilik yükü hesaplamalarında, nüfusa bağlı kişi başı oluşan kirlilik yükleri ise Tablo 5'te verilmiştir.

Tablo 4. Kişi başı atıksu oluşumu [10, 13, 17, 18] (Wastewater generation per capita)

Yıl	Nüfus (kişi)	Atıksu oluşumu (l/kişi.gün)	Sızma debisi (l/kişi.gün)	Toplam atıksu debi (l/kişi.gün)
2022	2000 altı	70	35	105
	2000-10.000	80	40	120
2025	2000 altı	85	38	123
	2000-10.000	95	43	138
2030	2000 altı	100	40	140
	2000-10.000	115	46	161
2035	2000 altı	115	40	155
	2000-10.000	135	47	182
2040	2000 altı	130	39	169
	2000-10.000	155	47	202
2045	2000 altı	145	36	181
	2000-10.000	175	44	219
2050	2000 altı	150	30	180
	2000-10.000	195	39	234

Çalışma alanı yerleşim yerlerini Kaman ve Bala ilçeleri olarak iki bölgeye ayırdığımızda; Bala ilçesinde kalan 5 yerleşim yerinin (Tepeköy, Küçükcamili, Büyükcamili, Bektaşlı, Küçükbıyık) kanalizasyon sisteminin olduğu ve atıksularının merkezi fosseptiklerde toplandığı tespit edilmiştir. Kaman ilçesinde 4 yerleşim yerinin (Hirfanlı, Tatık, Ağapınar, Büğüz) kanalizasyon siteminin olduğu ve atık suların merkezi fosseptiklerde toplandığı, 1 yerleşim yerinin (Kargınyenice) kanalizasyon sisteminin olduğu ancak toplanan atıksuların doğrudan Kızılırmak nehrine deşarj yapıldığı; bir adet yerleşim yerinin (İkizler) ise atık sularının ferdi fosseptiklerde toplandığı tespit edilmiştir.

Tablo 5. Nüfusa bağlı kişi başı kirlilik oluşumu [10, 13, 17, 18] (Pollution generation per capita based on population)

Yıl	Nüfus (kişi)	KOİ (g/kişi.gün)	BOİ (g/kişi.gün)	AKM (g/kişi.gün)	TN (g/kişi.gün)	TP (g/kişi.gün)
2022	2000 altı	50	35	30	4	0,8
	2000-10000	55	40	35	5	0,9
2025	2000 altı	51	37	32	4,5	0,85
	2000-10000	57	42	36	5	0,9
2030	2000 altı	53	38	34	5	0,9
	2000-10000	62	47	38	5,5	1
2035	2000 altı	55	41	36	5,5	0,95
	2000-10000	67	52	40	6	1,1
2040	2000 altı	57	43	38	6	1
	2000-10000	72	57	42	6,5	1,2
2045	2000 altı	58	45	40	6,5	1,05
	2000-10000	77	62	44	7	1,3
2050	2000 altı	60	47	42	7	1,1
	2000-10000	82	67	46	7,5	1,4

Çalışma alanı içinde bulunan santral ve tesislerden Tepeköy İçme Suyu Arıtma Tesisi, Vefa Mineral Maden Tesisi, HK GES Enerji santralinde oluşan evsel atıksuların merkezi fosseptiklerde toplanarak, belirli aralıklar ile havza dışına toplandığı tespit edilmiştir. Havza sınırına yakın mesafede bulunan, Hirfanlı Barajı HES'e ait evsel atıksular ise doğrudan Kızılırmak Nehri'ne deşarj edildiği tespit edilmiştir.

Havza içinde yerinde yapılan incelemelerde KAH-10 alt havzasında yer alan yerleşim yerlerinin (Büyükcamili, Bektaşlı ve Küçükbıyık) ve KAH-9 alt havzasında yer alan Küçükcamili yerleşim yerinin merkezi fosseptiklerinin oldukça bakımsız olduğu görülmüştür. Bu alanlarda merkezi fosseptiklerin betonarme yapısına rağmen atıksuyun üstte bulunan açıklıklardan sızarak Kızılırmak'a karıştığı, yerinde yapılan saha çalışmalarında tespit edildiğinden, noktasal kirlilik kaynağı olarak kabul edilmiştir. Bu yerleşim yerlerinden kaynaklanan atık su debisi ve kirlilik yükünün %50'sinin havza içine deşarj edildiği kabul edilerek hesaplamalara katılmıştır.

Yapılan saha çalışmalarında KAH-1 (Ağapınar-Karaosman), KAH-2 (Tatık ve Büğüz) ve KAH-13 (Tepeköy) alt havzalarında bulunan yerleşim yerlerinin evsel atık sularının toplandığı merkezi fosseptiklerin düzenli boşaltılmadığı ve bakımsızlığı nedeniyle, noktasal kirlilik kaynağı olarak kabul edilmiştir. Adı geçen yerleşim yerlerinden kaynaklanan atık su debisi ve kirlilik yükünün %20'sinin havza içine deşarj edildiği kabul edilerek hesaplamalara katılmıştır. KAH-11 alt havzasında bulunan İkizler köyü atık suları ferdi fosseptiklerde toplandığından dolayı, noktasal kirlilik kaynak olarak değerlendirilmemiştir. Kesikköprü baraj gölü havzası'nda bulunan Tepeköy İçme Suyu Arıtma Tesisi, Kesikköprü Madencilik işletme ruhsat alanında faaliyet gösteren Vefa Mineral Maden Tesis ve HK GES Enerji tesislerin oluşturduğu evsel atıksular merkezi fosseptiklerde toplandığından dolayı kirlilik yükü hesabına katılmamıştır. Hirfanlı Barajı HES tesisinin evsel atıksuları, tesiste çalışan sayısı dikkate alınarak, toplam evsel kirlilik yüklerinin %5 oranına arttırılarak dâhil edilmiştir. Oran belirlenirken literatür verilerinden yararlanılmıştır [10, 17, 18]. Yerleşim yerlerinde üretilen kentsel kirlilik yüklerinin havzaya ulaşma sürecinde izlediği yol Şekil 4'te verilmektedir.

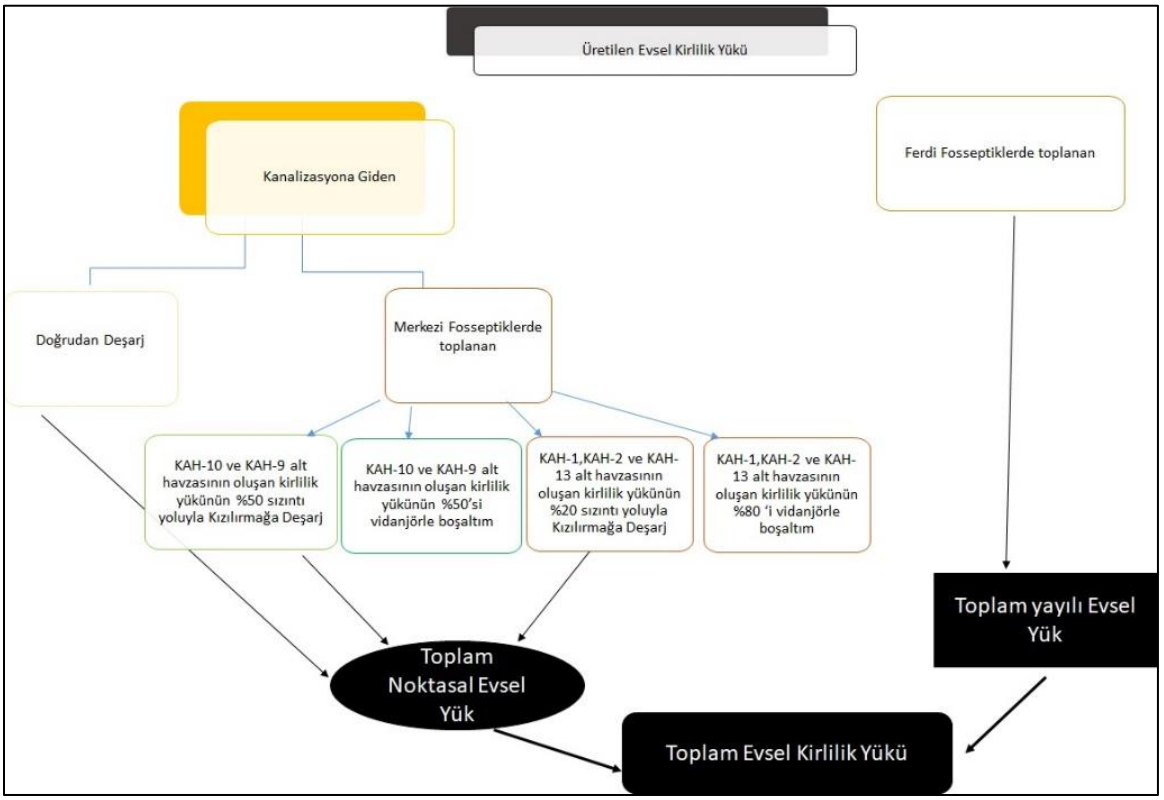

Şekil 4. Evsel atıksu kirlilik yükü şeması
(Domestic wastewater pollution load diagram)

Evsel kirlilik yüklerinin hesaplanmasında yapılan kabuller aşağıda verilmiştir. Buna göre;

- KAH-7 alt havzasında bulunan Kargınyenice köyünün atıksuları doğrudan deşarj yapıldığından dolayı debi ve kirletici yük hesabına katılmıştır.

- Evsel atıksuyunu doğrudan Kızılırmak Nehri'ne deşarj yapan Hirfanlı HES'in debi ve kirlilik yükleri, toplam kirlilik yükünün %5 arttırılması ile hesaplamalara katılmıştır.

- Havza alanı içerisindeki merkezi fosseptik kullanan yerleşim birimlerinin debi ve kirlilik yükleri hesaba katılmış olup; KAH-10 alt havzasında yer alan Bektaşlı, Küçükbıyık ve KAH-9 alt havzasında yer alan Küçükcamili yerleşim yerlerinin oluşturduğu toplam atıksu debi ve kirlilik yüklerinin %50'si hesaba katılmıştır.

- KAH-1 havzasında yer alan Ağapınar, Karaosman, KAH-2 alt havzasında yer alan Büğüz, Tatık ve KAH-13 alt havzasında yer alan Tepeköy yerleşim yerlerinin oluşturduğu toplam atıksu debi ve kirlilik yüklerinin %20'si hesaba katılmıştır.

Yıllık toplam evsel atıksu miktarı, kişi başı atıksu miktarı ile havzada bulunan yerleşim yerlerinin toplam nüfusu çarpılarak hesaplanmış, evsel atıksulardan kaynaklanan yıllık toplam kirlilik yükünün hesabı ise kişi başı kirlilik yükleri ile toplam nüfus çarpılarak bulunmuştur. Günlük olarak verilen kişi başı atıksu ve kirlilik yükleri yıllık toplamlar olarak hesaplanmıştır. Projeksiyon yıllarında oluşması muhtemel toplam atıksu miktarı ve toplam kirlilik yükleri de aynı yöntem kullanılarak hesaplanmıştır. Projeksiyon yılları için İller Bankası Metodu ile hesaplanan nüfus değerleri kullanılmıştır.

2.2. Katı atık (Solid waste)

Kesikköprü baraj gölü havzası sınırları içerisinde yer alan yerleşim yerlerinin İkizler köyü hariç hepsinin katı atıklarının belediye ve Kırşehir İl Özel İdare'ye ait çöp konteynerlerinde biriktirildiği ve düzenli aralıklar ile toplanarak havza alanı dışına taşındığı tespit edilmiştir. Kesikköprü baraj gölü havzası sınırları içerisinde herhangi bir düzenli katı atık depolama sahası ve transfer istasyonu bulunmamaktadır.

2.3. Endüstriyel kirleticiler (Industrial pollutants)

Kesikköprü baraj gölü havzası'na endüstriyel kirleticilerin etkisi oldukça azdır. Proje alanında, Büyükcamili ve Kargınyenice yerleşim yerlerinde küçük ölçekli besicilik çiftlikleri tespit edilmiştir. Alanda büyük ölçekli bir besi çiftliği bulunmamaktadır.

Kesikköprü baraj gölü havzası içerisinde herhangi bir Organize Sanayi Bölgesi veya Küçük Sanayi Sitesi bulunmamaktadır. 2022 yılı Sanayi Sicil Bilgi Sistemi'nde Bala ve Kaman ilçelerinde faaliyet gösteren ve Sanayi Sicil Bilgi Sistemi'ne kayıtlı 186 firmanın olduğu görülmüştür. Bu firmaların içerisinde Kesikköprü baraj gölü havzasında faaliyet gösteren üç işletmenin olduğu anlaşılmıştır. Bölgede geniş bir alana yayılı olarak bulunan maden sahaları içerisinde aktif bir maden işletmesi, bir güneş enerji santrali (GES) ve Kesikköprü baraj gölü membasında bulunan Hirfanlı hidroelektrik santrali (HES) işletmesi bulunmaktadır. Bu işletmeler ile ilgili bilgiler Tablo 6'de verilmiştir.

Tablo 6. Kesikköprü baraj gölü havzasındaki işletmeler (Industry in Kesikköprü dam lake basin)

İşletme Adı	Koordinatı			Sektör	NACE Kodu	Endüstriyel Atıksu Miktarı	Deşarj İzni/ Kanalizasyon	Atıksu Arıtma Tesisi
	Zon	UTMX	UTMY					
Vefa Mineral Maden	36S	540658	4361207	Maden	07.10.01	Deşarj yok	Merkezi Fosseptik	Yok
HK GES	36S	546986	4354503	Enerji	35.11.19	Deşarj yok	Merkezi Fosseptik	Yok
Hirfanlı HES	36S	544731	4347374	Enerji	35.11.19	Deşarj yok	Merkezi Fosseptik	Var*

* Hirfanlı HES İşletme Müdürlüğü lojmanlarında vardır. Havza sınırının dışında kalmaktadır.

Vefa Mineral Maden işletmesi Büğüz köyü sınırlarında faaliyet göstermektedir. İşletme, üretim aşamasında endüstriyel nitelikli atıksu oluşturmadığından, endüstriyel kirlilik yükü hesabına katılmamıştır. Sanayi ve Teknoloji Bakanlığı'ndan alınan bilgide işletmenin arıtma tesisi olmadığı anlaşılmıştır. Yetkililerle yapılan görüşmelerde işletmedeki çalışanların sosyal ihtiyaçları doğrultusunda oluşacak olan evsel nitelikli atıksuların sızdırmaz merkezi fosseptiklerde depolanarak, belirli periyotlarda vidanjör yardımıyla çekildiği bilgisi alınmıştır. Bu nedenle maden işletmesi atıksularının yakınındaki yüzey ve yeraltı su kaynaklarının kalitesi üzerinde etkisi bulunmadığı kabul edilmiştir.

Çalışma alanı sınırları içerisinde Kargınyenice köyü civarında bir adet işletmede olan 5 MWp gücünde HK GES işletmesi bulunmaktadır. Sanayi ve Teknoloji Bakanlığı'ndan alınan bilgide işletmenin arıtma tesisi olmadığı anlaşılmıştır. Tesis çalışanları ile yapılan görüşmelerde işletmede çalışan personel sayısının az olmasından dolayı oluşan evsel nitelikli atıksuların tesis içerisinde sızdırmaz merkezi fosseptikte toplandığı ve belirli periyotlarla vidanjör yardımıyla çekildiği belirtilmiştir. Bu nedenle işletme atıksularının yakınındaki yüzey ve yeraltı su kaynaklarının kalitesine etki etmediği kabul edilmiştir. Bununla birlikte panel yüzeylerinin yılda ortalama iki kez hava ile temizlendiği bilgisi alınmıştır. Panel temizliği ile ilgili su kullanım durumu söz konusu olmadığından bu işletmenin havzadaki yüzey ve yeraltı suları üzerinde herhangi bir endüstriyel atıksu kapsamında kirlilik etkisi bulunmamaktadır. Bu nedenle bu işletme, endüstriyel atıksu kirlilik yükü hesaplamalarına dâhil edilmemiştir.

Kesikköprü baraj gölü havzası çalışma alanı sınırının dışında ancak sınıra oldukça yakında yer alan ve işletmesi Elektrik Üretim Anonim Şirketi'ne (EÜAŞ) ait olan yıllık üretim kapasitesi 300 milyon kWh olan Hirfanlı HES bulunmaktadır. Bu işletmeye ait çalışanların sosyal ihtiyaçları doğrultusunda oluşacak olan evsel nitelikli atıksular, arıtım yapılmadan doğrudan Kızılırmak Nehri'ne deşarj edilmektedir. Oluşan evsel atıksular noktasal kirlilik olarak çalışma içerisinde değerlendirilmiştir.

Sonuç olarak; çalışma alanında adı geçen ve yukarıda detaylı değerlendirilmeleri verilen işletmelerin prosesleri boyunca endüstriyel atıksu üretilmediği tespit edilmiş olup, bu işletmeler için endüstriyel kirletici yükü hesaplanmamıştır.

3. Bulgular (Findings)

Evsel kirlilik yükleri hesaplamalarında deşarj edilen yük, havza içerisinde yaşayanlardan kaynaklanan evsel yükler ile kentsel alan içerisinde bulunan sanayi tesislerinden gelen endüstriyel yükleri de içermektedir. Havza içerisindeki yerleşim yerlerinin İller Bankası Metoduna göre hesaplanan nüfus projeksiyonları kullanılarak hesaplanan atıksu debi ve kirlilik yükleri Tablo 7'de verilmiştir.

Kesikköprü baraj gölü havzasına 2022 yılında toplamda 65.927,24 m^3/yıl evsel atıksu ile 31,38 ton/yıl KOİ, 22,30 ton/yıl BOİ, 18,79 ton/yıl AKM, 2,5 ton/yıl Toplam Azot ve 0,49 ton Toplam Fosfor yükü deşarjı yapıldığı ortaya konulmuştur (Şekil 5).

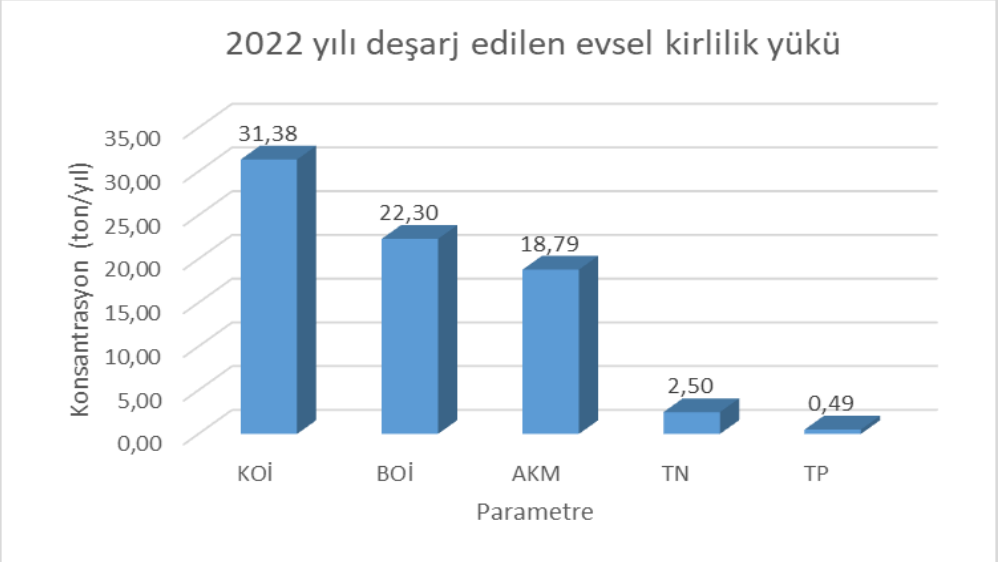

Şekil 5. 2022 Yılı evsel kirlilik yükü dağılımı (Domestic pollution load distribution in 2022)

Kesikköprü baraj gölü alt havzalarında 2022 yılı için hazırlanmış evsel atıksu kaynaklı KOİ (Kimyasal Oksijen İhtiyacı), BOİ (Biyolojik Oksijen İhtiyacı), AKM (Askıda Katı Madde), TN (Toplam Azot) ve TP (Toplam Fosfor) kirlilik yükleri haritası sırasıyla aşağıda verilmiştir (Şekil 6, Şekil 7, Şekil 8, Şekil 9, Şekil 10).

Tablo 7. Yıllık toplam evsel atıksu debisi ve evsel kirlilik yükleri
(Annual total domestic wastewater flow and domestic pollution loads)

Yıllar	Parametre	Alt Havzalar						Deşarj Edilen Kirlilik Yükü	Deşarj Edilen Toplam Kirlilik Yükü (%5 Arttırılmış)
		KAH-1 (%20)	KAH-2 (%20)	KAH-7	KAH-9 (%50)	KAH-10 (%50)	KAH-13 (%20)		
2022	Atıksu debi (m^3/yıl)	1824	2322	31579	7703	18453	904	62787	65927
	KOİ (ton/yıl)	0,87	1,10	15,03	3,67	8,79	0,43	29,88	31,38
	BOİ (ton/yıl)	0,61	0,77	10,84	2,57	6,15	0,30	21,24	22,30
	AKM (ton/yıl)	0,52	0,63	9,02	2,20	5,27	0,26	17,89	18,79
	TN (ton /yıl)	0,07	0,09	1,20	0,29	0,70	0,03	2,38	2,50
	TP(ton/yıl)	0,01	0,02	0,24	0,06	0,14	0,01	0,47	0,49
2025	Atıksu debi (m^3/yıl)	2343	2810	38115	11448	23637	1158	79513	83489
	KOİ (ton/yıl)	0,97	1,16	15,80	4,10	9,80	0,48	32,31	33,92
	BOİ (ton/yıl)	0,70	0,84	11,46	2,97	7,11	0,35	23,44	24,61
	AKM (ton/yıl)	0,61	0,73	9,91	2,57	6,15	0,30	20,26	21,27
	TN (ton /yıl)	0,08	0,10	1,39	0,36	0,86	0,04	2,83	2,98
	TP(ton/yıl)	0,02	0,02	0,26	0,07	0,16	0,01	0,53	0,55
2030	Atıksu debi (m^3/yıl)	3086	3362	45581	13030	31196	1533	97790	102679
	KOİ (ton/yıl)	1,17	1,27	17,25	4,93	11,81	0,58	37,01	38,86
	BOİ (ton/yıl)	0,84	0,91	12,37	3,54	8,47	0,42	26,53	27,86
	AKM (ton/yıl)	0,75	0,82	11,06	3,16	7,58	0,37	23,73	24,92
	TN (ton /yıl)	0,11	0,12	1,62	0,47	1,11	0,05	3,48	3,65
	TP(ton/yıl)	0,02	0,02	0,29	0,08	0,21	0,01	0,62	0,65
2035	Atıksu debi (m^3/yıl)	3960	3914	53010	16717	40055	1957	119616	125597
	KOİ (ton/yıl)	1,40	1,39	18,81	5,93	14,21	0,69	42,44	44,56
	BOİ (ton/yıl)	1,05	1,03	13,34	3,82	10,60	0,52	30,35	31,86

	AKM (ton/yıl)	0,92	0,91	12,31	3,88	9,30	0,45	27,77	29,16
	TN (ton /yıl)	0,14	0,14	1,88	0,59	1,42	0,07	4,24	4,45
	TP(ton/yıl)	0,02	0,02	0,32	0,10	0,25	0,01	0,73	0,76
2040	Atıksu debi (m^3/yıl)	5008	4478	60759	19376	50612	2479	142716	149851
	KOİ (ton/yıl)	1,69	1,51	20,49	7,13	17,07	0,84	48,72	51,15
	BOİ (ton/yıl)	1,27	1,14	15,45	5,38	12,88	0,63	36,74	38,58
	AKM (ton/yıl)	1,13	1,01	13,66	4,75	11,38	0,56	32,48	34,10
	TN (ton /yıl)	0,18	0,16	2,15	0,75	1,80	0,09	5,12	5,37
	TP(ton/yıl)	0,03	0,03	0,36	0,13	0,30	0,01	0,86	0,90
2045	Atıksu debi (m^3/yıl)	6223	5047	68443	26227	62860	3078	171881	180475
	KOİ (ton/yıl)	1,99	1,62	21,93	8,40	20,14	0,99	55,07	57,82
	BOİ (ton/yıl)	1,55	1,25	17,01	6,52	15,63	0,76	42,72	44,85
	AKM (ton/yıl)	1,37	1,11	15,12	5,75	13,89	0,68	37,93	39,82
	TN (ton /yıl)	0,22	0,17	2,45	0,94	2,26	0,11	6,14	6,45
	TP(ton/yıl)	0,04	0,03	0,40	0,15	0,36	0,02	0,99	1,04
2050	Atıksu debi (m^3/yıl)	7174	5269	71481	30254	94249	3560	211990	222590
	KOİ (ton/yıl)	2,40	1,76	23,87	10,08	33,03	1,19	72,32	75,93
	BOİ (ton/yıl)	1,87	1,37	18,66	7,90	26,99	0,93	57,71	60,59
	AKM (ton/yıl)	1,67	1,23	16,67	7,06	18,53	0,83	45,98	48,28
	TN (ton /yıl)	0,28	0,20	2,77	1,18	3,02	0,14	7,59	7,96
	TP(ton/yıl)	0,04	0,03	0,44	0,19	0,56	0,02	1,28	1,35

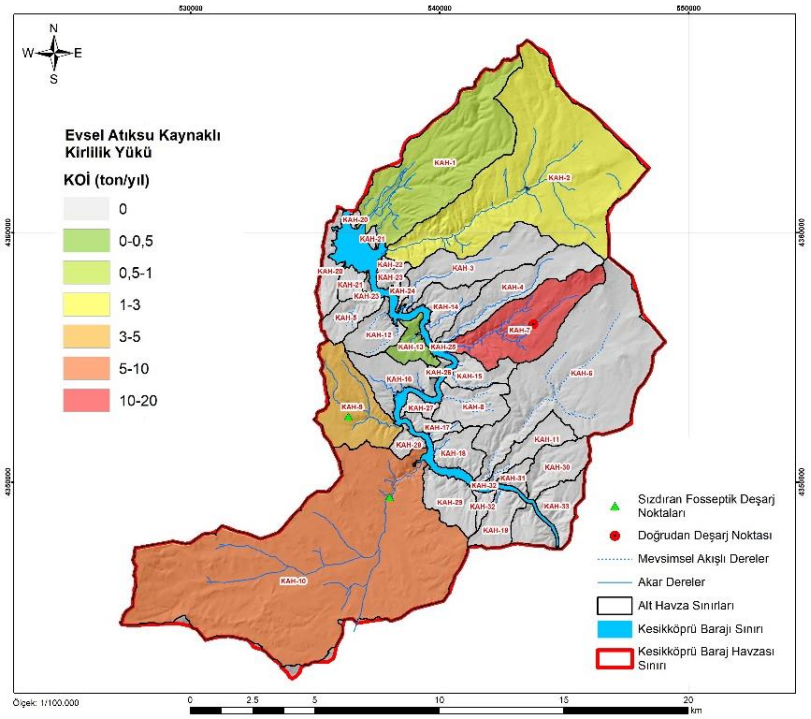

Şekil 6. Evsel atıksu kaynaklı 2022 yılı KOİ kirlilik yükü dağılımı
(Distrubution of COD pollution load in 2022 from domestic wastewater)

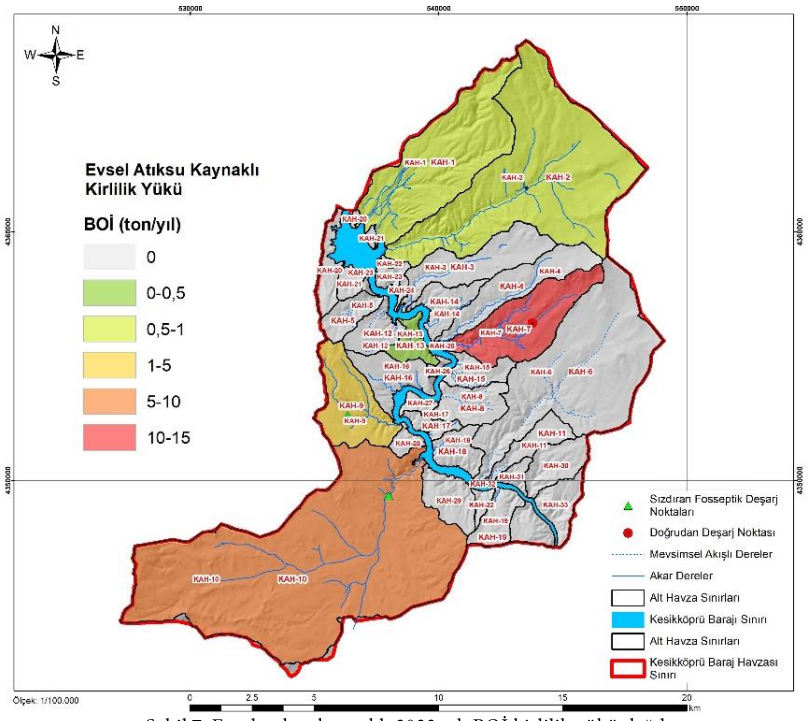

Şekil 7. Evsel atıksu kaynaklı 2022 yılı BOİ kirlilik yükü dağılımı
(Distrubution of BOD pollution load in 2022 from domestic wastewater)

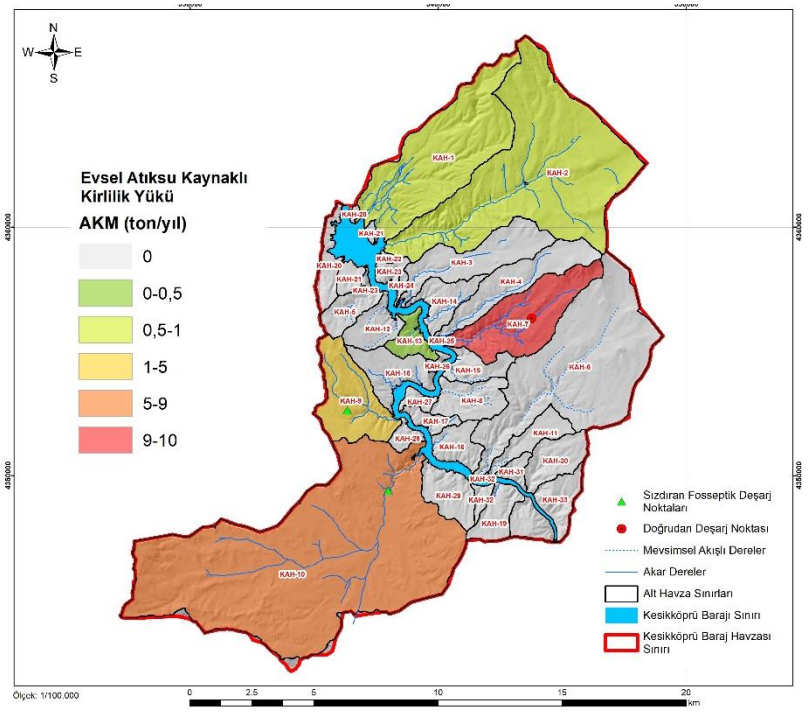

Şekil 8. Evsel atıksu kaynaklı 2022 yılı AKM kirlilik yükü dağılımı
(Distrubution of TSS pollution load in 2022 from domestic wastewater)

Kesikköprü baraj gölü havzasında bulunan alt havzalarda noktasal kaynaklı KOİ, BOİ ve AKM kirlilik yüklerinin yıllık toplamını gösteren Şekil 6, 7 ve 8'de görüldüğü gibi yıllık en fazla noktasal kirlilik deşarjı KAH-7'de gerçekleşmektedir. Bu noktasal kirlilik KAH-7 sınırları içerisinde bulunan Kargınyenice mahallesinden kaynaklanmaktadır. Kargınyenice havzadaki en kalabalık yerleşim yeri olmamasına rağmen atıksuları doğrudan deşarj yapıldığından dolayı herhangi bir azaltma olmadan kirletici yük hesabına katılmıştır. Nüfusu en fazla olan KAH-10 alt havzası ise merkezi fosseptik kullanan yerleşim birimlerine sahip olması sebebiyle kirlilik yüklerinin %50'si toplam yıllık noktasal

yüke dahil edilmiştir. Şekilde gri renkte bulunan alt havzalarda ise noktasal kirlilik kaynakları bulunmamaktadır.

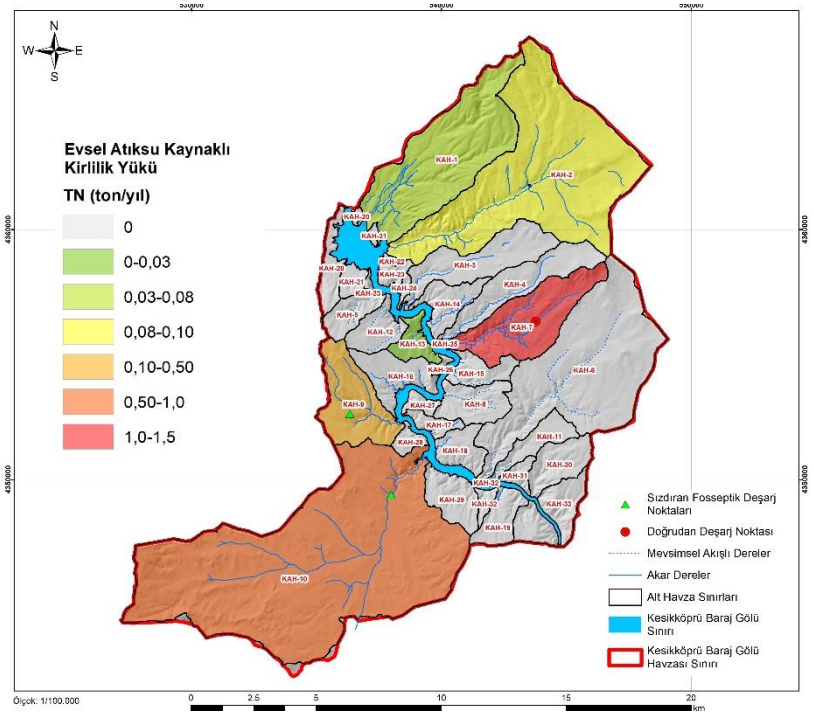

Şekil 9. Evsel atıksu kaynaklı 2022 yılı TN kirlilik yükü dağılımı
(Distrubution of TN pollution load in 2022 from domestic wastewater)

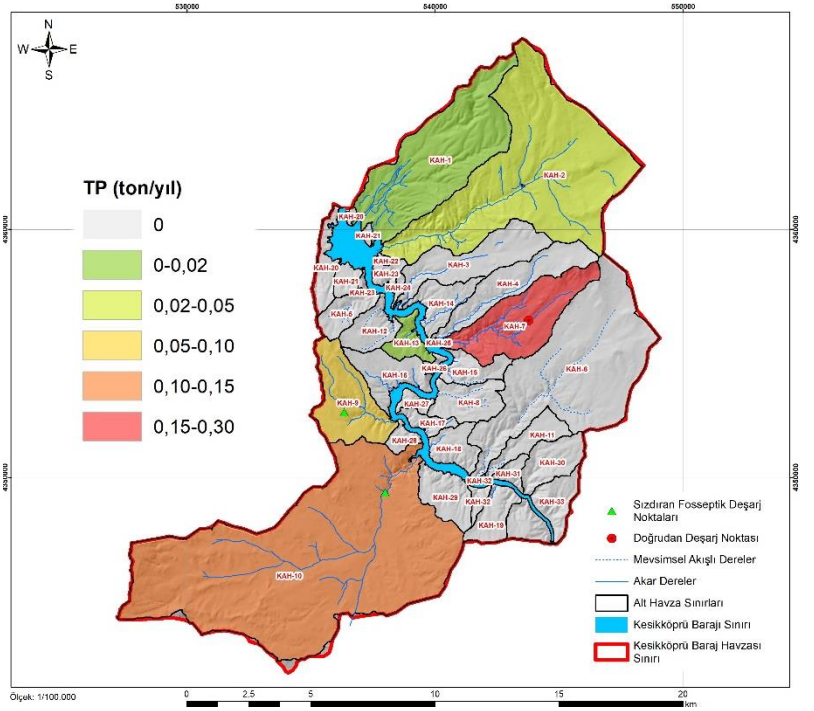

Şekil 10. Evsel atıksu kaynaklı 2022 yılı TP kirlilik yükü dağılımı
(Distrubution of TP pollution load in 2022 from domestic wastewater)

Benzer şekilde Şekil 9 ve 10'da gösterilen TN ve TP kirlilik yüklerinin dağılımında da KAH-7 ve KAH-10 en yoğun kirletici deşarjına sahiptir. 2022 yılına ait kirlilik yüklerine ait haritalar (Şekil 6-Şekil 10) incelendiğinde yerleşim yerlerine sahip olan alt havzalardan Kızılırmak Nehri ve nehirden beslenen baraj gölüne BOİ, KOİ, AKM, Toplam Azot (TN), Toplam Fosfor (TP) açısından kirlilik yükü baskılarının olduğu görülmektedir. Kesikköprü baraj gölü havzası sınırlarında mevcut kanalizasyon ve fosseptik alt yapısının 2050 yılına kadar

değişmeyeceği varsayılarak yapılan hesaplamalarda, nüfus artısı ile evsel kirlilik yüklerinin havza içi deşarj miktarlarında artış olacağı ortaya konulmuştur (Şekil 11, Şekil 12, Şekil 13, Şekil 14, Şekil 15).

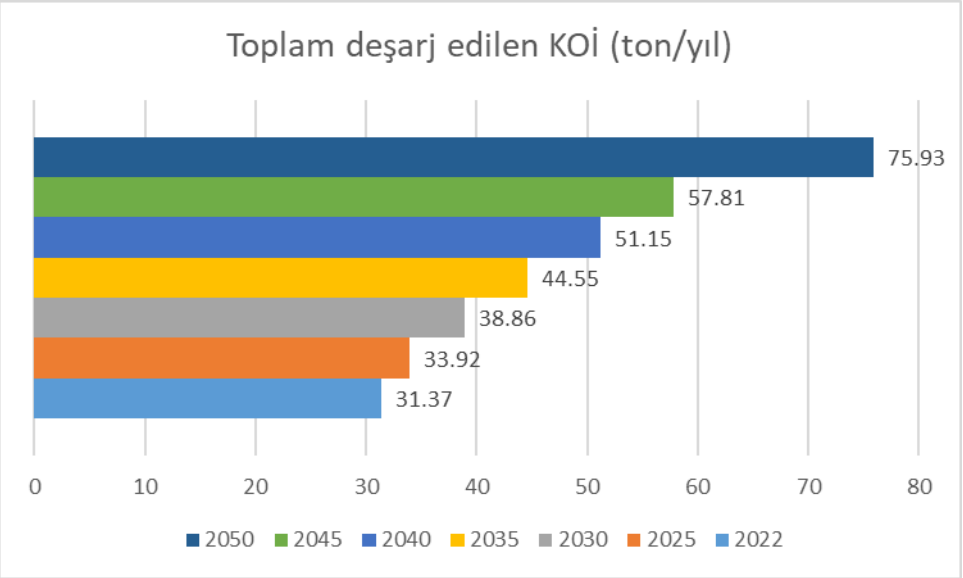

Şekil 11. 2022-2050 yılları arasında KOİ yükü dağılımı (COD load distribution between 2022-2050)

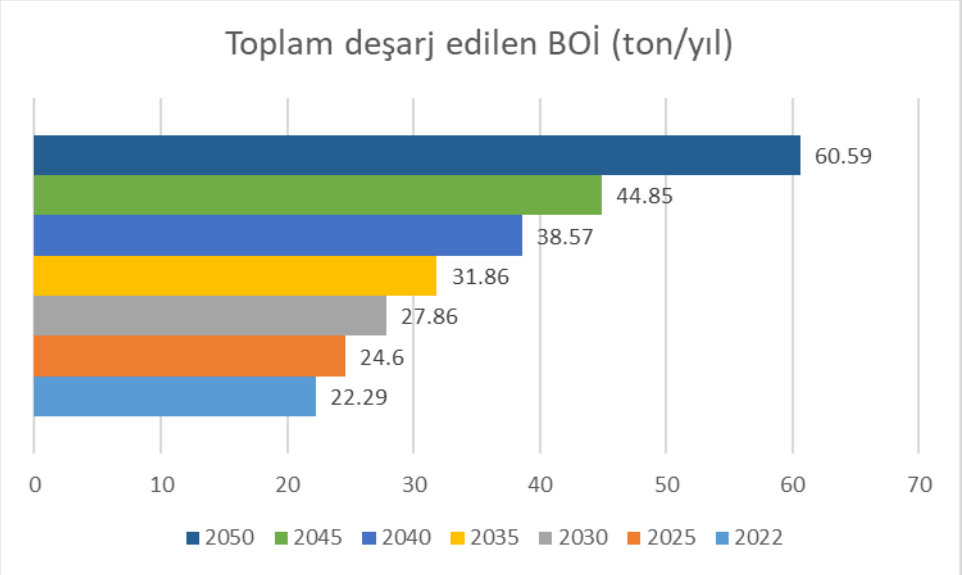

Şekil 12. 2022-2050 yılları arasında BOİ yükü dağılımı (BOD load distribution between 2022-2050)

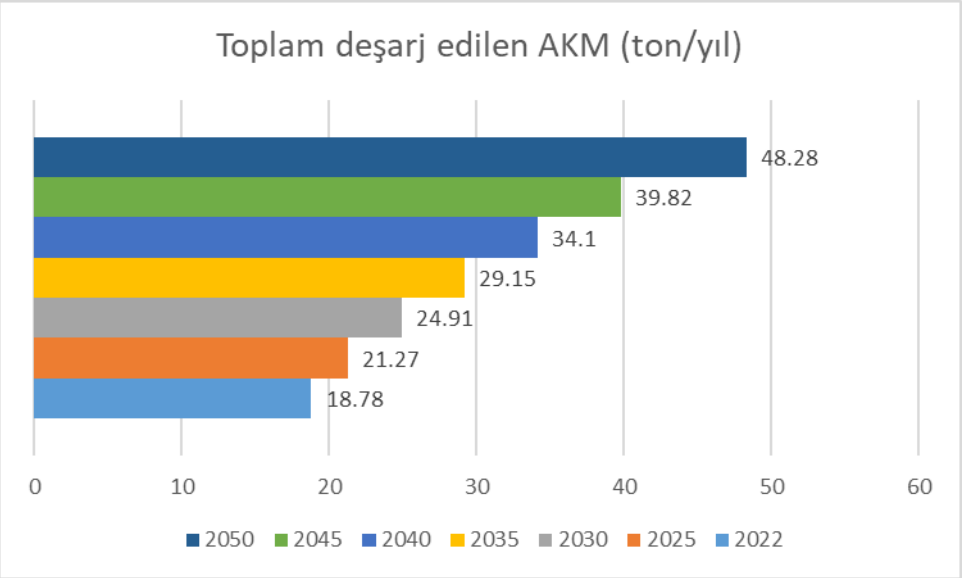

Şekil 13. 2022-2050 yılları arasında AKM yükü dağılımı (TSS load distribution between 2022-2050)

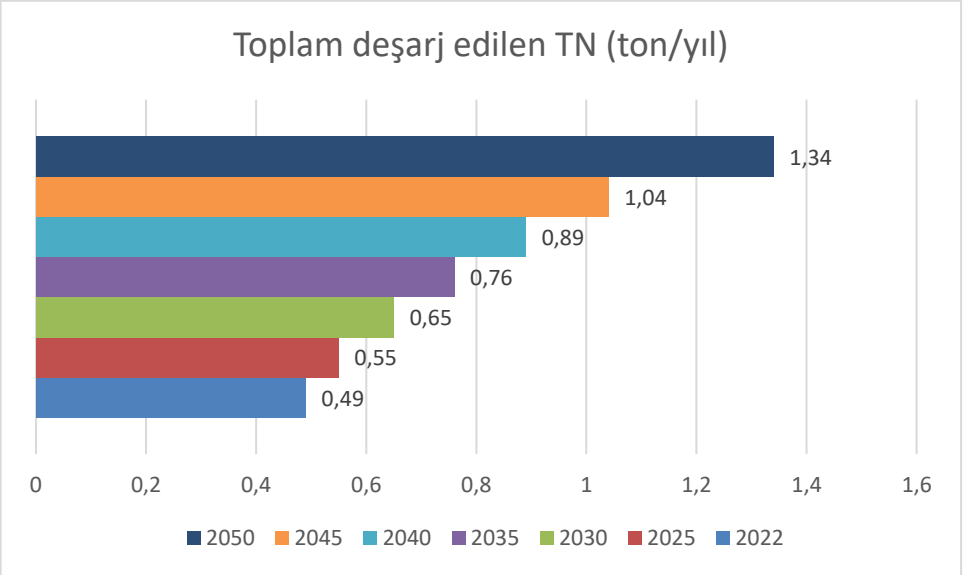

Şekil 14. 2022-2050 yılları arasında TN yükü dağılımı (TN load distribution between 2022-2050)

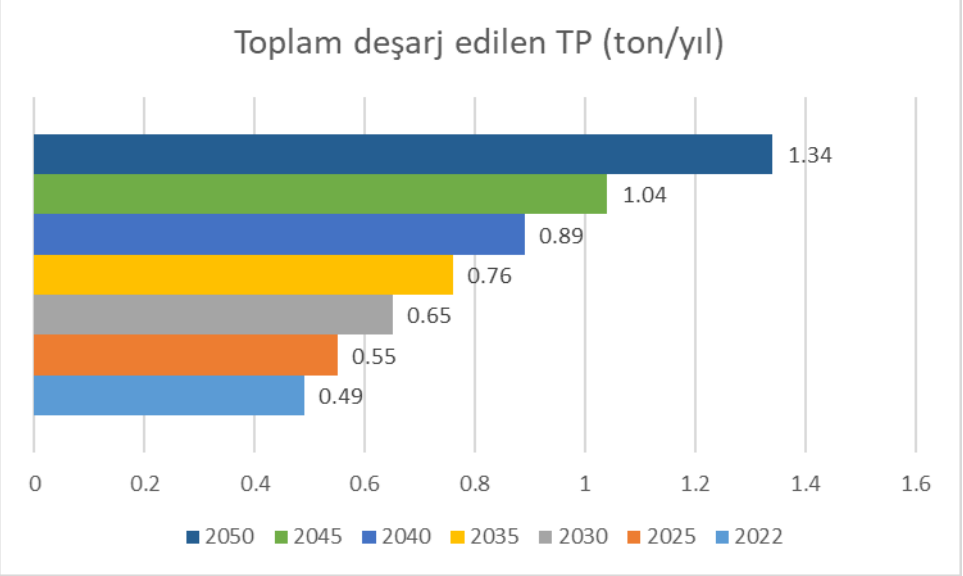

Şekil 15. 2022-2050 yılları arasında TP yükü dağılımı (TP load distribution between 2022-2050)

Kesikköprü Baraj Gölü Havzasındaki noktasal kaynaklı kirleticiler, atıksu deşarjlarından alıcı ortama ulaşan organik kirleticiler; KOİ, BOİ, AKM, TN ve TP hesaplanarak değerlendirilmiştir. Havzada yapılan incelemelerde endüstriyel kirlilik kaynağı bulunmadığı tespit edildiğinden, bu parametrelerin değerlendirilmesi sadece kentsel kaynaklı kirlenmeyi temsil etmektedir.

2022 yılında mevcut kirlilik yükleri baz alındığında (Şekil 11-Şekil 15), hiçbir iyileştirmenin ve endüstriyel büyümenin yapılmadığı durumda, 2050 yılında kirletici yüklerin artışı KOİ %142, BOİ %171,8, AKM %157,08, TN %219,67, TP %173,46 oranında tespit edilmiştir. Yüzdelik artışlar bazında değerlendirildiğinde, azot ve fosfor bileşiklerinin oranının yüksek olduğu ortaya konulmuştur. Yüzey sularının kalitesinin tehlikeli boyutlara ulaşması, öncelikli olarak azot ve fosfor bileşikleri olmakla birlikte, besin maddelerinin artan konsantrasyonlarının bir sonucudur [20, 21]. Çalışmada yapılan hesaplamalar ile elde edilen azot ve fosfor yüklerindeki artış, gelecekte baraj gölünün su kalitesinin olumsuz yönde etkileneceğini açıkça ortaya koymaktadır.

4. Sonuçlar ve Tartışma (Results and discussion)

Kesikköprü Baraj Gölü Havzası'nda kirletici yüklerin doğrudan baskısı altında kalan baraj gölünün de ilerleyen yıllarda olumsuz etkilenmesi kaçınılmazdır. Gölü besleyen ana su kaynağı Kızılırmak Nehri'nin, havza sınırlarının dışından taşıdığı kirlilik yükünün de kontrol altına alınması ve tespit edilmesi havzanın korunması için önemlidir. Kesikköprü Baraj Gölü'nün su kalitesinde gölü besleyen su kaynağının kalitesi ve suyun gölün içerisinde alıkonma süreside etkilidir.

Evsel kirlilik yüklerinin hesaplanmasında yapılan kabuller, havzada var olan noktasal kirletici kaynakların havza içerisinde bulunan su kaynaklarına katkısının ortaya konulmasına yardımcı olan literatüre dayalı kavramsal kabullerden oluşmaktadır. Noktasal kirlilikler büyük ölçüde atıksu üretiminde bulunan nüfusa bağlı olduğundan en yoğun nüfusa sahip olan KAH-7 ve KAH-10 alt havzaları en yoğun kirletici deşarjına sahiptir. Yapılan kabullerin bulgular üzerindeki etkisinin tam olarak ortaya konulabilmesi için, bölgenin adı geçen projeksiyon yıllarında takip ve izleme çalışmalarının da yapılması ile mümkün olacaktır.

Çalışma alanı su kaynakları kalitesi üzerine birincil baskı uygulamakta olan noktasal kirletici kaynak olarak yerleşim yerlerinden kaynaklanan evsel atıksuların olduğu ortadadır. Havza sınırları içindeki merkezi fosseptiklerin bakım ve onarımının yapılması, doğrudan Kızılırmak Nehri'ne yapılan atıksu deşarjının durdurularak, bölgede ilerleyen yıllarda artan nüfus da göz önüne alınarak, atıksu arıtma tesisi yapılması önerilmektedir. Noktasal kirlilik kaynağı olarak evsel atıksuların literatürde kontrol altına alınması yöntemlerinden biri arıtma tesislerinin yapılması olarak ortaya çıkmaktadır.

Önceki çalışmaların sonuçları incelendiğinde, noktasal kirlilik kaynağı olan evsel atıksuların bulunduğu ortama kirlilik yükü olarak değerlendirilmesinin önüne geçilmesi için atıksuyun arıtılmasının zorunlu olduğu görülmektedir. Alaşehir Çayı Alt Havzası'nda noktasal kirletici kaynakların iyileştirilmesi amacıyla işletmeye alınacak atıksu arıtma tesisi ile havzaya ulaşan KOİ yükünün yaklaşık %50, TN ve TP yüklerinin ise %25 oranında azalması öngörülmüştür [21]. Eren ve Kaya [22], 2020 yılında gerçekleştirdikleri çalışmada, Fırat Dicle Havzası'nın bir alt havzası olan Karasu Havzası'nın korunmasına yönelik olarak Erzurum Büyükşehir Belediyesi tarafından 2016 yılında faaliyete geçirilen Kentsel Atıksu Arıtma Tesisi'nin (AAT), havza içindeki su kalitesinin iyileştirilmesine önemli bir katkı sağladığını belirlemişlerdir. Çalışmalarının sonucunda AAT'nin faaliyette olduğu yaklaşık üç yıllık sürede özellikle debi ölçümleri ve kirlilik yükleri dikkate alındığında AAT'nin Karasu nehrinin su kalitesini korumada büyük katkısının olduğunu ortaya koymuşlardır.

Havzalarda mevcut kirliliğin ortaya konulması ne kadar önemliyse; kirliliğe sebep olan kaynakların tespiti ve kontrol altına alınmasına yönelik yapılan çalışmalar da havza koruma ve izlemede veri tabanı oluşturmak adına elzemdir.

Arıtılmamış evsel atıksuların, su kaynakları üzerindeki başlıca olumsuz etkileri aşağıda sıralanmaktadır:

- Evsel atık sularda bulunan biyolojik olarak parçalanabilen organik maddeler deşarj edildikleri alıcı ortamda su kalitesinin en önemli göstergelerinden olan oksijenin azalmasına sebep olarak sucul ekosistemin bozulmasına neden olur.
- Evsel atıksu deşarjlarında yoğun olarak bulunan azot ve fosfor bileşikleri alglerin aşırı artmasına neden olur. Bu durum özellikle durgun sularda su kalitesinin bozulmasına neden olmaktadır. Su kütlesinin eski durumuna döndürülmesi ise zor, maliyetli ve zaman alan bir süreç gerektirir.
- Evsel atıksularda bulunan, kimyasal ve toksik maddeler alıcı ortamdaki sucul canlılarda kümülatif birikimine neden olmaktadır.
- Evsel atıksulardaki bakteri ve virüsler, kirli suyla temas edilmesi durumunda insanlarda çeşitli sağlık sorunlarına neden olabilir.

Tüm bu etkileri göz önüne alarak, çalışma alanının Ankara İli için içme suyu kaynağı olarak da kullanılabilirliği değerlendirildiğinde, noktasal kirlilik kaynağı olarak alanda birçok soruna neden toplanması, uzun vadede ise toplanan atıksuların bölgede yapılacak bir atıksu arıtma tesisinde arıtılarak baskının azaltılması gerektiğini ortaya koymaktadır.

2000 yılında Avrupa Birliği üye ülkeleri tarafından EC/2000/60 Sayılı AB Su Çerçeve Direktifi yürürlüğe girmiş olup, ülkemiz de Avrupa Birliği (AB) uyum süreci kapsamında, bahsedilen direktifin uygulayıcısı konumundadır. Suyun entegre olarak yönetilmesi anlayışını benimseyen direktifin içeriğinde; nehir havza yönetimi planlarının, havzalarda su miktarlarının tespiti ve özellikleri, su kaynaklarının kirlilik durumunun belirlenmesi, kirletici kaynakların tanımlanmasını içermektedir. Ülkemiz 2009 yılında, direktife uygun olarak çalışmalara başlamış olup, nehir havzalarında su kaynaklarının entegre yönetimi adına önemli adımlar atmıştır. Yapılan ve yapılmaya devam eden bu çalışmalar ile su kaynaklarının mevcut ve ileriki yıllarda meydana gelebilecek kirlilik senaryoların ortaya konulması amaçlanmaktadır.

Bu çalışma ile ortaya konulan kirletici kaynakların ve bu kaynaklardan meydana gelen mevcut ve gelecek dönem tahminli kirlilik yükü verilerinin, alanda daha sonra yapılacak olan su kalitesi izleme ve önlenmesindeki çalışmalarda, farklı kirlilik senaryolarının üretilmesine, Su Çerçeve Direktifi uyum sürecinde ülkemiz adına yapılan çalışmalara ışık tutması amaçlanmaktadır.

Teşekkür (Acknowledgment)

Bu araştırma, Ankara Büyükşehir Belediyesi Su ve Kanalizasyon İdaresi Genel Müdürlüğü tarafından düzenlenen "Kesikköprü Barajı Havza Koruma Planı ve Özel Hüküm Belirleme Projesi" çerçevesinde yürütülmüştür.

Çıkar Çatışması Beyanı (Conflict of Interest Statement)

Yazarlar tarafından herhangi bir çıkar çatışması bildirilmemiştir.

Kaynaklar (References)

[1] A. du Plessis, *Water as an Inescapable Risk: Current global water availability, quality and risks with a specific focus on South Africa.* Springer International Publishing, 2019. doi: 10.1007/978-3-030-03186-2.

[2] A. Erol, "Su Kaynaklarının Korunmasında Havza Yönetimi İlkelerinin Önemi," in *TMMOB Su Politikaları Kongresi, Ankara, Türkiye, Mart 21-23, 2006*, cilt I, ss. 51-57.

[3] K. Dębska, B. Rutkowska, and W. Szulc, "The influence of a dam reservoir on water quality in a small lowland river," *Environmental Monitoring and Assessment*, vol. 193, no. 3, Feb. 2021, doi: 10.1007/s10661-021-08905-6.

[4] L. Carneiro, A. Ostroski, and E. G. F. Mercuri, "Trophic state index for heavily impacted watersheds: modeling the influence of diffuse pollution in water bodies," *Hydrological Sciences Journal*, vol. 65, no.15, pp. 2548-2560, Oct. 2020, doi: 10.1080/02626667.2020.1828588.

[5] *European waters: Assessment of status and pressures 2018*, European Environment Agency, Technical Report no: 7/2018, ISSN 1977-8449, Luxembourg: Publication Office of European Union, 2018.

[6] J. Frankenberger, S. Mcloud, and A. Faulkenburg, *Watershed inventory workbook for Indiana: A guide for watershed partnerships*, 2002. [Online]. Available: https://engineering.purdue.edu/SafeWater/watershed/inventoryf.pdf. [Accessed: Sept. 12, 20].

[7] T. O. Randhir, "Watershed Management: Issues and approaches", ISBN: 9781843391098, IWA Publication, UK, pp. 38-52, 2006. doi: 10.2166/9781780402338.

[8] M. N. Kumwimba, L. Bao, Z. Jie, X. Li, J. Huang, W. Wang, X. Li, J. Su, D K.. Muyembe, A. Guide and M. Dzakpasu,"Nutrients retention of a series of small dam-impacted urban rivers in northern China," *Journal of Environmental Chemical Engineering*, vol. 10, no. 3, p. 107967, 2022. doi: 10.1016/j.jece.2022.107967.

[9] *Stratejik çevresel Değerlendirme: Batı Akdeniz Nehir Havzası Nihai Kapsam Belirleme Raporu*, 3 Pilot Havzada Nehir Havza Yönetim Planları Kapsamında Ekonomik Analizler ve Su Verimliliği Çalışmaları İçin Teknik Destek Projesi, TR2013/0327.07.01-01/001, T.C. Tarım ve Orman Bakanlığı, Ankara, 2020.

[10] N. Erdoğan, "Doğu Karadeniz Havzası'nda kirlilik yüklerinin değerlendirilmesi", Yüksek Lisans Tezi, Sakarya Üniversitesi Fen Bilimleri Enstitüsü, Sakarya, Türkiye, 2017.

[11] S. Hacısalihoğlu ve F. Karaer, "Uluabat Gölü noktasal kirletici kaynaklar ve kirlilik yükleri," *Doğal Afetler ve Çevre Dergisi*, c. 6, sy. 2, ss: 258-267, 2020. doi: 10.21324/dacd.602385.

[12] N. Garipağaoğlu, "Marmara Havzası'nda kentleşme-atık su ilişkileri ve alıcı ortam üzerindeki etkileri," *Marmara Coğrafya Dergisi*, c.0, sy. 34, pp. 147-159, 2016.

[13] Atıksu Arıtma Tesisleri Teknik Usuller Tebliği, *Resmi Gazete*, 27527, 20.03.2010.

[14] *İklim Değişikliğinin Su Kaynaklarına Etkisi Projesi, Proje Nihai Raporu*, T.C. Tarım, Orman ve Su İşleri Bakanlığı, Su Yönetimi Genel Müdürlüğü, Ankara, 2016.

[15] *Kızılırmak Havzası Master Plan Raporu Hazırlanması İşi, Havza Çevre ve Su Kalitesi Nihai Raporu*, Devlet Su İşleri Genel Müdürlüğü, Ankara, 2006.

[16] Çelik, H., Kanıt, R., ve Öztürk, Y. "Kahramanmaraş İlinde İçme ve Kullanma Suyu İhtiyacının Tespiti," *Pamukkale Üniversitesi Mühendislik Bilimleri Dergisi*, c. 4, sy. 3, ss. 749-757, 1998.

[17] B. H. Gürsoy Haksevenler ve S. Ayaz, "Noktasal ve yayılı kirletici kaynaklarının yüzeysel su kalitesi üzerinde etkisi, Alaşehir Çayı alt havzası örneği," *Gümüşhane Üniversitesi Fen Bilimleri Dergisi*, c. 11, sy. 4, pp. 1258-1268, 2021, doi:10.17714/gumusfenbil.882693.

[18] Y. Kazancı, "Surface Water Quality Modeling For Best Management Practices - A Case Study From Bakırçay River Basin", Yüksek Lisans Tezi, İzmir Teknoloji Enstitüsü, İzmir, Türkiye, 2021.

[19] A. Tekile, I. Kim and J. Kim, "Mini-Review on River Eutrophication and Bottom Improvement Techniques, with Special Emphasis on the Nakdong River," *Journal of Environmental Sciences*, vol. 30, pp. 113–121, 2015, doi: 10.1016/j.jes.2014.10.014.

[20] R. Savic, M. Stajic, B. Blagojevi'c, A. Bezdan, M. Vranesevic, V. Nikoli´c Jokanovi´c, A. Baumgertel, M. Bubalo Kova˙ci´c, J. Horvatinec and G. Ondrasek, "Nitrogen and Phosphorus Concentrations and Their Ratios as Indicators of Water Quality and Eutrophication of the Hydro-System Danube–Tisza–Danube", *Agriculture*, vol. 12, no. 7, p. 935, 2022, doi: 10.3390/agriculture12070935.

[21] *Gediz Havzası Koruma Eylem Planı Final Raporu*, Hazırlayan: TÜBİTAK MAM, Orman ve Su İşleri Bakanlığı, Ankara, 2013.

[22] Z. Eren ve F. Kaya, "Fırat-Dicle Havza Koruma Eylem Planı Çerçevesinde Kentsel Atıksu Arıtma Tesisinin Karasu Nehrinin Su Kalitesi Üzerindeki Etkisinin İncelenmesi", *Ulusal Çevre Bilimleri Araştırma Dergisi*, c. 3, sy. 2, ss. 95-109, 2020.

This is an open access article under the CC-BY license

Research Article/Araştırma Makalesi

Gazi Akademik Yayıncılık

GAZİ
JOURNAL OF ENGINEERING SCIENCES

Experimental and Statistical Investigation of the Effect of Nanoparticle Minimum Quantity Lubrication (nano-MQL) Method on Cutting Performance

Fuat Kara [a,*]

Submitted: 20.12.2023 Revised: 31.01.2024 Accepted:12.02.2024 doi:10.30855/gmbd.2017.705N08

ABSTRACT

In this study, two distinc cutting tools, coated carbide and cermet, were used in turning 20NiCrMo2 case-hardened steel. Turning experiments were carried out with these tools at three distinc cooling methods (dry, MQL, nano-MQL), three distinc cutting speeds (80, 120, 160 m/min) and three distinc feed rates (0.125, 0.167, 0.2 mm/rev) has been carried out. As a result of the experiments, the effects of cutting parameters, cutting tool type and cooling method type on the average surface roughness (Ra) and cutting zone temperature (Ctemp) were examined. In the study, the Taguchi optimization method was also applied to the experimental Ra and Ctemp results. As a result of Taguchi optimization, the most effective cutting parameters on Ra and Ctemp were determined. This result was confirmed by ANOVA analysis. Optimum parameters for Ra; cermet cutting tool, nano-MQL cooling method, 160 m/min cutting speed and 0.12 mm/rev feed rate. Optimum parameters for Ctemp; carbide cutting tool, nano-MQL cooling method, 80 m/min cutting speed and 0.12 mm/rev feed rate. Ideal numbers for both Ra and Ctemp were not found in the 18 turning experiments performed. Therefore, the 19th experiment was conducted for both output parameters. The average surface roughness value for optimum parameters was measured as 1.08 µm.

Keywords: ANOVA, Cutting temperature, MQL, nano-MQL, Surface roughness, Taguchi analyses

[a,*] Duzce University, Engineering Faculty, Mechanical Engineering Dept. 81620 - Düzce, Türkiye
Orcid: 0000-0001-8566-3433
e mail: fuatkara@duzce.edu.tr

*Corresponding author: fuatkara@duzce.edu.tr

Nanopartikül Takviyeli Minimum Miktarda Yağlama (MMY) Yönteminin Kesme Performansına Etkisinin Deneysel ve İstatistiki Araştırılması

ÖZ

Bu çalışmada, 20NiCrMo2 çeliğinin tornalanmasında kaplamalı karbür ve sermet olmak üzere iki farklı kesici takım kullanılmıştır. Bu takımlar ile üç farklı soğutma yöntemi (kuru, MQL, nano-MQL) üç farklı kesme hızı (80, 120, 160 m/dak) ve üç farklı ilerleme hızı (0,125, 0,167, 0,2 mm/dev) değerlerinde tornalama deneyleri gerçekleştirilmiştir. Deneyler sonucunda ortalama yüzey pürüzlülüğü (Ra) ve kesme bölgesi sıcaklığı (Ctemp) üzerinde kesme parametrelerinin, kesici takım türünün ve soğtma yöntemi türünün etkileri incelenmiştir. Çalışmada ayrıca deneysel Ra ve Ctemp sonuçlarına Taguchi optimizasyon metodu uygulanmıştır. Taguchi optimizasyonu sonucunda Ra ve Ctemp üzerinde en etkili kesme parametreleri tespit edilmiştir. ANOVA analizi ile bu sonuç doğrulanmıştır. Ra için optimum parametreler; sermet kesici takım, nano-mql soğutma yöntemi, 160 m/dak kesme hızı ve 0,12 mm/dev ilerleme hızı olarak bulunmuştur. Ctemp için optimum parametreler; karbür kesici takım, nano-mql soğutma yöntemi, 80 m/dak kesme hızı ve 0,12 mm/dev ilerleme hızı olarak bulunmuştur. Yapılan 18 tornalama deneyi içerisinde optimum parametrelere ait deneyler yer almadığı için hem Ra hem de Ctemp için 19. deneyler yapılmıştır. Optimum parametreler için ortalama yüzey pürüzlülük değeri 1,08 µm olarak ölçülmüştür.

Anahtar Kelimeler: Kesme sıcaklığı, MQL, nano-MQL, Taguchi analizi, Yüzey pürüzlülüğü

To cite this article: F. Kara, "Experimental and Statistical Investigation of the Effect of Nanoparticle Minimum Quantity Lubrication (nano-MQL) Method on Cutting Performance," *Gazi Journal of Engineering Sciences,* vol.10, no.1, pp. 102-113, 2024. doi:10.30855/gmbd.0705N08

1. Introduction

Machining is an important process in production and is one of the issues that should be given special attention in terms of sustainability, as it has a direct impact affect the lifespan and functionality of numerous critical components as well as the cost of production [1,2]. Cutting fluids are used because of their primary roles in cooling and lubricating metal goods, which guarantee high production speed throughout the machining process. Cutting force and temperature rise during machining as a result of friction produced by the chip moving across the cutting tool's surface and the metal workpiece cutting directly in front of the tool. Cutting fluids can help minimize cutting forces at lower cutting speeds, enabling machining at relatively higher cutting speeds. They can also lessen or completely remove the heat created, which has the potential to harm high-speed cutting tools [3]. As a result, machining time can be reduced by using higher cutting speeds, resulting in increased production rate. Numerous researchers agree that MQL can be considered a better alternative to the traditional cooling technique for use in a variety of machining operations, including milling, turning, grinding, and drilling [4-7]. According to Najiha et al. [2], MQL is regarded as a workable approach for a cleaner production process since it is an affordable way to apply cutting fluid and ensures worker and environmental safety. Since very little cutting fluid was used, other researchers have also backed up this assertion [5,8]. Makhesana et al. [9] were investigated to influence of MoS2 and graphite-reinforced nanofluid-MQL on surface roughness, tool wear, cutting temperature and microhardness in machining of Inconel 625. The turning tests are conducted under dry, MQL, and nanofluid-MQL (nMQL) environments, and the findings are compared considering surface roughness, chip morphology, tool wear, cutting temperature, power consumption, and microhardness. The sunflower oil blended with MoS2 resulted in 56%, 42%, and 22% improved surface quality compared to dry, MQL, and nMQL (Graphite) conditions. Also, the efficacy of nMQL with graphite and MoS2 is seen in the form of slower tool wear progression. Also, MQL, nMQL with MoS2, and nMQL (Graphite) resulted in lower cutting temperatures by 18%, 35%, and 25%, respectively, compared to dry turning [9].

Rooprai et al. [10] implemented MQL for distinc injection rates in milling En 31 steel. Two distinc cutting depths, three distinct feed rates and three distinct cutting speeds and three distinc MQL oil flow rates were used in the experiments. The number of experiments was minimized by performing 18 experiments with Taguchi analysis instead of 54 experiments with these parameters. In this way, both time and cost were saved. As output parameters, surface roughness and micro hardness values were examined. ANOVA analysis was also performed on the experimental results. The most ideal processing conditions were determined by Taguchi analysis [10]. Özbek and Saruhan [11] tested tool steel on a lathe under dry and MQL conditions with two distinc cutting tools with PVD and CVD coating at a constant cutting depth (1 mm) and three distinc feed rates (60, 90 and 120 m/min). They examined the tool wear, cutting temperature and surface roughness of the part as a result of machining. As a result of the study, an 88% improvement in Ra values was achieved during processing with MQL. It has been observed that machining with MQL extends tool life by 267% with CVD-coated cutting tools and 200% with PVD-coated cutting tools in contrast to dry machining. Cutting temperatures were reduced using PVD-coated tools compared to CVD-coated tools. Better surface roughness values were displayed by PVD-coated tools in all cutting circumstances. Likewise, in terms of tool wear, PVD coated tools exhibited superior wear performance over CVD coated tools at all cutting speeds. They observed that in dry machining, tool life for PVD-coated tools was four times greater than tool life for CVD-coated tools. They stated that under MQL machining, PVD-coated tools exhibited three times longer tool life than CVD-coated tools [11].

Most of the mechanical load and friction used to remove chip from the workpiece is converted into heat energy. Therefore, one of the most important factors to be considered during machining is the heat generation and post-heat temperature formation in the cutting zone [12]. The heat generated during the metal cutting process and the heat removed from the environment determines the temperature increase. The temperature increase due to the heat generated affects the tool performance and workpiece quality [13]. A product's surface

roughness is a measurement of its surface texture, profile, irregularities or protrusions that determine the quality of that product and its compliance with design standards and specifications. The measurement of a product's surface roughness is so critical that mating parts may not fit properly if their roughness exceeds allowable limits; therefore such a situation may require rework or disposal as scrap. The probability of a product functioning well in service is a function of its quality, which is primarily dictated by the level of accuracy and precision in obtaining the perfect surface. Furthermore, tolerances and surface roughness place a crucial restriction on the choice of cutting parameter when developing a machining process [14]. Fatigue, corrosion, wear, warping, and poor dimensional and geometric precision are all encouraged by poor surface quality, and results in reduced functionality and lifespan of the product [15]. Chips formed at high temperatures on the surface of the metal can cause surface roughness if not cleaned intermittently. In addition, if left uncontrolled, the nature and thickness of the chips formed may reduce the surface integrity of the product [16]. Determining the ideal processing parameter values that will result in a smooth cutting action and, as a result, permissible surface roughness is necessary since certain cutters can badly break or fail when exposed to an intermittent rather than continuous operation mode. Past scholars have estimated surface roughness ratings using a variety of methodologies [17-22]. One of these techniques is the Taguchi optimization method. The Taguchi method is an acceptable method that can replace traditional methods, leading to a reduction in cost and time. The Taguchi method is one of the important quality strategies that minimizes the number of experiments and at the same time takes into account the effects of all controllable factors. There is a wide range of studies focused on determining the importance of parameters and their contribution percentages, and there are many studies showing that the Taguchi method is a tool suitable for application [23-26]. Gökçe [27] experimentally and statistically examined the cutting force, drill tip temperature and burr height in drilling Custom 450 martensitic stainless steel. Within the scope of the study, Taguchi and Response Surface Methods were applied to the experimental results and the most suitable drilling parameters were determined. They also applied using an analysis of variance to ascertain the effects and percentages of drilling parameters on the outputs. A correlation coefficient of over 94 percent was obtained for both optimization models, thus a successful optimization study was carried out [27].

In this study, the type of cooling method, type of cutting tool, cutting speed and feed rate were investigated in the turning of 20NiCrMo2 case-hardened steel, which is widely used in the manufacturing of machine parts such as shafts, gears, chain links, piston pins, discs, chain sprockets and pulleys, rolling bearings and rollers. Its effects on temperature and surface roughness were evaluated experimentally and statistically, and the most suitable turning conditions were determined for this purpose.

2. Material and Methods

The 20NiCrMo2 steel used in the experiments was prepared with a diameter of 50 mm and a length of 500 mm. The chemical composition of the test sample is presented in Table 1. Turning experiments were carried out on a ZMM BULGARIA CU500 brand universal lathe with 7.5 KW engine power. In the turning experiments, Taegutec TT8125B coded CVD coated carbide cutting tool and CT 3000 coded cermet turning inserts were used with PSBNR 2525M 12 turning bar. In the turning experiments, the STN-40 model device, produced by the Werte Company, was used as the MQL system. The visual of the MQL system used in the experiments is given in Figure 1. 100% biodegradable vegetable-based SAMNOS ZM22W cutting oil was used in turning experiments. Single variety nanopowder and nanoparticle-added MQL cutting fluid was prepared for the turning experiments. Multi-walled carbon nanotubes was used in MQL cutting fluid.

Table 1. Chemical components of 20NiCrMo2 steel

Element	C	Si	Mn	Cr	Mo	Nb
Wt.%	0.17-0.23	Max. 0.40	0.65-0.95	0.35-0.70	0.15-0.25	0.40-0.70

Mahr MarSurf PS 10 model device was used for surface roughness measurements. Surface roughness was measured from three areas of the turned surfaces, namely the beginning, middle and end, and these results were averaged, and the average values of surface roughness (Ra) were found. In the turning experiments, the

temperature data occurring in the cutting zone on the cutting tool was measured with an OPTRIS PI 450 thermal camera. The camera was mounted in a way to see the interaction between the workpiece and the cutting tool on the universal lathe, and during all turning experiments, the temperature signals were transferred to the computer with the manufacturer's software and the highest cutting temperature (Ctemp) was determined. In order to provide the most ideal outputs in experimental studies, optimum design is necessary. In this study, Taguchi technique was preferred for experimental design and optimization. In this technique, statistical performance criterions called utilizing the signal-to-noise ratio analyze the outputs and the resulting experimental results. Surface roughness and cutting zone temperature values acquired as a consequence of the turning process are converted into S/N ratios. When calculating noise rates; Depending on the type of characteristic, there are three approaches used: largest is best, nominal is best and smallest is best [28, 29]. The study's formula for the "smallest is best" tenet, as stated in Equation 1, was preferred for S/N values.

$$S/N = -10\log\left(\frac{1}{n}\sum_{i=1}^{n} y_i^2\right) \quad (1)$$

In the formula; The measured average surface roughness and cutting zone temperature values are expressed as yi, and the number of experiments performed is expressed as n. Cutting parameters in this study; cutting tool type (Ct), cooling method type (Cm), feed rate (f), and cutting speed (V). The control factors and control levels used when turning 20NiCrMo2 steel are given in Table 2. Using Analysis of Variance (ANOVA) and a 95% confidence interval, the factors' levels of impact on Ra and Ctemp were ascertained. Minitab 18 software was employed in the design of the experiment and Taguchi technique statistical analyses.

Table 2. Turning parameters and levels

Turning parameters	Level 1	Level 2	Level 3
Cutting tools (Ct)	TT8125B	CT3000	
Cooling method (Cm)	Dry	MQL	Nano-MQL
Cutting speed - V (m/min)	80	120	160
Feed rate - f (mm/rev)	0.12	0.16	0.20

3. Findings and Discussion

3.1. Optimization of experimental results

The orthogonal array experimental design, which was put forth by Taguchi, can be used to investigate the impact of numerous variables on the performance characteristic in a concentrated experimental group. Upon identifying the variables impacting a controllable process, it is important to ascertain the thresholds at which these parameters ought to be adjusted. A thorough understanding of the procedure, including the parameter's lowest, maximum, and current values, is necessary to decide which levels of a variable to test. The tested values may be farther apart or more values may be evaluated if there is a significant discrepancy between the parameter's minimum and maximum values. If the range of a parameter is small, fewer values may be tested or the tested values may be closer to each other [30, 31]. The average Ra and Ctemp values acquired as a consequence of the turning experiments carried out on case-hardened steel based on the Taguchi L18 experimental design, and the S/N ratios computed are given in Table 3.

Table 3. The experimental results and S/N ratios values

Exp. no.	Cutting tools (Ct)	Cooling method (Cm)	V (m/min)	f (mm/rev)	Ra (µm)	Ra - S/N ratio (dB)	Ctemp (°C)	Ctemp - S/N ratio (dB)
1	TT8125B	Dry	80	0.12	4.78	-13.5886	161.2	-44.1473
2	TT8125B	Dry	120	0.16	3.95	-11.9319	176.6	-44.9398
3	TT8125B	Dry	160	0.20	3.86	-11.7317	224.2	-47.0127

4	TT8125B	Mql	80	0.12	4.18	-12.4235	135.0	-42.6067
5	TT8125B	Mql	120	0.16	3.75	-11.4806	174.9	-44.8558
6	TT8125B	Mql	160	0.20	3.64	-11.2220	224.2	-47.0127
7	TT8125B	Nano-Mql	80	0.12	3.71	-11.3875	138.0	-42.7976
8	TT8125B	Nano-Mql	120	0.16	3.10	-9.8272	165.1	-44.3549
9	TT8125B	Nano-Mql	160	0.20	3.20	-10.1030	131.0	-42.3454
10	Cermet	Dry	80	0.12	2.70	-8.6273	206.1	-46.2816
11	Cermet	Dry	120	0.16	2.20	-6.8485	222.1	-46.9310
12	Cermet	Dry	160	0.20	1.94	-5.7560	230.0	-47.2346
13	Cermet	Mql	80	0.12	2.66	-8.4976	176.9	-44.9546
14	Cermet	Mql	120	0.16	1.92	-5.6660	189.7	-45.5613
15	Cermet	Mql	160	0.20	1.23	-1.7981	224.4	-47.0205
16	Cermet	Nano-Mql	80	0.12	2.36	-7.4582	166.8	-44.4439
17	Cermet	Nano-Mql	120	0.16	1.34	-2.5421	154.9	-43.8010
18	Cermet	Nano-Mql	160	0.20	1.11	-0.9065	176.0	-44.9103

The S/N response table acquired as a consequence of Taguchi optimization gives the turning parameters that provide the optimum values of cutting zone temperature and surface roughness and the order of influence of these parameters. The largest values in the response table show the ideal value for that parameter. The S/N response table created the outcome of the Taguchi analysis is displayed in Table 4.

Table 4. S/N response tables

Levels	**Ra**				**Ctemp**			
	Turning parameters							
	Ct	**Cm**	**V**	**f**	**Ct**	**Cm**	**V**	**f**
Level 1	-11.522	-9.747	-10.330	-7.884	-44.45	-46.09	-44.21	-44.48
Level 2	-5.344	-8.515	-8.049	-8.327	-45.68	-45.34	-45.07	-44.95
Level 3		-7.037	-6.920	-9.089		-43.78	-45.92	-45.78
Delta	6.177	2.710	3.411	1.205	1.23	2.32	1.72	1.30
Rank	1	3	2	4	4	1	2	3

According to Table 4's S/N response table, the optimum parameters for Ra are; Cermet cutting tool, which is the second kind of cutting tools, nano-mql, which is the third level of cooling method type, 160 m/min, which is the third level of cutting speed, and 0.12 mm/rev, which is the first level of feed rate. The optimum parameters for Ctemp are; The first level of the cutting tool type, coated carbide cutting tool, the third level of the cooling method type, nano-mql, the first level of the cutting speed, 80 m/min, and the first level, the feed rate, were determined as 0.12 mm/rev. The order in the bottom row of the table corresponds to the order of effect of the parameters on the outputs. Effect order of parameters for Ra according to response values; cutting tool type, cutting speed, cooling method type and feed rate. For Ctemp; cooling method type, cutting speed, feed rate and cutting tool type. According to Table 4, the most effective turning parameter on Ra is the cutting tool type, while the type of cooling method is the most effective parameter on Ctemp.

Primary effect diagrams displaying the ideal control factor values, that is, cutting parameters are presented in Figures 1 and 2. Similar to the results in the response table for S/N in Table 4, the primary effect graph's largest S/N values show the parameter's ideal level. As a result, the ideal Ra values for feed rate, cutting speed, cooling technique, and cutting tool type, respectively; cermet cutting tool, nano-mql cooling method, 160 m/min and 0.12 mm/rev. For the cutting zone temperature; coated carbide cutting tool, nano-mql cooling, cutting speed of 80 m/min and feed rate of 0.12 mm/rev. When Table 4 and Figure 1-2 are evaluated together, it is

noteworthy that the optimum parameters for Ra and the optimum turning parameters for Ctemp vary. While the cermet tool gave the lowest value for Ra, the carbide cutting tool gave the lowest temperature value for Ctemp. Similarly, while the ideal result was obtained for Ra at the fastest possible cutting speed value of 160 m/min, the lowest value for Ctemp was found at 80 m/min. The reason for this difference is; Ra values tend to decrease as the cutting zone's temperature rises to a certain level. Therefore, as the cutting speed increased from 80 m/min to 160 m/min, the cutting zone temperature increased and due to this increase, thermal softening occurred at the chip-cutting tool-workpiece interface. Due to this thermal softening, the cutting process becomes easier. As a result, since the cutting tool shapes the material more easily, the roughness of the processed surface is better [32,33].

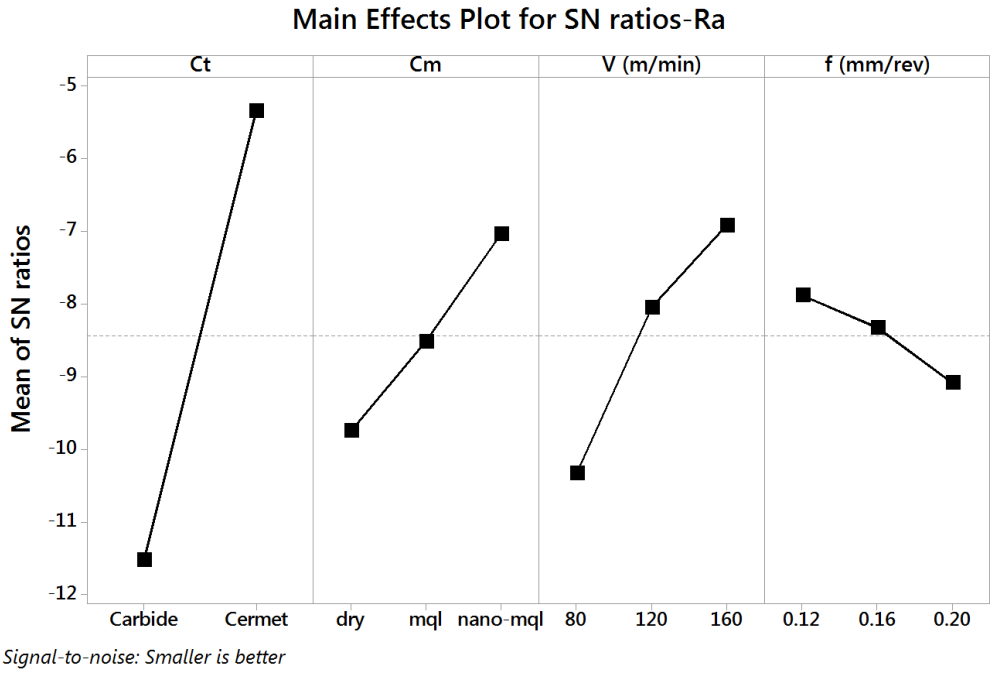

Figure 1. Main effects plot of S/N ratios for Ra

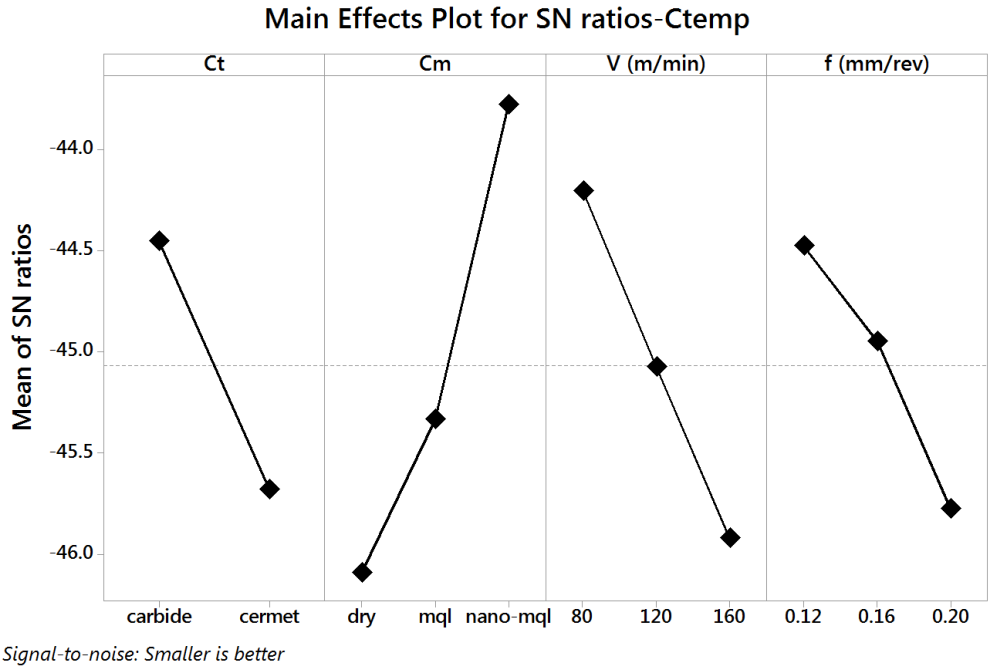

Figure 2. Main effects plot of S/N ratios for Ctemp

Ideal numbers for both Ra and Ctemp were not found in the 18 turning experiments performed. Therefore, the 19th experiment was conducted for both output parameters. The average surface roughness value for optimum parameters was measured as 1.08 µm. For optimum parameters, the cutting zone temperature was measured as 122 °C.

3.2. Variance analyses for experimental results

An experiment's variability can be divided into distinguishable causes of variance as well as the corresponding degrees of freedom using the analysis of variance technique. The analysis of the significant effects of the parameters comprising the quality features is done in statistics using the frequency test (F-test) [34]. Table 5 displays the findings of the variance analysis that was done to ascertain the rates at which turning parameters (type of cutting tool, feed rate, cutting speed, and cooling technique) affected the average surface roughness and temperature of the cutting zone. In the table; DF, SS, MS, F and PCR correspond to degrees of freedom, sum of squares, mean of squares, significance level and percentage effect ratio, respectively. ANOVA analysis was carried out using 5% significant levels and 95% confidence. F values are of great importance to ascertain the impact of control factors. The effect of turning parameters on the output parameters Ra and Ctemp is ascertained by contrasting F values. As a result, the cutting parameter with the largest F value is the parameter that affects the experimental result the most.

Table 5. Ra and Ctemp's ANOVA table

Source	DF	SS	MS	F ratio	P	PCR (%)
Ra						
Ct	1	15.5124	15.5124	360.50	0.000	75.96
Cm	2	1.7782	0.8891	20.66	0.000	8.71
V	2	2.6646	1.3323	30.96	0.000	13.05
f	2	0.0372	0.0186	0.43	0.660	0.18
Error	10	0.4303	0.0430			2.11
Total	17	20.4228				100.00
Vb						
Ct	1	2609	2608.8	10.47	0.009	14.11
Cm	2	7199	3599.5	14.44	0.001	38.95
V	2	4269	2134.7	8.56	0.007	23.10
f	2	1913	956.3	3.84	0.058	10.35
Error	10	2493	249.3			13.49
Total	17	18483				100.00

According to the ANOVA results in Table 5, it was seen that the primary influencing turning parameter Ra was the kind of cutting tools with a rate of 75.96%. Then comes the rate of cutting speed of 13.05%, the type of cooling method with a rate of 8.71% and finally the feed speed with a rate of 0.18%. The turning parameter that had the most impact on the cutting zone temperature was the cooling method type with a rate of 38.95%. Then comes cutting speed with 23.10%, cutting tool type with 14.11% and feed rate with 10.35%, respectively. Within the scope of this study, it was noted that the type of cutting tool was more effective on surface roughness than the type of cooling method, cutting speed and feed rate parameters. It has been established that the cooling method has a more significant effect on the cutting zone temperature than other turning parameters. If an evaluation is made between a cermet cutting tool and a coated carbide cutting tool in turning case-hardened steel, it is seen that the cermet cutting tool provides lower Ra values. Cutting speed, which is one of the most effective cutting parameters on Ra, was evaluated as the second effective parameter for both Ra and Ctemp in this study. It is clearly seen that the feed rate does not have a noteworthy impact on either output parameter.

3.3. Regression analyses for experimental results

Multiple regression analysis was performed for Ra and Ctemp values obtained after turning experiments.

Graphs of the regression analysis (Normal Probability Plot, Versus Fits, Histogram, and Versus Order) are given in Figure 3 and Figure 4.

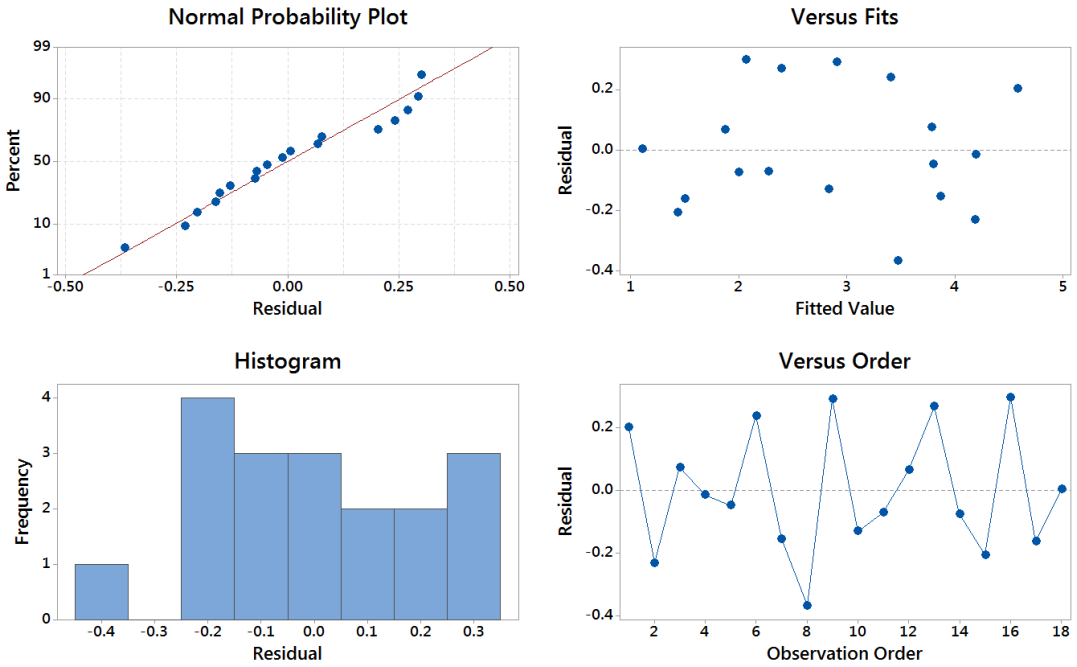

Figure 3. Residual plots for Ra

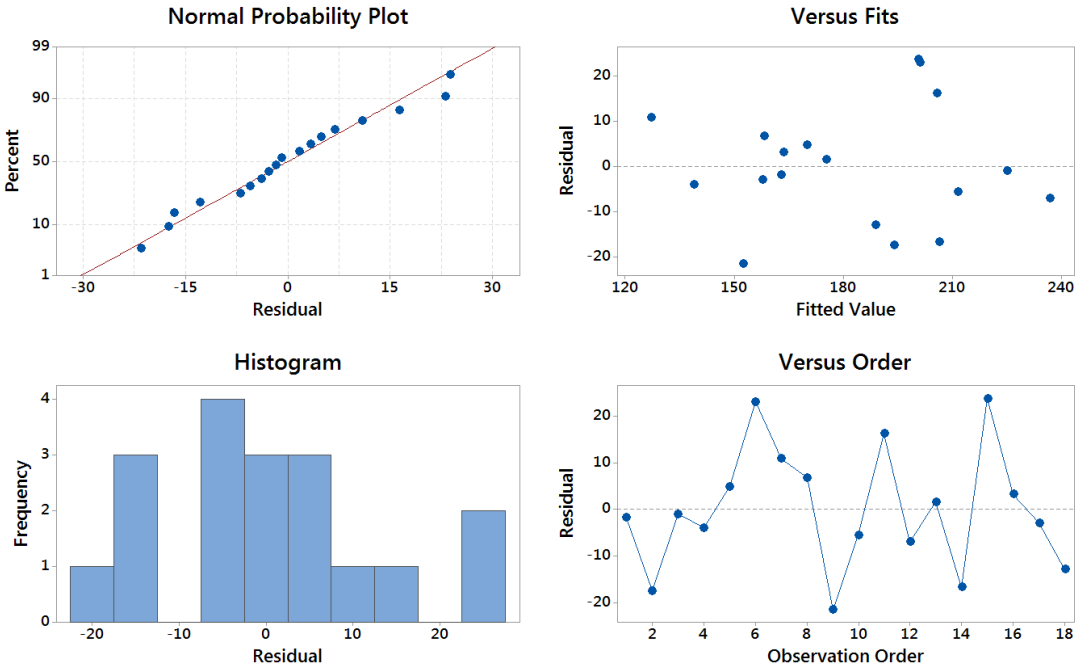

Figure 4. Residual plots for Ctemp

In Figures 3 and 4 statistical results for Ra and Ctemp are given. In Figure 3 and 4, showing the normal probability plot vs the residuals of the linearquadratic models, it can be seen that the residuals are arranged in a relatively straight line. This denoted a normal distribution of errors and signified that the terms stated in the model were significant. Moreover, a good correlation was found between the experimental vs predicted Ra and Ctemp values and their close similarity was noted. Multiple regression analysis was used to obtain the predictive equations (for linear regression model) for Ra and Ctemp, as seen in equations (2) and (3),

respectively:

$$Ra\ (\mu m) = 7.557 - 1.857\ Ct - 0.3842\ Cm - 0.01127\ V\ (m/min) + 1.35\ f\ (mm/rev) \quad (2)$$

$$Ctemp\ (°C) = 88.4 + 24.08\ Ct - 24.03\ Cm + 0.470\ V\ (m/min) + 307\ f\ (mm/rev) \quad (3)$$

The R^2 values of the equations obtained by the linear regression model for Ra and Ctemp were found to be 0.96 and 0.84, respectively. For reliable statistical analyses, the error values must be less than 20 per cent [28].

4. Conclusions

In this study, 20NiCrMo2 steel was subjected to turning process with distinc cutting tools, distinc cooling methods and distinc cutting parameters. Coated carbide and cermet cutting tools were preferred as the cutting tool type. Three distinc cooling methods were used: dry, mql and nano-mql. As turning parameters, three distinc cutting speeds (80, 120, 160 m/min) and three distinc feed rates (0.12, 0.16, 0.20 mm/rev) were used. Taguchi L18 orthogonal array was preferred for experimental design. In addition, analysis of variance was performed to determine the impact ratios of turning parameters on Ra and Ctemp. The results of the study are listed below.

- As a result of Taguchi analysis, average surface roughness was determined at the second level of the cutting tool type (cermet cutting tool), at the third level of the cooling method type (nano-mql), at the third level of the cutting speed of 160 m/min and at the first level of the feed rate of 0.12 mm/rev parameters. The lowest Ra values were reached.
- The average surface roughness value for optimum parameters was measured as 1.08 µm.
- Optimum result for cutting zone temperature; It was obtained at the first level of the cutting tool type (coated carbide cutting tool), at the third level of the cooling method type (nano-mql), at the first level of the cutting speed of 80 m/min and at the first level of the feed rate of 0.12 mm/rev.
- For optimum parameters, the cutting zone temperature was measured as 122 °C.
- The type of cutting tool is the most useful parameter for Ra, based on ANOVA data (75.96%), followed by cutting speed (13.05%), cooling method type (8.71%) and feed rate (0.18%) has been seen.
- The turning parameter that had the most impact on the cutting zone temperature was the type of cooling method with a rate of 38.95%. Then comes cutting speed with 23.10%, cutting tool type with 14.11% and feed rate with 10.35%, respectively.

When all the outcomes are assessed, it can be seen that the most suitable cutting parameters and cooling method type have been successfully determined for intermediate and finish turning conditions of 20NiCrMo2 steel. We can say that cermet cutting tools should be preferred for low Ra value when material with a hardness of approximately 30 Brinell is subjected to turning at a cutting speed of 80 to 160 m/min and a feed rate of 0.12 to 0.20 mm/rev. For low Ctemp values, coated carbide cutting tools should be preferred instead of hardmet tools. The nano-mql method provided the lowest values for both Ra and Ctemp. This result once again demonstrated the unique value of the study. According to the Taguchi analysis results, it is clearly seen that a valid optimization has been made for the lowest Ra and Ctemp values. According to all these results, it can be stated that the study successfully achieved its objectives. In addition to these results, the following recommendations can be made for future studies.

- Turning experiments can be performed with the same cutting parameters for higher hardness values of the workpiece sample.
- Tests can be performed on ceramic and uncoated carbide cutting tools as well as cermet and carbide cutting tools.
- Differences between dry cutting, mql and nano-mql can be detected with boron oil, which is the

traditional cooling method.
- Cutting experiments can be performed for distinc nanoparticle particles.
- Experiments can be performed for distinc outputs such as tool wear and vibration, as well as cutting zone temperature and surface roughness.

Conflict of Interest Statement

The authors declare that there is no conflict of interest.

References

[1] G. S. Goindi, A. D. Jayal, and P. Sarkar, "Application of ionic liquids in interrupted minimum quantity lubrication machining of Plain Medium Carbon Steel: Effects of ionic liquid properties and cutting conditions," *Journal of Manufacturing Processes*, vol. 32, pp. 357–371, Apr. 2018. doi:10.1016/j.jmapro.2018.03.007

[2] N. M.s, M. M. Rahman, and K. Kadirgama, "Parametric optimization of end milling process under minimum quantity lubrication with nanofluid as cutting medium using pareto optimality approach," *International Journal of Automotive and Mechanical Engineering*, vol. 13, no. 2, pp. 3345–3360, 2016. doi:10.15282/ijame.13.2.2016.5.0277

[3] N. N. N. Hamran, J. A. Ghani, R. Ramli, and C. H. C. Haron, "A review on recent development of minimum quantity lubrication for sustainable machining," *Journal of Cleaner Production*, p. 122165, May 2020. doi:10.1016/j.jclepro.2020.122165

[4] A. Marques, Mauro Paipa Suarez, Wisley Falco Sales, and Álisson Rocha Machado, "Turning of Inconel 718 with whisker-reinforced ceramic tools applying vegetable-based cutting fluid mixed with solid lubricants by MQL," vol. 266, pp. 530–543, Apr. 2019. doi:10.1016/j.jmatprotec.2018.11.032

[5] K. A. Osman, H. Ö. Ünver, and U. Şeker, "Application of minimum quantity lubrication techniques in machining process of titanium alloy for sustainability: a review," *The International Journal of Advanced Manufacturing Technology*, vol. 100, no. 9–12, pp. 2311–2332, Oct. 2018. doi:10.1007/s00170-018-2813-0

[6] U. M. R. Paturi, Y. R. Maddu, R. R. Maruri, and S. K. R. Narala, "Measurement and Analysis of Surface Roughness in WS2 Solid Lubricant Assisted Minimum Quantity Lubrication (MQL) Turning of Inconel 718," *Procedia CIRP*, vol. 40, pp. 138–143, 2016. doi:10.1016/j.procir.2016.01.082

[7] M. N. Sharif, S. Pervaiz, and I. Deiab, "Potential of alternative lubrication strategies for metal cutting processes: a review," *The International Journal of Advanced Manufacturing Technology*, vol. 89, no. 5–8, pp. 2447–2479, Aug. 2016. doi:10.1007/s00170-016-9298-5

[8] A. Eltaggaz, H. Hegab, I. Deiab, and H. A. Kishawy, "Hybrid nano-fluid-minimum quantity lubrication strategy for machining austempered ductile iron (ADI)," *International Journal on Interactive Design and Manufacturing (IJIDeM)*, vol. 12, no. 4, pp. 1273–1281, Jun. 2018. doi:10.1007/s12008-018-0491-7

[9] M.A. Makhesana, K. M. Patel, G. M. Krolczyk, M. Danish, Anil Kumar Singla, and N. Khanna, "Influence of MoS2 and graphite-reinforced nanofluid-MQL on surface roughness, tool wear, cutting temperature and microhardness in machining of Inconel 625," *CIRP Journal of Manufacturing Science and Technology*, vol. 41, pp. 225–238, Apr. 2023. doi:10.1016/j.cirpj.2022.12.015.

[10] R. Singh Rooprai, T. Singh, M. Singh, M. Rana, V. Kumar Sharma, and S. Sharma, "Multi-variable optimization for surface roughness and micro-hardness in MQL assisted face milling of EN31 steel using Taguchi based grey relational analysis," *Materials Today: Proceedings*, vol. 43, pp. 3144–3147, 2021. doi:10.1016/j.matpr.2021.01.624

[11] O. Özbek, and H. Saruhan, "The effect of vibration and cutting zone temperature on surface roughness and tool wear in eco-friendly MQL turning of AISI D2," *Journal of Materials Research and Technology*, vol. 9, no. 3, pp. 2762–2772, May 2020. doi:10.1016/j.jmrt.2020.01.010

[12] J. Ning and S. Liang, "Predictive Modeling of Machining Temperatures with Force–Temperature Correlation Using Cutting Mechanics and Constitutive Relation," *Materials*, vol. 12, no. 2, p. 284, Jan. 2019. doi:10.3390/ma12020284

[13] Y.-C. Lin, K.-D. Wu, W.-C. Shih, P.-K. Hsu, and J.-P. Hung, "Prediction of Surface Roughness Based on Cutting Parameters and Machining Vibration in End Milling Using Regression Method and Artificial Neural Network," *Applied Sciences*, vol. 10, no. 11, p. 3941, Jun. 2020. doi:10.3390/app10113941

[14] N. A. Özbek, "Effects of cryogenic treatment types on the performance of coated tungsten tools in the turning of AISI H11 steel," *Journal of Materials Research and Technology*, vol. 9, no. 4, pp. 9442-9456, 2020. doi:10.1016/j.jmrt.2020.03.038

[15] A. Agrawal, S. Goel, W. B. Rashid, and M. Price, "Prediction of surface roughness during hard turning of AISI 4340 steel (69 HRC)," *Applied Soft Computing*, vol. 30, pp. 279–286, May 2015. doi:10.1016/j.asoc.2015.01.059

[16] O. Özbek, "Evaluation of Nano Fluids with Minimum Quantity Lubrication in Turning of Ni-Base Superalloy UDIMET 720," *Lubricants*, vol. 11, no. 4, p. 159, Apr. 2023. doi:10.3390/lubricants11040159

[17] I. Ciftci and H. Gökçe, "Optimisation of cutting tool and cutting parameters in machining of molybdenum alloys through the Taguchi Method". *Journal of the Faculty of engineering and architecture of Gazi university*, vol. 2018, no. 2018. Apr. 2018. doi:10.17341/gazimmfd.416482

[18] C. Liu et al., "Effects of process parameters on cutting temperature in dry machining of ball screw," *ISA Transactions*, vol. 101, pp. 493–502, Jun. 2020. doi:10.1016/j.isatra.2020.01.031

[19] E. Nas, "Analysis of the electrical discharge machining (EDM) performance on Ramor 550 armor steel," *Materials Testing*, vol. 62, no. 5, pp. 481–491, May 2020. doi:10.3139/120.111510

[20] Y. Pan et al., "New insights into the methods for predicting ground surface roughness in the age of digitalisation," *Precision Engineering-journal of The International Societies for Precision Engineering and Nanotechnology*, vol. 67, pp. 393–418, Jan. 2021. doi:10.1016/j.precisioneng.2020.11.001

[21] M. Tomov, M. Kuzinovski, and P. Cichosz, "Development of mathematical models for surface roughness parameter prediction in turning depending on the process condition," *International Journal of Mechanical Sciences*, vol. 113, pp. 120–132, Jul. 2016. doi:10.1016/j.ijmecsci.2016.04.015

[22] C. Xia, Z. Pan, J. Polden, H. Li, Y. Xu, and S. Chen, "Modelling and prediction of surface roughness in wire arc additive manufacturing using machine learning," *Journal of Intelligent Manufacturing*, Jan. 2021. doi:10.1007/s10845-020-01725-4

[23] S. V. Alagarsamy, M. Ravichandran, M. Meignanamoorthy, S. Sakthivelu, and S. Dineshkumar, "Prediction of surface roughness and tool wear in milling process on brass (C26130) alloy by Taguchi technique," *Materials Today: Proceedings*, vol. 21, pp. 189–193, 2020. doi:10.1016/j.matpr.2019.04.219

[24] F. Kara, N. Bulan, Mahir Akgün, and Uğur Köklü, "Multi-Objective Optimization of Process Parameters in Milling of 17-4 PH Stainless Steel using Taguchi-based Gray Relational Analysis," *Engineered science*, Jan. 2023. doi:10.30919/es961

[25] H. Gokce, "Optimisation of Cutting Tool and Cutting Parameters in Face Milling of Custom 450 through the Taguchi Method," *Advances in Materials Science and Engineering*, vol. 2019, pp. 1–10, Sep. 2019. doi:10.1155/2019/5868132

[26] I. Tlhabadira, I. A. Daniyan, R. Machaka, C. Machio, L. Masu, and L. R. VanStaden, "Modelling and optimization of surface roughness during AISI P20 milling process using Taguchi method," *The International Journal of Advanced Manufacturing Technology*, vol. 102, no. 9–12, pp. 3707–3718, Feb. 2019. doi:10.1007/s00170-019-03452-4

[27] H. Gökçe, "Modelling and Optimization for Thrust Force, Temperature and Burr Height in Drilling of Custom 450," *Experimental Techniques*, vol. 46, no. 4, pp. 707–721, Sep. 2021 doi:10.1007/s40799-021-00510-z

[28] F. Kara, "Taguchi optimization of surface roughness and flank wear during the turning of DIN 1.2344 tool steel," *Materials Testing*, vol. 59, no. 10, pp. 903–908, Oct. 2017, doi:10.3139/120.111085

[29] Douglas Barrett, "Taguchi's Quality Engineering Handbook," Technometrics, vol. 49, no. 2, pp. 224–225, May 2007 doi:10.1198/tech.2007.s480

[30] M. Akgün, B. Özlü, and F. Kara, "Effect of PVD-TiN and CVD-Al2O3 Coatings on Cutting Force, Surface Roughness, Cutting Power, and Temperature in Hard Turning of AISI H13 Steel," *Journal of Materials Engineering and Performance*, vol. 32, no. 3, pp. 1390–1401, Aug. 2022. doi:10.1007/s11665-022-07190-9

[31] E. Nas, O. Özbek, F. Bayraktar, and F. Kara, "Experimental and Statistical Investigation of Machinability of AISI D2 Steel Using Electroerosion Machining Method in Different Machining Parameters," *Advances in Materials Science and Engineering*, vol. 2021, pp. 1–17, Oct. 2021. doi:10.1155/2021/1241797

[32] O. Özbek, N. Altan Özbek, F. Kara, and H. Saruhan, "Effect of vibration and cutting zone temperature on surface topography during hybrid cooling/lubrication assisted machining of Vanadis 10," *MP MATERIALPRUEFUNG - MP MATERIALS TESTING*, vol. 65, no. 9, pp. 1437–1452, Aug. 2023. doi:10.1515/mt-2023-0057

[33] S. Yağmur, "The effects of cooling applications on tool life, surface quality, cutting forces, and cutting zone temperature in

turning of Ni-based Inconel 625," *The International Journal of Advanced Manufacturing Technology*, vol. 116, no. 3–4, pp. 821–833, Jun. 2021. doi:10.1007/s00170-021-07489-2

[34] N. A. Özbek, O. Özbek, and F. Kara, "Statistical Analysis of the Effect of the Cutting Tool Coating Type on Sustainable Machining Parameters," *Journal of Materials Engineering and Performance*, vol. 30, no. 10, pp. 7783–7795, Aug. 2021. doi:10.1007/s11665-021-06066-8

This is an open access article under the CC-BY license

Research Article/Araştırma Makalesi

Gazi AKADEMİK YAYINCILIK

GAZİ
JOURNAL OF ENGINEERING SCIENCES

Calculations of Structural Parameters and Optical Constants of Size Dependent ZrO_2

Gülsen Şahin[*a], Sultan Göktaş[b]

Submitted: 23.10.2023 Revised: 21.12.2024 Accepted: 01.03.2024 doi:10.30855/gmbd.0705N10

ABSTRACT

In this study, structural parameters and optical constants of size dependent zirconium dioxide (ZrO_2) nanostructures were calculated. The effect of particle size was investigated on the calculated structural and optical parameters/constants. ZrO_2 nanostructures were produced by chemical route. To change the grain size of the ZrO_2 nanostructures, different annealing temperatures (450-550 °C) were applied. The x-ray diffraction (XRD), scanning electron microscope (SEM), and ultraviolet/visible region (UV-Vis) spectroscopy measurement results were used to calculate the structural and optical parameters/constants. The results of XRD measurement showed the ZrO_2 nanostructures were crystallized in single tetragonal (cubic) ZrO_2 phase. SEM results exhibited dense and homogeneous surfaces and enhanced surface grains with increased annealing temperature. The compositional formation of ZrO_2 nanostructures were proved by electron dissipated x-ray and mapping analysis. Optical measurements were strongly changed dependent on the grain size (G_S). The calculated structural parameters such as crystallite size, lattice parameter (a), microstrain, and dislocation density were showed that the powerful variation according to the G_S. The computed optical constants such as refractive index, extinction coefficient, reel and imaginer dielectric constants of the ZrO_2 samples were highly varied upon the G_S. The variant in these calculated parameters/constant were extremely promising for the optic and dielectric applications.

Keywords: ZrO_2, Optical constant, Extinction coefficient, Refractive index, Reel dielectric constant

[a,*] Adıyaman University, Faculty of Education, Department of Science
02040 - Adıyaman, Türkiye
Orcid: 0000-0003-4891-041X
e mail: gsahin@adiyaman.edu.tr

[b] Harran University, Faculty of Science and Arts, Department of Chemistry
63290 - Şanlıurfa, Türkiye
Orcid: 0009-0000-7084-9710

*Corresponding author:
gsahin@adiyaman.edu.tr

Büyüklüğe Bağlı ZrO_2 Nanoyapılarının Yapısal Parametreleri ve Optiksel Sabitlerinin Hesaplanması

ÖZ

Bu çalışmada boyuta bağlı zirkonyum dioksit (ZrO_2) nanoyapılarının yapısal parametreleri ve optik sabitleri hesaplanmıştır. Parçacık boyutunun, hesaplanan yapısal ve optik parametreler/sabitler üzerindeki etkisi araştırıldı. ZrO_2 nanoyapıları kimyasal yolla üretildi. ZrO_2 nanoyapılarının tane boyutunu değiştirmek için farklı tavlama sıcaklıkları (450-550°C) uygulandı. Yapısal ve optik parametreleri/sabitleri hesaplamak için x-ışını kırınımı (XRD), taramalı elektron mikroskobu (SEM) ve ultraviyole/görünür bölge (UV-Vis) spektroskopisi ölçüm sonuçları kullanıldı. XRD ölçümü sonuçları, ZrO_2 nanoyapılarının tek tetragonal (kübik) ZrO_2 fazında kristalleştiğini gösterdi. SEM sonuçları, yoğun ve homojen yüzeyler ve artan tavlama sıcaklığıyla sayısı artan yüzey taneleri sergiledi. ZrO_2 nanoyapılarının bileşiksel oluşumu elektron dağılımlı x-ışını ve haritalama analizi ile kanıtlanmıştır. Optik ölçümler tane boyutuna (G_S) göre büyük ölçüde değişti. Kristal boyutu, örgü parametresi (a), mikro-gerilim ve dislokasyon yoğunluğu gibi hesaplanan yapısal parametreler, G_S'ye bağlı olarak ciddi bir değişim gösterdi. ZrO_2 numunelerinin kırılma indisi, sönüm katsayısı, reel ve sanal dielektrik sabitleri gibi hesaplanan optik sabitleri G_S'ye bağımlı olarak ciddi oranda değişti. Hesaplanan bu parametrelerdeki/sabitlerdeki değişkenlik, optik ve dielektrik uygulamalar için son derece umut vericidir.

Anahtar Kelimeler: ZrO_2, Optiksel sabit, Yok olma katsayısı, Kırılma indisi, Reel dielektrik katsayısı

To cite this article: G. Sahin and S. Goktas "Calculation of Structural Paramaters and Optical Constants of Size Dependent ZrO2," *Gazi Journal of Engineering Sciences*, vol.10, no.1, pp. 114-124, 2024. doi:10.30855/gmbd.0705N10

1. Introduction

In many practical applications, it is possible to make life easier by using nanostructured thin films. They can be preferred for making reflective or antireflective filters, circuit candidates, memory disks, memory disc, biological ceramics, sensors, and lasers [1-5]. In this context, attractive physical characteristics of Zirconia (ZrO_2) thin film such as having a high dielectric constant, a relatively higher melting point (2680°C), high chemical stability and wide band gap (4.7eV-7.8eV), make it extraordinary metal oxide semiconductors [6]. In addition to, its high thermal stability, high refractive index, and low thermal conductivity capacities lead to be commercially used as dielectric and insulator in various microelectronic applications viz. dynamic random-access memory, radio frequency, analog/mixed signal (RF/AMS) integrated circuits, and non-volatile resistive random-access memory [3,5].

It was reported that ZrO_2 could have different crystal-like phases such as monoclinic, tetragonal, and cubic dependent on high temperature reflecting polymorphic structure [7,8]. However, this high temperature phases can be maintained at room temperature using suitable oxide dopants [9-11]. Even for the pure ZrO_2 thin films it can be achieved owing to low crystallite size and compressive stress [12]. But the undoped ZrO_2 has deteriorated by some consequential issues. The small crystallization due to low temperature processing resulted in the enhanced additional leakage currents through the crystal boundaries and creating highly thick intersectional sheets [13]. In addition to, producing high dielectric constant (κ) metal oxide nanostructured thin films utilizing chemical solution-based method needs a relatively high sintering temperature of over 450 °C due to high pyrolysis and desiccation temperature of prototypical forerunners [14]. Annealing at relatively high temperatures is an effectual way to remove the defects (like oxygen vacancies) and impurities (like secondary phases) from metal-based oxide nanomaterials resulting into tolerable discharge and electrical capacity as well as high crystallization [15,16].

Recently, several fabrication of nanostructured thin films have been followed to product zirconia-based high-κ gate dielectric viz. sol-gel dip/spin coating, atomic layer deposition, spray pyrolysis, chemical vapor deposition, reactive RF sputtering, and electron beam evaporation [13,17]. Amongest all the solution-based sol-gel technique is currently becoming the most popular route owing to its clarity, economic, low treating temperature, practical use, and pile of yield. Some concern study has been outlined about the size dependent characteristics of sol-gel derived ZrO_2 thin films. However, a detailed work on the structural and optical properties, structural parameters, and linear optical constants of the ZrO_2 is rare. Therefore, in the present study the grain size dependent structural and optical characteristics, structural parameters and optical constants have been investigated.

2. Experiment and Calculation Techniques

To prepare ZrO_2 solution, zirconyl chloride octahydrate ($ZrOCl_2 \cdot 8H_2O$) was used for the parent solution. The molar ratio (0.01M) of chemical powder was utilized as Zr^{+2} source and it was dissolved by mixed solution of methanol (96,15 at. %) and glacial acetic acid (3,85 at .%). The desired ZrO_2 solution was get ready via vigorously mixing on the magnetic stirrer for 30-60 minutes at 50 °C. The final solution bath was aged by stirring at room conditions for 24 hours to have gel solution, which is essential for highly uniform film structure. Before coating, the glass facets were rinsed with deionized water. It was then ultrasonically cleaned in an ethanol and acetone ultrasonic bath for 5 minutes. In cleaning process, the glass surfaces were finally placed in the plasma cleaner to remove waste organic hanging bonds and precision cleaning. The cleaned glass substrates were immersed in the resulting solution and covered in air at 350°C. Films grown on the glass surfaces by sol-gel dip coating method and they were annealed at 450 °C, 500 °C and 550°C for 60 minutes in an air atmosphere to get desired grain size (G_S).

The latest emerging ZrO_2 thin films were constructionaly characterized via X-ray diffraction (XRD) with a Rigaku Ultima III diffractometer though employing CuK_α radiation (λ =0.15406 nm) at 30 mA and 40 keV from 20 to 70°. To calculate the average crystallite size (D_{hkl}), [13] the Debye Sherrer's equation as following as:

$$D_{hkl}=0.9\lambda/\beta.cos\theta \quad (1)$$

where λ is the wavelength of X-rays used, θ is the angle of diffraction and is the full width at half maximum. Similarly the other structural parameters like dislocation density (δ) and micro strain (ε) were computed according to the followed formulas:

$$\delta = 1/(D_{hkl})^2 \quad (2)$$

$$\varepsilon = \beta/4\tan\theta \quad (3)$$

The lattice parameters, a and c of the tetragonal ZrO_2 can be obtained according to the equations given below:

$$a_t=d_{h00}\ h;\ c_t=d_{h0l}\ (h^2+l^2)^{1/2} \quad (4)$$

In this equation the d_{hkl} ($d_{hkl}=a_t/((h^2+k^2+l^2)/(c_t/a_t))^{1/2}$) represents interplanar distance for the tetragonal lattice and (hkl) shows Miller indices. The morphology, surface, grain size, and atomic analysis and mapping were recognized using a scanning electron microscope (SEM) equipped by an energy dispersive X-ray (EDX) tool.

To research the optical characteristics like transmittance and absorbance, the UV–Vis (PerkinElmer 45) spectra was performed. The corresponding transmittance, absorbance and reflectance were than represented and the band gap energy (E_g), refractive index (n), extinction coefficient (k), and reel/imaginer dielectric constants were computed. To calculate E_g and k as well as other related parameters of the nanostructures Beer-Lambert law [17] was used as following:

$$I=I_0e^{-\alpha d} \quad (5)$$

where I is the intensity of the transmitted light, I_0 is the intensity of the incident light, d shows the thickness of the nanostructured layer, and α is the linear absorption coefficient of the materials. In equation (5) α can be calculated as [18]:

$$\alpha = (1/d)\ ln\ (1/T) \quad (6)$$

in that T is the transmittance. The connection between the α and the photon energy ($h\upsilon$) is given as follows [19]:

$$(\alpha h\upsilon)^2 = A(h\upsilon - E_g)^m \quad (7)$$

where A and m are constant coefficients. For indirect transitions, m=2 and for direct transitions n=1/2. Moreover, k and n can be obtained by using reflectance (R) and α as given in equation of (8) and (9) as below [20]:

$$k\ (\lambda)=\alpha\lambda/4\pi \quad (8)$$

$$n(\lambda)= ((1+R(\lambda))/(1-R(\lambda)))+((4R(\lambda))/(1+R(\lambda)-k^2(\lambda))^{1/2} \quad (9)$$

where λ represents of the acted photon wavelength. Finally, the corresponding reel and imaginary dielectric

constants $\mathcal{E}_r$ and $\mathcal{E}_i$ are calculated via using the followed equations [19]:

$$\mathcal{E}_r(\lambda)=n(\lambda)^2-k(\lambda)^2 \quad (10)$$

$$\mathcal{E}_i(\lambda)=2n(\lambda)k(\lambda) \quad (11)$$

3. Results and Discussions

3.1. Calculation of structural parameters by using XRD analysis

The XRD analysis was used to investigate the crystal structure and phase composition of the deposited nanostructures. The XRD patterns of the ZrO_2 nanostructures sintered at 450 °C, 500 °C, and 550°C were given in Fig.1. All nanostructured films show the tetragonal phase with highly oriented (101) Miller crystal plane and polycrystalline nature. The observed other (110), (112), and (211) Miller crystal planes are also indexed for the tetragonal phase. XRD patterns also show there are no metallic or secondary phases in the host ZrO_2 lattice system. The results agree with the research on ZrO_2 thin film [18]. According to Fig. 1, the ZrO_2 nanostructures represent the best crystallization at 550 °C. The average crystallite size (D_{hkl}) [13] calculated using the Debye Sherrer's equation (1) was given in Table 1. The mean D_{hkl} for thin film samples turned out to be 21 nm.

Table 1. The full-width half-maximum, diffraction angle, crystallite size, dislocation density, micro-strain, and lattice parameter of the prepared ZrO_2 nanostructures having various grain sizes

Annealing temperature (°C)	FWHM (β_o)	2θ(deg.)	D_{hkl}(nm)	δx10^{-3}	Ɛx10^{-3}	a;c (Å)
Z3-450	0.80	30.42	10	10.0	12.8	0.5106;5.076
Z3-500	0.53	30.50	15	4.44	8.48	0.5092;5.063
Z3-550	0.38	30.52	21	2.26	6.08	0.5089;5.060

To obtain better crystalline quality, namely increased crystallite size, by providing crystallization in ZrO_2 thin film samples, annealing was done at different temperatures. Figure 1 shows the XRD patterns of ZrO_2 thin film samples annealed at different temperatures. Among all samples, the ZrO_2 nanostructure sintered at 550 °C has the best crystalline quality.

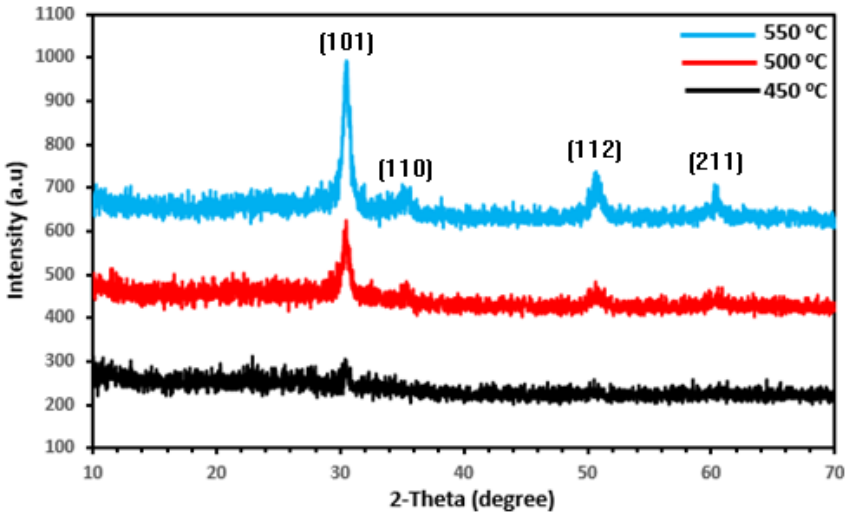

Figure 1. XRD patterns of the deposited ZrO_2 nanostructures with different grain sizes

The calculated D_{hkl} increases with increasing annealing temperature (Table 1). Considering the analysis of nanostructured ZrO_2 thin films prepared at different operating temperatures by Deshmukh and Bari's spray pyrolysis technique; they found that the structure of the film was completely crystallized with an increase in annealing temperature. Additionally, grain growth increased in mobility with increasing temperature. Again, when the literature on the effect of annealing temperature was scanned, it was seen that; Hadi et al., annealed and analyzed the Li doped (ZrO_2) nanostructures produced using the spray pyrolysis (CSP) method at 300^{O}C, 400^{O}C, and 500^{O}C. As a result, they observed that the grain size values, average roughness increased with increasing in sintering temperature. The lattice parameters, *a and c* of the ZrO_2 nanostructures calculated (by using formula 4) for different annealing temperatures (for 450 ^{o}C -550^{o}C) were obtained as in Table 1. It was observed that the *a* and *c* values decreased as the $D_{(hkl)}$ increased. Different ionic sizes in lattice defects, perfect arrangement of atoms, impurity formations can cause differences in *a* and *c* values (see Table 1) dislocation density, (see equation 2), and micro strain (formula 3) as obtained. Different values of δ and Ɛ in Table 1 confirm the variation in lattice parameters. The difference in the lattice parameters, *a* and *c* may also be due to the lattice mismatch between the ZrO_2 nanostructures and the glass sample holder [21-24].

3.2. Estimation of average grain size from SEM analysis

SEM images and EDX/mapping analysis of ZrO_2 nanostructures produced at different annealing temperatures were shown in Figs. 2a-d. The film surfaces have smooth and dense morphology. The grain sizes changes about 20-200 nm, 30-250 nm, and 20-300 nm were estimated for the ZrO_2 nanostructures sintered at temperature range of 450 ^{o}C, 500 ^{o}C, and 550 ^{o}C, respectively. This result is highly agreement with the XRD analysis. Spherical-like grains were observed for the ZrO_2 nanostructures annealed at different temperatures of 450 ^{o}C, 500 ^{o}C and 550 ^{o}C. As a result of thermal energy leading simple displacement of atoms and anisotropic aggregation of crystallites/grains; As seen in Figure 2, annealing temperature affects G_S. The particle or G_S of the nanostructured films increases due to annealing process. Méndez-López et al. [20] prepared ZrO_2 nanostructures by sol-gel dip coating method and investigated the effect of annealing temperature on the structural and optical properties of the ZrO_2 nanostructures. The SEM facet patterns of their nanostructures annealed at 450^{o}C, and 550^{o}C showed the increased G_S of ZrO_2 nanostructures with increasing sintering temperature (Figs. 2a-c). AISI 316L stainless steel was coated with nanostructured zirconia using the sucrose-supported sol-gel dip coating method by Mishra et al. [15]. As a result of SEM analysis, it was seen that the particle sizes of zirconia thin films increased dependent on enhanced sintering temperature, raised from 300 ^{o}C to 650 ^{o}C. The presence of the Zr and O was observed from the EDX and mapping analysis (red and green colors represent the Zr and O atom, respectively) as seen in Fig. 2d.

3.3. Calculation of optical parameters and constants

3.3.1. Determination of optical band gap and reflectance

Optical transmittance and absorbance spectrum of the prepared nanostructured ZrO_2 film samples were exhibited in Figs. 3a and b for the wavelength range of 200-900 nm. As seen in Fig.3a, the transmittance suddenly reduces as the particle size increases. On the other hand, the opposite trend has been observed as expected for the absorbance of the nanostructured ZrO_2 films. The sharp reduction in certain wavelengths and oscillations in Uv-Vis spectrums show homogeneity and quality
of the fabricated films [15, 22].

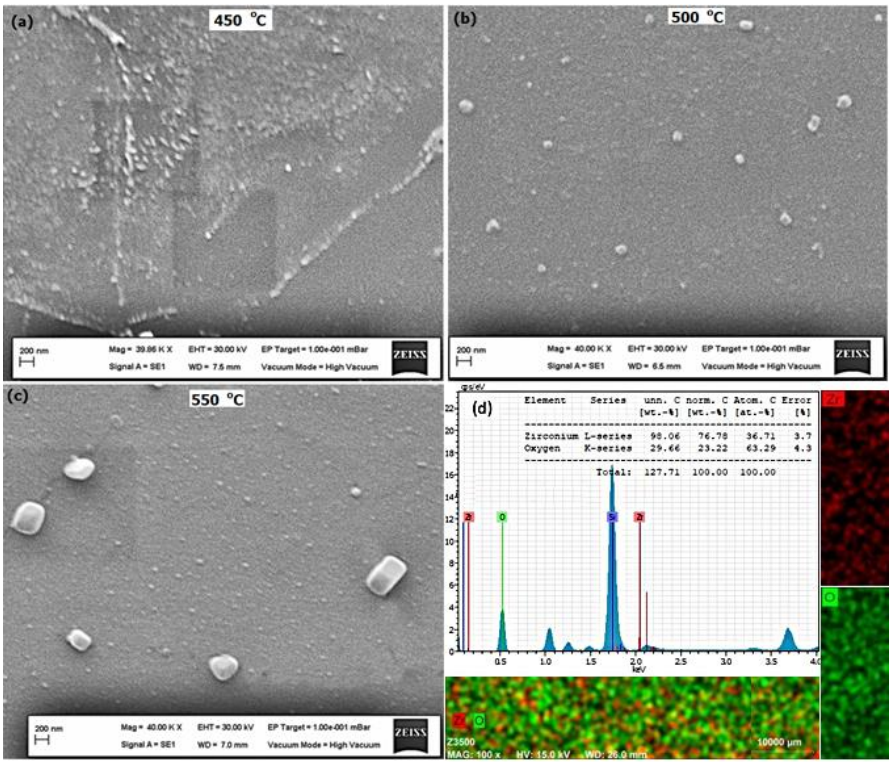

Figure 2. SEM surface images (a-c) and EDX/mapping analysis (d) of the deposited ZrO_2 nanostructures with different grain sizes

The band gap energy (E_g) of the nanostructures is found by extrapolation of the linear part of the curve between $(ah\nu)^2$ and $h\nu$ as given in Fig.3c (using equations 5, 6, and 7), indicating increment of the E_g from 3.96 to 4.24 eV with increase in grain size, accomplished by sintering process. This may be due to the increased crystallite/grain size or variation in lattice parameters of the film samples as well as the presence of the defects within the ZrO_2 lattice system [17,13].

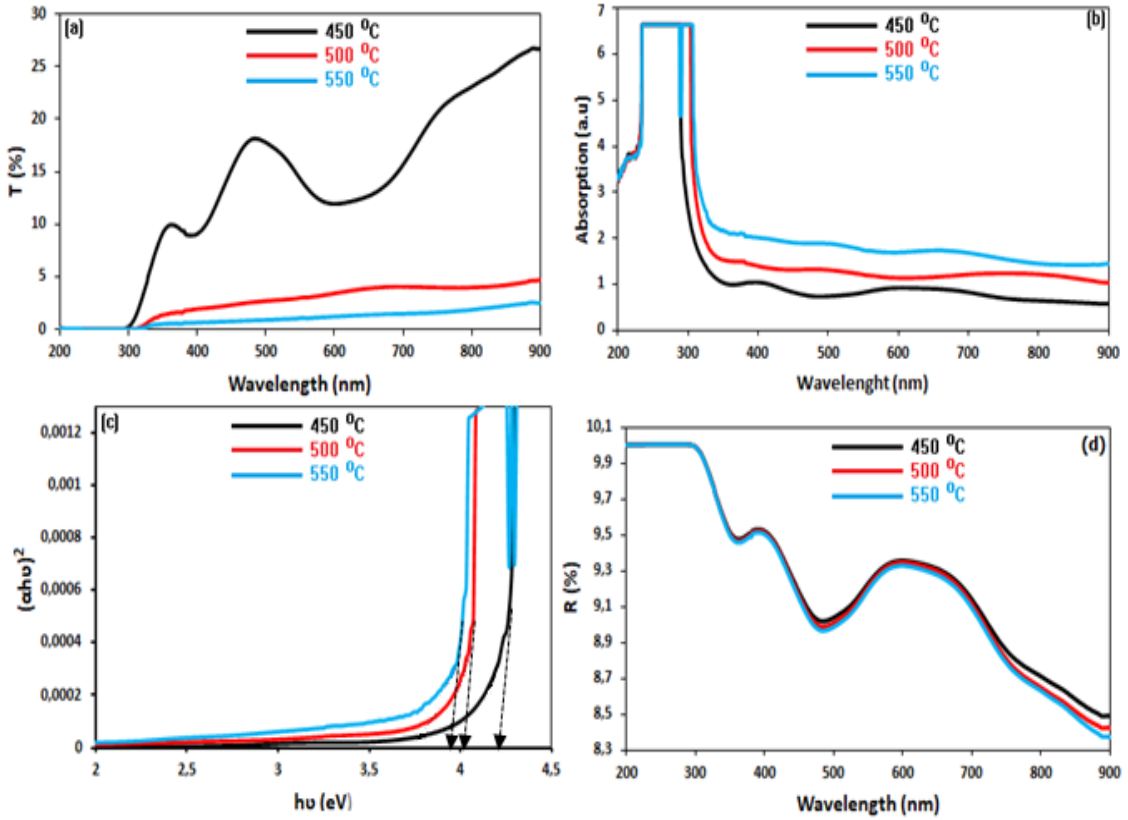

Figure 3. Transmittance (a), absorbance (b), variation of $(\alpha h\upsilon)^2$ dependent on $h\upsilon$ (c), and reflectance (d) plots of the deposited ZrO_2 nanostructures with different grain sizes

To calculate the optical constants of the presented ZrO_2 films, the reflectance has been obtained by using the relationship between the ($R=(1-T)^{1/2}*e^{\alpha}$) reflectance, absorption, and transmittance. Fig. 3d shows the plot of R upon on wavelength and annealing temperature (T_A). It shows decrement via enhanced particle size and T_A. This reduction and low values of R are mainly due to the poor transmission and relatively high absorbance as seen in Fig. 3a and b. The observations are in good agreement with previously reported studies on ZrO_2 nanostructures [13] and [15-24].

3.3.2. Determination of optical constants

It can be said that the n is one of the most main optical parameter, highly related to the electronic polarizability of ions and the internal field inside substances. On the other hand, the other important optical parameter k is closely associated to the absorbance of the matter. Their variations with the λ (200–900 nm) were presented Fig. 4 (a-b) for various grain size as determined above. The k of the film samples exhibits an enhancement with improved $D_{(hkl)}$ or G_S. These behaviors can be attributed to the α and hence absorbance as seen in Fig. 3b. Amongst all, the highest k values were observed for the ZrO_2 nanostructures having grain sizes within the range of 20-300 nm. On the contrary, the n values show opposite trend with k values, whereas it exhibits the same behavior with reflectivity. It is obvious that the n values of the ZrO_2 nanostructures decrease with increasing $D_{(hkl)}$ or G_S. Increasing or decreasing n is probably related to the compositional modifications due to the different grain sizes, which result in decrease/increase of the optical quality of the ZrO_2 nanostructures. These findings are in accordance with refs. [25] and [26].

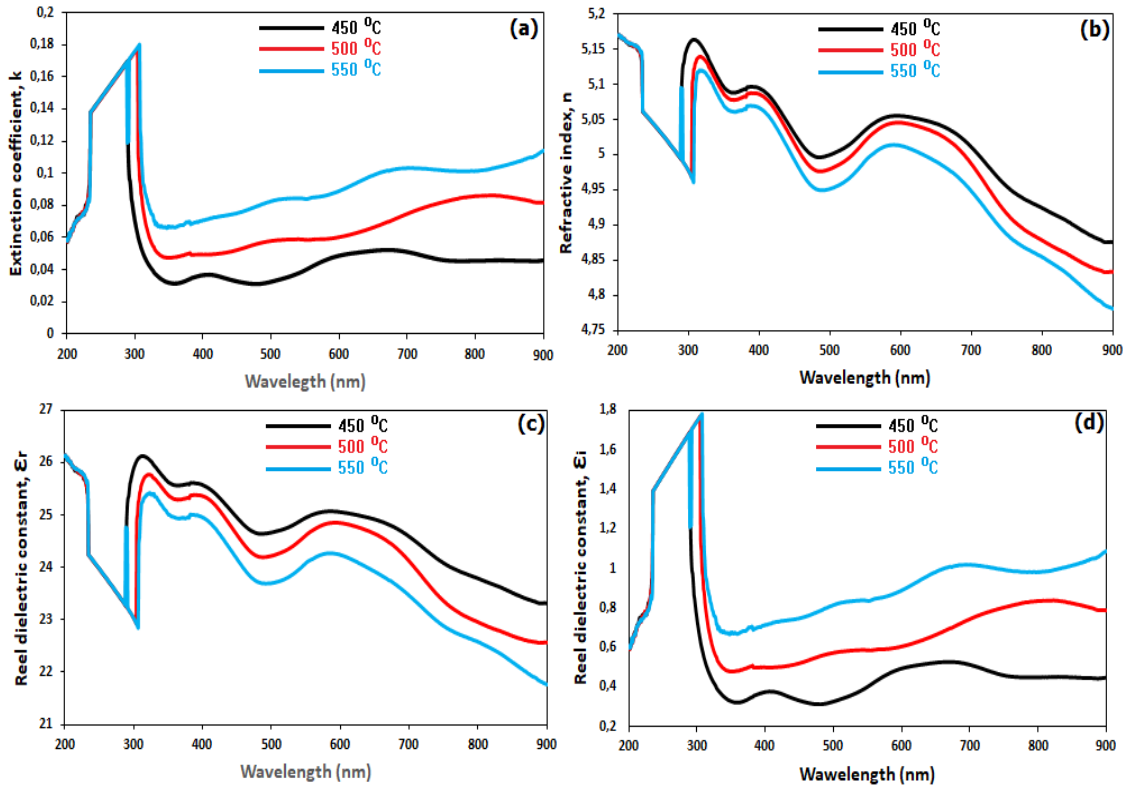

Figure 4. Wavelength depended on the extinction coefficient (a), refractive index (b), reel (c) and imaginary(d) dielectric constants of the deposited ZrO2 nanostructures with different grain sizes

It is possible to obtain reel and imaginary dielectric constants of the matter by using equations of 10 and 11 for the zirconia nanostructures. Both form the dielectric constant of the matter, representing the linear reaction of the order to action electromagnetic radiations i.e. interplay between the electrons of the structure with photons. The plots of both were given in Fig. 4c-d, with respect to the G_S and λ. As seen in these Figs., the $\mathcal{E}_r(\lambda)$values decrease, whereas the $\mathcal{E}_i(\lambda)$ values increase with increasing G_S. It is also seen that the $\mathcal{E}_r(\lambda)$values decrease by wavelength at visible region while the $\mathcal{E}_i(\lambda)$ values increase. In addition to, the trend of $\mathcal{E}_r(\lambda)$values is nearly same with the n, whereas the $\mathcal{E}_i(\lambda)$ values show the same trend with k. Moreover, $\mathcal{E}_r(\lambda)$values are higher than those of the $\mathcal{E}_i(\lambda)$ values because of their corresponding n and k values. These results can be attributed to the change in G_S carried out by sintering temperature, which leads to increase in polarizability of the system due to variant in charge imbalance, especially in the nanocrystalline structures. The observed outcomes are in good agreement with the study on ZrO_2 or oxide-based nanostructures having various G_S carried out by thickness or sintering temperatures [27,28].

Table 2. A comparison of the certain structural and optical parameters/constants of the sol-gel grown ZrO_2 thin films with the previously synthesized ZrO_2 thin films, produced by sol-gel method

GS/D_{hkl}(nm)	δx10^{-3}	ε x 10^{-3}	Eg(eV)	n (at visible range)	k (at visible range)	εr (at visible range)	Ref
(20-200)/10	10.0	30.42	3.96	5.02-5.10	0.039-0.041	24.6-25.7	This study
(30-250)/15	4.44	30.50	4.05	4.98-5.08	0.05-0.063	24.2-25.4	This study
(20-300)/21	2.26	30.52	4.24	4.95-5.07	0.071-0.098	23.4-24.9	This study
(----)/3-9.9	----	----	----	1.60-2.40	-----	-----	[31]
(----)/10.3	----	----	5.72	2.1	-----	-----	[18]
(----)/15.6	----	----	5.10	-----	-----	-----	[32]
(5-12)/---	----	----	----	-----	-----	-----	[23]

Table 2 summarizes some recent studies on ZrO_2 thin films derived by sol-gel technique. The presented characteristics and parameters are relatively superior to the previously reported studies on the ZrO_2 thin films. The observed relatively low E_g values and higher n values reflects the influences of different grain/crystallite

and used chemical precursors as well as experimental conditions. The presented study is also one of the best examples of the structural and optical properties and parameters/constant of the sol-gel derived ZrO_2 thin films at wide range of grain/crystallite size among all the considered ZrO_2 thin films, whose optical constant have not been studied in more detail yet, as given in table 2. In addition, this table also reflects the importance of the presented study accordingly [29,30].

4. Conclusions

In this study, the influences of the grain size (G_S) on the calculated structural and optical parameters and constants of the zirconia dioxide (ZrO_2) nanostructures have been investigated for the first time. The ZrO_2 nanostructures crystallized within a tetragonal phase and preferred direction onwards (111) Miller plane. Crystallite size (D_{hkl}) and orientation degree of ZrO_2 have significantly affected by G_S. As the G_S values rise the calculated structural parameters D_{hkl} increases while computed micro-strain, dislocation density, and lattice parameter values decrease. The increasing of the G_S has proved by SEM analysis, including EDX and mapping investigations, showing the existence of Zr and O elements. Uv-Vis spectrophotometer investigations show decreased absorbance while reflectance and transmittance increase with increasing G_S. The calculated band gap values increase from 3.85 to 4.05 eV by enhance of G_S. With enhanced G_S the opposite trend has been observed in the refractive index and the extinction coefficient values. Amongst all the highest refractive index values have been detected for the lowest G_S distribution, whereas the lowest extinction coefficient values have been determined. Like the refractive index values, the reel dielectric constant values of the ZrO_2 have also shown the same behavior, while the imaginer dielectric constant values show the same trend with the extinction coefficient values. The observed variants are possibly because of the disparity in crystallite/grain size, nanostructure, polarizability, and packing density of the ZrO_2 nanostructures. These findings are in good agreement with those issued on ZrO_2 nanostructures produced by various methods. In addition to, this research is the first record of the effects of G_S on the computed structural and optical parameters and constants of ZrO_2 synthesized by sol–gel dip-coating technique, relatively the most practical and economical process to fabricate nanostructured materials used for the number of demands in the next dielectric and optic applications.

Acknowledgments

The authors are grateful to thin film research group led by Prof. Dr. Abdullah GÖKTAŞ, Department of Physics, Faculty of Arts and Science to guide the authors during this scientific research at Harran University/TURKEY.

Conflict of Interest Statement

The authors declare that there is no conflict of interest.

References

[1] A. V. Rudakova, Alexei V. Emeline, Kirill M. Bulanin, Lyudmila V. Chistyakova, Maria V. Maevskaya and Detlef W. Bahnemann, "Self-cleaning properties of zirconium dioxide thin films," *Journal of Photochemistry & Photobiology A: Chemistry*, vol. 367, pp. 397–405, 2018. doi:10.1016/j.jphotochem.2018.08.037

[2] S. Goktas, A. Tumbul and A. Goktas, "Growth Technique–Induced Highly C-Axis-Oriented ZnO: Mn, ZnO: Fe and ZnO: Co Thin Films: A Comparison of Nanostructure, Surface Morphology, Optical Band Gap, and Room Temperature Ferromagnetism," *Journal of Superconductivity and Novel Magnetism*, vol. 36, pp. 1875–1892, 2023. doi:10.1007/s10948-023-06630-4

[3] S. Park, J.M. Vohs and R.J. Gorte, "Direct oxidation of hydrocarbons in a solid-oxide fuel cell," *Nature*, vol. 404, no. 6775, pp. 265-267, 2000. doi:10.1038/35005040

[4] S. Sultana, M.Z. Khan, K. Umar and M. Muneer, "Electrical, thermal, photocatalytic and antibacterial studies of metallic oxide nanocomposite doped polyaniline," *Journal of Materials Science & Technology*, vol. 29, no. 9, pp. 795–800, 2013. doi:10.1016/j.jmst.2013.06.001

[5] C-Y. Lin, C-Y. Wu, C-Y. Wu, T-C. Lee, F-L. Yang, C. Hu and T-Y. Tseng, "Effect of top electrode material on resistive switching properties of ZrO2 film memory devices," *IEEE Electron Device Letters*, vol. 28, no. 5, pp. 366–368, 2007. doi:10.1109/LED.2007.894652

[6] B. Coskun, T. Asar, U. Akgul, K. Yildiz and Y. Atici, "Investigation of structural and electrical properties of Zirconium dioxide thin films deposited by reactive RF sputtering technique," *Ferroelectrics*, vol. 502, no. 1, pp. 147-158, 2016. doi:10.1080/00150193.2016.1235453

[7] M. T. Soo, G. Kawamura, H. Muto, A. Matsuda, Z. Lockman and K. Y. Cheong, "Design of hierarchically meso–macroporous tetragonal ZrO2 thin films with tunable thickness by spin-coating via sol–gel template route," *Microporous and Mesoporous Materials*, vol. 167, pp. 198–206, 2013. doi:10.1016/j.micromeso.2012.09.010

[8] L. Liu, C. Li, Y. Chen, X. Zhang, L. Li and Y. Wang, "Phase transformation of ZrO2 nanocrystals induced by Li+," *Materials Letters*, vol. 79, pp. 75–77, 2012. doi:10.1016/j.matlet.2012.03.112

[9] S. Tekeli and U. Demir, "Colloidal processing, sintering and static grain growth behavior of alumina-doped cubic zirconia," *Ceramics International*, vol. 31, no. 7, pp. 973-980, 2005. doi:10.1016/j.ceramint.2004.10.011

[10] S.K. Durrani, J. Akhtar, M. Ahmad and M.A. Hussain, "Synthesis and characterization of low density calcia stabilized zirconia ceramic for high temperature furnace application," *Materials Chemistry and Physics*, vol. 100, no. 2–3, pp. 324-328, 2006. doi:10.1016/j.matchemphys.2006.01.010

[11] O. Bernard, A.M. Huntz, M. Andrieux, W. Seiler, V. Ji and S. Poissonnet, "Synthesis, structure, microstructure and mechanical characteristics of MOCVD deposited zirconia films," *Applied Surface Science*, vol. 253, no. 10, pp. 4626-4640, 2007. doi:10.1016/j.apsusc.2006.10.025

[12] M. Mishra, P. Kuppusami, A. Singh, S. Ramya, V. Sivasubramanian, E. Mohandas, "Phase evolution in zirconia thin films prepared by pulsed laser deposition," *Applied Surface Science*, vol. 258, no.12, pp. 5157–5165, 2012. doi:10.1016/j.apsusc.2012.01.160

[13] D.Q. Xiao, G. He, P. Jin, J. Gao, J.W. Zhang, X.F. Chen, C.Y. Zheng, M. Zhang and Z.Q. Sun, "Effects of boron incorporation on the structural, optical and electrical properties of sol-gel-derived ZrO2 gate dielectrics," *Journal of Alloys and Compounds*, vol. 649, pp. 1273-1279, 2015. doi:10.1016/j.jallcom.2015.07.210

[14] H.P. Jee, B.Y. Young, H.L. Keun, S.J. Woo, Y.O. Jin, S.C. Soo, W.L. Hyun, W.H. Sun and K.B. Hong, "Boron-doped peroxo-zirconium oxide dielectric for high-performance, low-temperature, solution-processed indium oxide thin-film transistor," ACS applied materials \& interfaces, vol.5, no. 16, pp.8067-8075, 2013. doi:10.1021/am402153g

[15] V. S. Anitha, S. S. Lekshmy and K. Joy, "Effect of annealing temperature on optical and electrical properties of ZrO2–SnO2 nanocomposite thin films," *Journal of Materials Science: Materials in Electronics*, vol. 24, pp. 4340–4345, 2013. doi:10.1007/s10854-013-1408-7

[16] A. Goktas, F. Aslan and İ.H. Mutlu, "Annealing effect on the characteristics of $La_{0.67}Sr_{0.33}MnO_3$ polycrystalline thin films produced by the sol–gel dip-coating process," *Journal of Materials Science: Materials in Electronics*, vol. 23, pp. 605–611, 2012. doi:10.1007/s10854-011-0448-0

[17] I. J. Berlin, S. S. Lekshmy, V. Ganesan, P.V. Thomas and K. Joy, "Effect of Mn doping on the structural and optical properties of ZrO_2 thin films prepared by sol–gel method," *Thin Solid Films*, vol. 550, pp. 199-205, 2014. doi:10.1016/j.tsf.2013.10.164

[18] A. Goktas, F. Aslan, A. Tumbul and S. Gunduz, "Tuning of structural, optical and dielectric constants by various transition metal doping in ZnO:TM (TM=Mn, Co, Fe) nanostructured thin films: A comparative study," *Ceramics International*, vol. 43, no. 1, pp. 704-713, 2017. doi:10.1016/j.ceramint.2016.09.217

[19] A. Goktas, I. H. Mutlu and Y. Yamada, "Influence of Fe-doping on the structural, optical, and magnetic properties of ZnO thin films prepared by sol–gel method," *Superlattices and Microstructures*, vol. 57, pp. 139-149, 2013. doi:10.1016/j.spmi.2013.02.010

[20] A. Méndez-López, O. Zelaya-Ángel, M. Toledano-Ayala, I. Torres-Pacheco, J. F. Pérez-Robles and Y. J. Acosta-Silva, "The Influence of Annealing Temperature on the Structural and Optical Properties of ZrO2 Thin Films and How Affects the Hydrophilicity," Crystals, vol. 10, no. 6, pp. 454. 2020. doi:10.3390/cryst10060454

[21] H. Gencer, A. Goktas, M. Gunes, H.I. Mutlu and S. Atalay, "Electrical Transport and Magnetoresistance Properties of La0.67Ca0.33MnO3 Film Coated On Pyrex Glass Substrate," *International Journal of Modern Physics B*, vol. 22, no. 05, pp. 497-506, 2008. doi:10.1142/S0217979208038776

[22] Y. Mansilla, M. D. Arce, C. González-Oliver, J. Basbus, H. Troiani and A. Serquis, "Characterization of stabilized ZrO_2 thin films obtained by sol-gel method," *Applied Surface Science*, vol. 569, pp. 150787, 2021. doi:10.1016/j.apsusc.2021.150787

[23] A. Göktaş, A. Tumbul, F. Aslan, "Grain size-induced structural, magnetic and magnetoresistance properties of $Nd_{0.67}Ca_{0.33}MnO_3$ nanocrystalline thin films," *Journal of Sol-Gel Science and Technology*, vol. 78, pp. 262–269, 2016. doi:10.1007/s10971-016-3960-0

[24] F. Mikailzade, F. Önal, M. Maksutoglu, M. Zarbali and A. Göktaş, "Structure and Magnetization of Polycrystalline $La_{0.66}Ca_{0.33}MnO_3$ and $La_{0.66}Ba_{0.33}MnO_3$ Films Prepared Using Sol-Gel Technique," *Journal of Superconductivity and Novel Magnetism*, vol. 31, pp. 4141–4145, 2018. doi:10.1007/s10948-018-4683-y

[25] M. Boulouz, L. Martin, A. Boulouz and A. Boyer, "Effect of the dopant content on the physical properties of Y_2O_3–ZrO2 and CaO–ZrO_2 thin films produced by evaporation and sputtering techniques," *Materials Science and Engineering: B*, vol. 67, no. 3, pp. 122-131, 1999. doi:10.1016/S0921-5107(99)00338-4

[26] W.T. Tang, Z.F. Ying, Z.G. Hu, W.W. Li, J. Sun, N. Xu and J.D. Wu, "Synthesis and characterization of HfO_2 and ZrO_2 thin films deposited by plasma assisted reactive pulsed laser deposition at low temperature," *Thin Solid Films*, vol. 518, no. 19, pp. 5442-5446, 2010. doi:10.1016/j.tsf.2010.04.012

[27] D. Tahir, E. Kyoung Lee, S. Kun Oh, H. Jae Kang, S. Heo, J. Gwan Chung, J. Cheol Lee and S. Tougaard, "Dielectric and optical properties of Zr silicate thin films grown on Si (100) by atomic layer deposition," *Journal of Applied Physics*, vol. 106, no. 8, pp. 084108-14, 2009. doi:10.1063/1.3246612

[28] A. Goktas, F. Aslan, B. Yeşilata and İ. Boz, "Physical properties of solution processable n-type Fe and Al co-doped ZnO nanostructured thin films: Role of Al doping levels and annealing," *Materials Science in Semiconductor Processing*, vol. 75, pp. 221-233, 2018. doi:10.1016/j.mssp.2017.11.033

[29] M. T. Soo, N. Prastomo, A. Matsuda, G. Kawamura, H. Muto, A. F. M. Noor, Z. Lockman and K. Y. Cheong, "Elaboration and characterization of sol–gel derived ZrO_2 thin films treated with hot water," *Applied Surface Science*, vol. 258, no. 13, pp. 5250-5258, 2012. doi:10.1016/j.apsusc.2012.02.008

[30] S. Chang and R. Doong, "The Effect of Chemical States of Dopants on the Microstructures and Band Gaps of Metal-Doped ZrO_2 Thin Films at Different Temperatures," *The Journal of Physical Chemistry B*, vol. 108, no. 46, pp. 18098-18103, 2004. doi:10.1021/jp047440n

This is an open access article under the CC-BY license

Research Article/Araştırma Makalesi

Gazi AKADEMİK YAYINCILIK

GAZİ
JOURNAL OF ENGINEERING SCIENCES

Calculations of Structural Parameters and Optical Constants of Size Dependent ZrO_2

Gülsen Şahin[*a], Sultan Göktaş[b]

Submitted: 23.10.2023 Revised: 21.12.2024 Accepted: 01.03.2024 doi:10.30855/gmbd.0705N10

ABSTRACT

In this study, structural parameters and optical constants of size dependent zirconium dioxide (ZrO_2) nanostructures were calculated. The effect of particle size was investigated on the calculated structural and optical parameters/constants. ZrO_2 nanostructures were produced by chemical route. To change the grain size of the ZrO_2 nanostructures, different annealing temperatures (450-550 °C) were applied. The x-ray diffraction (XRD), scanning electron microscope (SEM), and ultraviolet/visible region (UV-Vis) spectroscopy measurement results were used to calculate the structural and optical parameters/constants. The results of XRD measurement showed the ZrO_2 nanostructures were crystallized in single tetragonal (cubic) ZrO_2 phase. SEM results exhibited dense and homogeneous surfaces and enhanced surface grains with increased annealing temperature. The compositional formation of ZrO_2 nanostructures were proved by electron dissipated x-ray and mapping analysis. Optical measurements were strongly changed dependent on the grain size (G_S). The calculated structural parameters such as crystallite size, lattice parameter (a), microstrain, and dislocation density were showed that the powerful variation according to the G_S. The computed optical constants such as refractive index, extinction coefficient, reel and imaginer dielectric constants of the ZrO_2 samples were highly varied upon the G_S. The variant in these calculated parameters/constant were extremely promising for the optic and dielectric applications.

Keywords: ZrO_2, Optical constant, Extinction coefficient, Refractive index, Reel dielectric constant

[a,*] Adıyaman University, Faculty of Education, Department of Science
02040 - Adıyaman, Türkiye
Orcid: 0000-0003-4891-041X
e mail: gsahin@adiyaman.edu.tr

[b] Harran University, Faculty of Science and Arts, Department of Chemistry
63290 - Şanlıurfa, Türkiye
Orcid: 0009-0000-7084-9710

*Corresponding author:
gsahin@adiyaman.edu.tr

Büyüklüğe Bağlı Zro_2 Nanoyapılarının Yapısal Parametreleri ve Optiksel Sabitlerinin Hesaplanması

ÖZ

Bu çalışmada boyuta bağlı zirkonyum dioksit (ZrO_2) nanoyapılarının yapısal parametreleri ve optik sabitleri hesaplanmıştır. Parçacık boyutunun, hesaplanan yapısal ve optik parametreler/sabitler üzerindeki etkisi araştırıldı. ZrO_2 nanoyapıları kimyasal yolla üretildi. ZrO_2 nanoyapılarının tane boyutunu değiştirmek için farklı tavlama sıcaklıkları (450-550°C) uygulandı. Yapısal ve optik parametreleri/sabitleri hesaplamak için x-ışını kırınımı (XRD), taramalı elektron mikroskobu (SEM) ve ultraviyole/görünür bölge (UV-Vis) spektroskopisi ölçüm sonuçları kullanıldı. XRD ölçümü sonuçları, ZrO_2 nanoyapılarının tek tetragonal (kübik) ZrO_2 fazında kristalleştiğini gösterdi. SEM sonuçları, yoğun ve homojen yüzeyler ve artan tavlama sıcaklığıyla sayısı artan yüzey taneleri sergiledi. ZrO_2 nanoyapılarının bileşiksel oluşumu elektron dağılımlı x-ışını ve haritalama analizi ile kanıtlanmıştır. Optik ölçümler tane boyutuna (G_S) göre büyük ölçüde değişti. Kristal boyutu, örgü parametresi (a), mikro-gerilim ve dislokasyon yoğunluğu gibi hesaplanan yapısal parametreler, G_S'ye bağlı olarak ciddi bir değişim gösterdi. ZrO_2 numunelerinin kırılma indisi, sönüm katsayısı, reel ve sanal dielektrik sabitleri gibi hesaplanan optik sabitleri G_S'ye bağımlı olarak ciddi oranda değişti. Hesaplanan bu parametrelerdeki/sabitlerdeki değişkenlik, optik ve dielektrik uygulamalar için son derece umut vericidir.

Anahtar Kelimeler: ZrO_2, Optiksel sabit, Yok olma katsayısı, Kırılma indisi, Reel dielektrik katsayısı

To cite this article: G. Sahin and S. Goktas "Calculation of Structural Paramaters and Optical Constants of Size Dependent ZrO_2," *Gazi Journal of Engineering Sciences*, vol.10, no.1, pp. 114-124, 2024. doi:10.30855/gmbd.0705N10

1. Introduction

In many practical applications, it is possible to make life easier by using nanostructured thin films. They can be preferred for making reflective or antireflective filters, circuit candidates, memory disks, memory disc, biological ceramics, sensors, and lasers [1-5]. In this context, attractive physical characteristics of Zirconia (ZrO_2) thin film such as having a high dielectric constant, a relatively higher melting point (2680°C), high chemical stability and wide band gap (4.7eV-7.8eV), make it extraordinary metal oxide semiconductors [6]. In addition to, its high thermal stability, high refractive index, and low thermal conductivity capacities lead to be commercially used as dielectric and insulator in various microelectronic applications viz. dynamic random-access memory, radio frequency, analog/mixed signal (RF/AMS) integrated circuits, and non-volatile resistive random-access memory [3,5].

It was reported that ZrO_2 could have different crystal-like phases such as monoclinic, tetragonal, and cubic dependent on high temperature reflecting polymorphic structure [7,8]. However, this high temperature phases can be maintained at room temperature using suitable oxide dopants [9-11]. Even for the pure ZrO_2 thin films it can be achieved owing to low crystallite size and compressive stress [12]. But the undoped ZrO_2 has deteriorated by some consequential issues. The small crystallization due to low temperature processing resulted in the enhanced additional leakage currents through the crystal boundaries and creating highly thick intersectional sheets [13]. In addition to, producing high dielectric constant (κ) metal oxide nanostructured thin films utilizing chemical solution-based method needs a relatively high sintering temperature of over 450 °C due to high pyrolysis and desiccation temperature of prototypical forerunners [14]. Annealing at relatively high temperatures is an effectual way to remove the defects (like oxygen vacancies) and impurities (like secondary phases) from metal-based oxide nanomaterials resulting into tolerable discharge and electrical capacity as well as high crystallization [15,16].

Recently, several fabrication of nanostructured thin films have been followed to product zirconia-based high-κ gate dielectric viz. sol-gel dip/spin coating, atomic layer deposition, spray pyrolysis, chemical vapor deposition, reactive RF sputtering, and electron beam evaporation [13,17]. Amongest all the solution-based sol-gel technique is currently becoming the most popular route owing to its clarity, economic, low treating temperature, practical use, and pile of yield. Some concern study has been outlined about the size dependent characteristics of sol-gel derived ZrO_2 thin films. However, a detailed work on the structural and optical properties, structural parameters, and linear optical constants of the ZrO_2 is rare. Therefore, in the present study the grain size dependent structural and optical characteristics, structural parameters and optical constants have been investigated.

2. Experiment and Calculation Techniques

To prepare ZrO_2 solution, zirconyl chloride octahydrate ($ZrOCl_2 \cdot 8H_2O$) was used for the parent solution. The molar ratio (0.01M) of chemical powder was utilized as Zr^{+2} source and it was dissolved by mixed solution of methanol (96,15 at. %) and glacial acetic acid (3,85 at .%). The desired ZrO_2 solution was get ready via vigorously mixing on the magnetic stirrer for 30-60 minutes at 50 °C. The final solution bath was aged by stirring at room conditions for 24 hours to have gel solution, which is essential for highly uniform film structure. Before coating, the glass facets were rinsed with deionized water. It was then ultrasonically cleaned in an ethanol and acetone ultrasonic bath for 5 minutes. In cleaning process, the glass surfaces were finally placed in the plasma cleaner to remove waste organic hanging bonds and precision cleaning. The cleaned glass substrates were immersed in the resulting solution and covered in air at 350°C. Films grown on the glass surfaces by sol-gel dip coating method and they were annealed at 450 °C, 500 °C and 550°C for 60 minutes in an air atmosphere to get desired grain size (G_S).

The latest emerging ZrO_2 thin films were constructionaly characterized via X-ray diffraction (XRD) with a Rigaku Ultima III diffractometer though employing CuK_α radiation (λ =0.15406 nm) at 30 mA and 40 keV from 20 to 70°. To calculate the average crystallite size (D_{hkl}), [13] the Debye Sherrer's equation as following as:

$$D_{hkl}=0.9\lambda/\beta.cos\theta \quad (1)$$

where λ is the wavelength of X-rays used, θ is the angle of diffraction and is the full width at half maximum. Similarly the other structural parameters like dislocation density (δ) and micro strain (ε) were computed according to the followed formulas:

$$\delta = 1/(D_{hkl})^2 \quad (2)$$

$$\varepsilon = \beta/4\tan\theta \quad (3)$$

The lattice parameters, a and c of the tetragonal ZrO_2 can be obtained according to the equations given below:

$$a_t=d_{h00}\ h;\ c_t=d_{h0l}\ (h^2+l^2)^{1/2} \quad (4)$$

In this equation the d_{hkl} ($d_{hkl}=a_t/((h^2+k^2+l^2)/(c_t/a_t))^{1/2}$) represents interplanar distance for the tetragonal lattice and (hkl) shows Miller indices. The morphology, surface, grain size, and atomic analysis and mapping were recognized using a scanning electron microscope (SEM) equipped by an energy dispersive X-ray (EDX) tool.

To research the optical characteristics like transmittance and absorbance, the UV–Vis (PerkinElmer 45) spectra was performed. The corresponding transmittance, absorbance and reflectance were than represented and the band gap energy (E_g), refractive index (n), extinction coefficient (k), and reel/imaginer dielectric constants were computed. To calculate E_g and k as well as other related parameters of the nanostructures Beer-Lambert law [17] was used as following:

$$I=I_0e^{-\alpha d} \quad (5)$$

where I is the intensity of the transmitted light, I_0 is the intensity of the incident light, d shows the thickness of the nanostructured layer, and α is the linear absorption coefficient of the materials. In equation (5) α can be calculated as [18]:

$$\alpha = (1/d)\ ln\ (1/T) \quad (6)$$

in that T is the transmittance. The connection between the α and the photon energy ($h\upsilon$) is given as follows [19]:

$$(\alpha h\upsilon)^2 = A(h\upsilon - E_g)^m \quad (7)$$

where A and m are constant coefficients. For indirect transitions, m=2 and for direct transitions n=1/2. Moreover, k and n can be obtained by using reflectance (R) and α as given in equation of (8) and (9) as below [20]:

$$k\ (\lambda)=\alpha\lambda/4\pi \quad (8)$$

$$n(\lambda)= ((1+R(\lambda))/(1-R(\lambda)))+((4R(\lambda))/(1+R(\lambda)-k^2(\lambda))^{1/2} \quad (9)$$

where λ represents of the acted photon wavelength. Finally, the corresponding reel and imaginary dielectric

constants $\mathcal{E}_r$ and $\mathcal{E}_i$ are calculated via using the followed equations [19]:

$$\mathcal{E}_r(\lambda)=n(\lambda)^2-k(\lambda)^2 \quad (10)$$

$$\mathcal{E}_i(\lambda)=2n(\lambda)k(\lambda) \quad (11)$$

3. Results and Discussions

3.1. Calculation of structural parameters by using XRD analysis

The XRD analysis was used to investigate the crystal structure and phase composition of the deposited nanostructures. The XRD patterns of the ZrO_2 nanostructures sintered at 450 °C, 500 °C, and 550°C were given in Fig.1. All nanostructured films show the tetragonal phase with highly oriented (101) Miller crystal plane and polycrystalline nature. The observed other (110), (112), and (211) Miller crystal planes are also indexed for the tetragonal phase. XRD patterns also show there are no metallic or secondary phases in the host ZrO_2 lattice system. The results agree with the research on ZrO_2 thin film [18]. According to Fig. 1, the ZrO_2 nanostructures represent the best crystallization at 550 °C. The average crystallite size (D_{hkl}) [13] calculated using the Debye Sherrer's equation (1) was given in Table 1. The mean D_{hkl} for thin film samples turned out to be 21 nm.

Table 1. The full-width half-maximum, diffraction angle, crystallite size, dislocation density, micro-strain, and lattice parameter of the prepared ZrO_2 nanostructures having various grain sizes

Annealing temperature (°C)	FWHM (β_o)	2θ(deg.)	D_{hkl}(nm)	δx10^{-3}	Ɛx10^{-3}	a;c (Å)
Z3-450	0.80	30.42	10	10.0	12.8	0.5106;5.076
Z3-500	0.53	30.50	15	4.44	8.48	0.5092;5.063
Z3-550	0.38	30.52	21	2.26	6.08	0.5089;5.060

To obtain better crystalline quality, namely increased crystallite size, by providing crystallization in ZrO_2 thin film samples, annealing was done at different temperatures. Figure 1 shows the XRD patterns of ZrO_2 thin film samples annealed at different temperatures. Among all samples, the ZrO_2 nanostructure sintered at 550 °C has the best crystalline quality.

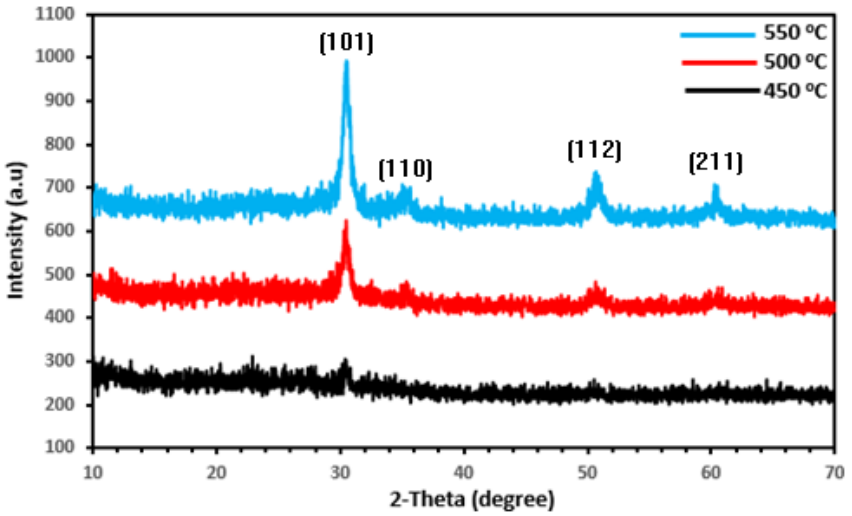

Figure 1. XRD patterns of the deposited ZrO_2 nanostructures with different grain sizes

The calculated D_{hkl} increases with increasing annealing temperature (Table 1). Considering the analysis of nanostructured ZrO_2 thin films prepared at different operating temperatures by Deshmukh and Bari's spray pyrolysis technique; they found that the structure of the film was completely crystallized with an increase in annealing temperature. Additionally, grain growth increased in mobility with increasing temperature. Again, when the literature on the effect of annealing temperature was scanned, it was seen that; Hadi et al., annealed and analyzed the Li doped (ZrO_2) nanostructures produced using the spray pyrolysis (CSP) method at 300^{O}C, 400^{O}C, and 500^{O}C. As a result, they observed that the grain size values, average roughness increased with increasing in sintering temperature. The lattice parameters, *a and c* of the ZrO_2 nanostructures calculated (by using formula 4) for different annealing temperatures (for 450 ^{o}C -550^{o}C) were obtained as in Table 1. It was observed that the *a* and *c* values decreased as the $D_{(hkl)}$ increased. Different ionic sizes in lattice defects, perfect arrangement of atoms, impurity formations can cause differences in *a* and *c* values (see Table 1) dislocation density, (see equation 2), and micro strain (formula 3) as obtained. Different values of δ and Ɛ in Table 1 confirm the variation in lattice parameters. The difference in the lattice parameters, *a* and *c* may also be due to the lattice mismatch between the ZrO_2 nanostructures and the glass sample holder [21-24].

3.2. Estimation of average grain size from SEM analysis

SEM images and EDX/mapping analysis of ZrO_2 nanostructures produced at different annealing temperatures were shown in Figs. 2a-d. The film surfaces have smooth and dense morphology. The grain sizes changes about 20-200 nm, 30-250 nm, and 20-300 nm were estimated for the ZrO_2 nanostructures sintered at temperature range of 450 ^{o}C, 500 ^{o}C, and 550 ^{o}C, respectively. This result is highly agreement with the XRD analysis. Spherical-like grains were observed for the ZrO_2 nanostructures annealed at different temperatures of 450 ^{o}C, 500 ^{o}C and 550 ^{o}C. As a result of thermal energy leading simple displacement of atoms and anisotropic aggregation of crystallites/grains; As seen in Figure 2, annealing temperature affects G_S. The particle or G_S of the nanostructured films increases due to annealing process. Méndez-López et al. [20] prepared ZrO_2 nanostructures by sol-gel dip coating method and investigated the effect of annealing temperature on the structural and optical properties of the ZrO_2 nanostructures. The SEM facet patterns of their nanostructures annealed at 450^{o}C, and 550^{o}C showed the increased G_S of ZrO_2 nanostructures with increasing sintering temperature (Figs. 2a-c). AISI 316L stainless steel was coated with nanostructured zirconia using the sucrose-supported sol-gel dip coating method by Mishra et al. [15]. As a result of SEM analysis, it was seen that the particle sizes of zirconia thin films increased dependent on enhanced sintering temperature, raised from 300 ^{o}C to 650 ^{o}C. The presence of the Zr and O was observed from the EDX and mapping analysis (red and green colors represent the Zr and O atom, respectively) as seen in Fig. 2d.

3.3. Calculation of optical parameters and constants

3.3.1. Determination of optical band gap and reflectance

Optical transmittance and absorbance spectrum of the prepared nanostructured ZrO_2 film samples were exhibited in Figs. 3a and b for the wavelength range of 200-900 nm. As seen in Fig.3a, the transmittance suddenly reduces as the particle size increases. On the other hand, the opposite trend has been observed as expected for the absorbance of the nanostructured ZrO_2 films. The sharp reduction in certain wavelengths and oscillations in Uv-Vis spectrums show homogeneity and quality
of the fabricated films [15, 22].

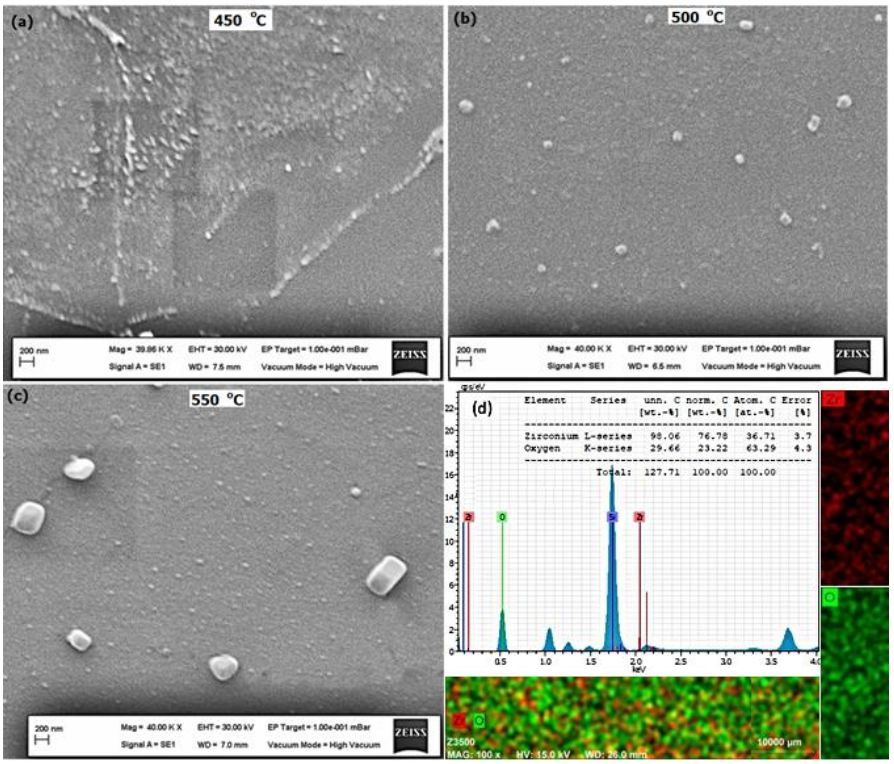

Figure 2. SEM surface images (a-c) and EDX/mapping analysis (d) of the deposited ZrO_2 nanostructures with different grain sizes

The band gap energy (E_g) of the nanostructures is found by extrapolation of the linear part of the curve between $(ah\nu)^2$ and $h\nu$ as given in Fig.3c (using equations 5, 6, and 7), indicating increment of the E_g from 3.96 to 4.24 eV with increase in grain size, accomplished by sintering process. This may be due to the increased crystallite/grain size or variation in lattice parameters of the film samples as well as the presence of the defects within the ZrO_2 lattice system [17,13].

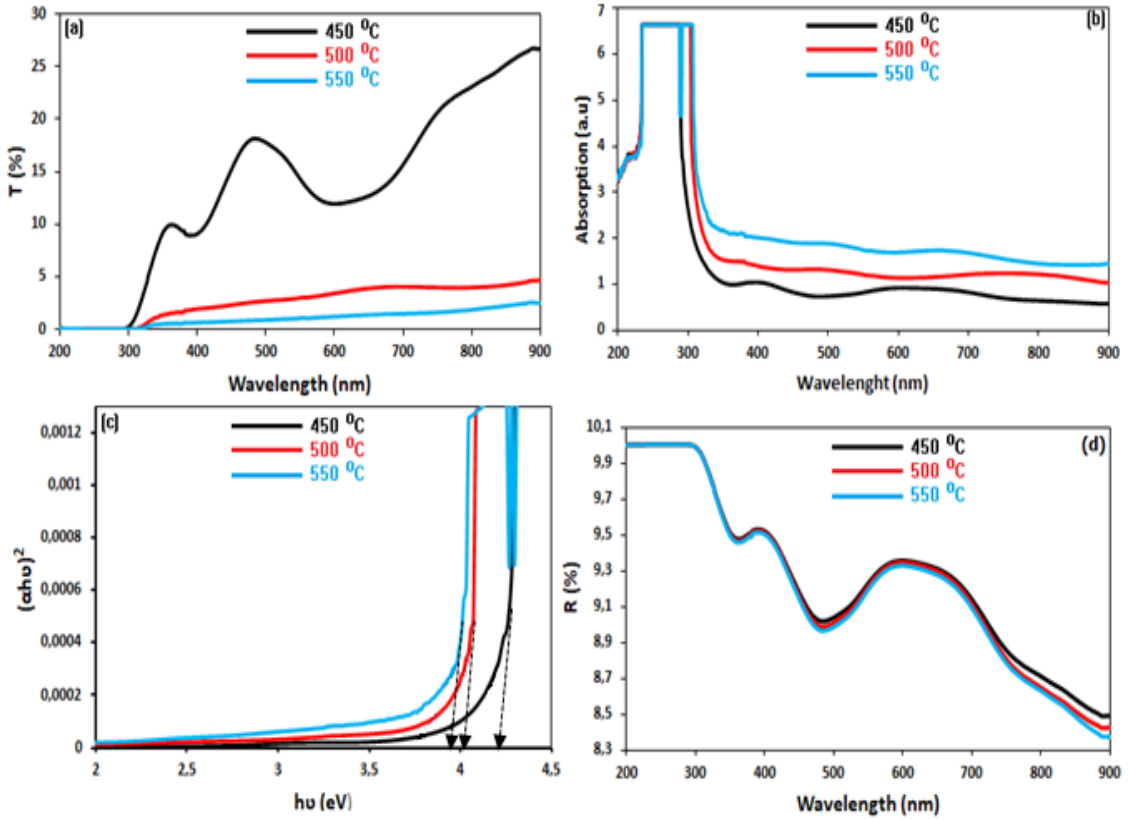

Figure 3. Transmittance (a), absorbance (b), variation of $(\alpha h\upsilon)^2$ dependent on $h\upsilon$ (c), and reflectance (d) plots of the deposited ZrO_2 nanostructures with different grain sizes

To calculate the optical constants of the presented ZrO_2 films, the reflectance has been obtained by using the relationship between the ($R=(1-T)^{1/2}*e^{\alpha}$) reflectance, absorption, and transmittance. Fig. 3d shows the plot of R upon on wavelength and annealing temperature (T_A). It shows decrement via enhanced particle size and T_A. This reduction and low values of R are mainly due to the poor transmission and relatively high absorbance as seen in Fig. 3a and b. The observations are in good agreement with previously reported studies on ZrO_2 nanostructures [13] and [15-24].

3.3.2. Determination of optical constants

It can be said that the n is one of the most main optical parameter, highly related to the electronic polarizability of ions and the internal field inside substances. On the other hand, the other important optical parameter k is closely associated to the absorbance of the matter. Their variations with the λ (200–900 nm) were presented Fig. 4 (a-b) for various grain size as determined above. The k of the film samples exhibits an enhancement with improved $D_{(hkl)}$ or G_S. These behaviors can be attributed to the α and hence absorbance as seen in Fig. 3b. Amongst all, the highest k values were observed for the ZrO_2 nanostructures having grain sizes within the range of 20-300 nm. On the contrary, the n values show opposite trend with k values, whereas it exhibits the same behavior with reflectivity. It is obvious that the n values of the ZrO_2 nanostructures decrease with increasing $D_{(hkl)}$ or G_S. Increasing or decreasing n is probably related to the compositional modifications due to the different grain sizes, which result in decrease/increase of the optical quality of the ZrO_2 nanostructures. These findings are in accordance with refs. [25] and [26].

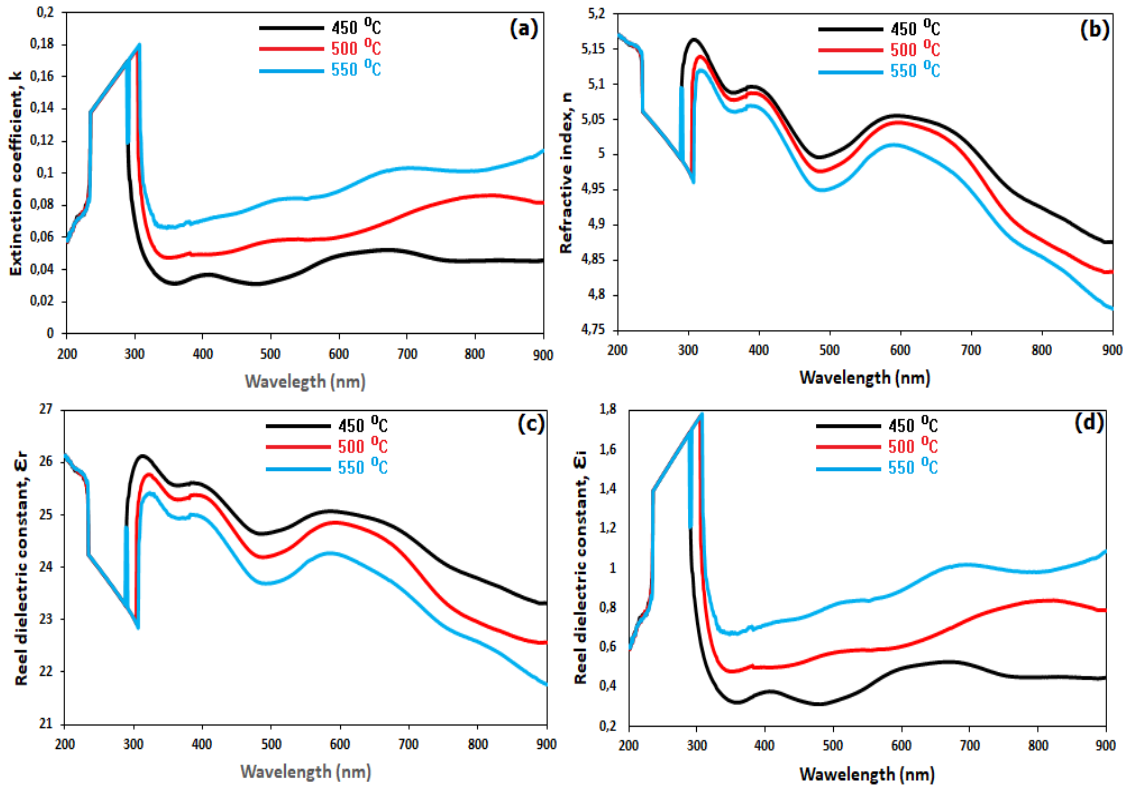

Figure 4. Wavelength depended on the extinction coefficient (a), refractive index (b), reel (c) and imaginary(d) dielectric constants of the deposited ZrO2 nanostructures with different grain sizes

It is possible to obtain reel and imaginary dielectric constants of the matter by using equations of 10 and 11 for the zirconia nanostructures. Both form the dielectric constant of the matter, representing the linear reaction of the order to action electromagnetic radiations i.e. interplay between the electrons of the structure with photons. The plots of both were given in Fig. 4c-d, with respect to the G_S and λ. As seen in these Figs., the $\mathcal{E}_r(\lambda)$values decrease, whereas the $\mathcal{E}_i(\lambda)$ values increase with increasing G_S. It is also seen that the $\mathcal{E}_r(\lambda)$values decrease by wavelength at visible region while the $\mathcal{E}_i(\lambda)$ values increase. In addition to, the trend of $\mathcal{E}_r(\lambda)$values is nearly same with the n, whereas the $\mathcal{E}_i(\lambda)$ values show the same trend with k. Moreover, $\mathcal{E}_r(\lambda)$values are higher than those of the $\mathcal{E}_i(\lambda)$ values because of their corresponding n and k values. These results can be attributed to the change in G_S carried out by sintering temperature, which leads to increase in polarizability of the system due to variant in charge imbalance, especially in the nanocrystalline structures. The observed outcomes are in good agreement with the study on ZrO_2 or oxide-based nanostructures having various G_S carried out by thickness or sintering temperatures [27,28].

Table 2. A comparison of the certain structural and optical parameters/constants of the sol-gel grown ZrO_2 thin films with the previously synthesized ZrO_2 thin films, produced by sol-gel method

GS/D_{hkl}(nm)	δx10^{-3}	ε x 10^{-3}	Eg(eV)	n (at visible range)	k (at visible range)	εr (at visible range)	Ref
(20-200)/10	10.0	30.42	3.96	5.02-5.10	0.039-0.041	24.6-25.7	This study
(30-250)/15	4.44	30.50	4.05	4.98-5.08	0.05-0.063	24.2-25.4	This study
(20-300)/21	2.26	30.52	4.24	4.95-5.07	0.071-0.098	23.4-24.9	This study
(----)/3-9.9	----	----	----	1.60-2.40	-----	-----	[31]
(----)/10.3	----	----	5.72	2.1	-----	-----	[18]
(----)/15.6	----	----	5.10	-----	-----	-----	[32]
(5-12)/---	----	----	----	-----	-----	-----	[23]

Table 2 summarizes some recent studies on ZrO_2 thin films derived by sol-gel technique. The presented characteristics and parameters are relatively superior to the previously reported studies on the ZrO_2 thin films. The observed relatively low E_g values and higher n values reflects the influences of different grain/crystallite

and used chemical precursors as well as experimental conditions. The presented study is also one of the best examples of the structural and optical properties and parameters/constant of the sol-gel derived ZrO_2 thin films at wide range of grain/crystallite size among all the considered ZrO_2 thin films, whose optical constant have not been studied in more detail yet, as given in table 2. In addition, this table also reflects the importance of the presented study accordingly [29,30].

4. Conclusions

In this study, the influences of the grain size (G_S) on the calculated structural and optical parameters and constants of the zirconia dioxide (ZrO_2) nanostructures have been investigated for the first time. The ZrO_2 nanostructures crystallized within a tetragonal phase and preferred direction onwards (111) Miller plane. Crystallite size (D_{hkl}) and orientation degree of ZrO_2 have significantly affected by G_S. As the G_S values rise the calculated structural parameters D_{hkl} increases while computed micro-strain, dislocation density, and lattice parameter values decrease. The increasing of the G_S has proved by SEM analysis, including EDX and mapping investigations, showing the existence of Zr and O elements. Uv-Vis spectrophotometer investigations show decreased absorbance while reflectance and transmittance increase with increasing G_S. The calculated band gap values increase from 3.85 to 4.05 eV by enhance of G_S. With enhanced G_S the opposite trend has been observed in the refractive index and the extinction coefficient values. Amongst all the highest refractive index values have been detected for the lowest G_S distribution, whereas the lowest extinction coefficient values have been determined. Like the refractive index values, the reel dielectric constant values of the ZrO_2 have also shown the same behavior, while the imaginer dielectric constant values show the same trend with the extinction coefficient values. The observed variants are possibly because of the disparity in crystallite/grain size, nanostructure, polarizability, and packing density of the ZrO_2 nanostructures. These findings are in good agreement with those issued on ZrO_2 nanostructures produced by various methods. In addition to, this research is the first record of the effects of G_S on the computed structural and optical parameters and constants of ZrO_2 synthesized by sol–gel dip-coating technique, relatively the most practical and economical process to fabricate nanostructured materials used for the number of demands in the next dielectric and optic applications.

Acknowledgments

The authors are grateful to thin film research group led by Prof. Dr. Abdullah GÖKTAŞ, Department of Physics, Faculty of Arts and Science to guide the authors during this scientific research at Harran University/TURKEY.

Conflict of Interest Statement

The authors declare that there is no conflict of interest.

References

[1] A. V. Rudakova, Alexei V. Emeline, Kirill M. Bulanin, Lyudmila V. Chistyakova, Maria V. Maevskaya and Detlef W. Bahnemann, "Self-cleaning properties of zirconium dioxide thin films," *Journal of Photochemistry & Photobiology A: Chemistry*, vol. 367, pp. 397–405, 2018. doi:10.1016/j.jphotochem.2018.08.037

[2] S. Goktas, A. Tumbul and A. Goktas, "Growth Technique–Induced Highly C-Axis-Oriented ZnO: Mn, ZnO: Fe and ZnO: Co Thin Films: A Comparison of Nanostructure, Surface Morphology, Optical Band Gap, and Room Temperature Ferromagnetism," *Journal of Superconductivity and Novel Magnetism*, vol. 36, pp. 1875–1892, 2023. doi:10.1007/s10948-023-06630-4

[3] S. Park, J.M. Vohs and R.J. Gorte, "Direct oxidation of hydrocarbons in a solid-oxide fuel cell," *Nature*, vol. 404, no. 6775, pp. 265-267, 2000. doi:10.1038/35005040

[4] S. Sultana, M.Z. Khan, K. Umar and M. Muneer, "Electrical, thermal, photocatalytic and antibacterial studies of metallic oxide nanocomposite doped polyaniline," *Journal of Materials Science & Technology*, vol. 29, no. 9, pp. 795–800, 2013. doi:10.1016/j.jmst.2013.06.001

[5] C-Y. Lin, C-Y. Wu, C-Y. Wu, T-C. Lee, F-L. Yang, C. Hu and T-Y. Tseng, "Effect of top electrode material on resistive switching properties of ZrO2 film memory devices," *IEEE Electron Device Letters*, vol. 28, no. 5, pp. 366–368, 2007. doi:10.1109/LED.2007.894652

[6] B. Coskun, T. Asar, U. Akgul, K. Yildiz and Y. Atici, "Investigation of structural and electrical properties of Zirconium dioxide thin films deposited by reactive RF sputtering technique," *Ferroelectrics*, vol. 502, no. 1, pp. 147-158, 2016. doi:10.1080/00150193.2016.1235453

[7] M. T. Soo, G. Kawamura, H. Muto, A. Matsuda, Z. Lockman and K. Y. Cheong, "Design of hierarchically meso–macroporous tetragonal ZrO2 thin films with tunable thickness by spin-coating via sol–gel template route," *Microporous and Mesoporous Materials*, vol. 167, pp. 198–206, 2013. doi:10.1016/j.micromeso.2012.09.010

[8] L. Liu, C. Li, Y. Chen, X. Zhang, L. Li and Y. Wang, "Phase transformation of ZrO2 nanocrystals induced by Li+," *Materials Letters*, vol. 79, pp. 75–77, 2012. doi:10.1016/j.matlet.2012.03.112

[9] S. Tekeli and U. Demir, "Colloidal processing, sintering and static grain growth behavior of alumina-doped cubic zirconia," *Ceramics International*, vol. 31, no. 7, pp. 973-980, 2005. doi:10.1016/j.ceramint.2004.10.011

[10] S.K. Durrani, J. Akhtar, M. Ahmad and M.A. Hussain, "Synthesis and characterization of low density calcia stabilized zirconia ceramic for high temperature furnace application," *Materials Chemistry and Physics*, vol. 100, no. 2–3, pp. 324-328, 2006. doi:10.1016/j.matchemphys.2006.01.010

[11] O. Bernard, A.M. Huntz, M. Andrieux, W. Seiler, V. Ji and S. Poissonnet, "Synthesis, structure, microstructure and mechanical characteristics of MOCVD deposited zirconia films," *Applied Surface Science*, vol. 253, no. 10, pp. 4626-4640, 2007. doi:10.1016/j.apsusc.2006.10.025

[12] M. Mishra, P. Kuppusami, A. Singh, S. Ramya, V. Sivasubramanian, E. Mohandas, "Phase evolution in zirconia thin films prepared by pulsed laser deposition," *Applied Surface Science*, vol. 258, no.12, pp. 5157–5165, 2012. doi:10.1016/j.apsusc.2012.01.160

[13] D.Q. Xiao, G. He, P. Jin, J. Gao, J.W. Zhang, X.F. Chen, C.Y. Zheng, M. Zhang and Z.Q. Sun, "Effects of boron incorporation on the structural, optical and electrical properties of sol-gel-derived ZrO2 gate dielectrics," *Journal of Alloys and Compounds*, vol. 649, pp. 1273-1279, 2015. doi:10.1016/j.jallcom.2015.07.210

[14] H.P. Jee, B.Y. Young, H.L. Keun, S.J. Woo, Y.O. Jin, S.C. Soo, W.L. Hyun, W.H. Sun and K.B. Hong, "Boron-doped peroxo-zirconium oxide dielectric for high-performance, low-temperature, solution-processed indium oxide thin-film transistor," ACS applied materials \& interfaces, vol.5, no. 16, pp.8067-8075, 2013. doi:10.1021/am402153g

[15] V. S. Anitha, S. S. Lekshmy and K. Joy, "Effect of annealing temperature on optical and electrical properties of ZrO2–SnO2 nanocomposite thin films," *Journal of Materials Science: Materials in Electronics*, vol. 24, pp. 4340–4345, 2013. doi:10.1007/s10854-013-1408-7

[16] A. Goktas, F. Aslan and İ.H. Mutlu, "Annealing effect on the characteristics of $La_{0.67}Sr_{0.33}MnO_3$ polycrystalline thin films produced by the sol–gel dip-coating process," *Journal of Materials Science: Materials in Electronics*, vol. 23, pp. 605–611, 2012. doi:10.1007/s10854-011-0448-0

[17] I. J. Berlin, S. S. Lekshmy, V. Ganesan, P.V. Thomas and K. Joy, "Effect of Mn doping on the structural and optical properties of ZrO_2 thin films prepared by sol–gel method," *Thin Solid Films*, vol. 550, pp. 199-205, 2014. doi:10.1016/j.tsf.2013.10.164

[18] A. Goktas, F. Aslan, A. Tumbul and S. Gunduz, "Tuning of structural, optical and dielectric constants by various transition metal doping in ZnO:TM (TM=Mn, Co, Fe) nanostructured thin films: A comparative study," *Ceramics International*, vol. 43, no. 1, pp. 704-713, 2017. doi:10.1016/j.ceramint.2016.09.217

[19] A. Goktas, I. H. Mutlu and Y. Yamada, "Influence of Fe-doping on the structural, optical, and magnetic properties of ZnO thin films prepared by sol–gel method," *Superlattices and Microstructures*, vol. 57, pp. 139-149, 2013. doi:10.1016/j.spmi.2013.02.010

[20] A. Méndez-López, O. Zelaya-Ángel, M. Toledano-Ayala, I. Torres-Pacheco, J. F. Pérez-Robles and Y. J. Acosta-Silva, "The Influence of Annealing Temperature on the Structural and Optical Properties of ZrO2 Thin Films and How Affects the Hydrophilicity," Crystals, vol. 10, no. 6, pp. 454. 2020. doi:10.3390/cryst10060454

[21] H. Gencer, A. Goktas, M. Gunes, H.I. Mutlu and S. Atalay, "Electrical Transport and Magnetoresistance Properties of La0.67Ca0.33MnO3 Film Coated On Pyrex Glass Substrate," *International Journal of Modern Physics B*, vol. 22, no. 05, pp. 497-506, 2008. doi:10.1142/S0217979208038776

[22] Y. Mansilla, M. D. Arce, C. González-Oliver, J. Basbus, H. Troiani and A. Serquis, "Characterization of stabilized ZrO_2 thin films obtained by sol-gel method," *Applied Surface Science*, vol. 569, pp. 150787, 2021. doi:10.1016/j.apsusc.2021.150787

[23] A. Göktaş, A. Tumbul, F. Aslan, "Grain size-induced structural, magnetic and magnetoresistance properties of $Nd_{0.67}Ca_{0.33}MnO_3$ nanocrystalline thin films," *Journal of Sol-Gel Science and Technology*, vol. 78, pp. 262–269, 2016. doi:10.1007/s10971-016-3960-0

[24] F. Mikailzade, F. Önal, M. Maksutoglu, M. Zarbali and A. Göktaş, "Structure and Magnetization of Polycrystalline $La_{0.66}Ca_{0.33}MnO_3$ and $La_{0.66}Ba_{0.33}MnO_3$ Films Prepared Using Sol-Gel Technique," *Journal of Superconductivity and Novel Magnetism*, vol. 31, pp. 4141–4145, 2018. doi:10.1007/s10948-018-4683-y

[25] M. Boulouz, L. Martin, A. Boulouz and A. Boyer, "Effect of the dopant content on the physical properties of Y_2O_3–ZrO2 and CaO–ZrO_2 thin films produced by evaporation and sputtering techniques," *Materials Science and Engineering: B*, vol. 67, no. 3, pp. 122-131, 1999. doi:10.1016/S0921-5107(99)00338-4

[26] W.T. Tang, Z.F. Ying, Z.G. Hu, W.W. Li, J. Sun, N. Xu and J.D. Wu, "Synthesis and characterization of HfO_2 and ZrO_2 thin films deposited by plasma assisted reactive pulsed laser deposition at low temperature," *Thin Solid Films*, vol. 518, no. 19, pp. 5442-5446, 2010. doi:10.1016/j.tsf.2010.04.012

[27] D. Tahir, E. Kyoung Lee, S. Kun Oh, H. Jae Kang, S. Heo, J. Gwan Chung, J. Cheol Lee and S. Tougaard, "Dielectric and optical properties of Zr silicate thin films grown on Si (100) by atomic layer deposition," *Journal of Applied Physics*, vol. 106, no. 8, pp. 084108-14, 2009. doi:10.1063/1.3246612

[28] A. Goktas, F. Aslan, B. Yeşilata and İ. Boz, "Physical properties of solution processable n-type Fe and Al co-doped ZnO nanostructured thin films: Role of Al doping levels and annealing," *Materials Science in Semiconductor Processing*, vol. 75, pp. 221-233, 2018. doi:10.1016/j.mssp.2017.11.033

[29] M. T. Soo, N. Prastomo, A. Matsuda, G. Kawamura, H. Muto, A. F. M. Noor, Z. Lockman and K. Y. Cheong, "Elaboration and characterization of sol–gel derived ZrO_2 thin films treated with hot water," *Applied Surface Science*, vol. 258, no. 13, pp. 5250-5258, 2012. doi:10.1016/j.apsusc.2012.02.008

[30] S. Chang and R. Doong, "The Effect of Chemical States of Dopants on the Microstructures and Band Gaps of Metal-Doped ZrO_2 Thin Films at Different Temperatures," *The Journal of Physical Chemistry B*, vol. 108, no. 46, pp. 18098-18103, 2004. doi:10.1021/jp047440n

This is an open access article under the CC-BY license

GAZİ
JOURNAL OF ENGINEERING SCIENCES

Predicting of Melanoma Skin Cancer Using Machine Learning Methods

Resul Bütüner[a], M. Hanefi Calp[*b]

Submitted: 23.06.2024 Revised: 12.02.2024 Accepted: 04.04.2024 doi:10.30855/gmbd.0705N12

ABSTRACT

Cancer disease is known as the second highest cause of death in the world. One of the most common types of this disease is skin cancer. As in almost all cancer diseases, early diagnosis and treatment of skin cancer is of great importance. In the process of diagnosing cancer, Machine Learning-based methods are also widely used in addition to traditional methods. The most important advantage of these methods is that they eliminate or minimize human errors that may arise during the cancer diagnosis process. In this study, skin cancer was diagnosed with K-Nearest Neighbor (KNN), Naive Bayes (NB), Random Forest (RO), Logistic Regression (LR), and Artificial Neural Networks (ANN) methods using images taken from patients. In these algorithms, the training and testing process was run, the results were analyzed and models were created. With these models, benign and malignant lesions were compared and skin cancerous lesions were detected and success percentages were revealed. As a result, the best results were obtained using the ANN method, with a training percentage of 99.1% and a testing percentage of 98.6%. When different inputs were given to the created and proposed ANN model, it was observed that the model predicted skin cancer with a high accuracy rate. The results obtained revealed the success of the study and that machine learning methods are a usable method in the cancer diagnosis process.

Keywords: Skin Cancer, Machine Learning, Diagnosis, Prediction

[a,*2]Ankara Beypazarı Fatih Vocational and Technical Anatolian High School, Dept. of Computer,
Orcid: 0000-0002-9778-2349
e mail:rbutuner@gmail.com

[b]Ankara Hacı Bayram Veli University, Faculty of Economics and Administrative Sciences,
Dept. of Management Information Systems
06560 - Ankara, Türkiye
Orcid: 0000-0001-7991-438X
e mail: hanefi.calp@hbv.edu.tr

[*]Corresponding author:
hanefi.calp@hbv.edu.tr

Makine Öğrenmesi Yöntemleri Kullanılarak Melanom Cilt Kanserinin Tahmin Edilmesi

ÖZ

Kanser hastalığı, dünyadaki en yüksek ikinci ölüm nedeni olarak bilinmektedir. Bu hastalığın en yaygın türlerinden biri de cilt kanseridir. Hemen hemen tüm kanser hastalıklarında olduğu gibi cilt kanserinde de erken teşhis ve tedavi sürecinde oldukça büyük bir öneme sahiptir. Kanser hastalığının teşhisi sürecinde, geleneksel yöntemlerin yanı sıra Makine Öğrenmesi tabanlı yöntemler de yaygın olarak kullanılmaktadır. Sözkonusu yöntemlerin en önemli avantajı, kanser teşhisi sürecinde insan kaynaklı doğabilecek hataları ortadan kaldırması veya minimize etmesidir. Bu çalışmada, hastalardan alınan görüntüler kullanılarak K-En Yakın Komşu (KNN), Naive Bayes (NB), Rastgele Orman (RO), Lojistik Regresyon (LR) ve Yapay Sinir Ağları (YSA) yöntemleri ile cilt kanseri hastalığı teşhis edilmiştir. Bu algoritmalarda eğitim ve test süreci işletilerek sonuçlar analiz edilmiş ve modeller oluşturulmuştur. Bu modeller ile iyi ve kötü huylu lezyonlar karşılaştırılmış ve cilt kanseri olan lezyonlar tespit edilerek başarı yüzdeleri ortaya konulmuştur. Sonuç olarak, en iyi sonuçlar eğitim yüzdesi %99.1, test yüzdesi ise %98.6'lık bir oran ile YSA yöntemi kullanılarak elde edilmiştir. Oluşturulan ve önerilen YSA modeline farklı girdiler verildiğinde, modelin cilt kanseri hastalığını yüksek bir doğruluk oranıyla tahmin ettiği görülmüştür. Elde edilen sonuçlar, yapılan çalışmanın başarısını ve makine öğrenmesi yöntemlerinin kanser teşhisi sürecinde kullanılabilir bir yöntem olduğunu ortaya koymuştur.

Anahtar Kelimeler: Cilt Kanseri, Makine Öğrenmesi, Teşhis, Tahmin

To cite this article: R. Butuner, M. H. Calp "Predicting of Melanoma Skin Cancer Using Machine Learning Methods," *Gazi Journal of Engineering Sciences*, vol.10, no.1, pp. 141-154, 2024. doi:10.30855/gmbd.0705N12

1. Giriş (Introduction)

Kanser, farklı organlarda bulunan hücrelerin kontrol dışında çoğalmasından dolayı meydana gelen bir hastalık olarak tanımlanır [1]. Kanser hastalığı, hastalıklar içerisinde dünya üzerinde en yüksek karşılaşılan ikinci ölüm sebebidir [2]. Yaygın görülen kanser türlerinden birisi de cilt kanseridir. Bunun içerisinde en ölümcül olanı Melanoma Cilt Kanseridir. Cilt kanseriyle ilgili ölümlerin yaklaşık %75'i ise melanomadan dolayıdır [3]. Melanoma türüne ait cilt kanseri metastaz yapmak suretiyle diğer dokulara yayılmaktadır. Dolayısıyla bu durum ölüm oranlarını artırmaktadır [4]. Melanin renk pigmentleri deriye renk vererek, melanosit adlı cilt hücreleri tarafından üretilir. Bu hücrelerin deride kontrolsüz olarak bölünüp çoğalması ile meydana gelen cilt kanserine melanom ya da melanoma olarak tanımlanmaktadır [5]. Cilt kanseri, hem Türkiye'de hem de dünyada diğer kanser türleri gibi artış göstererek büyük dikkat çeker. En çok melanom dışı deri kanseri beyaz ırkta görülen kanserlerdir. Burada hastanın melonomunda benign (iyi huylu) malignant (kötü huylu) olarak ifade edilmektedir. Yaşam boyunca oluşma oranı erkek bireylerde 33 kişide birinde iken kadın bireylerde ise 52 kişide birinde rastladığı görülür [6]. Melenomun en büyük nedeni ise ultraviyoleden (UV) kaynaklanan ışınlardır. Herkeste cilt kanserine yakalanma riski bulunur. Fakat cildinde açık ten olan, cildi fazlaca ben ve lekeleri bulunan, uzunca süre güneşin altında bulunan, çocukluk sürecinde güneş yanığı olan bireylerin cilt kanseri olma riski daha fazladır [7]. Tedavi sürecinde, hastanın geçmiş hayatından itibaren, kırmızımsı renk, kabarmış, tomografik açıdan anormal, büyüme gösteren, kanamış, kabuklanmış veya farklılaşan lezyonlar tanımlanarak daha sonrasında görsel olarak incelenir. Klinik uzman kontrolünde, şüphe görülen lezyonlar biyopsiye göre tedavi sürecine karar verilmektedir. Şu anda ise klinikteki tanının doğruluğunu artırmak için yeni teknolojiler de kullanılmaktadır. Neoplazm doku kitlesi 200 yıllık bir geçmişe dayanarak bir hastalık varlığı olarak kabul edilmiştir. Bundan dolayı melanomun tanısı ve tedavisi büyük ölçüde gelişim sağlamıştır. Fakat hastalarda melanom cilt kanserinin erken teşhisinin önemi çokça anlaşılmamaktadır [8]. Melenom cilt kanserinde önemli bir problem de lezyon bölütlemesinin yanlış yapılması ve lezyondaki kıl temizliğidir ve, bu durum yanlış kanser tanısına sebebiyet vermektedir [9]. Herhangi bir vücutun deri yüzeyinde melanositlerin fazlaca bulunduğu zaman melanoma sebep olur. Dermoskopi muayene tekniği, derideki yüzeylerin mikroskobik olarak incelenerek deride bulunan koyu renkli lekelere tanı koyulması için kullanılmaktadır. Melanom kişilerin ölümüne yol açan bir cilt kanseri olarak bilinir. Melanom cilt kanserine yakalanmış hastaların sadece %4'ünü oluşturmaktadır. Fakat tüm cilt kanserindeki ölümlerin %75'ini oluşturur. Uzman dermatologlar melanom tanısı için dermoskopi kullansalar bile, doğruluk başarısı %75 ile %84 arasında tahmini olarak bulunur [10]. Melanom cilt kanseri erken teşhis edilip, tedavi sürecine geçilirse iyileşmenin olumlu yönde sonuçlanmasını mümkün kılar. Ama melanomun teşhisi geç olursa bu sefer derinin daha diplerine doğru büyüme göstererek vücudun diğer bölgelerine yayılma imkânı doğar. İşte cildin yüzeyindeki diğer bölgelerine yayıldığı zaman tedavi süreci daha tehlikeli olabilir. Dünya da en yaygın şekilde görülen kanser türlerinden biri deri kanseridir ve giderek de artmaktadır [11]. Kişilerin cilt kanserine yakalanma riskinin ultraviyolenin ışınına maruz kalma, genetik ve çevresel faktörlerin bir oluşumundan kaynaklanır [12].

Deri anatomisinde iki ana katman bulunmaktadır. Bunlar epidermis yani dış katman ve dermis yani iç katman'dir. Epidermis, düz, ölçek benzeri hücreler ve bazal hücreler diye adı konulan yuvarlak Squamous hücreleri diye ifade edilen hücrelerden oluşmaktadır. Epidermisin de alt kısmında ise melanositi içermektedir. Melanositler, epidermisinin tam alt tarafında bulunmaktadır. Cilt kısmına doğal renk vererek pigment olan melanin üreten pigment hücreleridir. Cildin güneşle fazlaca kaldığında, melanositler daha fazla pigment üretir. Böylece cilt yüzeyinin bronzlaşması ya da koyulaşması gerçekleşerek melanomlara sebep olmaktadır [13]. Melanom cilt kanseri ise melanosit malign diye ifade edilen tümör olarak bilinir. Bu tarz hücrelerin çoğunlukla deri kısmında bulunmaktadır. Fakat bağırsak ve gözde de bulunma durumu görülür. Melanom diğerlerine göre görülme sıklığı daha azdır. Fakat cilt kanserinden dolayı ölüm vakalarının tümüne sebep olmaktadır. Uzun yıllardır devam eden laboratuvar ve klinik araştırmalarında, bu tümörlere uygulanacak erken cerrahi rezeksiyonu şuan da bile en büyük tedavi şansını sunar. Melanom en tehlikeli cilt kanseri türüdür ve melanosit diye tanımlanan cilt hücrelerinde başlamaktadır [14]. Avrupa'da yapılan araştırmaya göre malign melanom insidansı, 100 bin kişi başına 4 ile 14 hasta arasında sonuç vermektedir [15].

Günümüzde cilt kanseri teşhisinde geleneksel yöntemlerle (dermaskopi, gözle muayene ve cerrahi tabanlı) birlikte görüntü işleme, derin öğrenme ve makine öğrenmesi algoritmaları da kullanılmaktadır. Görüntülerin temizlenme sürecinde görüntü işleme ve yapay sinir ağları gibi tekniklerinden daha yaygın yararlanılmaktadır [16,17]. Derin Öğrenme ve Görüntü İşleme algoritmaları geleneksel yöntemlere göre, insan faktörünü ortadan kaldırdığı için daha güvenilir sonuçlar vermektedir. Bu kullanılan algoritmalarla, bir uzman kadar başarılı sonuçlar alınabilmekte ve insan hatası ortadan kaldırılmaktadır [18]. Kıl temizliği üzerine çözüm getiren ilk çalışmalardan biri kıl gürültüsünün temizliği için geliştirilen DullRazor algoritmasıdır. Bu algoritma sayesinde thresholding (eşikleme) ve morfolojik işlemler ile lezyonda kıl temizliği yapar ve hızlı, basit olmasından dolayı bu alanda yapılacak bilimsel çalışmalara katkı sağlamaktadır [19]. Melenom tespitinde, lezyonun kenarlarını tespit etmek ve doğru bölütleme amacıyla denetimsiz hızlı ve başarılı bir algoritma geliştirilmiştir [20]. Ayrıca, YUV renk uzayının kullanılmasıyla kıl temizliği ve bölütleme için yeni bir yaklaşım geliştirmiştir. Bu yaklaşım eşikleme ve morfolojik işlemler ile YUV renk uzayı üzerine temellenmiştir. Çalışmada 235 görüntü kullanılmış ve %98'lik başarı elde edilmiştir [3]. Başka bir çalışmada ise, kıl temizleme ve bölütleme çalışmalarında sadece görüntü işleme algoritmalarının yeterli olmadığı görülmüştür. Vnet tabanlı derin öğrenme ile bölütleme yapılmış ve %89 başarı değeri elde edilmiştir [21].

Literatürde, otomatik kodlayıcı, konuşma ve CNN dayalı başka bir yeni model önerilen çalışmaya da rastlanmıştır. Kullanılan veri kümesi, 1800 iyi huylu ve 1497 kötü huylu tümör görüntüsünü içeren Uluslararası Cilt Görüntüleme İş Birliği (ISIC) cilt kanseri adı verilen halka açık erişimli bir veri kümesidir. Veri kümesi, önerilen yöntemde otomatik kodlayıcı modeli kullanılarak yeniden oluşturulmuştur. Orijinal veri setini ve yapılandırılmış veri setini eğitmek ve sınıflandırmak için artık bloklardan ve artış ağlarından oluşan Mobile Net V2 modeli kullanılmıştır. Çalışmanın sınıflandırma başarı oranı %95,27 olarak gerçekleşmiştir [22]. Melanomu doğru bir şekilde tespit edip sınıflandırabilen bir sinir ağı oluşturmayı amaçlayan başka bir çalışmada, prosedürleri, görüntü geliştirmenin yanı sıra Maksimum Gradyan Yoğunluğu tekniği kullanılarak kılları çıkarmak için dermoskopik görüntülerin önceden işlenmesiyle başlamıştır. Cilt lezyonlarını görüntülerden ayırmak için Otsu Eşik algoritmasına dayalı bir segmentasyon tekniği kullanılmıştır. Bölümlere ayrılmış görüntüler daha sonra bir sinir ağını eğitmek için kullanılan ABCD, GLCM ve LBP gibi birçok özelliği hesaplamak için kullanılmıştır. ISIC arşivinin birleşik veri kümesi ve PH2 dermoskopik görüntü veritabanında ağ %97,7'lik bir doğruluk elde edilmiştir [23]. Yine, üç sınıf cilt kanseri görüntülerini tanımak amacıyla önceden eğitilmiş GoogLeNet ve AlexNet modelleri kullanılmıştır. Kullanılan veri seti, bölütlemesiz veri seti ve bölütlemeli veri seti olmak üzere iki formata ayrılmıştır. Sınıflandırma başarı oranı bölütlemeli veri seti için %92.2 ve bölütlemesiz veri seti için % 89.8 olmuştur [24]. Başka bir araştırmada ise yazarlar cilt kanseri görüntülerini Melanoma ve Nevus olarak iki sınıfa ayırmıştır. Sınıflandırmak amacıyla ResNet-50 modeli seçilmiştir. ResNet-50 modeli kullanılırken, sabit bir öğrenme oranının aksine modelin her katmanı için farklı bir öğrenme oranı kullanılmıştır. Ayrıca, öğrenme hızlarını düşürmek için kosinüs işlevine dayalı yeni yöntemler denenmiş ve bu yöntem ile % 82.3'lük bir başarı oranı elde edilmiştir [25]. Son olarak, farklı bir çalışmada veri setindeki her bir görüntüyü veri artırma yöntemini kullanarak veri seti arttırılmış ve transfer öğrenmesi yaklaşımı ile sınıflandırma işlemi gerçekleştirilmiştir. Bu yöntem ile %95.91'lik başarı oranına ulaşılmıştır [26].

Çalışmada, günümüzde sıkça görülen cilt kanseri teşhisinde hızlı ve doğru tahminde bulunan bir makine öğrenmesi modelinin tasarlanması ve uygulanması amaçlanmıştır. Ulaşılmak istenen hedeflerden birisi, biyoloji alanında makine öğrenmesi uygulamalarını hayata geçirmektir. Böylece hastalık teşhisinde zaman ve emek kaybını minimuma indirmek ve hastalığı en yüksek doğruluk oranıyla teşhis edebilmek amaçlanmıştır. Çalışmanın bir başka hedefi ise, oluşturulan modelin farklı ve çok sayıda verileri kullanarak kendi kendini eğitmesi ve teşhis sürecindeki doğruluk oranını veya performansını giderek arttırmasıdır. Bu çerçevede, ikinci bölümde çalışma kapsamında kullanılan Materyal ve Yöntem, üçüncü bölümde elde edilen Bulgular ve Tartışma, dördüncü bölümde ise Sonuç ve Öneriler yer almaktadır.

2. Materyal ve Yöntem (Material and Method)

Bu bölümde, çalışma sürecinde makine öğrenmesi yöntemleri kullanılarak modeller oluşturulmuş, en yüksek performansa sahip model önerilmiş ve gerçekleştirilen tüm adımlar ayrıntılarıyla birlikte sunulmuştur. Öncelikle çalışmada kullanılan algoritmalar kısaca açıklanmış, daha sonra veriler hakkında bilgi verilmiş (veri setinin temini ve organize edilmesi), son olarak bu veriler kullanılarak oluşturulan modelin ayrıntılarına yer verilmiştir. Girdi değeri olarak sisteme cilt lezyonu görüntüsü verilmiş ve daha sonra görüntü işleme yöntemleri kullanılarak cilt kanseri varlığının olup olmadığı hakkında bir sonuç çıkarmak amacıyla analizler yapılmıştır.

2.1. Veri seti ve önişleme (Dataset and preprocessing)

Çalışmanın verileri herkese açık bir platform olan https://www.kaggle.com/datasets/fanconic/skin-cancer-malignant-vs-benign adresinden elde edilmiştir. Bu aşamada; veriler analiz edilmiş ve en yüksek performans üretecek modeller için ön işlemeden geçirilmiştir. Ayrıca, veri hazırlama, keşifsel veri analizi ve modelleme gibi süreçler de icra edilmiştir. Çalışmada kullanılan veriler iyi ve kötü huylu cilt lezyonlarına aittir. Bu veri setinde toplam 2637 tane cilt lezyonu görüntüleri vardır. Bu görüntülerin her biri 224×224 yükseklik ve genişlikle JPG formatında kaydedilmiştir. Verilerin ayrıntılarına Tablo 1'de yer verilmiştir.

Tablo 1. Çalışmada kullanılan veri sayıları ve yüzdeleri (Data numbers and percentages used in the study)

Kullanım Alanı	Veri Sayısı	Yüzde (%)	İyi Huylu	Kötü Huylu
Eğitim (training)	1977	75	1482	495
Test (testing)	660	25	360	300
Toplam	2637	100	1842	795

2.2. Algoritma seçimi (Algorithm selection)

Melenom cilt kanserini tespit etmek amacıyla gerçekleştirilen çalışmada, KNN, RO, NB, YSA ve LR algoritmalarından faydalanılmış ve modeller oluşturulmuştur. Literatürdeki çalışmalar incelendiğinde, görüntü sınıflandırma ve tahmine yönelik yaygın olarak kullanılan algoritmalar çalışmada yer almıştır. Sözkonusu algoritmaların kısaca açıklamalarına bu bölümde yer verilmiştir.

2.2.1. KNN

En basit makine öğrenmesi algoritması olarak kabul edilir ve yaygın olarak kullanılan bir sınıflandırma algoritmasıdır. Bu yöntemde k sayısı önemlidir ve öncelikle bu sayı belirlenir. k sayısı, bir nesnenin hangi sınıfta olacağına karar vermek için o nesneye en yakın olan kaç tane komşu kullanılacağıyla ilgili bir sayıdır. k sayısı içinde en fazla hangi sınıfa yakınlık varsa, bilinmeyen nesne o sınıfa dâhil edilir. Ayrıca KNN eğitim aşamasına sahip değildir [27-29].

2.2.2. RO

Leo Breiman ve Adele Cutler tarafından oylama metodu ile geliştirilen bir sınıflandırma yöntemidir. Birden çok karar ağacının birleşmesiyle meydana gelmektedir. Bireysel ağaçlar tarafından oylanmasıyla kazanan sınıf belirlenir ve karar ağaçlarının oluşumunda, birbirinden bağımsız şekilde ve veri setinden bootstrap tekniği ile çekilen örneklerden faydalanılmaktadır. Torbalama yönteminin gelişmiş bir şekli olarak kabul edilmektedir [30].

2.2.3. NB

Birçok alanda yüksek performans gösteren istatistik tabanlı etkili bir tahmin etme tekniğidir. Çalışma prensibi olarak verideki nitelikleri sadece belirli bir sınıfa bağlı olması dikkate alınarak en uygun etikete göre sınıflandırma yapma işlemini gerçekleştirir [31-33].

2.2.4. YSA

İnsan beyninin özelliklerinden biri olan öğrenmeyi dikkate alarak çalışır. Bir nöron ağı ve bu ağların ilişkilendirmiş ağırlık değerleri ve toplama fonksiyonlarından meydana gelmektedir. Yeni veriler oluşturabilme, tahmin etme ve keşfedebilme gibi yetenekleri, başka hiçbir yardım almadan otomatik bir şekilde gerçekleştirebilen bir yöntemdir [34-36].

2.2.5. LR

Bir veriye ait öğeyi gerçek değerli tahmin değişkenine eşleştirmek amacıyla kullanılmaktadır. Bu fonksiyonun öğrenilmesini kapsar. Temel amaç, verinin bilinen bir fonksiyon tipine uymasıdır. Regresyon tekniğinde sürecinde verilen veriyi en iyi modelleyen fonksiyon bulunmaya çalışılmaktadır. Gerçek beklenen değerler ile tahmin değerleri arasındaki farka göre hangi fonksiyonun en başarılı performansa sahip olduğu belirlenir [37].

3. Bulgular ve Tartışma (Results and Discussion)

Melanom cilt kanserine ait görüntüler ile cilt beni fotoğrafları kullanılarak modelin eğitilmesi sağlanmıştır. Modele ait girdi değerlerinin tanımlanması yapılmıştır. Girdiye ait değerler iyi huylu (benign) ve kötü huylu (malignant) cilt lezyonlarıdır. Şekil 1'de çalışmada kullanılan iyi ve kötü huylu cilt lezyon görüntüleri verilmiştir.

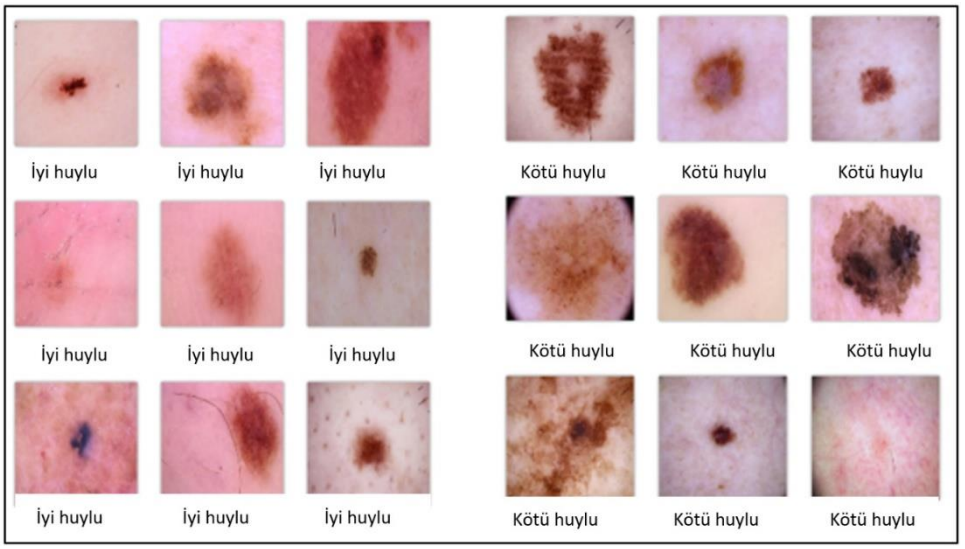

Şekil 1. İyi ve kötü huylu cilt lezyonları (Benign and malignant skin lesions)

Şekil 2'de hastaların cilt kanseri teşhisi için oluşturulan modele yer verilmiştir. Eğitim ve test olmak üzere iki bölümden oluşan görüntüler işlenmiştir. Görüntüler VGG-16 ağ modeli ile işlendikten sonra seçilen 5 adet algoritma ile modeller oluşturulmuştur. Bu modeller ile test ve skor (score) kısmında başarı değerleri tablolar ile verilmiştir. Daha sonraki kısımda ise test verilerinin algoritmalara göre görselleştirilmesi yapılmıştır. Her algoritmaya ait yüzdelik doğruluk değerleri, çıkış katmanına göre doğruluk ve kayıp (hata) grafiği vb. verilmiştir.

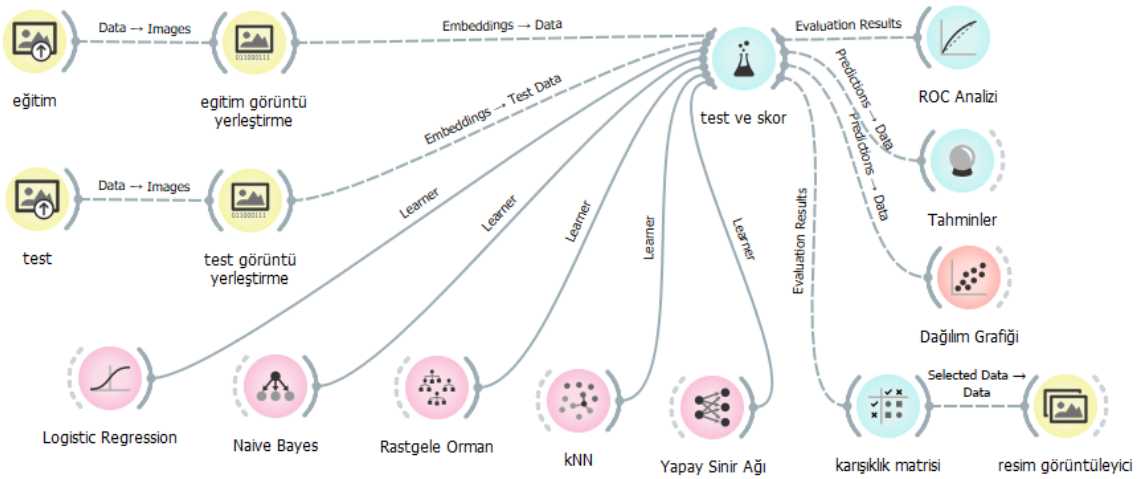

Şekil 2. Çalışmanın modeli (Model of the study)

Çalışmada, en iyi sonuç üreten veya en yüksek performansa sahip modele odaklanılmış olup sadece sözkonusu modelin genel tasarımına yer verilmiştir (Şekil 3). Bu bağlamda, yapay sinir ağına gelen veriler; giriş, gizli ve çıkış katmanlarından geçerek sınıflandırma yapılmış ve cilt lezyonu görüntüsünün melanom cilt kanseri olduğu tespit edilmiştir. Şekil 3'te, YSA mimarisine yer verilmiştir.

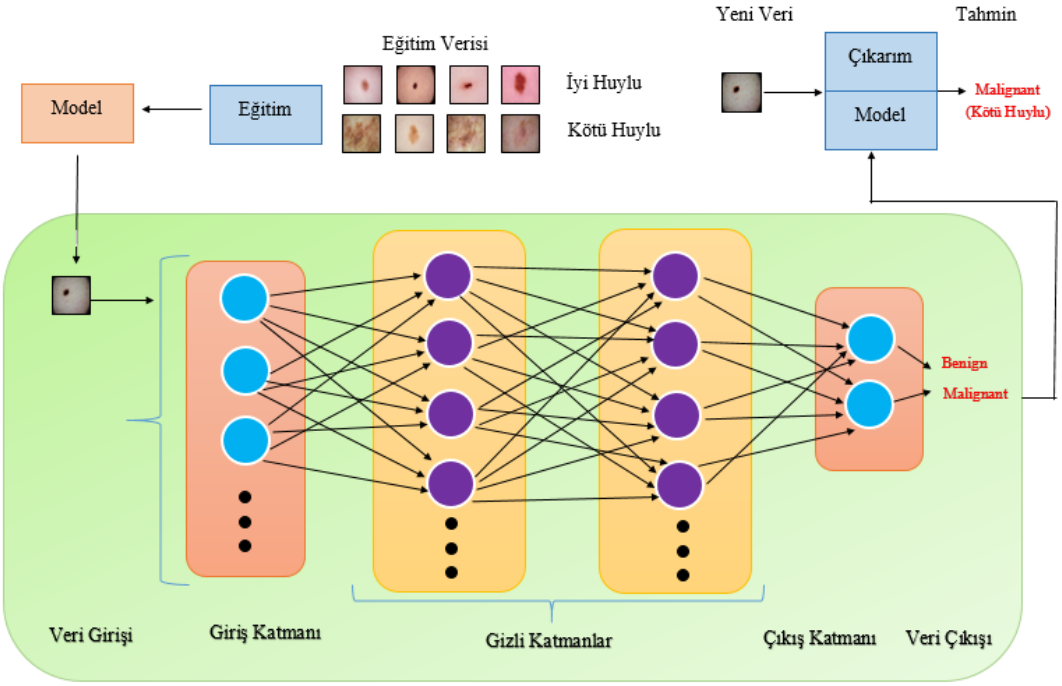

Şekil 3. YSA modeli ve sınıflandırma (ANN model and classification)

Bu algoritmalarda iyi huylu (benign) ve malignant (kötü huylu) kategorilerine göre Yapay Sinir Ağının en başarılı sonuçlar verdiği görülmektedir. YSA tekniğinde, %98.8 iyi huylu ve %98.4 ile kötü huylu olarak elde edilmiştir. Tablo 2'de, çalışmada kullanılan algoritmalara yönelik Karışıklık Matrisi (Confusion Matrix) değerleri verilmiştir.

Tablo 2. Algoritma modellerinin karışıklık matrisi sonuçları (Confusion matrix results of algorithm models)

KNN

	İyi huylu	Kötü Huylu	∑
İyi huylu	%81.4	%15.3	360
Kötü huylu	%18.6	%84.7	300
∑	385	275	660

NB

	İyi huylu	Kötü Huylu	∑
İyi huylu	%83.9	%24.1	360
Kötü huylu	%16.1	%%75.9	300
∑	336	324	660

RO

	İyi huylu	Kötü Huylu	∑
İyi huylu	%86.2	%17.7	360
Kötü huylu	%13.8	%82.3	300
∑	362	238	660

YSA

	İyi huylu	Kötü Huylu	∑
İyi huylu	%98.8	%1.2	360
Kötü huylu	%1.6	%98.4	300
∑	362	298	660

LR

	İyi huylu	Kötü Huylu	∑
İyi huylu	%84.3	%17.9	360
Kötü huylu	%15.7	%82.1	300
∑	364	296	660

Tablo 3'te, çalışmada kullanılan algoritmaların eğitim ve test değerlerine göre yüzdelik değerleri verilmiştir. En başarılı sonuçlar, YSA yöntemi kullanılarak elde edilmiş olup Naive Bayes algoritması ise, eğitim %85.7 ve %80 test değeri ile en düşük performansa sahiptir.

Tablo 3. Modellerin karşılaştırılması (Comparison of models)

Model Adı	AUC	F1 Skor	Kesinlik	Duyarlılık
RO	0.920	0.844	0.844	0.844
LR	0.912	0.833	0.833	0.833
KNN	0.899	0.826	0.829	0.827
NB	0.857	0.800	0.803	0.800
YSA	0.991	0.987	0.986	0.986

Buna ilaveten, YSA algoritmasında bulunan farklı optimizasyonlar kullanılarak en başarılı eğitim ve test başarı yüzdeleri SGD optimizasyonu ile elde edilmiştir (Tablo 4).

Tablo 4. YSA'da kullanılan optimizasyon modellerinin karşılaştırılması (Comparison of optimization models used in ANN)

Optimizasyon Adı	Eğitim (%)	Test (%)
Adam	0.984	0.978
SGD	0.991	0.986
L-BFSG-B	0.988	0.981

Cilt kanseri teşhisinde ikili sınıflandırma algoritması ele alınırsa, bu model ile eldeki veriler 1 ya da 0 olarak sınıflandırılır ve bu iki durumdan hangisine uyduğu belirlenir. 1 ya da 0 olma kararı, bir eşik (threshold) yardımıyla ele alınır. Eşik değerinden düşük olan veriler 0, eşik değerinden büyükler ise 1 olarak sınıflandırılır. Denetimli öğrenme tekniğinde modelin öngörüleri eldeki verilerle test edilir ve modelin geçerliliği ve performansı bu şekilde denenmiş olur. İkili sınıflandırma modelinin tahminleri test verisi ile kıyas yapıldığında aşağıdaki durum oluşmaktadır.

Model 1 olarak tahmin etmiş ve test verisi 1 ise: Doğru Pozitif (True Positive) (TP)

Model 0 olarak tahmin etmiş ve test verisi 0 ise: Doğru Negatif (True Negative) (TN)
Model 1 olarak tahmin etmiş ve test verisi 0 ise: Yanlış Pozitif (False Positive) (FP)
Model 0 olarak tahmin etmiş ve test verisi 1 ise: Yanlış Negatif (False Negative) (FN) olarak oluşturulur [38].

Buna göre Şekil 4'te hastaların cilt kanseri teşhisinde iyi huyluya göre TP ve FP grafiği ROC analiz grafiği verilmiştir. Çalışmada kullanılan algoritmalar için deneysel sonuçlar da Tablo 5'te verilmiştir. Duyarlılık oranı 0'dan başlamış, 0,986'ya kadar yükselmiştir. En yüksek doğruluk oranı YSA yöntemi ile elde edilmiştir.

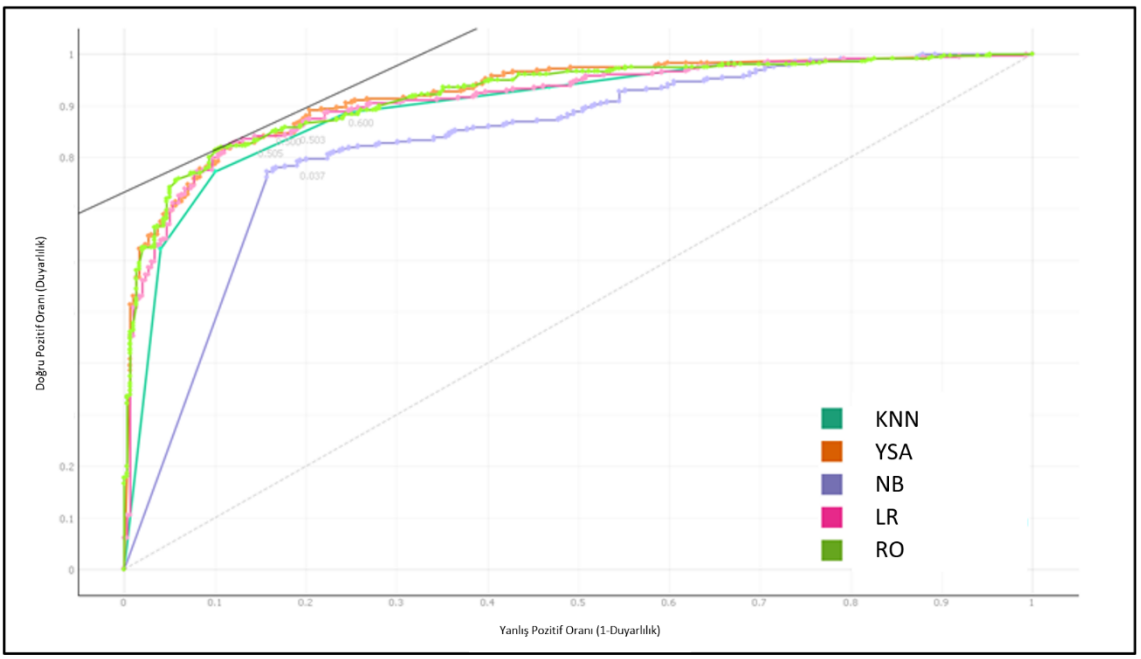

Şekil 4. İyi Huylu TP (Doğru Pozitif) ve FP (Yanlış Pozitif) ROC analiz grafiği (Benign TP (True Positive) and FP (False Positive) ROC analysis chart)

Tablo 5. Kullanılan modellerin performansları (iyi huylu) (Performances of the models used (well-behaved))

Model	Doğruluk Oranı (%)
KNN	81,4
RO	86,2
NB	83,9
LR	84,8
YSA	98,8

Şekil 5'te, cilt kanserinde kötü huylu olan hastaların çalışmada kullanılan algoritmalara göre ROC analiz grafiği verilmiştir. Deneysel sonuçlar da Tablo 6'da verilmiştir. Buna göre en yüksek doğruluk oranı YSA yöntemi ile elde edilmiştir.

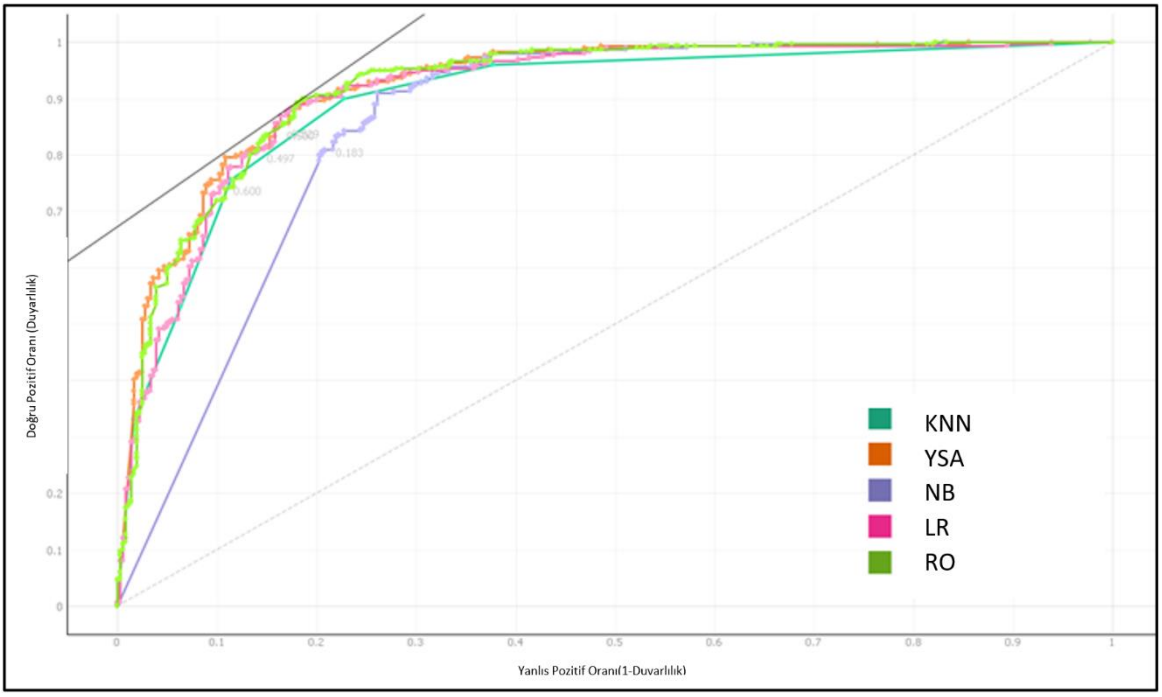

Şekil 5. Kötü huylu TP (Doğru Pozitif) ve FP (Yanlış Pozitif) ROC Analiz Grafiği (Malignant TP (True Positive) and FP (False Positive) ROC Analysis Graph)

Tablo 6. Kullanılan modellerin performansları (kötü huylu) (Performances of the models used (malignant))

Model	**Doğruluk Oranı (%)**
KNN	84,7
RO	82,3
NB	83,9
LR	82,1
YSA	98,4

Şekil 6'da çalışmadaki algoritmalara göre, doğruluk ve kayıp (hata) grafiğinde YSA algoritmasının hem eğitim hem de test sürecinde %99,1 ve %98,6 oranları ile daha başarılı olduğu görülmektedir.

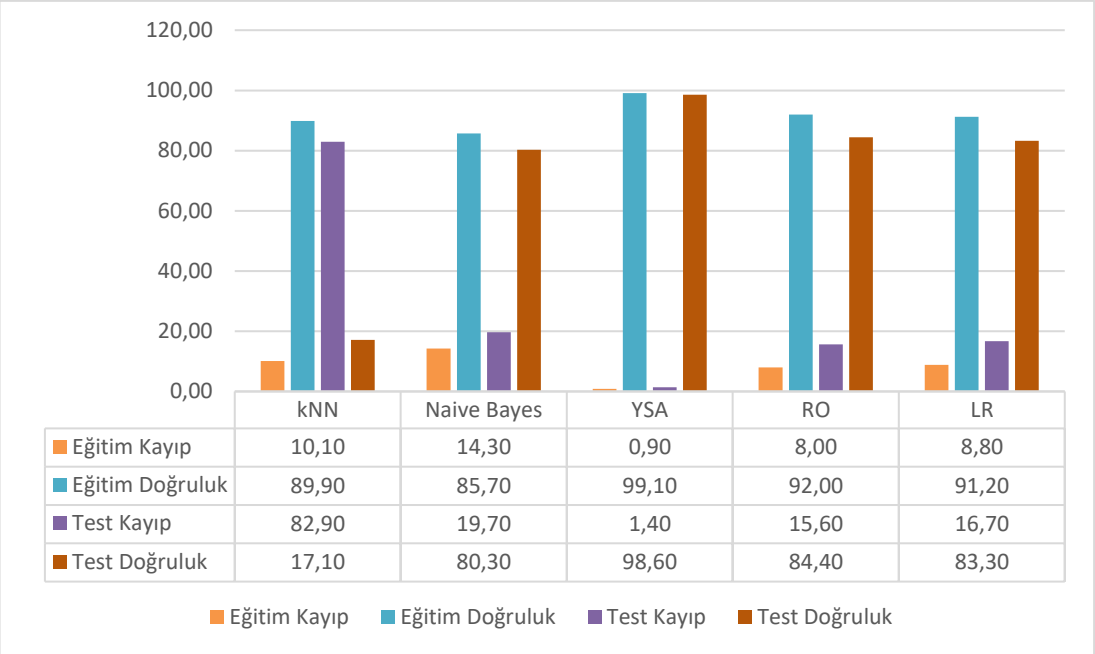

	kNN	Naive Bayes	YSA	RO	LR
Eğitim Kayıp	10,10	14,30	0,90	8,00	8,80
Eğitim Doğruluk	89,90	85,70	99,10	92,00	91,20
Test Kayıp	82,90	19,70	1,40	15,60	16,70
Test Doğruluk	17,10	80,30	98,60	84,40	83,30

Şekil 6. Kullanılan modellerin başarı oranları (Success rates of the models used)

Şekil 7'de test verisindeki YSA iyi huylu (benign) ve kötü huylu (malignant) çıktıları arasındaki dağılım diyagramı (Scatter Plot) verilmiştir. Bu diyagram aracılığıyla, değişkenler arasındaki ilişkinin sebebi görülemese de ilgili iki değişkenin arasında direkt olarak bir ilişki bulunup bulunmadığı ve bu ilişkinin ne derece güçlü olduğu görülmektedir.

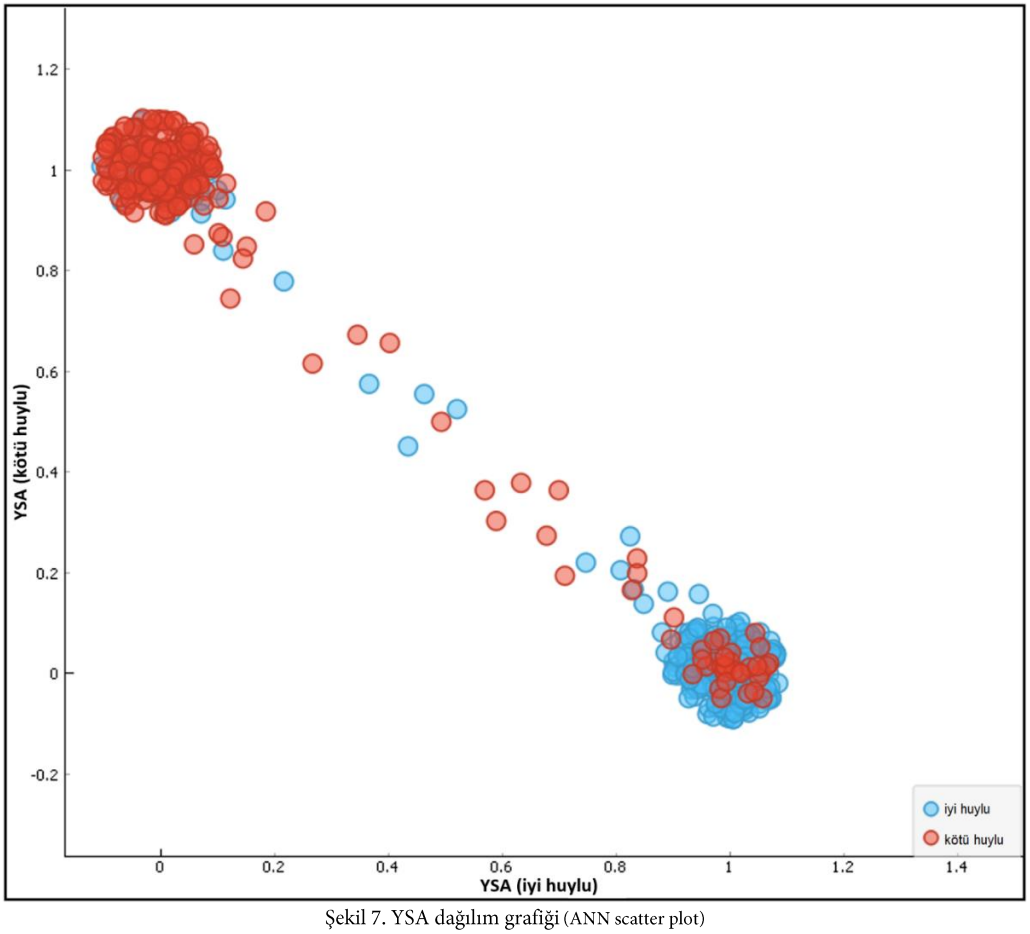

Şekil 7. YSA dağılım grafiği (ANN scatter plot)

Son olarak, önerilen 5 adet algoritma modelleri ile gerçek veriler kullanılarak 15 (onbeş) farklı test gerçekleştirilmiştir. Bu testlerden elde edilen deneysel sonuçlar Tablo 7'de verilmiştir. Tablo 7'de elde edilen bulgular incelendiğinde, oluşturulan YSA modelinin melanom cilt kanserini tahmin etmede diğer kullanılan algoritmalara göre daha yüksek bir başarıya sahip olduğu görülmektedir.

Tablo 7. Modellerden elde edilen deneysel sonuçlar (Experimental results obtained from models)

No	KNN	Hata (KNN)	RO	Hata (RO)	NB	Hata (NB)	LR	Hata (LR)	YSA	Hata (YSA)
1	79,4	20,6	81,1	18,9	80,4	19,6	89,4	10,6	98,7	1,3
2	81,41	18,59	85,3	14,7	80,3	19,7	81,41	18,59	98,5	1,5
3	90,14	9,86	84,8	15,2	83,2	16,8	85,14	14,86	97,6	2,4
4	83,6	16,4	80,6	19,4	82,17	17,83	83,6	16,4	98,8	1,2
5	79,15	20,85	88,81	11,19	81,65	18,35	79,15	20,85	98,6	1,4
6	81,96	18,04	89,3	10,7	80,78	19,22	81,96	18,04	98,7	1,3
7	81,6	18,4	83,5	16,5	79,5	20,5	81,6	18,4	99	1
8	81,6	18,4	85,41	14,59	78,24	21,76	81,6	18,4	98,3	1,7
9	85,4	14,6	80,39	19,61	77,53	22,47	95,4	4,6	98,4	1,6
10	82,6	17,4	86,98	13,02	83,46	16,54	82,6	17,4	98,9	1,1
11	80,56	19,44	81,63	18,37	84,79	15,21	82,56	17,44	98,7	1,3
12	85,8	14,2	86,74	13,26	80,2	19,8	85,8	14,2	98,6	1,4
13	85,04	14,96	81,12	18,88	83,88	16,12	85,04	14,96	98,7	1,3
14	81,96	18,04	85,15	14,85	75,1	24,9	79,96	20,04	98,7	1,3
15	85,01	14,99	85,27	14,73	80,32	19,68	80,01	19,99	99	1
Ortalama	83,02	16,98	84,41	15,59	80,77	19,23	83,68	16,32	98,61	1,39

Tablo 8, önerilen YSA ile literatürde yer alan diğer çalışmaları karşılaştırmayı temsil etmektedir. Tablo 8 incelendiğinde, Namozov ve ark. tarafından gerçekleştirilen çalışma sonucu hariç, diğer üç modelin birbirine yakın doğruluk oranlarına sahip olduğu, önerilen modelin ise diğer tüm modellerden daha yüksek performansa sahip olduğu açıkça görülmektedir.

Tablo 8. Literatürde elde edilen diğer sonuçlarla karşılaştırma (Comparison with other results obtained in the literature)

Çalışma	Model	Doğruluk
Farooq ve ark., [39]	Inception-V3 ve MobileNetV1	86%
Demir [40]	MobileNetV2, L1Norm, RD ve DVM	88.35%
Namozov ve ark.,[41]	CNN model with keratosis/vascular LeNet approach	95.86%
Harangi ve ark., [42]	CNN as single neural-net architecture	83.8%
Bütüner ve Calp (Önerilen Metot)	YSA tekniği	98.4%

4. Sonuçlar ve Öneriler (Conclusions and Recommendations)

Bu çalışmada, hastalardan alınan gerçek görüntüler kullanılarak KNN, NB, RO, LR ve YSA yöntemleri ile cilt kanseri hastalığı tahmin edilmiştir. Bu çerçevede, her bir yöntem için birer model oluşturulmuş ve gerçek verilerle test edilmiştir. Oluşturulan modeller içerisinden en iyi model belirlenmiş ve önerilmiştir. Önerilen model, cilt kanseri tespiti için hem zamandan hem de maliyetten büyük tasarruf sağlamaktadır. Ayrıca oluşturulan model, çok daha fazla veri setine ulaşarak kapsamlı bir değerlendirme yapabilen bir model ile daha sağlıklı sonuçlara ulaşılması sağlanabilir. Bu verilerin kullanılabilmesi, küresel, ulusal veya bölgesel çapta çeşitli analizlerin ve yeni bilimsel çalışmaların yapılmasına şüphesiz katkı sunacaktır.

Bununla birlikte, bu tür çalışmalar sağlıkla ilgili tüm alanlarda uygulanarak önemli gelişmelere ve sonuçlara katkı sağlayacaktır. Çalışmada, önerilen makine öğrenmesi tekniklerinin erken melanom cilt kanseri tanı

koymada geleneksel biyopsi yöntemlerinden daha etkili olduğu görülmüştür. Bu noktada, özellikle YSA yöntemi ile sınıflandırma ve tanıma uygulamalarında karar verme sürecinde çok etkili olduğu kanaatine varılmıştır. Geliştirilen bu sistemin melanom cilt kanserinin otomatik tanılama amacına hizmet etmesi beklenmektedir.

Bu çalışmanın sonraki aşamasında, önceden eğitilmiş modellerle birlikte farklı özellik seçme yöntemleri kullanılarak diğer veri kümelerinde de benzer başarı oranlarının elde edilmesi amacıyla araştırmalar yapılarak geliştirilecektir. Bu geliştirilecek araştırma veriseti genişletilerek gerçekleştirilecek ve elde edilen sonuçlar analiz edilecektir. Sonuç olarak yapılan çalışma, düşük hata oranı minimum maliyetle tanı ve teşhisin sağlanabilmesi ve makine öğrenme tekniklerinin sağlık alanında kullanılmasında etkili olduğunu ortaya koymuştur.

Çıkar Çatışması Beyanı (Conflict of Interest Statement)

Yazarlar tarafından herhangi bir çıkar çatışması bildirilmemiştir.

Kaynaklar (References)

[1] O. Baykara, "Kanser Tedavisinde Güncel Yaklaşımlar," *Balıkesir Sağlık Bilimleri Dergisi,* vol.5, no. 3, pp. 154-165, 2016.

[2] WHO, "Cancer," *WHO-Home/Newsroom/Fact sheets/Detail/Cancer,* [Online]. Available: https://www.who.int/news-room/fact-sheets/detail/cancer. [Accessed: 3.02. 2023].

[3] Z. Faisal and N. Abbadi, "New Segmentation Method for Skin Cancer Lesions," *Journal of Engineering and Applied Sciences,* vol. 12, no. 21, pp. 5598-5602, 2017.

[4] K. H. Güngör, "Metastaz Yapmamış Melanoma ve Melanoma Dışı Deri Kanserleri için Geliştirilmiş Olan Deri Kanseri İlişkili Yaşam Kalitesi Ölçeğinin (Dkykö) Türkçe Geçerlilik ve Güvenilirliğinin Araştırılması," Tıpta Uzmanlık Tezi, Ankara Üniversitesi Tıp Fakültesi, Ankara, 2016.

[5] E. Acer ve H. K. Erdoğan, "Sık Görülen Deri Kanserlerinin Epidemiyolojisi," *Dermatoloji ve Halk Sağlığı Özel Sayısı,* vol.4, no. 1, ss. 52-60, 2019. doi:10.35232/estudamhsd.499257

[6] A. Staff, "Cancer Facts and Figures Atlanta: American Cancer Society," *Cancer,* vol. 9, pp. 19-20, 2018.

[7] A. Sümen ve S. Öncel, "Türkiye'de cilt kanseri ve güneşten korunmaya yönelik yapılan araştırmaların incelenmesi," *Türkiye Klinikleri Hemşirelik Bilimleri Dergisi,* vol. 10, no. 1, ss. 59-69, 2018. doi:10.5336/nurses.2017-56858

[8] A. M. Glazer, D. S. Rigel, R. R. Winkelmann and A. S. Farberg "Clinical diagnosis of skin cancer: enhancing inspection and early recognition," *Dermatologic Clinics,* vol. 35, no. 4, pp. 409-416, 2017. doi:10.1016/j.det.2017.06.001

[9] C. P Akyel, ve N. Arıcı, "Cilt kanserinde kıl temizliği ve lezyon bölütlemesinde yeni bir yaklaşım," *Politeknik Dergisi,* vol. 23, no. 3, ss. 821-828, 2020.

[10] Ü. Yılmaz, Yapay Sinir Ağları ile Melanom Cilt Kanseri Tespiti, Geleceğin Dünyasında Bilimsel ve Mesleki Çalışmalar, Ekin Basım Yayın Dağıtım, 2019, pp.104-114.

[11] K. Lacy and W. Alwan, "Skin cancer," *Medicine,* vol. 41, no. 7, pp. 402-405, 2013. doi:10.1016/j.mpmed.2013.04.008

[12] E. Craythorne and F. Al-Niami, "Skin cancer," *Medicine,* vol. 45, no. 7, pp. 431-434, 2017. doi:10.1016/j.mpmed.2017.04.003

[13] A. H. Alasadi and B. M. ALsafy, "Early detection and classification of melanoma skin cancer," *Int. Journal of Information Technology and Computer Science,* vol. 7, no.12, pp. 67-74, 2017.

[14] P. Das, N., Deshmukh, N., Badore, C., Ghulaxe, and P., Patel, "A review article on melanoma," *Journal of Pharmaceutical Sciences and Research,* vol. 8, no. 2, pp. 112-117, 2016.

[15] F. Alendar, I., Drljević, K., Drljević, and T., Alendar, "Early detection of melanoma skin cancer," *Bosnian Journal of Basic Medical Sciences,* vol. 9, no. 1, pp. 77-80, 2009. doi:10.17305/bjbms.2009.2861

[16] M. Demirci ve İ. Yabanova, "Model Tabanlı Tasarım Metotları Kullanılarak Gerçek Zamanlı Bir Görüntü İşleme Sisteminin Tasarımı ve Gerçeklemesi," *Politeknik Dergisi,* vol. 22, no. 4, pp. 827-838, 2019. doi:10.2339/politeknik.423603

[17] Ş. Sağıroğlu ve E. Beşdok, "A Novel Approach for Image Denoising Based on Artificial Neural Networks," *Politeknik Dergisi,* vol. 15, no. 2, pp. 71-86, 2012. doi:10.2339/2012.15.2, 71-86

[18] A. Kassam, "Segmentation of Skin Cancer by Using Image Processing Techniques," Master Thesis, Yıldız Technical University Department Of Computer Engineering, İstanbul, 2016.

[19] T. Lee, V., Ng, R., Gallagher, A., Coldman, and D., McLean, "Dullrazor: A Software Approach to Hair Removal from Images," *Computers in biology and medicine,* vol. 27, no. 6, pp. 533-543, 1997. doi:10.1016/S0010-4825(97)00020-6

[20] E.C. Celebi, Y., Alp Aslandogan, W. V., Stoecker, H., Iyatomi, H., Oka, and X. Chen,, "Unsupervised Border Detection in Dermoscopy Images," *Skin Researchand Technology,* vol. 13, no. 4, pp. 454- 462, 2007. doi:10.1111/j.1600-0846.2007.00251.x

[21] M.Z. Alom, T. Aspiras, T.M. Taha and V. K. Asari, "Skin Cancer Segmentation and Classification with NABLA-N and Inception Recurrent Residual Convolutional Networks," 2019. doi:10.48550/arXiv.1904.11126

[22] M. Toğaçar, Z. Cömert, and B. Ergen, "Intelligent skin cancer detection applying autoencoder, MobileNetV2 and spiking neural networks," *Chaos, Solitons and Fractals,* vol. 144, no. 1, pp.110714, 2021. doi:10.1016/J.CHAOS.2021.110714

[23] P. P. Tumpa and M. A. Kabir, "An artificial neural network based detection and classification of melanoma skin cancer using hybrid texture features," *Sensors International,* vol. 2, no. 1, pp.100128, 2021. doi:10.1016/J.SINTL.2021.100128

[24] A.M. Alqudah, H. Alquraan and I.A. Qasmieh, "Segmented and non-segmented skin lesions classification using transfer learning and adaptive moment learning rate technique using pretrained convolutional neural network," *Journal of Biomimetics, Biomaterials and Biomedical Engineering,* vol. 42, pp. 67–78, 2019. doi:10.4028/www.scientific.net/JBBBE.42.67

[25] T.J. Brinker, A. Hekler, A.H. Enk, C. Berking, S. Haferkamp, A. Hauschild and J.S. Utikal, "Deep neural networks are superior to dermatologists in melanoma image classification," *European Journal of Cancer,* vol. 119, pp. 11–17, 2019. doi:10.1016/j.ejca.2019.05.023

[26] K.M. Hosny, M.A. Kassem and M.M. Foaud, "Classification of skin lesions using transfer learning and augmentation with AlexNet," *PloS one,* vol. 14, no. 5, pp. 217-293, 2019. doi:10.1371/journal.pone.0217293

[27] J. Han, J. Pei and Kamber, M. Data Mining: Concepts and Techniques, Elsevier, 2011, pp. 2-10.

[28] D. Kilinc, E. Borandag, F. Yucalar, V. Tunali, M. Simsek, and A. Ozcift, "Classification of Scientific Articles Using Text Mining with KNN Algorithm and R Language," *Marmara Journal of Pure and Applied Sciences,* vol.3, pp. 89-94, 2016. doi:10.7240/mufbed.69674

[29] T. Savaş and S. Savaş, "Tekdüzen Kaynak Bulucu Yoluyla Kimlik Avı Tespiti için Makine Öğrenmesi Algoritmalarının Özellik Tabanlı Performans Karşılaştırması," *Politeknik Dergisi,* vol. 25, no. 3, ss. 1261-1270, 2022. doi:10.2339/politeknik.1035286

[30] L. Breiman, Random Forest. Machine Learning, Statistics Department-University of Californiavol, vol. 45, pp. 5-32, 2001. doi:10.1023/A:1010933404324

[31] D.D. Lewis, "Naive Bayes at forty: The independence assumption in information retrieval," *Proceedings of the Tenth European Conference on Machine Learning,* Part of the Lecture Notes in Computer Science book series (LNAI), vol.1398, pp. 4-15, 1998.

[32] H.K. Yıldız, M. Gençtav, N. Usta, B. Diri and M. F. Amasyalı, "Metin Sınıflandırmada Yeni Özellik Çıkarımı," *15. Sinyal İşleme ve İletişim Uygulamaları Kurultayı,* 2007.

[33] S. Savaş, "Naive Bayes Sınıflandırıcısı," Teori ve Uygulamada Makine Öğrenmesi, Nobel Akademik Yayıncılık Eğitim Danışmanlık Tic. Ltd. Şti, ss. 69-92, 2022.

[34] C. Yerdelen, "Mevsimlik Kar Erimesinin Yapay Sinir Ağları Yöntemi ile Tahmin Edilmesi," *Sakarya Üniversitesi Mühendislik ve Mimarlık Fakültesi Dergisi,* vol. 21, pp. 3-4, 2006.

[35] M.H. Calp and U. Kose, "Estimation of burned areas in forest fires using artificial neural networks," *Ingeniería Solidaria,* vol. 16, no. 3, pp. 1-22, 2022.

[36] M. H. Calp and M. A. Akcayol, "Yazılım projeleri için yapay sinir ağlarına dayalı web tabanlı risk yönetim sisteminin tasarımı ve gerçekleştirilmesi: WEBRISKIT," *Pamukkale Üniversitesi Mühendislik Bilimleri Dergisi,* vol. 26, no. 5, ss. 993-1014, 2020. doi:10.5505/pajes.2019.29964

[37] M.H. Dunham, "Data Mining introductori and advanced topics," New Jersey: Prentige Hall, 2003.

[38] B. Ekici and H. Takcı, "Bilgisayar Ağlarında Anomali Tespiti Yaklaşımı ile Saldırı Tespiti," *Afyon Kocatepe Üniversitesi Fen ve Mühendislik Bilimleri Dergisi,* vol. 22, no. 5, ss. 1016-1027, 2022. doi:10.35414/akufemubid.1114906

[39] M.A. Farooq, A., Khatoon, V., Varkarakis, and P. Corcoran, "Advanced Deep Learning Methodologies for Skin Cancer Classification in Prodromal Stages 2020," *arXiv preprint* arXiv:2003.06356.

[40] F. Demir, "Derin öğrenme tabanlı yaklaşımla kötü huylu deri kanserinin dermatoskopik görüntülerden saptanması," *Fırat Üniversitesi Mühendislik Bilimleri Dergisi,* vol. 33, no. 2, ss. 617-624, 2021.

[41] A. Namozov, D. Ergashev and Y.I. Cho, "Adaptive activation functions for skin lesion classification using deep neural networks," in *Proceedings- 2018 Joint 10th International Conference on Soft Computing and Intelligent Systems and 19th International Symposium on Advanced Intelligent Systems,* SCIS-ISIS 2018, ss. 232– 235, 2018. doi:10.1109/SCIS-ISIS.2018.00048

[42] B. Harangi, A. Baran and A. Hajdu, "Classification of Skin Lesions Using An Ensemble of Deep Neural Networks," in *Proceedings of the Annual International Conference of the IEEE Engineering in Medicine and Biology Society,* EMBS, 2018-July, pp. 2575–2578, 2018. doi:10.1109/EMBC.2018.8512800

This is an open access article under the CC-BY license

Research Article/Araştırma Makalesi

Gazi AKADEMİK YAYINCILIK

GAZİ
JOURNAL OF ENGINEERING SCIENCES

Lightweight Periodic Vibration Isolator Design via Compliant Inertial Amplification Mechanisms with Stiffness Maximized Topologies

Osman Yüksel[*a], Erol Türkeş[b]

Submitted: 28.11.2023 Revised: 20.04.2024 Accepted: 25.04.2024 doi:10.30855/gmbd.0705N13

ABSTRACT

As a novel innovative approach in the literature, periodic structures can be utilized as vibration isolators. In this paper, vibration isolation performance of a lightweight periodic structure is studied. The periodic structure is formed by using inertial amplification mechanisms with stiffness maximized topologies. First of all, inertial amplification concept is introduced on a lumped parameter model. Then, a compliant inertial amplification mechanism, which is the repetitive building block of the periodic structure (i.e., unit cell), is presented. Topology optimization is conducted on this mechanism to attain a stiffness maximized unit cell with reduced weight. After that, a one-dimensional periodic structure is constructed by attaching the lightweight inertial amplification unit cells with stiffness maximized topologies to each other. Finally, vibration isolation performance of the constructed periodic structure is demonstrated via transmissibility plots. It is observed that the designed topologically optimized lightweight periodic structure provides high performance vibration isolation for a wider frequency range with the same stiffness value and less weight, compared to the original structure.

Keywords: Compliance minimization, inertial amplification, periodic structure, topology optimization, vibration isolator

[a,*] Kırklareli University, Faculty of Engineering, Dept. of Mechanical Engineering 39010 - Kırklareli, Türkiye
Orcid: 0000-0001-9492-1756
e-mail: osmanyuksel@klu.edu.tr

[b] Kırklareli University, Faculty of Engineering, Dept. of Mechanical Engineering 39010 - Kırklareli, Türkiye
Orcid: 0000-0002-9601-7119
e-mail: erol.turkes@klu.edu.tr

*Corresponding author: osmanyuksel@klu.edu.tr

Direngenliğin Maksimize Edildiği Topolojilere Sahip Esnek Atalet Artırımı Mekanizmaları ile Düşük Ağırlıklı Periyodik Titreşim Yalıtıcısı Tasarımı

ÖZ

Periyodik yapıların titreşim yalıtıcısı olarak kullanılması son zamanlarda literatürde karşılaşılan yenilikçi bir yaklaşımdır. Bu makalede, düşük ağırlıklı bir periyodik yapının titreşim yalıtımı performansı çalışılmıştır. Periyodik yapı, direngenliğin maksimize edildiği topolojilere sahip atalet artırımı mekanizmaları kullanılarak oluşturulmuştur. İlk olarak, atalet artırımı kavramı toplu parametreli bir model üzerinde tanıtılmıştır. Ardından, periyodik yapının tekrar eden yapı bloğu (birim hücre) olan esnek bağlantılı bir atalet artırımı mekanizması sunulmuştur. Direngenliğin maksimize edildiği düşük ağırlıklı bir birim hücre elde etmek için, bu esnek bağlantılı mekanizma üzerinde topoloji eniyilemesi gerçekleştirilmiştir. Daha sonrasında, direngenliğin maksimize edildiği topolojilere sahip bu düşük ağırlıklı atalet artırımı birim hücreleri birleştirilerek bir boyutlu periyodik bir yapı elde edilmiştir. Son olarak, titreşim iletkenliği grafikleri vasıtasıyla, oluşturulan periyodik yapının titreşim yalıtımı performansı gösterilmiştir. Tasarlanan topolojik olarak eniyilenmiş düşük ağırlıklı periyodik yapının, aynı direngenlikteki eniyileme yapılmamış orijinal yapıya nazaran, daha düşük bir ağırlık ile çok daha geniş bir bant aralığında yüksek performanslı titreşim yalıtımı sağladığı saptanmıştır.

Anahtar Kelimeler: esneklik minimizasyonu, atalet artırımı, periyodik yapı, topoloji eniyilemesi, titreşim yalıtıcısı

To cite this article: O. Yuksel and E. Turkes, "Lightweight Periodic Vibration Isolator Design via Compliant Inertial Amplification Mechanisms with Stiffness Maximized Topologies", *Gazi Journal of Engineering Sciences*, vol.10, no.1, pp. 155-171, 2024. doi:10.30855/gmbd.0705N13

1. Introduction

Achieving vibration control is crucial for mechanical and/or civil engineers, since uncontrolled excitations can result in catastrophic failure situations such as broken apart machine parts and collapsed mechanical structures. In order to mitigate undesired oscillations, active [1-6] and passive [7-11] vibration control methods can be employed. Active control methods require power sources and controllers to deal with mechanical oscillations. On the other hand, propagating waves can be isolated or absorbed by means of passive methods, without employing any electronic device, power source and circuit.

As a subgenre of passive methods, in vibration isolation technique, excitation source and target structure to be protected are separated by an object called vibration isolator. Incoming mechanical waves are directed back to the source by the isolator, hence target end is protected from exposure to excessive oscillations. Traditionally, vibration isolators are constructed with employing springs and dampers [12,13]. On the other hand, as an innovative approach, periodic structures can be utilized as passive vibration isolators, as well [14-18]. These periodic structures can be Bragg [19,20], local resonance [21,22], or inertial amplification [23,24] types.

In the literature, by employing inertial amplification type periodic structures, one can obtain high performance vibration isolators, in which satisfactory levels of isolation can be achieved for wide frequency ranges. Acar and Yilmaz [25] designed a two-dimensional periodic structure via compliant inertial amplification mechanisms of rectangular type. On that structure, size optimization was performed to enhance vibration stop band properties in the low frequency region. Taniker and Yilmaz [26] investigated a three-dimensional periodic structure constructed with lumped parameter inertial amplification mechanisms in face centered cubic and body centered cubic formations for the purpose of mitigating incoming mechanical vibrations for the low frequency band. Yuksel and Yilmaz [27] designed a two-dimensional periodic structure via shape optimized compliant inertial amplification mechanisms to achieve low frequency vibration isolation. On that study, superiority of shape optimization over size optimization on vibration stop band characteristics was also demonstrated. Taniker and Yilmaz [28] designed a three-dimensional octahedron type periodic structure with triangular type compliant inertial amplification mechanisms for the purpose of achieving three-dimensional vibration isolation for the low frequency region. Frandsen et al. [29] connected periodic lumped parameter inertial amplification mechanisms to a continuous beam structure for the purpose of attaining vibration isolation for a certain frequency band. Taniker and Yilmaz [30] designed a one-dimensional periodic structure via compliant inertial amplification mechanisms with flexure hinges to obtain an ultrawide vibration stop band for the mechanical waves coming from one direction. Yuksel and Yilmaz [31] compared size and topology optimized compliant inertial amplification mechanisms with the same mass regarding to their vibration stop band characteristics. As one suggests, topology optimized periodic structure provided better vibration isolation for a wider frequency range. Barys et al. [32] composed periodic structures with lumped parameter inertial amplification mechanisms and local resonators and they compared these structures with each other. Besides, efficacy of inertial amplification method over local resonance method was investigated and discussed. Orta and Yilmaz [33] designed a one-dimensional periodic low frequency vibration isolator by utilizing compliant inertial amplification mechanisms which converts axial motion to rotary motion. Li et al. [34], formed a periodic structure with composite sandwich beams, which has a lattice structure constructed with both translational and rotational springs inside and lumped inertial amplification mechanisms outside. Yuksel and Yilmaz [35] designed a two-dimensional ultrawide low frequency periodic vibration isolator with topologically optimized compliant inertial amplification mechanisms with flexure hinge connections and instant center of rotation. The proposed design provided ultrawide vibration isolation for the low frequency band, for longitudinal and transverse incoming mechanical waves. Muhammad et al. [36] studied a one-dimensional periodic beam with variable cross-sectional area and attached lumped parameter inertial amplification mechanisms, in order to mitigate transverse mechanical vibration propagation along the structure for a certain frequency range. Yuksel and Yilmaz [37] designed a two-dimensional broadband periodic structure as a vibration isolator with topologically optimized triangular type

basic compliant inertial amplification mechanisms. Mizukami et al. [38] designed a two-dimensional periodic vibration isolator utilizing truss type compliant inertial amplification mechanisms with carbon-fiber composite material. Xi et al. [39], improved a corrugated-core sandwich panel structure's vibration properties by using periodically attached lumped parameter inertial amplification mechanisms with four bar connections. Mi and Yu [40], added periodic lumped parameter inertial amplification mechanisms to the host structure in order to enhance sound transmission of a beam. Miniaci et al. [41], discussed the effect of prestress conditions on vibration isolation stop band properties of a periodic structure constructed with rectangular type compliant inertial amplification mechanisms. Banerjee et al. [42] investigated a lumped parameter periodic structure's vibration isolation band gap properties. The periodic structure was composed of periodic inclusion of lumped inertial amplification mechanisms coupled with local resonators. Li and Zhou [43] formed a periodic structure by using scissor-like inertial amplification mechanisms to reduce low frequency vibration transmission. Er et al. [44], conducted a parametric study on basic rhombus type compliant inertial amplification mechanism configurations to enhance periodic structure's vibration isolation performance. Zeng et al. [45] formed a periodic structure using a distributed parameter inertial amplification model with levered mass configuration. Li et al. [46], examined a periodic structure constructed with lumped parameter elastic inertial amplification mechanism building blocks. Li et al. [47] analyzed a periodic structure, which set up by utilizing a nonlinear lumped parameter inertial amplification mechanism model. Li et al. [48] improved a double beam structure's vibration characteristic via periodically employing double inertial amplification mechanisms throughout the body. Ni and Shi [49] proposed a beam structure with periodically attached levered mass type lumped parameter inertial amplifiers and they studied vibration transmission properties of the suggested frame. As can be seen from the literature review, there are numerous designs that consider vibration isolation properties primarily. However, it is also important for the structure to withstand static loads, as well. To that end, stiffness based optimized isolator designs should also be addressed.

In this study, a one-dimensional periodic vibration isolator is designed using compliant inertial amplification mechanisms as unit cells. In order to maximize the structure's stiffness and reduce the material amount used, topology optimization is conducted on the compliant mechanism. The vibration isolation performance of the topologically stiffness maximized lightweight periodic structure is demonstrated via transmissibility plots.

2. Inertial Amplification Method

Inertial amplification [23, 24] is one of the stop band generation methods available in the literature [50]. A stop band is described as a frequency range (band) in which waves cannot propagate [51]. Hence, a structure with a stop band can be considered to be used as a vibration isolator for the stop band frequency range. Inertial amplification is a powerful stop band creation method, so that, one can obtain vibration isolation frequency bands at low frequency regions without decreasing stiffness or increasing mass of an isolator structure.

2.1. Lumped parameter model

In Figure 1, a lumped parameter inertial amplification mechanism model [25,27] is shown. In this mechanism, masses at two ends (donated with m) are connected with a spring with stiffness k, whereas amplifier mass m_a is connected both of the masses m with rigid links. Rigid links and spring do not possess any mass. At the same time, all masses do not deform, that is to say, they do not have any stiffness value. Hence, the mechanism shown in Figure 1 indicates a discrete (lumped parameter) model. The acute angle between the rigid links and the spring is called as θ. The input vibration y is given from the left side and the output vibration x is received from the right side of the mechanism. Therefore, for small y, and x values, the horizontal displacement of amplifier mass m_a becomes $(x+y)/2$ whereas, the vertical displacement is $(y-x)\cot(\theta)/2$ [52].

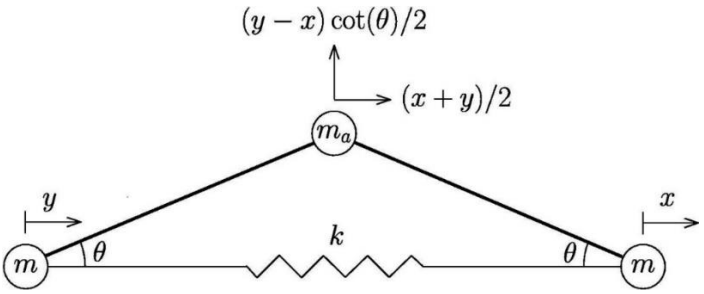

Figure 1. Lumped parameter inertial amplification mechanism.

The equation of motion of the lumped parameter model provided in Figure 1 can be obtained by employing the Lagrange method. For this purpose, the kinetic (T) and the potential (V) energies of the system need to be defined:

$$T = \frac{1}{2}m_a\left[\left(\frac{\dot{x}+\dot{y}}{2}\right)^2 + \left(\frac{\dot{y}-\dot{x}}{2}\cot\theta\right)^2\right] + \frac{1}{2}m\dot{x}^2 + \frac{1}{2}m\dot{y}^2 \quad (1)$$

$$V = \frac{1}{2}k(x-y)^2 \quad (2)$$

Moreover, the Lagrange function ($\mathscr{L}$) is defined as:

$$\mathcal{L} = T - V \quad (3)$$

Hence, the Lagrange function of the system shown in Figure 1 becomes:

$$\mathcal{L} = \frac{1}{2}m_a\left[\left(\frac{\dot{x}+\dot{y}}{2}\right)^2 + \left(\frac{\dot{y}-\dot{x}}{2}\cot\theta\right)^2\right] + \frac{1}{2}m\dot{x}^2 + \frac{1}{2}m\dot{y}^2 \;\; - \frac{1}{2}k(x-y)^2 \quad (4)$$

Besides, the Lagrange equation for the generalized coordinate x is given as:

$$\frac{d}{dt}\left(\frac{\partial\mathcal{L}}{\partial\dot{x}}\right) - \frac{\partial\mathcal{L}}{\partial x} = 0 \quad (5)$$

Finally, when Equation (5) is solved for Equation (4), the equation of motion is obtained:

$$[m_a\,(\cot^2\theta + 1)/4 + m]\ddot{x} + kx = [m_a\,(\cot^2\theta - 1)/4]\ddot{y} + ky \quad (6)$$

When the right side of Equation (6) is equated to zero and the left side is solved for the output x, one can obtain the resonance frequency (ω_p) as:

$$\omega_p = \sqrt{\frac{k}{m_a\,(\cot^2\theta+1)/4+m}} \quad (7)$$

As can be seen from Equation (7), the stiffness value of the system remains as k. On the other hand, by using displacement amplification mechanism, the single degree of freedom system's dynamic mass is increased by $m_a\,(\cot^2\theta + 1)/4$ amount compared to the ordinary mass-spring system's mass m.

Besides, when the left side of Equation (6) is equated to zero and the right side is solved for the input y, one can obtain the antiresonance frequency (ω_z) as:

$$\omega_z = \sqrt{\frac{k}{m_a\,(\cot^2\theta-1)/4}} \quad (8)$$

As seen from Equations (7) and (8), mechanism's resonance frequency (ω_p) is always lower than its antiresonance frequency (ω_z), which implies that the lumped parameter model in Figure 1 is a vibration isolator of low pass filter type [8]. Vibration transmissibility of this type of isolator can be calculated as a

function of a given excitation frequency by using input and output displacements (respectively y and x) or input and output accelerations (respectively $\ddot{y}$ and $\ddot{x}$) as [25, 27]:

$$TR(\omega_e) = \frac{|x(\omega_e)|}{|y(\omega_e)|} = \frac{|\ddot{x}(\omega_e)|}{|\ddot{y}(\omega_e)|} = \frac{|1-(\omega_e/\omega_z)^2|}{|1-(\omega_e/\omega_p)^2|} \tag{9}$$

where ω_e denotes excitation frequency. When transmissibility value for a given excitation frequency (ω_e) is lower than 1, it means less amount of input oscillations sent from one end can arrive to the output end. Vibration isolation frequency band starts at the frequency limit where the vibration transmissibility value is equal to 1 [25, 27]:

$$\omega_s = \sqrt{\frac{2\omega_p^2\omega_z^2}{\omega_p^2+\omega_z^2}} \tag{10}$$

For the frequencies, which are higher than the stop band starting frequency ω_s, vibration transmissibility value is always lower than 1, hence vibration isolation is achieved. The lumped parameter system in Figure 1 has only one resonance and one antiresonance frequencies. Therefore, vibration stop band created via this mechanism does not have any upper bound (i.e., semi-infinite stop band).

2.2. Compliant inertial amplification mechanism

In Figure 2, a compliant inertial amplification mechanism [25,27] is presented. In compliant mechanisms, bearings and hinges are not utilized. Instead, relative motion between the links are achieved as a result of deflecting flexible members [53]. The compliant inertial amplification mechanism shown in Figure 2 is a distributed parameter system. Hence, it has multiple resonance and antiresonance frequencies, which imply that vibration isolation stop band has an upper bound. It has shown in the literature that, inertial amplification induced vibration stop bands can be created between the first and the second non rigid in plane vibration modes of the compliant mechanism [25,27]. In Figure 2; l_1, l_2, l_3, l_4 denote the lengths and t_1, t_2, t_3, t_4 denote the thicknesses of the corresponding beams.

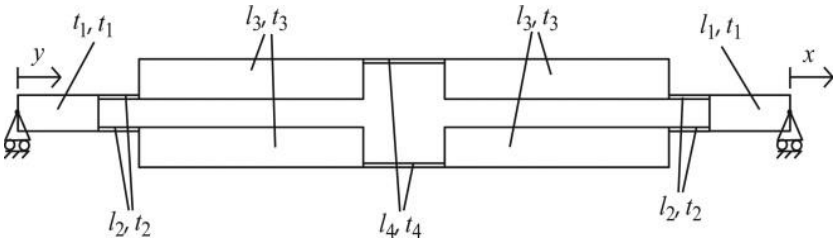

Figure 2. Compliant inertial amplification mechanism.

In order to perform structural topology optimization on this compliant mechanism, finite element method needs to be employed. For this purpose, two-dimensional four node eight degrees of freedom square plane stress finite elements are utilized.

3. Topology Optimization

3.1. General stiffness maximization problem

Topology optimization is the most comprehensive form of structural optimization field since it involves both size and shape optimization while altering a structure's topology [54]. For stiffness maximization (i.e., compliance minimization) topology optimization problems, for a prescribed loading and boundary

conditions, the aim is to find the stiffest structure with certain amount of material. The mathematical description for this kind of optimization problem can be formulated as [55]:

$$\begin{aligned} &\text{minimize}_{\ \boldsymbol{d}}: && comp(\boldsymbol{d}) = \boldsymbol{u}^T \boldsymbol{K}\boldsymbol{u} \\ &\text{subject to}\ : && \boldsymbol{K}\boldsymbol{u} = \boldsymbol{f} \\ & && V(\boldsymbol{d}) = aV_0 \\ & && \mathbf{0} \le \boldsymbol{d} \le \mathbf{1} \end{aligned} \tag{11}$$

where; $\boldsymbol{u}$ is the global displacement vector, $\boldsymbol{K}$ is the global stiffness matrix, $\boldsymbol{f}$ is the global force vector, V_0 is the design domain volume, $V(\boldsymbol{d})$ is the material volume, a is the volume fraction, $\boldsymbol{d}$ is the design variable vector. Each finite element constituting the design space has an individual design variable value between 0 (void) and 1 (solid). At the end of the optimization process, the aim is to reach a solid or void type of design.

3.2. Topology optimized compliant inertial amplification mechanism

In the literature it has shown both numerically and experimentally that, various versions of structurally optimized compliant inertial amplification mechanism given in Figure 2 isolate incoming excitations effectively for wide frequency bands [25,27,31]. In these optimization studies, vibration isolation frequency band is increased for a given amount of material, hence for the same mass, vibration isolation is achieved for wider frequency regions. On the other hand, for some circumstances, it could be desirable for a vibration isolator to be able to carry load. Therefore, stiffness of a vibration isolator should also be taken into account in the design process, as well. So far, the effort shown concentrated on increasing the stop band frequency range. Yet, in this study, another important design criterion, stiffness is considered. In order to observe the relationship between the stiffness and vibration isolation performance of the compliant mechanism provided in Figure 2, topology optimization studies are conducted.

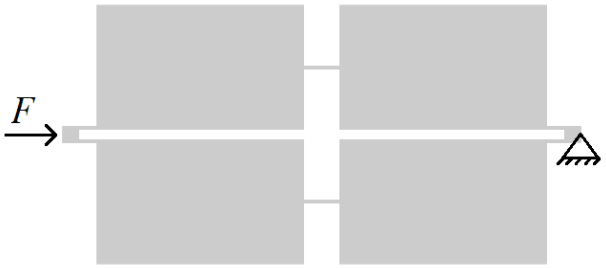

Figure 3. Stiffness maximization (compliance minimization) topology optimization problem design space.

In Figure 3, stiffness maximization topology optimization problem design space is shown. A unit static force is applied on the left side of the mechanism while at the right end pinned boundary condition is employed. Since, a one-dimensional periodic structure will be formed via incorporating the mechanism in horizontal alignment, stiffness maximization for this direction is considered. The mechanism has 120 mm length in horizontal and 60 mm width in vertical dimensions. The finite element discretization of the design space is 120 × 60. That is to say, 7200 four node eight degrees of freedom plane stress elements with 1 mm × 1 mm dimensions are utilized. Besides, beam dimensions are determined as: l_1=4 mm, t_1 = 4 mm, l_2 = 4 mm, t_2 = 1 mm, l_3 = 48 mm, t_3 = 29 mm, l_4 = 8 mm, t_4 = 1 mm. Moreover, the 4th beams connect to the 3rd beams at the middle. An isotropic material with modulus of elasticity E=210 GPa, Poisson's ratio ν = 0.3 and density ρ = 7800 kg/m^3 is considered.

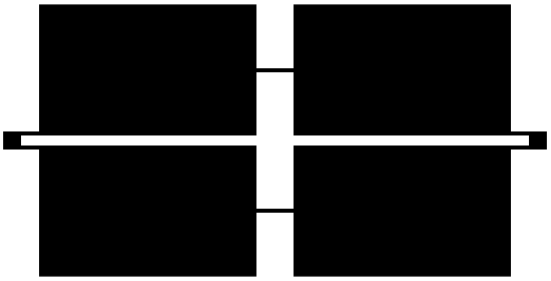

Figure 4. Compliant inertial amplification mechanism design with 100 % material utilized.

In topology optimization, an open source MATLAB code [55] and a post-processing filter [56] are utilized, and stiffness maximized inertial amplification mechanisms are obtained for several percent material volume fraction values. In Figure 4, a design, which has 100 % material utilized, is shown. As can be seen, it is a design in which the design space in Figure 3 is fully solid. For other material volume fraction values, the optimization problem presented in Eq. (11) is solved. In Figure 5, several stiffness maximized designs are shown, for which, 100 %, 80 %, 60 % and 40 % material in the design space is utilized. Figure 5, also shows the evolutionary path of the stiffness maximized mechanism as a function of material percentage utilized. It is important to note that, optimized structures' stiffness values almost remain the same. For instance, the difference between the stiffness values of the mechanism with 100 % material utilized (Figure 5a) and the mechanism with 40 % material utilized (Figure 5d) is only 0.06 %, which implies that the stiffness values are essentially the same. Such a result is expected, since the axial stiffness of the mechanism primarily depends on the dimensions of the flexure hinges (i.e., beams enumarated as 2 and 4) and their connection positions to the remaining parts (i.e., beams enumarated as 1 and 3) [31,35].

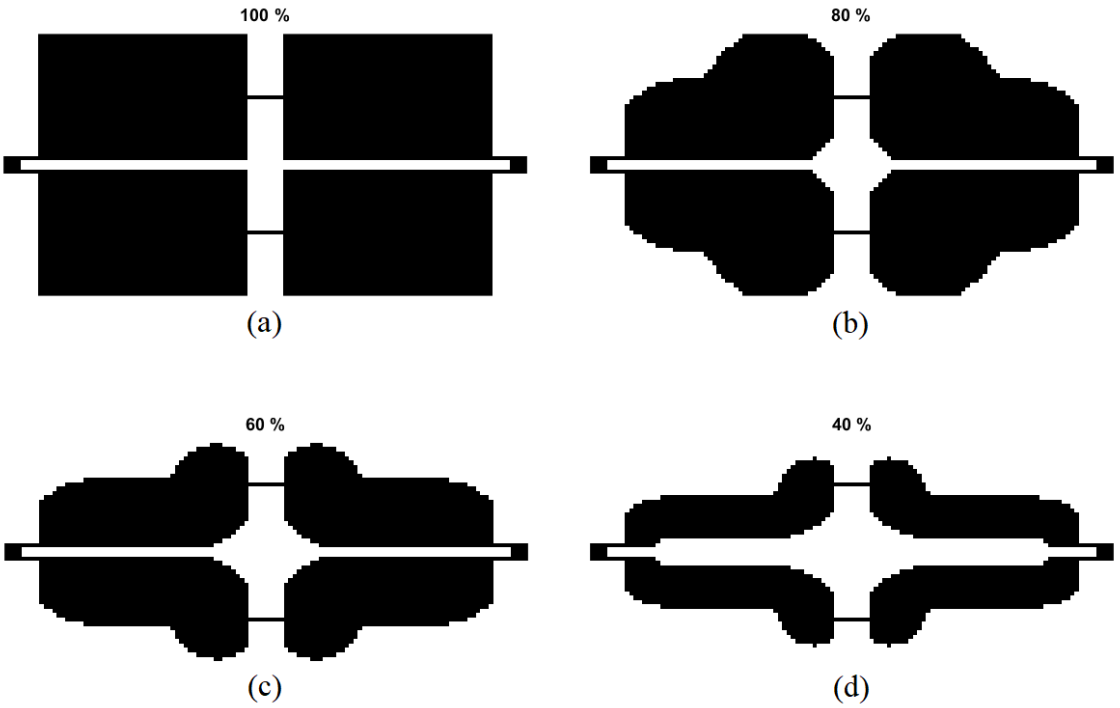

Figure 5. Designs with various material percentages utilized in the design space: (a) design with 100 % material used, (b) design with 80 % material used, (c) design with 60 % material used, (d) design with 40 % material used. To note that, stiffness values for all of the mechanisms from (a) to (d) are essentially the same (e.g., the difference between the stiffness values for 100 % material utilized design and 40 % material utilized design is only 0.06 %.)

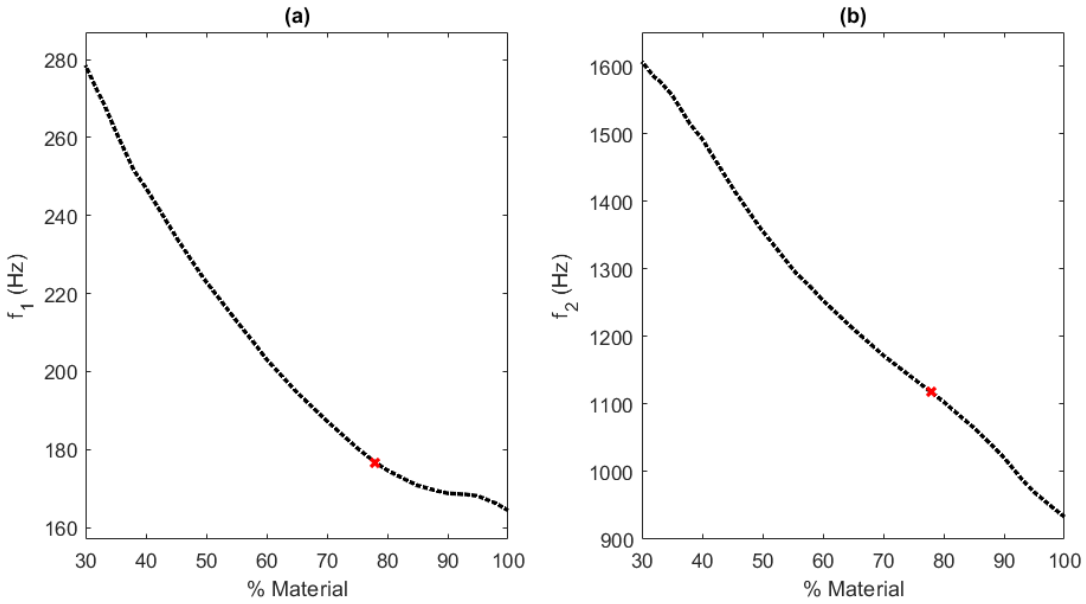

Figure 6. Variation of (a) first and (b) second natural frequencies of distributed parameter inertial amplification mechanism model with respect to % material (volume fraction) of the design space given in Fig. 3. Red cross indicates the values for the topology optimized design in Fig. 8 and 100 % indicates the values for the design in Fig. 4.

As stiffness of the structure given in Figure 3 essentially remains the same independent of the material amount used, an optimization process's rational aim becomes to achieve the widest vibration stop band possible with the least amount of material utilized. To that end, vibration isolation performance of several stiffness maximized compliant mechanisms are compared for material volume fraction values of 30 % to 100 %. As the stop band occurs between the first and the second non rigid in-plane modes of the compliant mechanism [25, 27,31], the lower and the upper limits of vibration isolation frequency region are dictated by these two frequencies. As a result, in Figure 6 in order to compare stop band widths, the first and the second non rigid in-plane mode frequency values are tabulated. Moreover, to analyze the stop band width more clearly, the ratio of these two mode frequencies (i.e., f_2/f_1) are calculated in the literature frequently [25,27,31,57]. In Figure 7, the variation of f_2/f_1 ratio with respect to percent material utilized is shown. As can be seen, the maximum stop band width is achieved for 78% material volume fraction value with f_2/f_1 ratio value of 6.32. Whereas, for the original mechanism shown in Figure 4 with 100 % material volume fraction value, f_2/f_1 ratio value is found as 5.68. Therefore, as a result of topology optimization, vibration isolation stop band width can be increased by 11 % by using 22 % less material in the compliant mechanism. The topology optimized compliant inertial amplification mechanism design with 78 % material volume fraction value is presented in Figure 8.

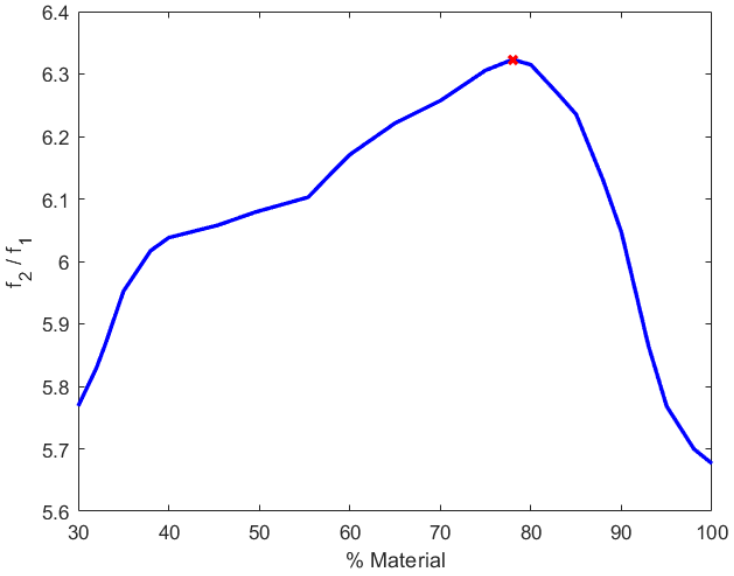

Figure 7. Variation of f_2/f_1 ratio with respect to % material (volume fraction). Red cross indicates the values for the design in Figure 8 and 100 % indicates the values for the design in Figure 4.

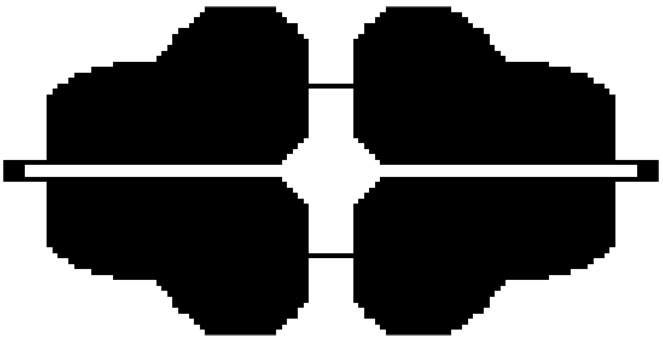

Figure 8. Topology optimized inertial amplification mechanism, i.e., the design with 78 % material used.

4. Numerical Results

In this section, vibration isolation performance of unit cell and periodic structures are demonstrated via transmissibility plots and compared.

4.1. Unit cell mechanisms

A unit cell is the smallest repeating unit of a periodic structure. The first unit cell considered is the compliant inertial amplification mechanism design with 100 % material utilized (see Figure 4). The second unit cell is the topology optimized inertial amplification mechanism with 78 % material used (see Figure 8). The first two non rigid mode shapes of these two unit cell mechanisms are provided in Figure 9. Both mechanisms perform similar mode shape motions for their first two modes, which is a result that is in accordance with the literature [25,27,31]. Note that, for both of the unit cells, vibration isolation stop band starts just above the first natural frequency and ends just below the second natural frequency, which can be regarded (with small error introduced) as the stop band limits are f_1 and f_2 [25,27,31]. As the stiffness value remains essentially the same, the first modes appear almost for the same frequency values. The small discrepancy stems from the fact that topology optimized design has less weight, which shifts the first natural frequency of the topology optimized

design by a factor of $1/\sqrt{m}$, a result which can be observed in nonlinear behavior seen in Figure 6(a). On the other hand, as a result of topology optimization, second natural frequency is shifted away for the topology optimized design compared to the original compliant mechanism.

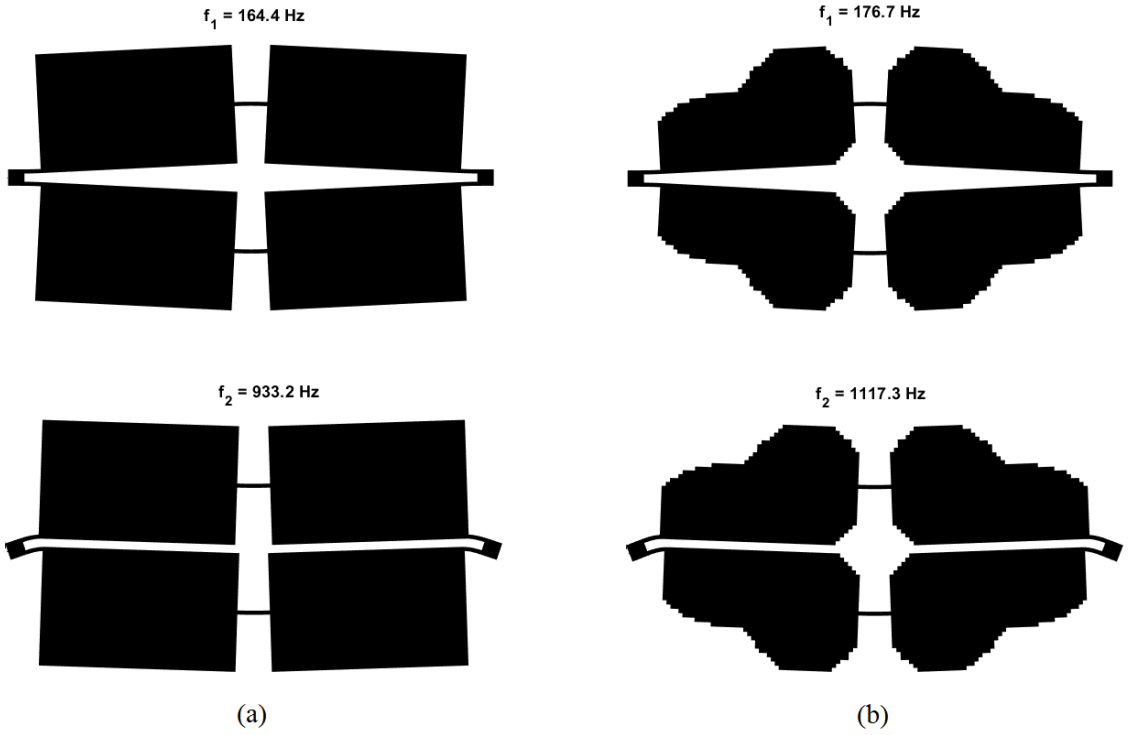

Figure 9. The first two mode shapes of distributed parameter inertial amplification mechanisms. (a) Compliant mechanism. (b) Topology optimized mechanism.

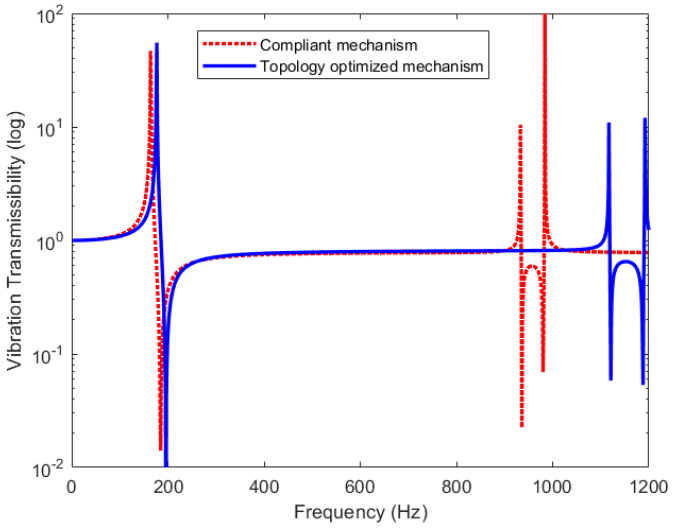

Figure 10. Vibration transmissibility comparison of unit cell compliant (red dotted line) and topology optimized (blue solid line) inertial amplification mechanisms.

In order to compare the vibration isolation performances of the original (Figure 4) and the topology optimized (Figure 8) unit cell designs, vibration transmissibility plots for these two mechanisms are provided in Figure 10. As can be seen, for both of the designs, similar vibration isolation levels (around 20 %) are achieved for most of the stop band. On the other hand, topology optimized design provides wider vibration stop band compared to the original compliant mechanism. For the original compliant mechanism in Figure 4 vibration isolation is achieved between 174 Hz – 926 Hz, whereas for the topology optimized compliant mechanism in Figure 8 vibration isolation is obtained between 186 Hz – 1106 Hz. Therefore, by utilizing 22

% less construction material, topology optimized design provides vibration isolation for wider frequency band as compared to the original mechanism.

4.2. Periodic structures

In order to achieve high performance vibration isolation, compliant mechanisms demonstrated in Figure 4 and Figure 8 can be used as unit cells to form periodic structures. It has been shown in the literature that, vibration isolation starting and ending frequencies will be approximately the same as the unit cell mechanisms', whereas vibration isolation levels rise as the number of unit cells (compliant mechanisms) utilized in the periodic structures is increased [25, 27, 31, 35]. In Figure 11, a sample periodic structure, which is formed via incorporating 3 original compliant inertial amplification mechanisms in a one-dimensional array, is shown. Input excitation (y) is provided to this periodic structure from one end and output response (x) is taken from the other end. Then, vibration transmissibility is calculated with finite element method. The vibration transmissibility of the periodic structure in Figure 11 is demonstrated in Figure 12 as red dashed line. As can be seen, between 168 Hz – 931 Hz, vibration isolation is achieved. Moreover, in Figure 12, the effect of employing more mechanisms (unit cells) in the formation of periodic structures are clearly seen. As the number of, unit cells utilized increases, vibration isolation levels increase, as well. For instance, the periodic structure formed via incorporating 8 original compliant inertial amplification mechanisms provide 99.9 % vibration isolation for almost entire of the stop band frequency range between 165 Hz – 933 Hz (blue solid line in Figure 12). Please note that, as the number of unit cell mechanisms utilized in the periodic structure increase, stop band starting and ending frequencies closely resemble the first and the second natural frequencies of the unit cell (i.e., f_1 = 164.4 Hz, f_2 = 933.2 Hz; also see Figure 9a).

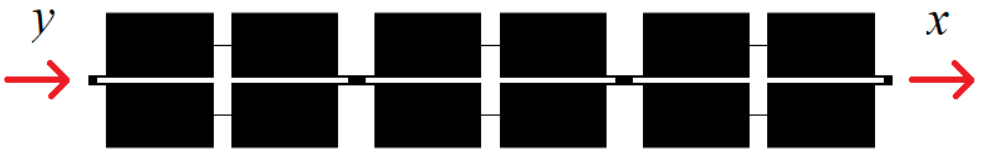

Figure 11. Sample periodic structure constructed with 3 compliant unit cell mechanisms given in Figure 4.

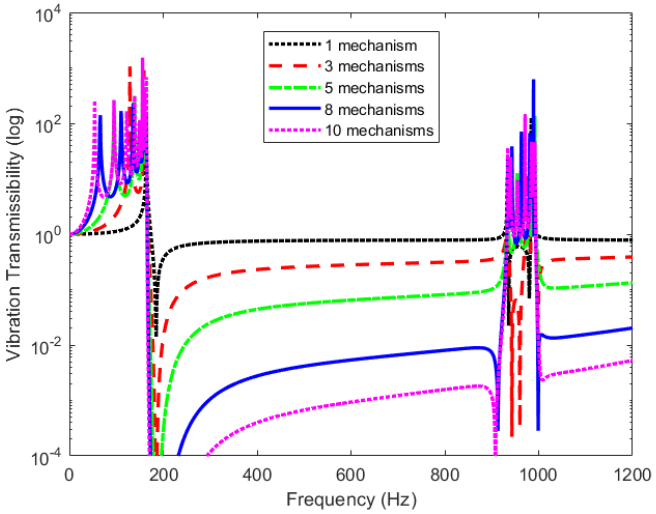

Figure 12. Vibration transmissibility plots of periodic structures formed with various number of compliant unit cell mechanisms shown in Figure 4.

With the same methodology, periodic structures by utilizing various number of topology optimized unit cell mechanisms in Figure 8 can be constructed, as well. A sample one-dimensional periodic structure, formed via incorporating 3 topology optimized inertial amplification mechanisms, is shown in Figure 13. As for the

previous case, input excitation (y) is provided from one end and output response (x) is taken from the other end. Consequently, vibration transmissibility is calculated (the red dashed line in Figure 14). Vibration transmissibilities of periodic structures, formed using several topology optimized inertial amplification mechanisms as unit cells, are shown in Figure 14. As can be seen, for all of the periodic structures, vibration isolation frequency range (stop band) closely resembles the first and the second natural frequencies of the topology optimized design (see Figure 9b). On the other hand, as the number of unit cell mechanisms utilized in the periodic structure increase, vibration isolation levels increase, as well. For example, for almost all of the frequency range between 178 Hz – 1117 Hz, 99 % vibration isolation is achieved by the periodic structure formed via incorporation of 8 topology optimized compliant inertial amplification mechanisms (see the blue solid line in Figure 14).

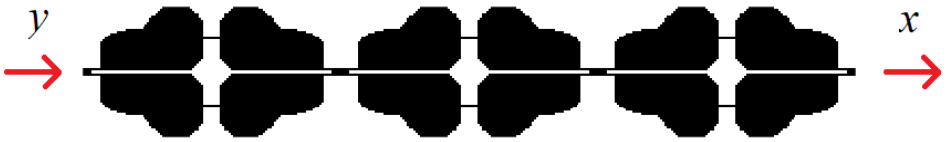

Figure 13. Sample periodic structure constructed with 3 topology optimized unit cell mechanisms given in Figure 8.

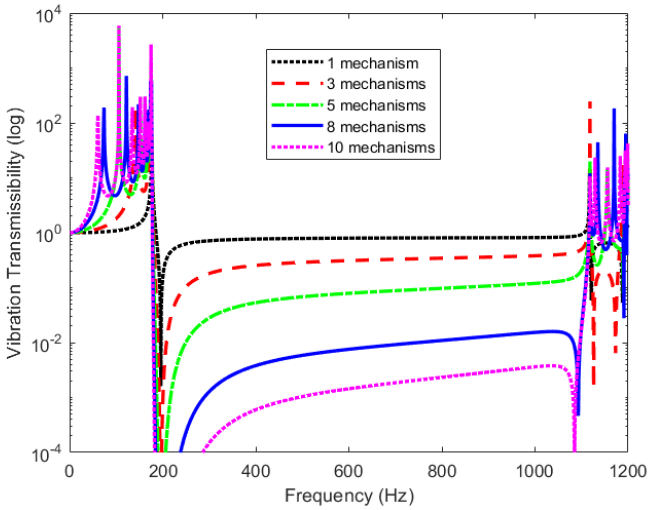

Figure 14. Vibration transmissibility plots of periodic structures formed with various number of topology optimized unit cell mechanisms shown in Figure 8.

As can be observed from Figures 12 and 14, periodic structures formed with topology optimized inertial amplification mechanisms provide satisfactory vibration isolation for wider frequency range with utilizing less construction material but having the same axial stiffness value of the original mechanism. In order to make the comparison more comprehensive, vibration transmissibility plots of two periodic structures formed with utilizing 8 original and 8 topology optimized mechanisms is shown in Figure 15. As can be seen, topology optimized periodic structure provides vibration isolation for 11 % wider frequency range by using 22 % less material. On the other hand, the vibration isolation levels of topology optimized periodic structure is slightly less than the original periodic structure, i.e., 99 % vs 99.9 %, which is a difference that can be neglected for practical purposes. Moreover, as the axial stiffness values of the unit cell mechanisms are almost the same, both periodic structures can withstand the same loading conditions.

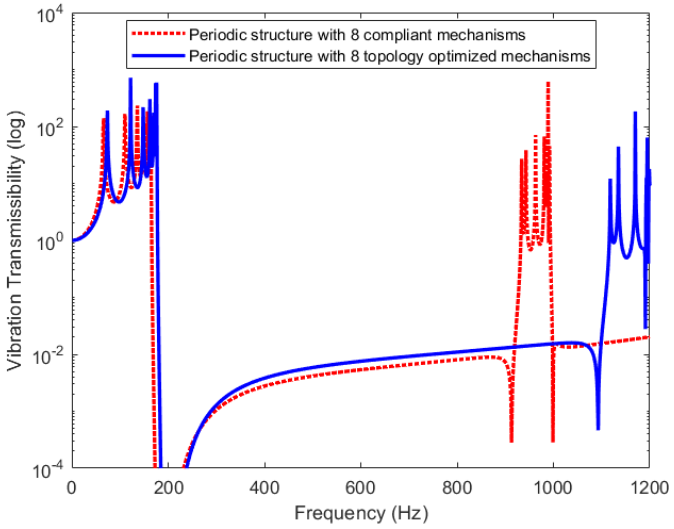

Figure 15. Vibration transmissibility comparison of periodic structures formed with 8 compliant (red dotted line) and 8 topology optimized (blue solid line) inertial amplification mechanisms.

4.3. Comparison of the results with the literature

Although the compliant inertial amplification mechanism topology represented in Fig. 2 has been studied before [25,27,28,31,37,58], there is not a study conducted on design of such mechanisms considering stiffness properties as its main objective function yet. Therefore, this work's major contribution to the literature is obtaining a topologically optimized complaint inertial amplification mechanism with maximized stiffness value. However, a comparison of the results of the current study and the existing ones [27,58] which considers stiffness as a constraint in their optimization problem formulation can be insightful, as well.

In Yuksel and Yilmaz [27], size optimized and shape optimized mechanisms were designed with each has a stiffness value of 1000 kN/m. The material selected was steel with modulus of elasticity value of 205 GPa, Poisson's ratio value of 0.29 and density value of 7800 kg/m^3. Using shell elements in the finite element analysis, shape optimized design's f_2/f_1 ratio was calculated as 3.13 whereas, size optimized design has a 2.63 f_2/f_1 ratio value. Moreover, two dimensional structural area of the designs were each 896 mm^2. Again, in Yuksel and Yilmaz [58], size optimized and shape optimized mechanisms were obtained with each has a stiffness value of 1000 kN/m. The material selected was steel with modulus of elasticity value of 210 GPa, Poisson's ratio value of 0.29 and density value of 7800 kg/m^3. Using one dimensional beam elements with eccentricity in the finite element analysis, shape optimized design's f_2/f_1 ratio was calculated as 3.34 whereas, size optimized design has a 2.82 f_2/f_1 ratio value. Besides, two dimensional structural area of the designs were each 961 mm^2. As a result, the values obtained for these two studies can be considered as almost identical ignoring the finite element type utilized and small differences in material area. It should be noted that, in the studies mentioned in Yuksel and Yilmaz [27] and [58], the objective function was to maximize the ratio of f_2/f_1, whereas stiffness is given as a constraint of both size and shape optimization problems.

On the other hand, in this study, final topologically optimized design has a stiffness value of 55500 kN/m which is much higher compared to the designs provided in Yuksel and Yilmaz [27] and [58]. Although the material properties are similar, the discrepancy stems from thick compliant hinge connections (i.e., 2nd and 4th beams) and the objective function of the topology optimization problem which is stiffness maximization. Moreover, material area of the current design is 3488 mm^2, which is much larger than the structures' indicated in Yuksel and Yilmaz [27] and [58]. As a result, a higher value of 6.32 for f_2/f_1 ratio is achieved. In summary, a much stiff structure with a broad vibration isolation frequency band is attained with a cost of increased material area compared to the investigated studies [27,58] that are found in the literature.

Moreover, as a final comparison with the work of Yuksel and Yilmaz [31] can be done to investigate the differences between the topologically optimized designs obtained with employment of different objective functions. In Yuksel and Yilmaz [31], the topology optimization problem's objective function was the maximization of the f_2/f_1 ratio of the unit cell mechanism. Although the material of construction was steel with the same modulus of elasticity and Poisson's ratio values used in this study, the design space was 100 mm by 50 mm, which is significantly smaller than the current study. Since the primary concern was achieving the highest frequency gap (i.e., vibration stop band) available, f_2/f_1 ratio was obtained as 6.07 as a result of solution of the dynamic topology optimization problem. f_1 is achieved at 304.4 Hz whereas f_2 is achieved at 1847.7 Hz. Material area of the topologically optimized design obtained in Yuksel and Yilmaz [31] is 1512 mm^2 which is 56.7 % less than the current design obtained in this study. The discrepancy between the results obtained from Yuksel and Yilmaz [31] and the current study stems from the fact that, the current study's design has much more weight, hence its first natural frequency occurs at 176.7 Hz, which is 41.6 % below than the design in Yuksel and Yilmaz [31]. In addition to the increase in the weight, the current design is longer and wider, hence the resulting second frequency is 39.5 % lower than the design in Yuksel and Yilmaz [31]. That, difference makes f_2/f_1 ratio of the design provided in Yuksel and Yilmaz [31] as 3.96 % less than the current design presented in this study. Moreover, the stiffness value for the design given in Yuksel and Yilmaz [31] is calculated as 41400 kN/m, which is 25.4 % less than the current design. To sum up, the topologically optimized mechanism in Yuksel and Yilmaz [31] provides a vibration isolation for a fairly large frequency range with much less amount of material, which is a result coincides with the objective function of that study, which is frequency gap maximization. On the other hand, in the current study, the objective function is to attain the stiffest possible structure, hence a stiffer structure which has approximately the same frequency range of vibration is achieved at the expense of increasing the optimized mechanism's weight.

4. Conclusion

In this study, a lightweight periodic structure, which can be used as a high-performance vibration isolator, is considered. A compliant mechanism's weight is reduced via topology optimization while stiffness of the structure is maintained. Among available topology optimized mechanisms, a design which provides vibration isolation for the widest frequency range possible, is chosen. The selected design has 22 % less weight and provides vibration isolation for a frequency range which is 11 % higher than the original mechanism. By using the topology optimized mechanisms, sample periodic structures are formed and vibration transmissibility plots indicate that high vibration isolation levels can be achieved. It is shown that, a periodic structure formed with 8 topology optimized mechanisms provide 99 % vibration isolation for almost all of the frequency range between 178 Hz – 1117 Hz.

Conflict of Interest Statement

The authors declare that there is no conflict of interest

References

[1] S. Daley, F. A. Johnson, J. B. Pearson and R. Dixon, "Active vibration control for marine applications," *Control Engineering Practice*, vol. 12, no. 4, pp. 465-474, 2004. doi:10.1016/S0967-0661(03)00135-7

[2] Y. H. Guan, T. C. Lim and W. S. Shepard, "Experimental study on active vibration control of a gearbox system," *Journal of Sound and Vibration*, vol. 282, no. 3-5, pp. 713-733, 2005. doi:10.1016/j.jsv.2004.03.043

[3] S. M. Kuo, S. Mitra and W. S. Gan, "Active noise control system for headphone applications," *IEEE Transactions on Control Systems Technology*, vol. 14, no. 2, pp. 331-335, 2006. doi:10.1109/TCST.2005.863667

[4] S. M. Khot, P. Y. Nitesh, R. Tomar, S. Desai and S. Vittal, "Active vibration control of cantilever beam by using PID based output feedback controller," *Journal of Vibration and Control,* vol. 18, no. 3, pp. 366-372, 2012. doi:10.1177/1077546311406307

[5] O. Yuksel and C. Yilmaz, "Active noise control in a duct with flow," *Journal of Dynamic Systems, Measurement and Control,* vol. 136, no. 3, p. 031014, 2014. doi:10.1115/1.4026410

[6] A. Zippo, G. Ferrari, M. Amabili, M. Barbieri and F. Pellicano, "Active vibration control of a composite sandwich plate," *Composite Structures,* vol. 128, pp. 100-114, 2015. doi:10.1016/j.compstruct.2015.03.037

[7] M. Moshrefi-Torbati, A. J. Keane, S. J. Elliott, M. J. Brennan and E. Rogers, "Passive vibration control of a satellite boom structure by geometric optimization using genetic algorithm," *Journal of Sound and Vibration,* vol. 267, no. 4, pp. 879-892, 2003. doi:10.1016/S0022-460X(03)00192-5

[8] C. Yilmaz and N. Kikuchi, "Analysis and design of passive low-pass filter-type vibration isolators considering stiffness and mass limitations," *Journal of Sound and Vibration,* vol. 293, no. 1-2, pp. 171-195, 2006. doi:10.1016/j.jsv.2005.09.016

[9] D. Kamesh, R. Pandiyan and A. Ghosal, "Passive vibration isolation of reaction wheel disturbances using a low frequency flexible space platform," *Journal of Sound and Vibration,* vol. 331, no. 6, pp. 1310-1330, 2012. doi:10.1016/j.jsv.2011.10.033

[10] E. A. Ribeiro, J. T. Pereira and C. A. Bavastri, "Passive vibration control in rotor dynamics: Optimization of composed support using viscoelastic materials," *Journal of Sound and Vibration,* vol. 351, pp. 43-56, 2015. doi:10.1016/j.jsv.2015.04.007

[11] Z. Wu, X. Jing, B. Sun and F. Li, "A 6DOF passive vibration isolator using X-shape supporting structures," *Journal of Sound and Vibration,* vol. 380, pp. 90-111, 2016. doi:10.1016/j.jsv.2016.06.004

[12] S. S. Rao, "Vibration Control," Mechanical Vibrations. Upper Saddle River: Prentice Hall, 2011.

[13] D. J. Inman, "Design for Vibration Suppression," Engineering Vibration. Upper Saddle River: Pearson Education, 2014.

[14] J. Wen, G. Wang, D. Yu, H. Zhao and Y. Liu, "Theoretical and experimental investigation of flexural wave propagation in straight beams with periodic structures: Application to a vibration isolation structure," *Journal of Applied Physics,* vol. 97, no. 11, p. 114907, 2005. doi:10.1063/1.1922068

[15] G. Wang, X. Wen, J. Wen and Y. Liu, "Quasi-one-dimensional periodic structure with locally resonant band gap," *Journal of Applied Mechanics,* vol. 73, no. 1, pp. 167-170, 2006. doi:10.1115/1.2061947

[16] J. H. Oh, S. Qi, Y. Y. Kim and B. Assouar, "Elastic metamaterial insulator for broadband low-frequency flexural vibration shielding," *Physical Review Applied,* vol. 8, no. 5, p. 054034, 2017. doi:10.1103/PhysRevApplied.8.054034

[17] R. Prasad and A. Sarkar, "Broadband vibration isolation for rods and beams using periodic structure theory," *Journal of Applied Mechanics,* vol. 86, no. 2, p. 021004, 2019. doi:10.1115/1.4042011

[18] L. D'Alessandro, R. Ardito, F. Braghin and A. Corigliano, "Low frequency 3D ultra-wide vibration attenuation via elastic metamaterial," *Scientific Reports,* vol. 9, p. 8039, 2019. doi:10.1038/s41598-019-44507-6

[19] M. Sigalas and E. N. Economou, "Elastic and acoustic wave band structure," *Journal of Sound and Vibration,* vol. 158, no. 2, pp. 377-382, 1992. doi:10.1016/0022-460X(92)90059-7

[20] M. Sigalas and E. N. Economou, "Band structure of elastic waves in two dimensional systems," *Solid State Communications,* vol. 86, no. 3, pp. 141-143, 1993. doi:10.1016/0038-1098(93)90888-T

[21] Z. Liu, X. Zhang, Y. Mao, Y. Y. Zhu, Z. Yang, C. T. Chan and P. Sheng, "Locally resonant sonic materials," Science, vol. 289, no. 5485, pp. 1734-1736, 2000. doi:10.1126/science.289.5485.1734

[22] C. Goffaux and J. Sánchez-Dehesa, "Two-dimensional phononic crystals studied using a variational method: application to lattices of locally resonant materials," *Physical Review B,* vol. 67, no. 14, p. 144301, 2003. doi:10.1103/PhysRevB.67.144301

[23] C. Yilmaz, G. M. Hulbert and N. Kikuchi, "Phononic band gaps induced by inertial amplification in periodic media," *Physical Review B,* vol. 76, no. 5, p. 054309, 2007. doi:10.1103/PhysRevB.76.054309

[24] C. Yilmaz and G. M. Hulbert, "Theory of phononic gaps induced by inertial amplification in finite structures," *Physics Letters A,* vol. 374, no. 34, pp. 3576-3584, 2010. doi:10.1016/j.physleta.2010.07.001

[25] G. Acar and C. Yilmaz, "Experimental and numerical evidence for the existence of wide and deep phononic gaps induced by inertial amplification in two-dimensional solid structures," *Journal of Sound and Vibration*, vol. 332, no. 24, pp. 6389-6404, 2013. doi:10.1016/j.jsv.2013.06.022

[26] S. Taniker and C. Yilmaz, "Phononic gaps induced by inertial amplification in BCC and FCC lattices," *Physics Letters A*, vol. 377, no. 31-33, pp. 1930-1936, 2013. doi:10.1016/j.physleta.2013.05.022

[27] O. Yuksel and C. Yilmaz, "Shape optimization of phononic band gap structures incorporating inertial amplification mechanisms," *Journal of Sound and Vibration*, vol. 355, pp. 232-245, 2015. doi:10.1016/j.jsv.2015.06.016

[28] S. Taniker and C. Yilmaz, "Design, analysis and experimental investigation of three-dimensional structures with inertial amplification induced vibration stop bands," *International Journal of Solids and Structures*, vol. 72, pp. 88-97, 2015. doi:10.1016/j.ijsolstr.2015.07.013

[29] N. M. M. Frandsen, O. R. Bilal, J. S. Jensen and M. I. Hussein, "Inertial amplification of continuous structures: Large band gaps from small masses," *Journal of Applied Physics*, vol. 119, p. 124902, 2016. doi:10.1063/1.4944429

[30] S. Taniker and C. Yilmaz, "Generating ultra wide vibration stop bands by a novel inertial amplification mechanism topology with flexure hinges," *International Journal of Solids and Structures*, vol. 106, pp. 129-138, 2017. doi:10.1016/j.ijsolstr.2016.11.026

[31] O. Yuksel and C. Yilmaz, "Size and topology optimization of inertial amplification induced phononic band gap structures," in *Proceedings of the ASME International Mechanical Engineering Congress and Exposition*, Tampa, Florida, USA, 2017. p. V013T01A007. doi:10.1115/IMECE2017-71342

[32] M. Barys, J. S. Jensen and N. M. M. Frandsen, "Efficient attenuation of beam vibrations by inertial amplification," *European Journal of Mechanics-A/Solids*, vol. 71, pp. 245-257, 2018. doi:10.1016/j.euromechsol.2018.04.001

[33] A. H. Orta and C. Yilmaz, "Inertial amplification induced phononic band gaps generated by a compliant axial to rotary motion conversion mechanism," *Journal of Sound and Vibration*, vol. 439, pp. 329-343, 2019. doi:10.1016/j.jsv.2018.10.014

[34] J. Li, P. Yang and S. Li, "Phononic band gaps by inertial amplification mechanisms in periodic composite sandwich beam with lattice truss cores," *Composite Structures*, vol. 231, p. 111458, 2020. doi:10.1016/j.compstruct.2019.111458

[35] O. Yuksel and C. Yilmaz, "Realization of an ultrawide stop band in a 2-D elastic metamaterial with topologically optimized inertial amplification mechanisms," *International Journal of Solids and Structures*, vol. 203, pp. 138-150, 2020. doi:10.1016/j.ijsolstr.2020.07.018

[36] S. Muhammad, S. Wang, F. Li and C. Zhang, "Bandgap enhancement of periodic nonuniform metamaterial beams with inertial amplification mechanisms," *Journal of Vibration and Control*, vol. 26, no. 15-16, pp. 1309-1318, 2020. doi:10.1177/1077546319895630

[37] O. Yuksel and C. Yilmaz, "Design of a broadband elastic metamaterial via topologically optimized inertial amplification mechanisms," in *Proceedings of the 11th International Conference on Structural Dynamics*, Athens, Greece, 2020. pp. 4125-4138. doi:10.47964/1120.9337.19454

[38] K. Mizukami, K. Funaba and K. Ogi, "Design and three-dimensional printing of carbon-fiber-composite elastic metamaterials with inertial amplification mechanisms," *Journal of Sound and Vibration*, vol. 513, p. 116412, 2021. doi:10.1016/j.jsv.2021.116412

[39] C. Xi, L. Dou, Y. Mi and H. Zheng, "Inertial amplification induced band gaps in corrugated-core sandwich panels," *Composite Structures*, vol. 267, p. 113918, 2021. doi:10.1016/j.compstruct.2021.113918

[40] Y. Mi and X. Yu, "Sound transmission of acoustic metamaterial beams with periodic inertial amplification mechanisms," *Journal of Sound and Vibration*, vol. 499, p. 116009, 2021. doi:10.1016/j.jsv.2021.116009

[41] M. Miniaci, M. Mazzotti, A. Amendola and F. Fraternali, "Effect of prestress on phononic band gaps induced by inertial amplification," *International Journal of Solid and Structures*, vol. 216, pp. 156-166, 2021. doi:10.1016/j.ijsolstr.2020.12.011

[42] A. Banerjee, S. Adhikari and M. I. Hussein, "Inertial amplification band-gap generation by coupling a levered mass with a locally resonant mass," *International Journal of Mechanical Sciences*, vol. 207, p. 106630, 2021. doi:10.1016/j.ijmecsci.2021.106630

[43] Y. Li and W. Zhou, "Bandgap and vibration transfer characteristics of scissor-like periodic metamaterials," *Journal of Applied Physics*, vol. 130, p. 025103, 2021. doi:10.1063/5.0047119

[44] E. Er, E. Türkeş and O. Yüksel, "A parametric investigation on various compliant inertial amplification mechanisms for a periodic vibration isolator design," *Gazi Journal of Engineering Sciences*, vol. 8, no. 3, pp. 511-523, 2022. doi:10.30855/gmbd.0705039

[45] Y. Zeng, L. Cao, S. Wan, T. Guo, Y. F. Wang, Q. J. Du, B. Assouar and Y. S. Wang, "Seismic metamaterials: Generating low-frequency bandgaps induced by inertial amplification," *International Journal of Mechanical Sciences,* vol. 221, p. 107224, 2022. doi:10.1016/j.ijmecsci.2022.107224

[46] Y. Li, N. Zhao and S. Yao, "Theoretical analysis of 2D meta-structure with inertia amplification," *International Journal of Mechanical Sciences,* vol. 235, p. 107717, 2022. doi:10.1016/j.ijmecsci.2022.107717

[47] Y. Li, N. Zhao and S. Yao, "Nonlinear dynamics of 1D meta-structure with inertia amplification," *Applied Mathematical Modelling,* vol. 118, pp. 728-744, 2023. doi:10.1016/j.apm.2023.01.039

[48] H. Li, Y. Li and X. Liu, "Double-beam metastructure with inertially amplified resonators for flexural wave attenuation," *European Journal of Mechanics – A / Solids,* vol. 97, p. 104794, 2023. doi:10.1016/j.euromechsol.2022.104794

[49] A. Ni and Z. Shi, "Inertial amplified topological metamaterial beams," *Journal of Applied Physics,* vol. 133, p. 065105, 2023. doi:10.1063/5.0140790

[50] Y. F. Wang, Y. Z. Wang, B. Wu, W. Chen and Y. S. Wang, "Tunable and active phononic crystals and metamaterials," *Applied Mechanics Reviews,* vol. 72, no. 4, p. 040801, 2020. doi:10.1115/1.4046222

[51] C. Yilmaz and G. M. Hulbert, "Dynamics of Locally Resonant and Inertially Amplified Lattice Materials," Dynamics of Lattice Materials. West Sussex: John Wiley & Sons, 2017.

[52] H. W. Ma, S. M. Yao, L. Q. Wang and Z. Zhong, "Analysis of the displacement amplification ratio of bridge-type flexure hinge," *Sensors and Actuators A: Physical,* vol. 132, no. 2, pp. 730-736, 2006. doi:10.1016/j.sna.2005.12.028

[53] L. L. Howell, "Introduction to Compliant Mechanisms," Handbook of Compliant Mechanisms. West Sussex: John Wiley & Sons, 2013.

[54] O. Yüksel, "An overview on topology optimization methods employed in structural engineering," *Kırklareli University Journal of Engineering and Science,* vol. 5, no. 2, pp. 159-175, 2019. doi:10.34186/klujes.606666

[55] E. Andreassen, A. Clausen, M. Schevenels, B. S. Lazarov and O. Sigmund, "Efficient topology optimization in MATLAB using 88 lines of code," *Structural and Multidisciplinary Optimization,* vol. 43, no. 1, pp. 1-16, 2011. doi:10.1007/s00158-010-0594-7

[56] O. Sigmund and K. Maute, "Topology optimization approaches," *Structural and Multidisciplinary Optimization,* vol. 48, no. 6, pp. 1031-1055, 2013. doi:10.1007/s00158-013-0978-6

[57] J. S. Jensen and N. L. Pedersen, "On maximal eigenfrequency separation in two-material structures: the 1d and 2d scalar cases," *Journal of Sound and Vibration,* vol. 289, no. 4-5, pp. 967-986, 2006. doi:10.1016/j.jsv.2005.03.028

[58] O. Yuksel and C. Yilmaz, "Obtaining inertial amplification induced phononic gaps via structural optimization of a compliant mechanism," in *Proceedings of the 11th International Conference on Vibration Problems,* Lisbon, Portugal, 2013. pp. 1-10.

This is an open access article under the CC-BY license

Research Article/Araştırma Makalesi

Gazi AKADEMİK YAYINCILIK

GAZİ
JOURNAL OF ENGINEERING SCIENCES

Cooling of Rubber Embossing Cylinder for Tissue Paper

Uğur Cem Sari[a], Bayram Kesmen[a], Ali Kibar[*b]

Submitted: 13.02.2024 Revised: 02.03.202024 Accepted: 18.05.2024 doi:10.30855/gmbd.0705N14

ABSTRACT

Traditional embossing processes applied to papers generate significant amounts of heat, leading to the degradation and decreased efficiency of the rubber cylinder, a critical component of the machine, over time. This study investigates a novel internal cooling system designed to address this issue and extend the lifespan of the rubber cylinder. Experiments were conducted using tap water and ethylene glycol aqueous solution as coolants at a machine speed of 350 m/min and a specified pattern density. The results suggests that the non-cooled cylinder started to deteriorate at a surface temperature of approximately 46 °C. However, with the implemented cooling system, the surface temperature was effectively maintained at 4-5 °C below this threshold, significantly extending the operational life of the rubber cylinder. Therefore, this study emphasizes the effectiveness of internal cooling in mitigating heat-induced damage and extending the lifespan of embossing cylinders.

Keywords: Embossing, Cooling, Tissue paper, Rolling cylinder

[a]ICM Machinery and Engineering, 41040 - Kocaeli, Türkiye
Orcid: 0000-0001-7277-1021

[a]ICM Machinery and Engineering, 41040 - Kocaeli, Türkiye
Orcid: 0000-0002-1636-9676

[*b]Kocaeli University Department of Mechanical and Material Technologies, Uzunciftlik Nuh Cimento Campus, 41180 – Kocaeli, Türkiye
Orcid: 0000-0002-2310-1088

[*]Corresponding author: alikibar@kocaeli.edu.tr

Temizlik Kâğıdı Gofraj Sistemindeki Lastik Silindirin Soğutulması

ÖZ

Temizlik kağıtlarına uygulanan geleneksel gofraj işlemleri, makinenin önemli bir bileşeni olan kauçuk silindirin zamanla bozulmasına ve verimliliğinin düşmesine neden olan önemli miktarda ısı üretir. Bu çalışmada, bu sorunu çözmek ve kauçuk silindirin ömrünü uzatmak için tasarlanmış yeni bir dahili soğutma sistemi incelenmiştir. Deneyler, soğutucu olarak musluk suyu ve etilen glikol sulu çözeltisi kullanılarak 350 m/dakika makine hızı ve belirli bir desen yoğunluğu altında gerçekleştirildi. Sonuç olarak, soğutulmayan silindir yaklaşık olarak 46 °C yüzey sıcaklığında bozulmaya başladı. Bununla birlikte, uygulanan soğutma sistemiyle, yüzey sıcaklığı bu eşik değerin 4-5°C altında etkin bir şekilde korundu ve kauçuk silindirin çalışma ömrü önemli ölçüde uzatıldı. Bu nedenle, bu çalışmada dahili soğutmanın ısı kaynaklı hasarı azaltma ve kabartma silindirlerinin ömrünü uzatmada etkili olduğu gösterilmektedir.

Anahtar Kelimeler: Gofraj, soğutma, temizlik kağıdı, döner silindir

To cite this article: U. C. Sari, B. Kesmen and A. Kibar, "Cooling of rubber embossing cylinder for tissue paper," *Gazi Journal of Engineering Sciences,* vol.10, no.1, pp. 172-182, 2024. doi:10.30855/gmbd.2017.0705N14

1. Introduction

The embossed pattern on tissue paper is achieved using an embossing machine integrated into the tissue paper production lines, as shown in Figure 1. This process involves applying pressure between a steel embossing cylinder with a negative pattern and a rubber cylinder rotating in the opposite direction at the same speed [1]. Consequently, patterns are imprinted on the tissue paper flowing continuously between the two cylinders. However, the rubber cylinder undergoes wear and deformation over time as the system operates. The extent of rubber cylinder deformation is primarily driven by excessive surface temperature, which is influenced by various factors such as machine speed, pattern shape, pressing force, and pattern density.

The rubber cylinder used in the embossing process consists of natural rubber adhered to a steel cylinder with a negative embossing pattern. The surface temperature of the rubber cylinder increases because of the pressure applied by the negative pattern embossed steel cylinder [1]. The pressure must surpass a certain threshold to create patterns, although excessive pressure can accelerate the deformation of the rubber cylinder, thereby reducing its lifespan [2]. Additionally, the machine operating speed (cylinder revolution speed) and the pattern density of the steel embossing cylinder also affect the temperature increase on the rubber cylinder surface. Consequently, the temperature increases on the rubber cylinder surface limits the machine operating speed and pattern selection. To achieve high-quality production and optimal performance, it is imperative to regulate the temperature increase on the rubber cylinder surface. Otherwise, the rubber cylinder becomes unusable once it reaches a certain threshold temperature.

Embossed pattern quality depends on several critical parameters required for the embossing process. These parameters include roller speed, embossing temperature, and roller embossing pressure [3]. By controlling and optimizing these variables, it is possible to achieve the desired pattern outcomes with precision and consistency. It is important to control these factors to ensure the production of high-quality embossed patterns on tissue paper.

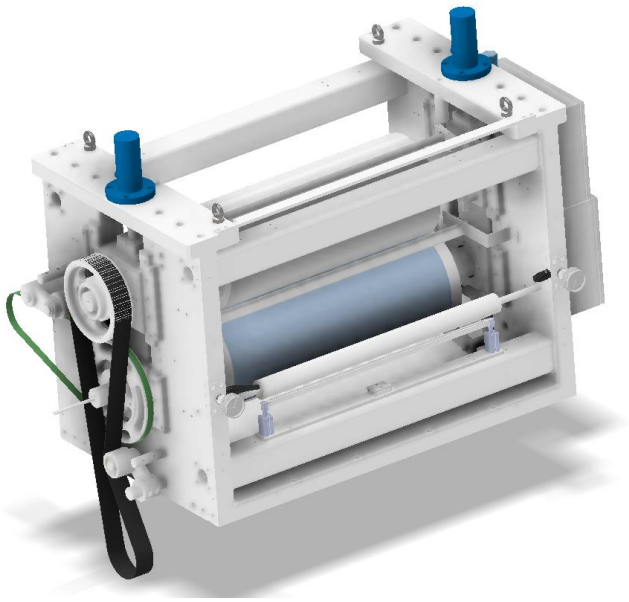

Figure 1. Embossing system

Researchers have been exploring ways to improve the life of the rubber cylinder, including using different materials, shapes, and adding cooling systems. Recent studies have shown the effectiveness of cooling systems for similar geometries. For instance, Fagan [4] and Fagan and Kim [5] designed a cooling system for a cylinder with a similar structure to maintain the desired temperature and prevent overheating. This system employed a nested and interlocked structure, evenly distributing air to 15 cooling slots along the embossed perimeter to facilitate the cooling process. Ma et al. [6] conducted numerical analyses on the use of a cooling cylinder for

the continuous cooling of a thin rubber film flowing over a cylinder. Their study concluded that the temperature of the rubber film entering the cylinder significantly affected the cooling efficiency, whereas the width of the rubber film had minimal influence. Deng et al. [7] studied the polymer flow behaviour in roll-to-roll (R2R) hot embossing for continuous micro/nanostructure fabrication on polymers. Analysing micro-pyramids on PVC film with a 3D finite element model, they examined deformation and recovery during filling and remoulding. The temperature distribution showed notable gradients due to poor thermal conductivity, impacting creep strains. Effective cooling reduced pyramid recovery, especially at high mold temperatures.

Perez et al. [8] used gas as a cooling fluid in a comparable cooling system. They adopted a dual cryostat topology for the ASuMED motor, featuring separate cryostats for the rotor and stator. Their study recommended an externally controlled cooling system with forced gas circulation for optimal rotor cooling. The key factors considered were critical heat transfer and the influence of rotor stack temperature on cooling effectiveness.

Li et al. [9] studied micropyramid array fabrication on EVA copolymer films via roll-to-roll hot embossing. They found that EVA rheology correlates with micropyramid height. Films with 28% VA content, embossed at 60°C, exhibit high transmittance and are suitable for various applications. Optimal demoulding occurs at 40–60 °C, particularly with low VA content. The study introduced frequency-dependent viscosity for the demoulding analysis, showing the impact of viscosity and relaxation on micropyramid height. Li et al. [10] successfully produced micropyramid arrays on transparent PETG films by optimizing the applied force, roller temperature and speed for array quality. This study demonstrated the practical feasibility of fabricating micropyramid arrays on PETG films via roll-to-roll hot embossing, providing valuable insights for industrial applications.

Vieira et al. [11] investigated the impact of engraving finishing geometry on tissue paper properties during embossing. They observed that while straight finishing geometry led to higher individual hand-feel values, round finishing geometry enhanced softness in two-ply prototypes. Hand-feel values decreased with increased bulk, especially for micropatterns, but liquid droplet spreading kinetics were unaffected by finishing geometry. Finite element modelling revealed that round patterns left more pronounced marks on tissue paper, which was correlated with increased bulk. This modelling tool aids in optimizing process parameters and minimizing trial and error. This study highlights the significance of finishing geometry in embossing and provides valuable insights into tissue paper product properties.

Vieira et al. [1] studied the effect of engraving finishing geometry on tissue paper properties during embossing. They found that straight finishing geometry increased individual hand-feel values, whereas round finishing geometry enhanced softness in two-ply prototypes. Hand-feel values decreased with increased bulk, particularly for micropatterns, but liquid droplet spreading kinetics remained unaffected. Finite element modelling showed that round patterns left more pronounced marks on the tissue paper, correlating with increased bulk. This modelling approach facilitates process parameter optimization, thus reducing trial and error.

Morega [12] developed a small-power HTS synchronous motor prototype and explored cooling technologies for HTS field winding. They proposed supercooled nitrogen as an efficient and economical option but recommended cooling the HTS coils with liquid Ne for optimal performance. This study involved numerical simulations and mathematical modelling of heat transport in the stator, using 2D and 3D simulations to assess heat transfer properties and thermal loads. Various heat transfer mechanisms were found to influence the thermal stability of the motor, as determined by these simulations.

The influence of pattern type and density as well as the sensitivity of embossed pattern depth to preheating and cooling were investigated by Kim et al. [13]. They identified key factors affecting embossed pattern quality in roll-to-roll hot embossing and investigated time-dependent heat transfer effects using custom preheating and cooling systems. The results revealed that extended preheating time significantly influences embossed

depth, whereas substrate cooling effects vary. In addition, they found that horizontal patterns with lower density yield larger embossed depths. This review sheds light on the importance of considering duration factors in heat transfer for roll-to-roll hot embossing, particularly concerning mold pattern characteristics.

Considering the high flammability of the cooling fluid and the abundance of tissue paper dust, implementing a gas-based cooling system poses significant safety hazards in this environment. Due to the risk of fire, a liquid-based approach was adopted instead. Compared to gas-based systems, liquid cooling offers several advantages in this context [14]. Primarily, liquids pose a lower fire risk than flammable gasses. Additionally, liquid coolants provide better heat transfer efficiency, allowing for effective cooling of the rubber cylinder surface. By circulating the liquid, heat is efficiently dissipated, maintaining the rubber cylinder within the ideal temperature range. Finally, liquid-based cooling allows for flexibility in coolant selection and temperature control, ensuring optimal operating conditions for the embossing process.

This study focuses on the inability to apply external cooling for rubber embossing rollers, which is a significant challenge in paper tissue manufacturing. While advancements have been made in embossing technology, addressing the heat-induced degradation of rubber cylinders remains a crucial area with limited existing research. This study aims to fill this gap in the literature by investigating novel internal cooling techniques to significantly extend the operational lifespan of rubber cylinders. This study also focuses on controlling the surface temperature increase of these cylinders within embossing machines. The study will involve comprehensive research into rubber cylinder design and materials, the development of a novel internal cooling system, experimental testing with prototypes, meticulous data analysis, and a comprehensive evaluation of the outcomes.

2. Materials and Methods

2.1. Cooling of the Cylinder

Preventing the temperature increase on the surface of the rubber cylinder is a critical parameter for extending its lifespan and increasing machine operating speed. Due to its low thermal conductivity [15] and surface-based heating, external cooling would be the ideal solution. However, implementing an external cooling system to prevent temperature increases on the surface of the rubber cylinder during operation is impractical because of the prevailing working conditions. The presence of paper dust, particularly in the working environment, requires internal cooling through the cylinder.

Figure 2 shows the geometry of the rubber cylinder. Heat transfer calculations were conducted by considering only conduction in the heat transfer process while neglecting other heat transfer mechanisms. In this context, upon examining the cross-section of the design, a resemblance to a bundle of pipes is noted. Heat transfer calculations were executed based on conduction, similar to heat transfer calculations in a pipe bundle, to determine heat loads and resistances. The necessary heat load to achieve the desired surface temperature, along with the requisite cooling fluid temperature and flow rate, was determined.

As previously stated, because of the prevailing working conditions, external cooling of the rubber cylinder surface by direct contact is unfeasible. Therefore, internal cooling from within the cylinder is expected to indirectly cool the rubber cylinder surface. In this regard, the temperature at point T_3 must be maintained as low as possible relative to the maximum temperature that the rubber can withstand. The temperature value at point T_1 is computed based on the T_3 temperature.

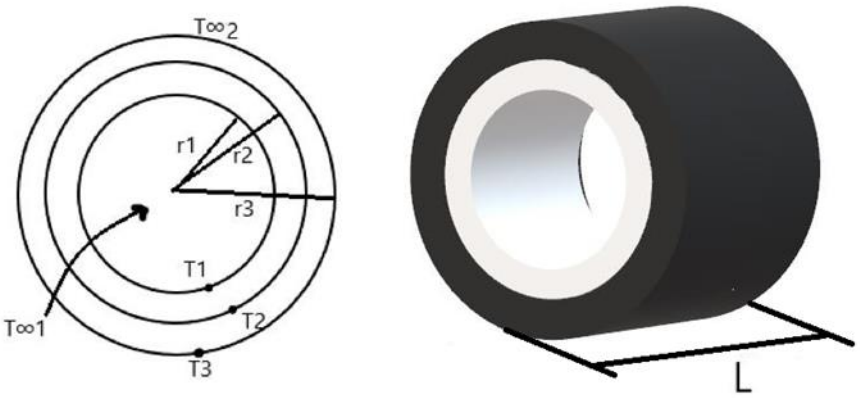

Figure 2. Rubber cylinder geometry

The total thermal resistance for multilayered cylindrical or spherical shells can be calculated as follows:

$$R_{\text{Total}} = R_{\text{Conv.i1}} + R_{\text{Cyl.1}} + R_{\text{Cyl.2}} + R_{\text{Conv.i2}} \quad (1)$$

$$= \frac{1}{h_{Conv.i1}A_1} + \frac{ln(\frac{r_2}{r_1})}{2\pi L k_{\text{cyl1}}} + \frac{ln(\frac{r_3}{r_2})}{2\pi L k_{\text{cyl2}}} + \frac{1}{h_{Conv.i2}A_2} \quad (2)$$

$$A_{1=2\pi r_1 L} \text{ ve } A_{2=2\pi r_3 L} \quad (3)$$

The heat transfer rate (Q) is given by

$$Q = \frac{T_{\infty 1} - T_{\infty 2}}{R_{\text{Total}}} \quad (4)$$

The heat energy of the cooling fluid, which is used as the heat energy medium, can be calculated as follows:

$$Q = mc_p \Delta t \quad (5)$$

The values r_1, r_2, and r_3 used in the formulas represent, respectively, the inner diameter of the steel cylinder, the outer radius of the steel cylinder or the inner radius of the rubber coating, and the outer radius of the rubber coating (see Figure 3). R_{Total}, $R_{Conv.i1}$, $R_{Cyl.1}$, $R_{Cyl.2}$, and $R_{Conv.i2}$ represent, respectively, the total heat, convective heat transfer for the coolant, heat conduction through the steel cylinder, heat conduction through the rubber, and convective heat transfer for the air. A_1 and A_2 represent, respectively, the inner surface area of the steel cylinder and the outer surface area of the rubber coating. The mass flow rate, specific heat capacity of water, and temperature difference are represented by m, c_p and Δt, respectively. $T_{\infty 1}$ and $T_{\infty 2}$ represent the temperatures of the fluid or surroundings on the inner and outer sides of the system.

In the context of the presented formulas, Figure 3 illustrates the meanings of r_1, r_2, and r_3 as the inner diameter of the steel cylinder, outer radius of the steel cylinder or inner radius of the rubber coating, and outer radius of the rubber coating, respectively.

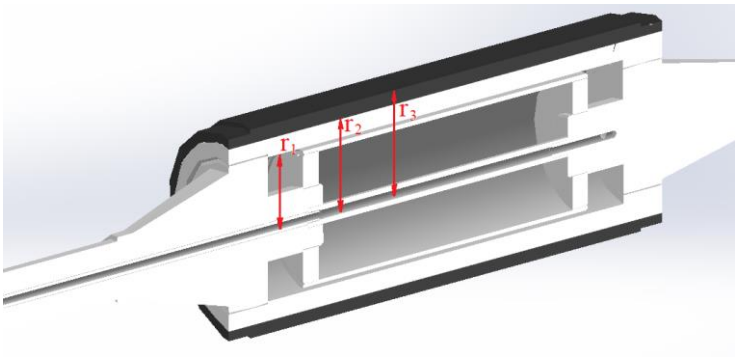

Figure 3. Cross-sectional view of the cylinder and its radii

2.2. Experimental Study

Figures 4a and 4b show the embossing machine group used in these experiments and the resulting pattern, respectively. The process of imprinting patterns onto tissue paper involves the steel embossing cylinder, featuring negative embossed patterns, rotating at a specified speed while exerting pressure against the rubber cylinder. The rubber cylinder rotates in the opposite direction at the same speed. This configuration transfers the patterns onto the tissue paper as it flows continuously between the two cylinders.

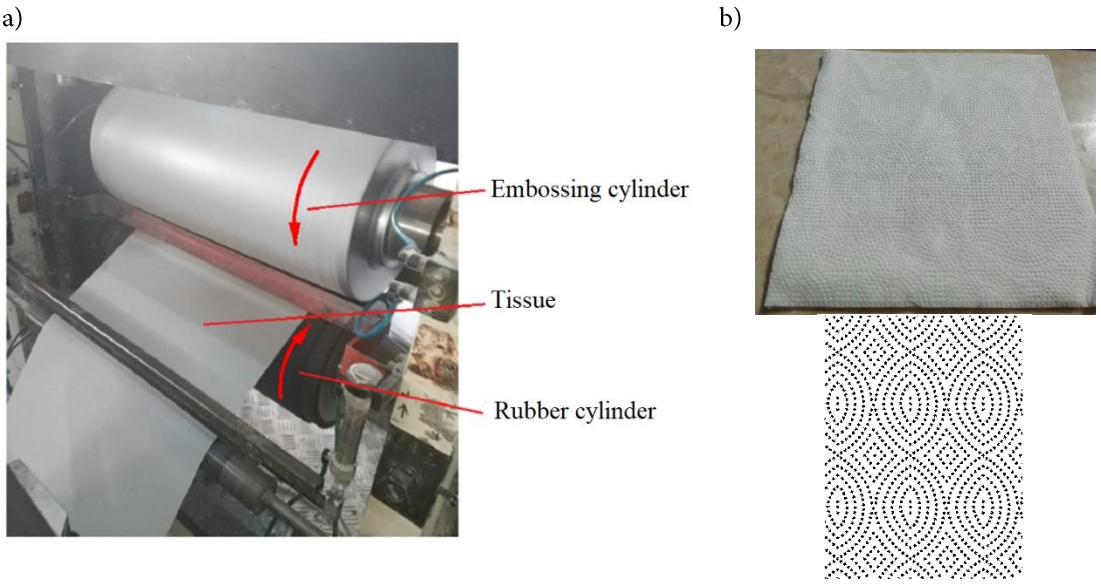

Figure 4. a) Embossing machine used in the experiment and b) created pattern

The embossing machine shown in Figure 4a operated at a speed of 350 m/min, causing the cylinders to rotate at approximately 440 rpm. During design studies, temperature fluctuations on the rubber cylinder's surface were measured within the operational environment using a laser thermometer and thermal camera. Based on these observations, an internal cooling system for the rubber cylinder was designed and prototyped. Subsequently, experiments were conducted with the fabricated prototype.

An SMC-HRSE-024 liquid circulation chiller was employed to circulate the liquid within the cylinder of the cooling system. A rotating head facilitated the liquid's inlet and outlet. Cold fluid entered the cylinder through the inlet pipe (1), illustrated in Figure 5. This inlet pipe (1) was connected to the cylinder shaft (2), with teeth left vacant to ensure liquid exit. Cold liquid was introduced into the system through the apertures depicted in Figure 5 (6). Upon entering the cylinder, the cold liquid traversed through the inner cylinder (5) and the steel cylinder (7), diminishing the volume of the cylinder's inner space. Heat transfer occurred between the steel cylinder (7) and the liquid during this phase. Subsequently, heat exchange between the steel and rubber cylinders cooled the latter.

The heated liquid exited the system through outlet apertures (3), flowing between the cylinder shaft (2) and inlet pipe (1) via the rotating head. This cooled fluid circulated continuously throughout operation. Table 1 presents data obtained from observations of the current model running with the cooling system, under the specified operating conditions.

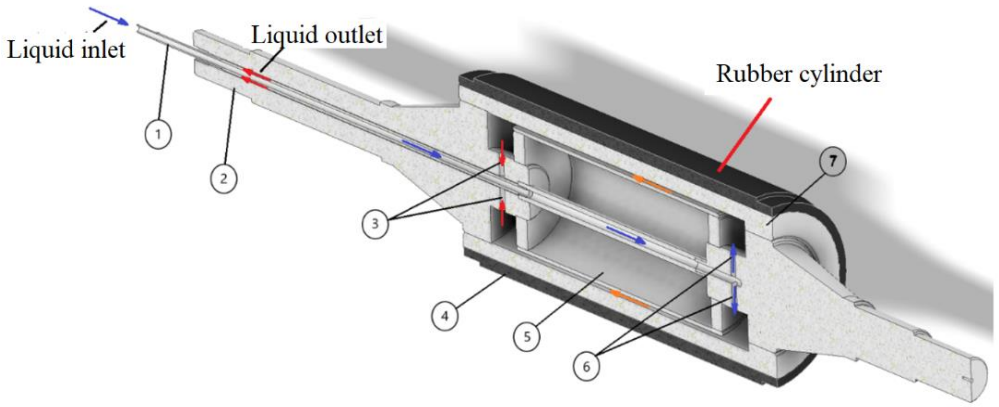

Figure 5. 1) Inlet pipe for the cooling fluid system, 2) Cylinder shaft, 3) Outlet path from the cooling fluid system, 4) Rubber coating, 5) Inner cylinder, 6) Inlet path for the cooling fluid system, 7) Steel cylinder

Table 1. Experimental conditions of the chiller machine

Parameters	Value
Inlet pressure of the cooling fluid system (kPa)	140.0
Cooling fluid flow rate (L/min)	4.1
Operating pressure of the embossing piston (bar)	120.0
Inlet temperature of the cooling liquid (°C)	10.0
Outlet temperature of the cooling liquid (°C)	13.3

2. Results and Discussion

Figure 6 shows the temperature variations on the surface of the natural rubber-coated cylinder, measured in the current system at 350 m/min with an embossing unit featuring the pattern density of Figure 4b. This data includes both cooled and non-cooled conditions. During machine operation, the surface temperature of the rubber cylinder exhibits a near-linear increase over time. Upon reaching a critical temperature of approximately 46 °C, the rubber cylinder experiences damage. As noted in the introduction, numerous factors contribute to the deterioration of rubber cylinders; however, this study specifically investigates the impact of temperature on this phenomenon.

In the experiment with the cooling system applied, as shown in Figure 6, the cooling process commenced at approximately 43 °C. Due to limitations in the circulation capacity of the chiller unit used for circulating the cooling liquid (specifically, the operational capacity of the unit used in the experiment), a cooling liquid flow rate of 4.1 L/min is adopted. Following an initial temperature rise, the temperature gradually decreases. This temperature reduction continues for approximately 90 minutes before stabilizing around 41 °C. Consequently, the surface of the rubber cylinder is maintained at approximately 4-5 °C below the critical temperature threshold, thereby delaying the onset of damage.

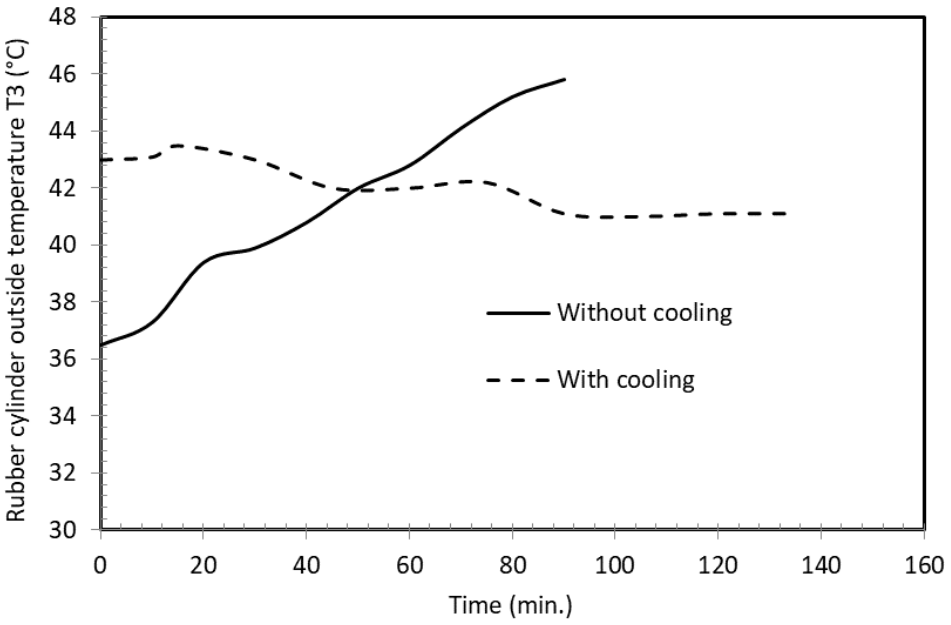

Figure 6. Experimental results at a machine operating speed of 350 m/min with and without cooling

Furthermore, the implemented cooling system not only prevents the rubber cylinder from reaching damaging temperatures but also significantly enhances the overall performance and operational efficiency of the embossing machine. By maintaining the surface temperature within an acceptable range, the cooling system minimizes the risk of premature wear and deformation of the rubber cylinder. Therefore, downtime and production interruptions may be prevented. This highlights the critical role of temperature control in enhancing the reliability and longevity of embossing equipment in tissue paper manufacturing.

In Figure 7, the thermal camera images offer a visual representation of the contrasting temperature profiles of the embossing and rubber cylinders. Firstly, the embossing cylinder maintains a consistently low temperature throughout the observation period. This characteristic thermal behaviour is attributed to its material composition. Typically constructed from steel or other high-conductivity materials, the embossing cylinder possesses a high heat transfer coefficient. This property allows for efficient heat dissipation, keeping the cylinder at a relatively low temperature even under extended operational durations. In contrast, the rubber cylinder exhibits a completely different thermal response, with its temperature escalating to elevated levels. The underlying cause of this temperature increase lies in the dynamic interplay between pressure, material properties, and mechanical action. As both cylinders engage in the embossing process, the longitudinally flexible rubber cylinder experiences repeated compression. This cyclical compression-decompression occurs at a rapid rate, with the rubber cylinder undergoing approximately 400 compressions per minute along the designated line pattern.

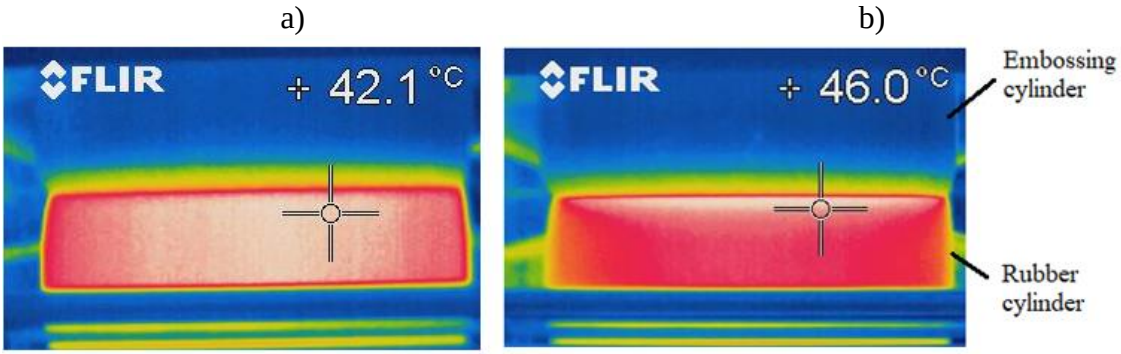

Figure 7. Temperature of the embossing and rubber cylinders during operation. a) Cooling system and b) non-cooling system

The cumulative effect of these compressions is dual. Firstly, repeated mechanical loading induces significant

frictional forces within the rubber cylinder, leading to internal energy dissipation and consequent temperature rise. Secondly, the compressive forces generate localized heating within the rubber material, further contributing to its thermal elevation. As a result, the temperature of the rubber cylinder escalates rapidly, forming a sharp contrast with the relatively cool performance of the embossing cylinder. As observed in Figure 7a, the cooling system maintains the rubber cylinder at approximately 4-5 °C cooler temperatures. While the lower heat transfer coefficient of rubber limits the potential for drastic temperature reductions, this modest decrease can significantly extend the cylinder's operational lifespan.

3. Conclusions

This study investigated the use of an internal cooling system to extend the lifespan of the rubber cylinder in a tissue paper embossing machine. A prototype system utilizing a chiller unit was designed, manufactured, and tested. Because of the rubber cylinder's low thermal conductivity and considerable thickness, achieving a substantial cooling effect internally proved challenging. During the experiments, the rubber cylinder starts to damage at a temperature of approximately 46 °C and a speed of 350 m/min, consistent with the specified pattern density. With the implemented cooling system, a cooling of approximately 4-5 °C is attained. Although this 4-5 °C cooling increment helps delay the rubber cylinder's progression to the damage threshold temperature, it remains susceptible to damage at operational temperatures. It is evident that when the machine operating speed is elevated or the pattern density of the paper is increased, the designed system may fall short of providing adequate cooling.

While external cooling may indeed seem like the simplest and ideal approach, certain circumstances may necessitate internal cooling, as demonstrated in this study. Despite the challenges posed by the low thermal conductivity of the rubber cylinder, our research showcases the feasibility of internal cooling for moderate temperature differentials, albeit not without its limitations.

Potential future enhancements and research avenues include the following:

- Employing a chiller unit: a chiller unit capable of operating at lower temperatures and higher flow rates than those employed in the experiments could achieve cooling below 10 °C.
- Redesigning the experimental system: Enhancing heat transfer by refining the contact surface and flow dynamics inside the cylinder could optimize cooling efficiency. This may involve redesigning the cooling system to enhance fluid circulation and maximize contact with the rubber cylinder surface.

Nomenclature

Symbols

A_1	Inner surface area of the steel cylinder (m^2)
A_2	Outer surface area of the rubber coating (m^2)
c_p	Specific heat capacity of the cooling fluid (J/kg.K)
Δt	Temperature difference (°C)
$h_{conv_1,i1}$	Convective heat transfer coefficient for the coolant at the inner surface ($W/m^2.K$)
$h_{conv_2,i2}$	Convective heat transfer coefficient for the air at the outer surface ($W/m^2.K$)
k_{cyl1}	Thermal conductivity of the steel cylinder (W/m·K)
$R_{Cyl.1}$	Thermal resistance, ($K \cdot m^2/W$)
k_{cyl2}	Thermal conductivity of the rubber (W/m·K)
$R_{Cyl.2}$	Thermal resistance ($K \cdot m^2/W$)
M	Mass flow rate of the cooling fluid (kg/s)
Q	Heat transfer rate (W)
r_1	Inner diameter of the steel cylinder (m)
r_2	Outer radius of the steel cylinder (m)
r_3	Outer radius of the rubber coating (m)

$R_{conv_1,i1}$	Convective heat transfer resistance at the inner surface (K·m²/W)
$R_{conv_2,i2}$	Convective heat transfer resistance at the outer surface (K·m²/W)
R_{total}	Total thermal resistance (K·m²/W)
T	Temperature (°C)
$T_{\infty 1}$	Temperature of the cooling fluid or surrounding on the inner side (°C)
$T_{\infty 2}$	Temperature of the air or surrounding on the outer side (°C)

Subscripts

i:	Inner surface
o:	Outer surface
cyl:	Cylinder
conv:	Convection

Conflict of Interest Statement

The authors declare that there is no conflict of interest

References

[1] J. C. Vieira, P. T. Fiadeiro, and A. P. Costa, "Converting Operations Impact on Tissue Paper Product Properties – A Review," *Bioresources*, vol. 18, no. 1, 2023. doi:10.15376/BIORES.18.1.VIEIRA

[2] Y. Chen *et al.*, "Parameter optimization of rubber cylinder of expansion liner hanger based on numerical simulation," *Journal of Engineering and Applied Science*, vol. 69, no. 1, pp. 1–18, Dec. 2022. doi:10.1186/S44147-022-00086-4

[3] J. Zhang, M. Sahli, J. C. Gelin, and T. Barrière, "Roll manufacturing of polymer microfluidic devices using a roll embossing process," *Sens Actuators A Phys*, vol. 230, pp. 156–169, Jul. 2015. doi:10.1016/J.SNA.2015.03.002

[4] M. D. Fagan, "A Novel Process for Continuous Thermal Embossing of Large- Area Nanopatterns onto Polymer Films," Masters Theses, University of Massachusetts Amherst, Massachusetts, USA, 2008.

[5] M. D. Fagan and B. H. Kim, "A Novel Process for Continuous Thermal Embossing of Large-Area Nanopatterns onto Polymer Films," *Advances in Polymer Technology*, vol. 28, no. 4, pp. 246–256, 2009. doi:10.1002/adv.20167

[6] W. Ma, H. Yu, Y. Liu, and C. Qian, "Numerical simulation and parameter sensitivity analysis for the cooling of rolling rubber-film on cooling-drums," *J Phys Conf Ser*, vol. 1549, no. 4, p. 042115, 2020. doi:10.1088/1742-6596/1549/4/042115

[7] Y. Deng, P. Yi, L. Peng, X. Lai, and Z. Lin, "Flow behavior of polymers during the roll-to-roll hot embossing process," *Journal of Micromechanics and Microengineering*, vol. 25, no. 6, p. 065004, May 2015. doi:10.1088/0960-1317/25/6/065004

[8] A. Perez, R. R. Van Der Woude, and R. Dekker, "Rotor Cooling Concept for the ASuMED Superconductive Motor," *IOP Conf Ser Mater Sci Eng*, vol. 502, no. 1, p. 012139, Apr. 2019. doi:10.1088/1757-899X/502/1/012139

[9] W. Li, S. Song, Y. Zhai, Y. Zhang, P. Yi, and X. Lai, "Rheological behavior of ethylene–vinyl acetate copolymer and fabrication of micropyramid arrays by roll-to-roll hot embossing on its thin films," *J Appl Polym Sci*, vol. 134, no. 34, pp. 1–9, 2017. doi:10.1002/app.45228

[10] W. Li, Y. Zhai, P. Yi, and Y. Zhang, "Fabrication of micro-pyramid arrays on PETG films by roll-to-roll hot embossing," *Microelectron Eng*, vol. 164, pp. 100–107, 2016. doi:10.1016/j.mee.2016.08.001

[11] J. C. Vieira *et al.*, "Embossing Lines and Dots Geometry Effect on the Key Tissue Paper Properties with Finite Element Method Analysis," *Polymers 2022, Vol. 14, Page 3448*, vol. 14, no. 17, p. 3448, Aug. 2022. doi: 10.3390/POLYM14173448

[12] A. M. Morega, I. Dobrin, M. Popescu, and M. Morega, "Heat transfer analysis in the design phase of a high temperature superconductor motor," in *Proceedings of the 12th International Conference on Optimisation of Electrical and Electronic Equipment, OPTIM*, pp. 401–406, 2010. doi:10.1109/OPTIM.2010.5510528

[13] S. Kim, Y. Son, H. Park, B. Kim, and D. Yun, "Effects of Preheating and Cooling Durations on Roll-to-Roll Hot Embossing," *Microscopy and Microanalysis*, vol. 21, no. 1, pp. 164–171, Feb. 2015. doi:10.1017/S1431927614013324

[14] J. Liu, H. Chen, S. Huang, Y. Jiao, and M. Chen, "Recent Progress and Prospects in Liquid Cooling Thermal Management System for Lithium-Ion Batteries," *Batteries 2023, Vol. 9, Page 400*, vol. 9, no. 8, p. 400, Aug. 2023. doi:10.3390/BATTERIES9080400

[15] J. Zhang, X. Jia, and Q. He, "Mechanical, thermal, and friction properties of addition-type fluororubber co-filled with Al2O3 particles at high temperature," *Polym Test*, vol. 96, p. 107131, Apr. 2021. doi:10.1016/J.POLYMERTESTING.2021.107131

This is an open access article under the CC-BY license

Research Article/Araştırma Makalesi

GAZİ
JOURNAL OF ENGINEERING SCIENCES

Ontology-Based Generalized Zero-Shot Learning with Generative Networks

Emre Akdemir*[a], Necattin Barışçı[b]

Submitted: 15.12.2023 Revised: 17.04.2024 Accepted: 25.04.2024 doi:10.30855/gmbd.0705N15

ABSTRACT

Zero-Shot Learning (ZSL) aims to classify images of new categories in the testing phase without labeled images during training, using examples from categories with labeled images and some auxiliary information. The auxiliary information includes semantic attributes, textual descriptions, word embeddings, etc., for both labeled and unlabeled classes, utilizing Natural Language Processing (NLP) approaches. The word embeddings created are limited by the semantic attributes and textual descriptions where the semantics of categories are insufficient. In this paper, introduces a study for Generalized Zero-Shot Learning (GZSL), a type of ZSL, by integrating the rich semantics offered by ontology. Semantic attributes used for semantic representation are supported by ontology. Variational Autoencoder (VAE) and Generative Adversarial Network (GAN) network architectures are used together to synthesize visual features. Our work was evaluated on the AWA2 dataset, and improvement in GZSL performance was achieved.

Keywords: Generalized zero-shot learning, Natural language processing, Ontology, Variational autoencoder, Generative adversarial network

[a,*] Gazi University,
Graduate School of Informatics,
Dept. of Computer Science
06500 - Ankara, Türkiye
Orcid: 0000-0003-2507-9264
e mail: emre.akdemir@gazi.edu.tr

[b] Gazi University,
Technology Faculty,
Dept. of Computer Engineering
06560 - Ankara, Türkiye
Orcid: 0000-0002-8762-5091

*Corresponding author:
emre.akdemir@gazi.edu.tr

Üretici Ağlar ile Ontoloji Tabanlı Genelleştirilmiş Sıfır-Atışlı Öğrenme

ÖZ

Sıfır-Atışlı Öğrenme (Zero-Shot Learning - ZSL), eğitim sırasında, etiketli görüntülerin bulunduğu kategorilere ait örneklerden ve bazı yardımcı bilgilerden yararlanarak test aşamasında etiketli görüntüleri bulunmayan yeni kategorilere ait örnekleri sınıflandırmayı amaçlamaktadır. Buradaki yardımcı bilgiler hem etiketli hem de etiketsiz sınıflar için semantik öznitelikler, metinsel açıklamalar, sözcük gömme gibi doğal dil işleme yaklaşımlarıdır. Oluşturulan sözcük gömmeleri, kategorilerin anlambiliminin yetersiz olduğu semantik öznitelikler ve metinsel açıklamalar ile kısıtlıdır. Bu yazıda ontolojinin sunduğu zengin semantiği üretici ağlara entegre ederek ZSL'nin bir türü olan Genelleştirilmiş Sıfır-Atışlı Öğrenme (Generalized Zero-Shot Learning - GZSL) görevi için bir çalışma tanıtılmıştır. Semantik temsil için kullanılan semantik öznitelikleri ontoloji ile desteklenmiştir. Görsel özellikleri sentezlemek için VAE ve GAN ağlarını birlikte kullanılmıştır. Çalışmamızı AWA2 veri seti üzerinde değerlendirilmiştir ve GZSL performansında iyileştirme sağlanmıştır.

Anahtar Kelimeler: Genelleştirilmiş sıfır-atışlı öğrenme, Doğal dil işleme, Ontoloji, Varyasyonel otomatik kodlayıcı, Çekişmeli üretici ağ

To cite this article: E. Akdemir and N. Barisci, "Ontology-Based Generalized Zero-Shot Learning with Generative Networks," *Gazi Journal of Engineering Sciences,* vol.10, no.1, pp. 183-192, 2024. doi:10.30855/gmbd.0705N15

1. Introduction

Deep learning has made significant advances in image processing, but it relies on collecting sufficient labeled data for recognizing each category. In some cases, it may not be feasible to gather labeled training data for every category [1]. The absence of labeled data makes the task considerably challenging for machine learning and deep learning technologies [2] . In recent years, Zero-Shot Learning (ZSL) has gained attention for its successful results in classifying unlabeled images [3]. ZSL consists of seen classes (with labeled image examples), unseen classes (without labeled image examples), and semantic representations. ZSL aims to recognize examples from unseen classes by transferring knowledge from examples in seen classes and semantic representations[1]. During the testing phase of the ZSL task, only the performance of unseen classes is evaluated. For a more realistic evaluation, Generalized Zero-Shot Learning (GZSL) studies have started to replace ZSL studies. In the testing phase of the GZSL task, the performance of both seen and unseen classes is assessed.

Due to the absence of labeled examples for new classes, GZSL encounters a data imbalance issue between seen and unseen classes. Generative approaches, such as Generative Adversarial Networks (GAN) and Variational Autoencoders (VAE), are highly effective in addressing this problem. Using generative networks, synthetic visual features are produced for unseen classes by leveraging both visual and semantic features. However, textual features are not generated for semantic relationships and contextual information of unseen classes [4]. Therefore, there is a need for structured data, such as semantic web, to address this issue [5].

The use of various Natural Language Processing (NLP) methods in deep learning tasks is quite common [6]. Extracting meaning from textual data such as web pages and documents using deep learning methods is a challenging task. To address these challenging tasks, there is a need for rich models consisting of semantic concepts offered by NLP tasks. Successful results have been achieved in tasks such as extracting meaning from texts and establishing relationships between images and text using NLP-based deep learning methods [7-9]. Most words have multiple meanings. Relationships such as synonyms, antonyms, similar meanings, as well as positive or negative connotations can exist for a word. In short, there are relationships and representations between words. The semantic concept mentioned in NLP refers to how the meaning of a word is represented and the information obtained from its relationship with other words[10].

Semantic Web emerges from the relationships established among semantic information. The goal of the Semantic Web is to enable machines to make inferences. To achieve this, a structure is formed through the collaboration of humans and computers. This structure is obtained by comprehending and linking data on the web. Ontology is often used to create a robust structure with Semantic Web. Ontologies provide a strong structure where machines can understand relationships between concepts. An ontology can be specific to a domain or an advanced ontology resulting from the integration of ontologies from different domains. Commonly, Resource Description Framework (RDF) and Web Ontology Language (OWL) are used to describe the Semantic Web[11-13].

Fig. 1 provides an example representation for the seen class, unseen class, and ontological schema. The semantic attributes used for images contain values for specific features in a given category. The ontological schema, in addition to semantic attributes, presents a relational structure by utilizing class hierarchy and descriptions. To create the ontological schema, the class hierarchy offered by RDF, such as "subClassOf," is initially employed. Subsequently, class concepts are associated with attribute concepts like "hasTexture." As depicted in Fig. 1, class concepts are represented by ovals, and attribute concepts are represented by rectangles. Additionally, each class includes text-based descriptions. The created ontological schema is an RDF triple. For example, the triple "killer_whale," "hasTexture," "spots" expresses that the killer whale has a spotted texture. The ontological schema enhances the information transfer between seen and unseen classes more effectively.

Building on this, in our study, we aimed to enhance the performance of GZSL by enriching semantic representations. For this purpose, we augmented the semantic attributes in the datasets with an ontology created using RDF. Subsequently, we designed a VAE-GAN architecture for the learning model. We evaluated our proposed GZSL model on the AWA2 dataset. In the conducted experiments, our proposed method resulted in a 1.19% improvement in GZSL performance. To the best of our knowledge, our GZSL study is the first to incorporate RDF and semantic attributes together into a VAE-GAN-based model.

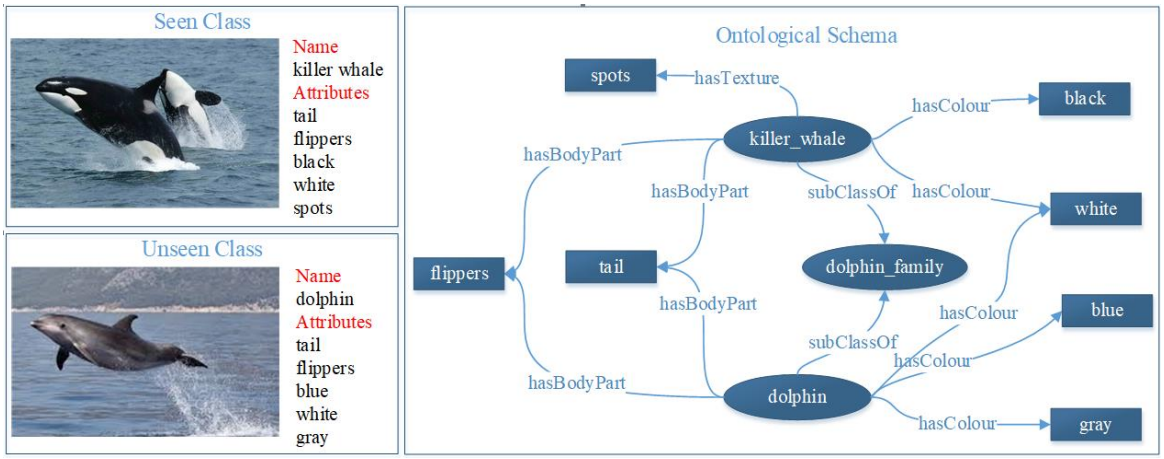

Figure 1. Semantic attribute and ontological schema representations

The rest of the article is organized as follows: Section 2 provides a summary of related works in the literature. Section 3 introduces the proposed model in detail. Section 4 presents the experimental results of the study. Finally, Section 5 concludes with conclusions and discussion.

2. Related Work

GZSL is the recognition of an object without any instance images of that object during the training phase, utilizing textual and image data from other examples. GZSL is categorized into embedding-based methods and generative-based methods. Embedding-based methods find a projection function from the visual space to the semantic space during the training phase of the GZSL method, using information from seen categories. During the testing phase, unseen image feature data is used as input to the trained model, and a semantic embedding is obtained. Classification is then performed based on the category corresponding to the nearest semantic embedding. [14-15]. Generative-based methods enable unseen classes to behave like seen classes by synthesizing synthetic features for the unseen classes. In studies using generative-based methods, GAN is first used and then VAE is employed to learn the synthesis of visual features for unseen classes from semantic attributes. In subsequent studies, a VAE-GAN model, combining the strengths of both VAE and GAN, was developed. [16]. Wu et al. utilized Stacked Autoencoder (StAE) to learn the relationship between extracted features and semantic representations [17]. Gao et al. proposed a shared generative model known as Zero-VAE-GAN to generate high-quality visual features for unseen classes. In the model, a conditionally guided VAE based on semantic features is combined with a GAN conditioned on both categories and features. Additionally, a classification network and perceptual reconstruction loss are included to generate high-quality features [18]. Narayan et al. worked on an approach for both image and video datasets by adding a feedback module to a VAE-GAN-based model [19]. Bao et al. colleagues utilized the VAE-GAN model to create realistic and diverse new examples from natural images of faces, birds, and flowers within a class [20]. Han et al. suggested a comparative embedding. In the proposed method, they used a parallel inference network and a feature generation framework to project visual features into a semantic descriptive space [21].

Semantic web technologies enhance the restructuring of information and facilitate machine readability. Semantic web technologies have been repeatedly used in machine learning and deep learning tasks. To enable

a structure like ontology to be utilized by a deep neural network, there is a need for a framework that can produce multiple hierarchical outputs representing the data. Each output of the neural network corresponds to a concept in the ontology. Thus, a taxonomic assumption relationship architecture is defined for all concepts for which inferences can be made based on these outputs [22,23]. In Semantic Web-based applications, formal representation languages such as RDF and OWL, as well as structures like ontologies and knowledge graphs, are commonly used. Geng et al. proposed a new generative zero-shot learning method called KG-GAN by incorporating rich semantics from a knowledge graph into GANs. They developed graph neural networks to investigate the effects of class semantics on feature transfer in zero-shot learning and to learn semantic class nodes. They utilized the original taxonomy structure of WordNet along with the class and subclass relationships of ImageNet to create the knowledge graph [24]. Geng et al. proposed an ontology-based GAN to create more distinctive example features for ZSL. Their approach, named Onto-ZSL, demonstrated the effectiveness of ZSL on image classification and knowledge graph completion tasks [25]. In addition to the image classification and knowledge graph completion tasks introduced in their previous work, Geng et al. presented another study involving ZSL with a relation extraction task [26].

Upon examining previous studies, it is evident that the use of VAE-GAN-based generative approaches has led to highly successful results in GZSL tasks. In GZSL classification, the synthesized image features for unseen classes are crucial. At the same time, semantic relationships play a significant role. Therefore, we propose a GZSL framework that enriches semantic relationships with ontology, incorporating generative approaches to enhance GZSL classification.

3. Method

In this section, we first address the problem, and then we introduce the architecture of our approach in three sub-sections with detailed explanations.

3.1. Problem definition

GZSL aims to classify examples from both seen class S and unseen class U, using examples from the training dataset, which contains seen classes, and examples from the test dataset, which contains both seen and unseen classes. During the training phase of GZSL, both the seen class S and the semantic features A are trained, and during the testing phase, it learns examples from both the seen class S and the unseen class U. Here, the classes S and U are disjoint, meaning $S \cap U = \emptyset$. The semantic features A are represented as A^S for the semantic features of seen classes and A^U for the semantic features of unseen classes. Thus, the semantic features A are expressed as $A = \{a_{(k)}\}_{k=1}^{S+U}$. The dataset for the seen class S containing examples X^S corresponding to labels Y^S is denoted as $S = \{X^S, Y^S\}$. Similarly, the dataset for the unseen class U, containing examples X^U corresponding to labels Y^U, is denoted $U = \{X^U, Y^U\}$. While ZSL learns the classifier $f_{zsl}: X \rightarrow Y^U$I GZSL learns the classifier $f_{gzsl}: X \rightarrow Y^S \cup Y^U$.

3.2. Visual feature extraction

In this study, visual features obtained from a pre-trained Convolutional Neural Network (CNN) with the ResNet-101 architecture from ImageNet [27] were used. The ResNet-101 architecture is a CNN with a depth of 101 layers. These networks have been trained on over a million images and can classify images into 1000 object categories. Using a pre-trained network with transfer learning is often faster and easier than training a network from scratch. With this architecture, rich feature representations for a variety of images are learned, and 2048-dimensional visual features of images are extracted through average pooling. CNN has a powerful capability for extracting visual features. However, unlike traditional image recognition, GZSL involves unlabeled images, which leads to a decrease in the discriminative power of visual features extracted by CNN [28]. Therefore, for GZSL, it is not sufficient to rely solely on visual feature extraction, and semantic feature extraction is also utilized.

3.3. Semantic feature extraction

3.3.1. Semantic embedding

Semantic information is represented with semantic vector embeddings. A semantic vector is a representation of a word in a multi-dimensional semantic space. Semantic embeddings provide an effective way to represent the meaning of words and analyze the semantic aspects of language. The use of language models such as word2vec, GloVE, and BERT is common for representing the meaning of words. In recent years, the positive impact of word embeddings on the performance of many applications has been observed [10,29,30]. In traditional word embedding methods, the lack of word order information leads to a lack of semantic information for words. Therefore, there is a problem of semantic compositionality in word embeddings. To address this issue, a Recurrent Neural Network (RNN)-based language model that represents the meaning of words has been developed, resulting in more meaningful word embeddings [31,32].

In traditional GZSL studies, semantic attributes are used to create semantic embeddings. In our study, in addition to semantic attributes, textual descriptions and ontology are also utilized to create semantic embeddings.

3.3.2. Ontology

In this study, RDF (Resource Description Framework) was used to create an ontology. RDF represents web resources using triple statements, consisting of subject, predicate, and object. Subjects and objects represent entities, while predicates represent the relationships between these entities. When given the statement "Ankara is the capital of Turkey," RDF should be able to infer "Ankara" and "Turkey" as entities and the relationship "is the capital of" between them [33]. As seen, manually coding information with human input is crucial for developing semantic web-based applications [34]. Ontologies are hierarchical representations of elements in a domain. These hierarchical representations are used to define categories at each level [35]. In our study, an ontology schema containing class hierarchy, semantic attributes, and textual descriptions, created using RDF triples, was employed [25]. The statistics of the created ontological schemas are shown in Table 1. In Table 1, concepts refer to entities such as class names and class attributes. Properties represent relationships established between concepts, such as color, texture, subclass, etc. RDF triples consist of three elements, two concepts, and a property.

Table 1. Ontological schema information for the AWA2 dataset

Dataset	RDF Triples	Concepts	Properties
AWA2	1256	180	12

In GZSL applications, the input dimensions of generative networks are determined by the dimensions of visual features and semantic attributes. The visual and semantic feature dimensions of the AWA2 dataset used in our study are shown in Table 2. The visual features of the images are 2048-dimensional. For semantic embeddings, 85-dimensional class-level attributes, 100-dimensional structure-based representation, and 100-dimensional text-based representation are utilized.

Table 1. Feature dimensions for the AWA2 dataset

Dataset	Visual Features	Semantic Attributes	RDF	Textual Descriptions
AWA2	2048	85	100	100

3.4. Generative-based networks

The examples generated by VAE are often blurry. Similarly, the examples generated by GAN are not natural. However, the combination of VAE and GAN produces much more realistic, natural images [20]. In this study,

the VAE-GAN-based model includes Encoder, Generator, Discriminator, and Decoder networks. All networks in the model have 4096 hidden units and are two-layer fully connected networks. The proposed architecture is shown in Fig. 2. In the workflow, first, the real features of seen classes x and semantic embedding a are applied to the input of the Encoder, and the parameters of a noise distribution z are extracted. Then, the extracted z and semantic embedding a are applied to the input of the Generator, and synthetic features $\hat{x}$ are generated. Synthetic features $\hat{x}$ and original features x are compared using Binary Cross-Entropy loss (L_{BCE}). Up to this point, it is the standard VAE approach. Encoder and Generator, which constitute the VAE, are trained using the L_{BCE} and the Kullback-Leibler divergence (L_{KL}). The synthetic feature $\hat{x}$ or the original feature x, along with semantic embedding a, is applied to the input of the Discriminator, and the Discriminator learns to distinguish synthetic and original features. Here, Generator and Discriminator follow the standard GAN approach. Generator and Discriminator are trained using the Wasserstein GAN loss (L_W). To improve classification performance, the synthetic feature $\hat{x}$ or the original feature x is applied to the input of the Decoder, and the developed synthetic feature $\hat{x}$ is applied to the hidden layer of the Generator. The enhanced synthetic feature $\hat{x}$ is again applied to the inputs of the Discriminator and Decoder. Discriminator calculates the L_W to determine whether the visual feature is real or fake. The latent embeddings transformed by the decoder are combined with the corresponding visual features x and $\hat{x}$, and trained using a cycle-consistency loss (L_R). Finally, the losses obtained from the Discriminator and Decoder are calculated for training and used for ZSL and GZSL classification.

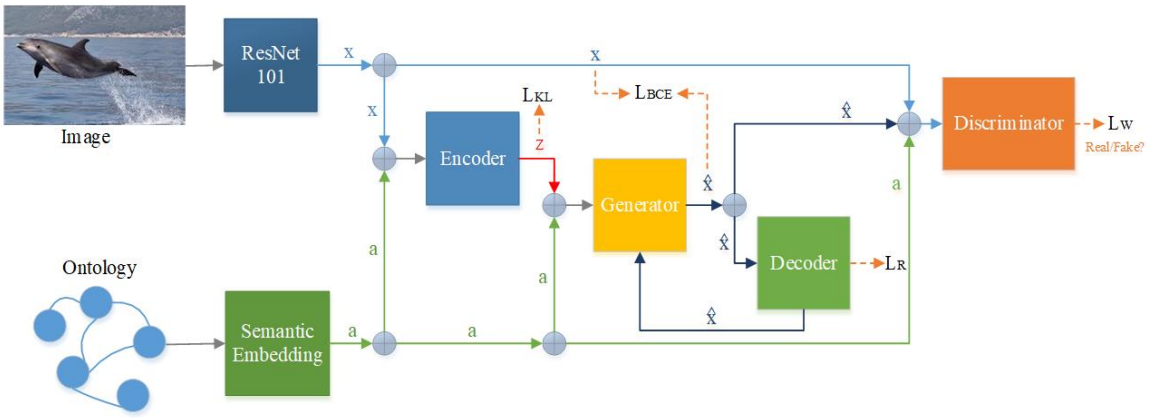

Figure 2. Illustration of the proposed architecture

4. Experimental Result

In this section, the evaluation of our proposed study, comparisons with other methods, and analyses of the model are presented.

4.1. Dataset

We evaluate our method using the AWA2 (Animals with Attributes 2) [34] dataset, which is suitable for ontology creation. The AWA2 dataset contains images from 50 classes, with 40 of these classes proposed as seen classes and 10 as unseen classes based on the Proposed Split (PS). AWA2, comprising a total of 37,322 images, is a coarse-grained dataset suitable for ontology creation. Statistical information about the AWA2 dataset is provided in Table 3.

Table 2. Statistics for the AWA2 dataset.

Dataset	Seen Classes	Unseen Classes	Total Classes	Total Images
AWA2	40	10	50	37322

4.2. Performance metrics and evaluation

In our study, we examine classification performances for both GZSL and traditional ZSL tasks. The best accuracy rate is used for ZSL performance measurements in the experiments. For GZSL performance measurements, the commonly used harmonic mean is selected. To calculate the harmonic mean, the accuracy rates of seen and unseen classes are utilized, as shown in Equation 1. In the equation, the harmonic mean (H) is defined in terms of the accuracy rates of seen classes (Acc_S) and unseen classes (Acc_U).

$$H = \frac{2 \times Acc_S \times Acc_U}{Acc_S + Acc_U} \quad (1)$$

Table 4 displays the experimental results of the proposed method and state-of-the-art methods for both ZSL and GZSL on the AWA2 dataset. The table indicates the best accuracy (T1) for ZSL performance, and for GZSL performance, it shows the results for unseen classes (U), seen classes (S), and the harmonic mean (H). Performance measurements are calculated as percentages, and the best results are highlighted in bold. Looking at Table 4, our proposed method achieved the best H value with a GZSL performance of 66.29%. For ZSL tasks, it secured the third position with a performance of 69.69%. The proposed method demonstrates a 1.19% improvement for the GZSL task.

Table 3. ZSL and GZSL experimental results performed with the AWA dataset.

Methods	**T1**	**S**	**U**	**H**
MVAAD [36].	69.50	93.40	30.70	49.20
Cramer GAN [37].	72.40	-	-	65.00
Tf-GCZSL [38].	-	64.89	40.23	48.33
DGEM [39].	67.30	69.80	43.40	53.40
SRSA [40].	68.30	59.60	38.10	46.50
Niu et al. [41].	-	66.00	59.30	62.50
ZSLGC-MLO [42].	**73.10**	71.20	57.80	63.80
Zhang et al. [43]	-	72.40	59.10	65.10
Geng et al. [26]	62.65	59.59	50.58	54.71
Ours	69.69	79.05	57.08	**66.29**

4.3. Model analysis

4.3.1. Ablation study

Ablation experiments were conducted to investigate the impact of semantic representations in our study. We evaluated different combinations of semantic attributes (att), ontology (onto), and textual descriptions (text). The results obtained from the experiments are shown in Table 5, with the best results highlighted in bold. According to the results, the best T1 and H values were achieved when using semantic attributes and ontology together.

Table 4. Ablation experiments for the AWA dataset

Methods	**T1**	**S**	**U**	**H**
Ours + att + onto	**69.69**	79.05	57.08	**66.29**
Ours + att + text	60.40	77.95	49.55	60.58
Ours + att + onto + text	67.43	73.79	60.10	66.25

4.3.2. Parameter analysis

In our experiments, we examined the effects of classification learning rates of 0.00001, 0.0001, and 0.0005 on U, S, and H. The results of the classification learning rates are shown in Fig. 3. Looking at Fig. 3, the best result was obtained with a learning rate of 0.0005. Additionally, the results indicate that different classification learning rates have an impact on the outcomes.

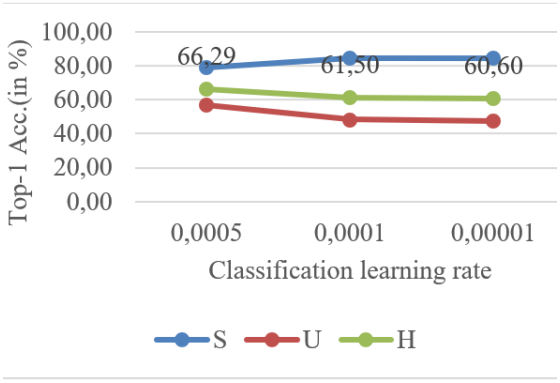

Figure 3. Results of classification learnibg rates

5. Conclusions and Discussion

In this paper, we proposed a generative-based model enriched with semantic representations for GZSL tasks. We utilized VAE-GAN generator networks to generate synthetic images for unseen classes. We leveraged an ontology created with RDF for the semantic representations of classes. Thus, by using both the numerical values of semantic attributes and their meaningful relationships, we created a highly discriminative semantic embedding. VAE establishes tight relationships between the visual and semantic domains. It is known that GAN prevents mode collapse issues. Taking advantage of the strong features of VAE and GAN, we synthesized image features and addressed data imbalance. We evaluated the performance of our proposed model on both standard ZSL and generalized ZSL using the AWA2 dataset. We compared the performance of our proposed model with the performances of the latest technology methods, achieving an additional improvement of 1.19 points for the GZSL task.

In our future work, we aim to enhance the success achieved in this study. We plan to create an ontology using the OWL language. We believe that incorporating the innovations brought by the OWL language into our ontology structure will contribute to the literature by improving the performance of our model.

Conflict of Interest Statement

The authors declare that there is no conflict of interest.

References

[1] F. Lv, J. Zhang, G. Yang, L. Feng, Y. Yu, and L. Duan, "Learning cross-domain semantic-visual relationships for transductive zero-shot learning," *Pattern Recognit.*, vol. 141, p. 109591, Sep. 2023. doi:10.1016/j.patcog.2023.109591

[2] W. Alhoshan, A. Ferrari, and L. Zhao, "Zero-shot learning for requirements classification: An exploratory study," *Inf. Softw. Technol.*, vol. 159, p. 107202, Jul. 2023. doi:10.1016/j.infsof.2023.107202

[3] E. Çelik and T. Dalyan, "Unified benchmark for zero-shot Turkish text classification," *Inf. Process. Manag.*, vol. 60, no. 3, p. 103298, May 2023. doi:10.1016/j.ipm.2023.103298

[4] "Zero-shot stance detection via multi-perspective contrastive learning with unlabeled data - ScienceDirect," [Online]. Available: https://www.sciencedirect.com/science/article/abs/pii/S0306457323000985. [Accessed: 07 Dec. 2023].

[5] X. Li *et al.*, "A structure-enhanced generative adversarial network for knowledge graph zero-shot relational learning," *Inf. Sci.*, vol. 629, pp. 169–183, Jun. 2023. doi:10.1016/j.ins.2023.01.113

[6] J. Eronen, M. Ptaszynski, and F. Masui, "Zero-shot cross-lingual transfer language selection using linguistic similarity," *Inf. Process. Manag.*, vol. 60, no. 3, p. 103250, May 2023. doi:10.1016/j.ipm.2022.103250

[7] X. Liu, J. Gao, X. He, L. Deng, K. Duh, and Y.-Y. Wang, "Representation Learning Using Multi-Task Deep Neural Networks for Semantic Classification and Information Retrieval," in *Proceedings of the 2015 Conference of the North American Chapter of the*

Association for Computational Linguistics: Human Language Technologies, Denver, Colorado: Association for Computational Linguistics, 2015, pp. 912–921. doi:10.3115/v1/N15-1092

[8] F. Al Kassar and F. Armetta, "Extracting Tags from Large Raw Texts Using End-to-End Memory Networks," in *Proceedings of the 2nd Workshop on Semantic Deep Learning (SemDeep-2)*, D. Gromann, T. Declerck, and G. Heigl, Eds., Montpellier, France: Association for Computational Linguistics, Sep. 2017, pp. 33–40. [Online]. Available: https://aclanthology.org/W17-7305. [Accessed: 04 Dec. 2023].

[9] G. Petrucci, C. Ghidini, and M. Rospocher, "Ontology Learning in the Deep," in *Knowledge Engineering and Knowledge Management*, vol. 10024, E. Blomqvist, P. Ciancarini, F. Poggi, and F. Vitali, Eds., in Lecture Notes in Computer Science, vol. 10024. , Cham: Springer International Publishing, 2016, pp. 480–495. doi:10.1007/978-3-319-49004-5_31

[10] D. Jurafsky and J. H. Martin, "Speech and Language Processing," [Online]. Available: https://web.stanford.edu/~jurafsky/slp3/. [Accessed: 04 Dec. 2023].

[11] S. Russell and P. Norvig, *Artificial Intelligence: A Modern Approach*, 3 edition. Upper Saddle River: Pearson, 2009.

[12] "Semantic Web - W3C," [Online]. Available: https://www.w3.org/standards/semanticweb/. [Accessed: 04 Dec. 2023].

[13] J. Hendler, T. Berners-Lee, and E. Miller, "Integrating applications on the semantic web," *J. Inst. Electr. Eng. Jpn.*, vol. 122, pp. 676–680, Jan. 2002. doi:10.1541/ieejjournal.122.676

[14] F. Pourpanah *et al.*, "A Review of Generalized Zero-Shot Learning Methods," *IEEE Trans. Pattern Anal. Mach. Intell.*, pp. 1–20, 2022. doi:10.1109/TPAMI.2022.3191696

[15] "LearnOpenCV," [Online]. Available: https://learnopencv.com/zero-shot-learning-an-introduction/. [Accessed: 04 Dec. 2023].

[16] C. Patrício and J. C. Neves, "Zero-shot face recognition: Improving the discriminability of visual face features using a Semantic-Guided Attention Model," *Expert Syst. Appl.*, vol. 211, p. 118635, Jan. 2023. doi:10.1016/j.eswa.2022.118635

[17] J. Wu, Y. Zhang, X. Zhao, and W. Gao, "A Generalized Zero-Shot Framework for Emotion Recognition from Body Gestures," arXiv, Oct. 20, 2020. doi:10.48550/arXiv.2010.06362

[18] R. Gao *et al.*, "Zero-VAE-GAN: Generating Unseen Features for Generalized and Transductive Zero-Shot Learning," *IEEE Trans. Image Process.*, vol. 29, pp. 3665–3680, Jan. 2020. doi:10.1109/TIP.2020.2964429

[19] S. Narayan, A. Gupta, F. S. Khan, C. G. M. Snoek, and L. Shao, "Latent Embedding Feedback and Discriminative Features for Zero-Shot Classification." arXiv, Jul. 18, 2020. doi:10.48550/arXiv.2003.07833

[20] J. Bao, D. Chen, F. Wen, H. Li, and G. Hua, "CVAE-GAN: Fine-Grained Image Generation through Asymmetric Training." arXiv, Oct. 12, 2017. doi:10.48550/arXiv.1703.10155

[21] Z. Han, Z. Fu, G. Li, and J. Yang, "Inference guided feature generation for generalized zero-shot learning," *Neurocomputing*, vol. 430, pp. 150–158, Mar. 2021. doi:10.1016/j.neucom.2020.10.080

[22] "Semantic Deep Learning," [Online]. Available: https://www.dfki.de/~declerck/semdeep-4/index.html. [Accessed: 04 Dec. 2023].

[23] H. Wang, "Semantic Deep Learning," 2015.

[24] Y. Geng *et al.*, "Generative Adversarial Zero-shot Learning via Knowledge Graphs," arXiv, Apr. 06, 2020. doi:10.48550/arXiv.2004.03109

[25] Y. Geng *et al.*, "OntoZSL: Ontology-enhanced Zero-shot Learning," arXiv.org, [Online]. Available: https://arxiv.org/abs/2102.07339v1. [Accessed: 08 Dec. 2023].

[26] Y. Geng *et al.*, "Benchmarking knowledge-driven zero-shot learning," *J. Web Semant.*, vol. 75, p. 100757, Jan. 2023. doi:10.1016/j.websem.2022.100757

[27] K. He, X. Zhang, S. Ren, and J. Sun, "Deep Residual Learning for Image Recognition." arXiv, Dec. 10, 2015. doi:10.48550/arXiv.1512.03385

[28] H. Zhang, H. Que, J. Ren, and Z. Wu, "Transductive semantic knowledge graph propagation for zero-shot learning," *J. Frankl. Inst.*, vol. 360, no. 17, pp. 13108–13125, Nov. 2023. doi:10.1016/j.jfranklin.2023.07.009

[29] L. Nieto-Piña and R. Johansson, "Automatically Linking Lexical Resources with Word Sense Embedding Models," in *Proceedings of the Third Workshop on Semantic Deep Learning*, L. E. Anke, D. Gromann, and T. Declerck, Eds., Santa Fe, New Mexico: Association

for Computational Linguistics, Aug. 2018, pp. 23–29. [Online]. Available: https://aclanthology.org/W18-4003. [Accessed: 04 Dec. 2023].

[30] Y. Zhou, J. Shah, and S. Schockaert, "Learning Household Task Knowledge from WikiHow Descriptions," in *Proceedings of the 5th Workshop on Semantic Deep Learning (SemDeep-5)*, L. Espinosa-Anke, T. Declerck, D. Gromann, J. Camacho-Collados, and M. T. Pilehvar, Eds., Macau, China: Association for Computational Linguistics, Aug. 2019, pp. 50–56. [Online]. Available: https://aclanthology.org/W19-5808.

[31] D. Loureiro and A. Jorge, "LIAAD at SemDeep-5 Challenge: Word-in-Context (WiC)," in *Proceedings of the 5th Workshop on Semantic Deep Learning (SemDeep-5)*, L. Espinosa-Anke, T. Declerck, D. Gromann, J. Camacho-Collados, and M. T. Pilehvar, Eds., Macau, China: Association for Computational Linguistics, Aug. 2019, pp. 1–5. [Online]. Available: https://aclanthology.org/W19-5801. [Accessed: 04 Dec. 2023].

[32] J. Park, K. Kim, W. Hwang, and D. Lee, "Concept embedding to measure semantic relatedness for biomedical information ontologies," *J. Biomed. Inform.*, vol. 94, p. 103182, Jun. 2019. doi:10.1016/j.jbi.2019.103182

[33] T. Murata *et al.*, "Predicting Relations Between RDF Entities by Deep Neural Network," Nov. 2017, pp. 343–354. doi:10.1007/978-3-319-70407-4_43

[34] G. Petrucci, M. Rospocher, and C. Ghidini, "Expressive ontology learning as neural machine translation," *J. Web Semant.*, vol. 52–53, pp. 66–82, Oct. 2018. doi:10.1016/j.websem.2018.10.002

[35] J.-R. Ruiz-Sarmiento, C. Galindo, J. Monroy, F.-A. Moreno, and J. Gonzalez-Jimenez, "Ontology-based conditional random fields for object recognition," *Knowl.-Based Syst.*, vol. 168, pp. 100–108, Mar. 2019. doi:10.1016/j.knosys.2019.01.005

[36] L. Tian *et al.*, "Multi-scale visual attention for attribute disambiguation in zero-shot learning," *Signal Process. Image Commun.*, vol. 103, p. 116614, Apr. 2022. doi:10.1016/j.image.2021.116614

[37] J. Liu, L. Fu, H. Zhang, Q. Ye, W. Yang, and L. Liu, "Learning discriminative and representative feature with cascade GAN for generalized zero-shot learning," *Knowl.-Based Syst.*, vol. 236, p. 107780, Jan. 2022. doi:10.1016/j.knosys.2021.107780

[38] C. Gautam, S. Parameswaran, A. Mishra, and S. Sundaram, "Tf-GCZSL: Task-free generalized continual zero-shot learning," *Neural Netw.*, vol. 155, pp. 487–497, Nov. 2022. doi:10.1016/j.neunet.2022.08.034

[39] J. Zhang, Y. Geng, W. Wang, W. Sun, Z. Yang, and Q. Li, "Distribution and gradient constrained embedding model for zero-shot learning with fewer seen samples," *Knowl.-Based Syst.*, vol. 251, p. 109218, Sep. 2022. doi:10.1016/j.knosys.2022.109218

[40] Y. Liu, X. Gao, J. Han, L. Liu, and L. Shao, "Zero-shot learning via a specific rank-controlled semantic autoencoder," *Pattern Recognit.*, vol. 122, p. 108237, Feb. 2022. doi:10.1016/j.patcog.2021.108237

[41] C. Niu *et al.*, "Unbiased feature generating for generalized zero-shot learning," *J. Vis. Commun. Image Represent.*, vol. 89, p. 103657, Nov. 2022. doi:10.1016/j.jvcir.2022.103657

[42] X. Xu, X. Bao, X. Lu, R. Zhang, X. Chen, and G. Lu, "An end-to-end deep generative approach with meta-learning optimization for zero-shot object classification," *Inf. Process. Manag.*, vol. 60, no. 2, p. 103233, Mar. 2023. doi:10.1016/j.ipm.2022.103233

[43] J. Zhang, S. Liao, H. Zhang, Y. Long, Z. Zhang, and L. Liu, "Data driven recurrent generative adversarial network for generalized zero shot image classification," *Inf. Sci.*, vol. 625, pp. 536–552, May 2023. doi:10.1016/j.ins.2023.01.039

This is an open access article under the CC-BY license